Entrapment of mobile radioactive elements with coordination polymers and supported nanoparticles

Giovanni Massasso

ICG Montpellier | Institut Charles Gerhardt

POLE chimie Balard

UNIVERSITE MONTPELLIER 2

SCIENCES ET TECHNIQUES DU LANGUEDOC

THESE

Pour obtenir le grade de

DOCTEUR DE L'UNIVERSITE MONTPELLIER II

Discipline: Chimie

Ecole Doctoral Sciences Chimiques et Physiques

Pôle Chimie Balard

Entrapment of mobile radioactive elements with coordination polymers and supported nanoparticles

Présentée et soutenue publiquement

par

Giovanni MASSASSO

Le 13 octobre 2014 devant le jury composé de

Dr. Yannick GUARI	Directeur de thèse
Prof. Guillaume MAURIN	Examinateur
Dr. Agnès GRANDJEAN	Examinatrice
Prof. Barbara ONIDA	Examinatrice
Dr. Christian SERRE	Rapporteur
Prof. José Antonio REAL	Rapporteur

cnrs

um2 Université Montpellier 2

ICGM

Politecnico di Torino 1859 1906

Resumé en français

La production d'énergie nucléaire nécessite des systèmes adaptés pour améliorer les procédures de stockage et de confinement des déchets radioactifs. De plus, la capture des éléments radioactifs mobiles dans les effluents des centrales nucléaires demande une amélioration de la capacité et de la sélectivité des matériaux utilisés. L'iode 129-I est un des produits les plus critiques à confiner et il est produit pendant le procédé de recyclage des déchets nucléaires pour extraire l'uranium et le plutonium dans les centrales de type MOX (Mixed Oxide Fuel Plants). Dans ce travail de thèse, la classe de matériaux moléculaires, dénommée structures de type Hofmann, a été étudiée en tant que matériaux massifs et sous la forme de nanoparticules supportées, pour la capture sélective d'iode moléculaire. Cette famille de matériaux à pour formule générale M'(L)[M''$(CN)_4$] où M' = Ni^{II} or Co^{II}; L = pyrazine, 4,4'-bipyridine, 4,4'-azopyridine; M'' = Ni^{II}, Pd^{II} or Pt^{II}. Ces matériaux étaient précédemment connus pour leur habilité à former des clathrates, c'est-à-dire pour leur capacité à accueillir dans leur microporosité des molécules de nature différentes, retenues par des forces faibles (Van der Waals). En premier lieu, les matériaux M'(L)[M''$(CN)_4$] ont été précipités sous la forme de poudres microcristallines à l'état massif. L'insertion d'iode dans le réseau des matériaux massifs a été effectuée par différents protocoles: 1) adsorption d'iode dans des solutions de cyclohexane à température ambiante; 2) adsorption de vapeurs d'iode en phase gazeuse à 80 °C; 3) adsorption de vapeurs d'iode en phase gazeuse à 80 °C et en présence de vapeurs d'eau. Les matériaux contenants l'iode ont été caractérisés par les techniques DRX (et affinement de LeBail), spectroscopie IR et Raman, spectroscopie UV-VIS solide, ATG couplée masse, mesures de conductivité. Les différents protocoles pour l'insertion d'iode dans les différents réseaux présentent parfois des différences au niveau des capacités maximales mais la nature de l'iode confiné est influencée uniquement par la nature de la structure de type Hofmann. Pour la capture en solution, les structures Ni^{II}(pz)[$Ni^{II}(CN)_4$], Ni^{II}(pz)[$Pd^{II}(CN)_4$] et Co^{II}(pz)[$Ni^{II}(CN)_4$] présentent une capacité d'adsorption d'une molécule d'iode par unité de maille. L'iode confiné est physisorbé sous la forme d'iode moléculaire en interaction avec le réseau. Les modélisations Monte-Carlo ont confirmé la capacité maximale expérimentale observée et ont indiqué que l'iode interagit soit avec la pyrazine, soit avec les cyanures. Sur la base des données expérimentales, la modulation des métaux dans le réseau a montré une légère différence dans la force d'interaction entre l'iode et le réseau et une adaptation de la maille spécifique pour chaque composition. L'adaptation de la maille a été corrélée avec le signal Raman pour l'iode en interaction avec le réseau et avec la température de désorption de l'iode. Le réseau Ni^{II}(pz)[$Ni^{II}(CN)_4$] a montré un léger gonflement (2%) après adsorption d'iode; le signal Raman pour l'iode confiné a été observé à 165 cm^{-1} et sur la base des mesures ATG couplée masse, la désorption commence à 150 °C. Dans le cas de Ni^{II}(pz)[$Pd^{II}(CN)_4$], nous avons observé un signal Raman légèrement plus élevé (167 cm^{-1}) et une température de désorption plus basse (140 °C), par rapport à Ni^{II}(pz)[$Ni^{II}(CN)_4$]. Par ailleurs, la structure Co^{II}(pz)[$Ni^{II}(CN)_4$] a montré une contraction de la maille d'environ 5% du fait d'une

interaction plus forte. Cette interaction plus forte a été confirmée par un signal Raman plus faible (160 cm^{-1}) pour l'iode et une température de désorption d'iode plus élevée, par rapport au cas $Ni^{II}(pz)[Ni^{II}(CN)_4]$. Une complète régénération du réseau à été possible, puisque l'iode est complètement désorbé avant que le réseau ne commence à se décomposer. Le cycle d'adsorption et désorption a été répété 3 fois pour les réseaux $Ni^{II}(pz)[Ni^{II}(CN)_4]$ et $Ni^{II}(pz)[Pd^{II}(CN)_4]$ et nous avons observé une excellente résistance au cycles et une capacité toujours élevée. De plus, d'autres études concernant cette structure ont permis d'évaluer la capture sélective d'iode en présence de vapeurs d'eau. Nous avons observé une diminution de la capacité pour les réseaux contenants le cation Ni^{2+} (en position octaédrique). Nous avons corrélé les résultats avec des mesures de spectroscopie IR *in-situ* d'adsorption d'eau sur les réseaux étudiés, qui ont montré que le réseau $Ni^{II}(pz)[Ni^{II}(CN)_4]$ formait des complexes avec l'eau plus stables que pour $Co^{II}(pz)[Ni^{II}(CN)_4]$. Nous avons émis l'hypothèse que les complexes se formaient avec les cations Ni^{2+} non-saturés sur la surface des grains et que cela pouvait avoir une influence sur la diffusion de l'iode dans le réseau. Pour le réseau $Ni^{II}(pz)[Pt^{II}(CN)_4]$, nous avons observé un mécanisme de capture différent puisque ce réseau contenant Pt a réagi avec l'iode en donnant le complexe de coordination $Ni^{II}(pz)[Pt^{II/IV}(CN)_4].I^-$. La formation de ce type de complexe était déjà observée dans la littérature par Ohtani *et al.* lesquels avaient préparé le complexe *via* une synthèse *in-situ.* L'iodure Pt^{IV}-I s'est décomposé après 250 °C et a montré un signal Raman caractéristique à 129 cm^{-1}. Les mesures de conductivité ont montré également que l'iodure dans la structure $Ni^{II}(pz)[Pt^{II/IV}(CN)_4]•I^-$ est bloqué et qu'il n'y a pas d'augmentation significative de la conductivité après insertion d'iode. Par contre, les mesures de conductivité ont montré que l'introduction d'iode dans les structures $M'^{I}(pz)[M'(CN)_4]$ avec M' = Ni^{II} ou Co^{II} et M'' = Ni^{II} ou Pd^{II} augmentait la conductivité en raison de phénomènes de propagation de charge entre les molécules d'iode. Ensuite, la substitution du ligand organique pyrazine par d'autres ligands plus longs, c'est-à-dire la 4,4'-bipyridine (bpy) ou la 4,4'-azopyridine (azpy), qui possèdent des cages plus grandes a conduit à une diminution de la capacité maximale de capture d'iode. Les données expérimentales ont suggéré que pour un meilleur confinement d'iode, le réseau doit disposer de cages avec une dimension très proche de la molécule d'iode (0.5 nm). L'utilisation du ligand 4,4'-azopyridine a conduit à une capacité double par rapport à l'utilisation du ligand 4,4'-bipyridine, c'est-à-dire $Ni^{II}(azpy)[Ni^{II}(CN)_4]•0.5I_2$ au lieu de $Ni^{II}(bpy)[Ni^{II}(CN)_4]•0.25I_2$, probablement en raison d'une interaction différente avec le ligand organique. Après l'étude des matériaux massifs, nous avons considéré la préparation de nanoparticules supportées de $Ni^{II}(pz)[Ni^{II}(CN)_4]$ pour la capture d'iode. Nous avons obtenu des nanoparticules *via* un procédé étape-par-étape*,* avec imprégnation d'une série de silices mésoporeuses greffées par un ligand diamine, en utilisant les précurseurs de $Ni^{II}(pz)[Ni^{II}(CN)_4]$. Nous avons utilisé comme supports, une silice SBA-15 modifiée et des billes de verre poreux pour obtenir respectivement les nanocomposites Sil@NP and Glass@NP. Nous avons estimé un dépôt d'environ 39 wt% de nanoparticules pour Sil@NP et environ 17 wt% pour Glass@NP. Les différences de quantité déposée étant liées à la différence de surface spécifique et à la quantité de diamine. Par microscopie électronique à transmission, nous avons observé pour Sil@NP des nanoparticules de diamètre moyen 2.8 nm. L'adsorption

d'iode dans les nanoparticules a été confirmée par spectroscopie FT-IR. Nous avons observé le même déplacement de la bande IR des cyanures que dans le cas du matériau massif (de 2174 cm^{-1} avant capture d'iode à 2165 cm^{-1} après capture d'iode). Les traitements thermiques ont indiqué que l'iode dans les nanoparticules pouvait être désorbé dans l'intervalle 150-250 °C, mais que par contre l'iode chimisorbé sur la diamine était retenu jusqu'à décomposition du matériau. Nous avons pu estimer que la capacité de capture des nanoparticules était très proche de la capacité du massif $Ni^{II}(pz)[Ni^{II}(CN)_4]\bullet I_2$. Finalement, les structures de type Hofmann sous la forme de matériaux massifs et de nanoparticules supportées ont montré une excellente affinité pour l'iode moléculaire et une capacité de capture élevée dans différentes conditions.

En parallèle aux études d'adsorption de l'iode, une partie secondaire de la thèse traite de la capture du cation Co^{2+} en solution aqueuse. Le projet a ciblé l'évaluation de l'utilisation de matériaux à base de Bleu de Prusse pour la capture sélective de l'isotope radioactif ^{60}Co présent dans les effluents des centrales nucléaires. La meilleure performance a été observée pour les nanoparticles supportées de Bleu de Prusse, même en présence d'autres cations bivalents (Mg^{2+} and Ca^{2+}).

Remerciements / *Ringraziamenti*

Mes trois premières années en France viennent de se terminer et la réussite de cette excellente expérience à l'étranger a été possible grâce à la contribution de beaucoup de gens, je vais donc chercher à n'oublier personne. Je remercie d'abord le responsable d'équipe **Hubert Mutin**, pour m'avoir accueilli dans le laboratoire CMOS de l'UM2. Le remerciement le plus sincère va sûrement à mes encadrants **Yannick Guari**, **Prof. Joulia Larionova** et **Jérôme Long** pour tout ce que j'ai pu apprendre grâce à eux dans le domaine de la recherche scientifique, pour leur énorme soutien et le travail ensemble, qui a été très agréable, pas seulement pour leur professionnalité, mais aussi pour leur cordialité et leur constante disponibilité. Je remercie également énormément les collaborateurs français **Prof. Guillaume Maurin**, **Sabine Devautour-Vinot**, **Agnès Grandjean**, **Bruno Donnadieu** et **Julien Haines** pour leur contribution au travail de thèse, leurs conseils importants et leur support.

*Un ringraziamento speciale va anche: alla Prof.ssa **Barbara Onida**, grazie alla quale ho trovato questo dottorato in Francia e con la quale ho avuto la fortuna di continuare a collaborare in questi anni imparando ancora di più dalla sua esperienza; a **Sonia Fiorilli, Edivge Celasco** e **Micaela Castellino** del Politecnico di Torino per la loro partecipazione alle misure svolte a Torino; a **Yulyanna Carrasco**, stagista durante il mio secondo anno di dottorato, per la sua partecipazione al lavoro sperimentale; a **mio padre**, **mia madre** e **mia sorella** per il loro costante sostegno e il loro prezioso affetto, che sono stati soprattutto fondamentali per la riuscita di questa (prima) esperienza francese; alle mie zie **Pina** e **Rosetta** per avermi sempre pensato provvedendo alle scorte di cibo nostrano; agli **amici italiani** che ho conosciuto nel corso dei tre anni a Montpellier per il tempo passato insieme e per avermi fatto sentire un po' di più a casa; agli **amici di vecchia data** di Torino e quelli sparsi per l'Europa che pur a distanza hanno sempre saputo farsi sentire vicini.*

En revenant au français, je tiens à remercier encore: ma voisine de paillasse **Maria Rodriguez Castillo** pour l'aide dans le labo et la bonne compagnie pendant le travail; l'ex-postdoc **Alexey Tokarev** pour toutes les connaissances transmises au début de la thèse; les techniciens **Serge Bertrand**, **José-marie Ruiz**, **Frédéric Fernandez, Veronique Richard, Franck Godiard, Dominique Granier, David Bourgogne** pour leur travail toujours très utile; les autres participants au **projet MEMFIS** (Yves Barré, Eric Loradour, Bernard Rottner); toutes les autres personnes du **labo CMOS** (étudiants, post-docs, permanents) pour leur cordialité et leur aide occasionnelle dans le labo; **Prof. André Ayral** et **Ing. Sylvain Petigny** pour l'excellente expérience d'encadrement dans le cadre des projets tuteurés Objectif Recherche et les étudiants encadrés **Matthieu, Vincent, Adrien, Julien, Jérémy** et **Vanessa** pour leur formidable travail et leur sympathie; **Prof. Jeffrey Culp** de Pittsburgh et **Prof. Antonio Real** de Valence pour avoir inspiré le travail et pour avoir gentiment partagé les données CIFs; merci encore à Prof. Real et à **Christian Serre** pour avoir accepté d'être les rapporteurs de ma thèse et finalement je remercie encore C. Serre et son

équipe de l'ILV pour m'avoir motivé encore plus vers la fin en m'offrant une excellente opportunité pour l'*après-thèse*.

Summary

Background of the project	11
Thesis plan	12
GENERAL INTRODUCTION	**13**
State of the art for the entrapment of the volatile $^{129}I_2$	13
Coordination chemistry and applications in the nuclear industry	17
CHAPTER 1 – Entrapment of the molecular iodine with the bulk Hofmann-type structures	**25**
Introduction to the Hofmann-type clathrates	27
1.1 – Characterization of the iodine adsorption with the Hofmann-type structures in solution and in vapours	39
1.1.1 – The Hofmann-type structure $Ni^{II}(pz)[Ni^{II}(CN)_4]$ and the capture of the molecular iodine	39
1.1.2 – Replacement of the square planar metallic centre: $Ni^{II}(pz)[M''(CN)_4]$ series with M'' = Ni^{II}, Pd^{II}, Pt^{II}	60
1.1.3 – Replacement of the octahedral metallic centre: M'(pz)[$Ni^{II}(CN)_4$] series with M' = Ni^{II}, Co^{II}	76
1.1.4 – Combined effect with concurrent replacement of both metallic centres	86
1.1.5 – Replacement of the bidentate ligand L: $Ni^{II}(L)[Ni^{II}(CN)_4]$ series	89
1.2 – Supplementary studies	105
1.2.1 – Selective entrapment of iodine in water vapours by the Hofmann-type structures	105
1.2.2 – Grand Canonical Monte-Carlo modelling of the entrapment of iodine with the Hofmann-type Structures	111
1.2.3 – Electrical properties of the Hofmann-type structures	114
Conclusion	119
CHAPTER 2 – Supported nanoparticles for the entrapment of mobile radioactive elements	**127**
Introduction to the supported nanoparticles of coordination polymers	129
2.1 – Supported nanoparticles of $Ni^{II}(pz)[Ni^{II}(CN)_4]$ for the reversible capture of the molecular Iodine	133
2.1.1 – Mesoporous silica based nanocomposite (Sil@NP) containing $Ni^{II}(pz)[Ni^{II}(CN)_4]$ nanoparticles and the iodine entrapment	134
2.1.2 - Porous glass beads based nanocomposite (Glass@NP) containing $Ni^{II}(pz)[Ni^{II}(CN)_4]$ nanoparticles and the iodine entrapment	143
2.1.3 - Cycling ability of Sil@NP and Glass@NP	148
2.2 - Nanocomposites of Prussian Blue for the selective entrapment of Co^{2+}	152
Conclusion	162
GENERAL CONCLUSION	**165**
EXPERIMENTAL SECTION	**169**
ANNEXES	**181**

Background of the project.

Nowadays nuclear industry still seems a competitive technology for the energy supply at both household and industrial level, especially with current increasing concerns about CO_2 emissions and the high prices of fossil fuels. France, the second worldwide biggest producer of nuclear energy after the U.S.A., has produced about 407 TWh in 2012 and 405 TWh in 2013,[1] granting low prices for household and industrial customers and remaining an important exporter to neighbours as Italy, Belgium, Switzerland and Germany. The accident in Fukushima in 2011 has newly created concerns about the safety and the future of the nuclear industry, pushing Germany to reconsider the coal extraction and U.S.A. to bet on the natural gas option as alternative fuel.[2] On the other side, China keeps on planning 30 new nuclear plants and France is considering to go on with next generation nuclear power plants as well, by reducing anyway the amount of produced nuclear energy to 50% of the total produced amount (from current 75%) by the year 2025.[3] After the lessons taken from Fukushima as well as older nuclear accidents (notably, Three Mile Island in 1979 and Chernobyl in1986) the next generation of nuclear power plants must imperatively enhance the safety and minimize the impact on the environment. The main environmental concern after the nuclear accident in Fukushima in 2011 was the contamination of the seawater that they injected in the plant for cooling the reactor. Decontamination of aqueous effluents is only one of the concerns to consider in the next generation power plants. The entrapment of the volatile $^{129}I_2$ is one of the major issues that still demands a suitable solution, granting for concurrent high selectivity, high storage capacity and low costs. Enhanced systems for the nuclear safety can derive from new advanced research in nanomaterials science.

Objectives of the thesis.

The present PhD thesis was carried out inside the ANR funded project MEMFIS ("Extraction of Radioelement using Innovative Functionalized Membranes"), coordinated by the Institut of Separative Chemistry in the nuclear site of Marcoule (ISCM) and the Institut Charles Gerhardt of Montpellier (ICGM). The aim of this project is to investigate functionalized materials for the selective entrapment of mobile radionuclides in solution and in vapours. The thesis project has seen as well the collaboration of several academic and industrial partners as CEA, ICT, Onectra, UM2, Politecnico di Torino. The present thesis includes the study of supported nanoparticles for the selective decontamination of radioactive $^{129}I_2$ and $^{60}Co^{2+}$ in solution. For each specific pollutant to confine, a suitable class of decontaminant materials was chosen, *i.e.* the Hofmann-type structures for I_2 and Prussian Blue analogues for Co^{2+}. For safety reasons, we focused on the entrapment of the stable isotopes. Since no exhaustive study about the affinity between the molecular iodine and the family of Hofmann-type structures has been published yet in literature, a consistent part of the thesis will be dedicated to this topic, as necessary introduction to the supported Hofmann-type nanoparticles.

Thesis Plan.

This manuscript is articulated in a general introduction and in a discussion about the most relevant results from the thesis research project. The discussion is articulated in two chapters. Chapter 1 introduces the Hofmann-type clathrates $M'(L)[M''(CN)_4].xG$ (where M' = Ni^{II}, Co^{II}; L = pyrazine, 4,4'-bipyridine or 4,4'-azopyridine; M'' = Ni^{II}, Pd^{II}, Pt^{II}) and is divided in 2 parts.

Part 1.1 will treat in the 4 sections, how this class of bulk materials was studied in the present experimental work for the entrapment of the molecular iodine:

- section 1.1.1 is about the capture of I_2 with $Ni^{II}(pz)[Ni^{II}(CN)_4]$;
- section 1.1.2 considers the analogue structures, where the square planar Ni^{II} is replaced by Pd^{II} and Pt^{II} and consequences on the cycling ability will be also discussed;
- section 1.1.3 treats the replacement of the octahedral Ni^{II} with Co^{II};
- section 1.1.4 considers a case of replacement of both metallic centres;
- section 1.1.5 focuses on the change of bidentate ligand pyrazine with other ligands;

Part 1.2 will include complementary studies of different nature, presented in 3 distinct sections:

- section 1.2.1 presents some considerations about the selective entrapment of iodine in vapours of water;
- section 1.2.2 will focus on the GCMC modelling performed on most of the analysed structures to simulate the adsorption of iodine;
- Section 1.2.3 includes the dielectric measurements performed on the structure $Ni^{II}(pz)[Ni^{II}(CN)_4]$ at different I_2-loadings and on a series Hofmann-type analogues.

Chapter 2 is about the nanocomposites for the selective entrapment of mobile radioactive elements and it consists of two parts. Part 2.1 focuses on the preparation of supported $Ni^{II}(pz)[Ni^{II}(CN)_4]$ nanoparticles inside mesoporous silicas and their performance in the entrapment of I_2 in solution. Part 2.2 considers the supported Prussian Blue nanoparticles for the entrapment of Co^{2+} in aqueous solutions and selectivity towards other cations.

GENERAL INTRODUCTION

-

State of the art for the entrapment of the volatile $^{129}I_2$

Nuclear fission of ^{235}U in the core of a nuclear power plant is responsible for the production of a large variety of radionuclides during the production of the nuclear energy as well as during the reprocessing methods to recover the fuel. The reprocessing of the spent nuclear fuel for the recovery of radionuclides ^{235}U and ^{239}Pu is a practice used in the *back-end* stage of the new generation Mixed Oxide Fuel (MOX) power plants (Figure 1).[4] However, the drawback of this technique is the production of radioactive volatile by-products during the thermal conditioning step (voloxidation) when the spent fuel is dissolved in a bath containing nitric acid. Volatile by-products mainly consist of ^{129}I (94-99%) together with other isotopes with a short lifetime as ^{131}I and ^{125}I and other radionuclides as ^{14}C, ^{3}H, ^{99}Tc, ^{85}Kr and ^{133}Xe.[5]

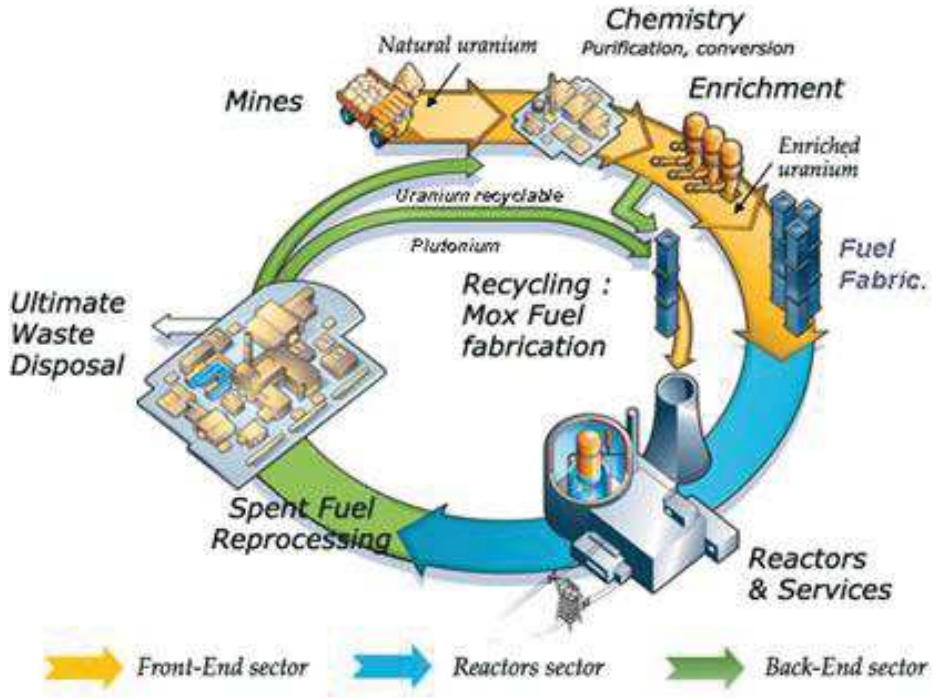

Figure 1 - Representation of the fuel cycles in a nuclear site (Source: www.laradioactivite.fr).

Iodine is believed to leave as iodide I^- but the contact with nitric acid oxidizes the iodide to molecular I_2.[6] The radionuclide ^{129}I is produced by the decay of natural uranium and it is stored mainly in seawater.[7] It has a long half-life time of $1.5 \cdot 10^7$ years that also means a low activity, with emissions of β, γ and X rays.[8] The decay product is the stable ^{129}Xe. The low energy β emissions of I^{129} do not present a significant hazard since they barely penetrate the outer layers of the

human skin, but γ and X rays are, by contrast, a hazard with consequences for the metabolism. The 30% of the iodine uptake is stored in the thyroid (the remaining 70% being expulsed with biological activities) and it is retained during a biological half-time of 120 days.[9] A long-term exposure can cause the insurgence of a thyroid cancer. Due to the hazard of ^{129}I released in the environment and its high volatility, precautions for the entrapment and the safe confinement of this radionuclide are demanded in the power plants with a reprocessing cycle of the spent fuel. It was estimated by the Ridge National Laboratory (RNL) that a single light-water reactor (LWR) produces 234 g of ^{129}I based on a uranium burn-up of 30'000 MWd/t (megawatt-day per ton). In handling the spent fuel, a single 5-tonn-per-day nuclear fuel reprocessing plant should process $3.2 \cdot 10^5$ g of ^{129}I per year.[10] The US Nuclear Regulatory Commission (NRC) has established limits of emissions, which in the case of ^{129}I means less than 0.185 GBq for the maximal fuel cycle emissions per GWy (gigawatt per year) of electric energy.[11] To respect the imposed limits, high performing methods for the entrapment of the radioactive iodine must be highly selective, since iodine is released in vapours containing not only other radionuclides but also NO_x, water and iodide compounds (ICN, HI, HOI, CH_3I).6 Efficiency must be high at the operating temperature of the out-gasses that are generally around 80 °C. Also, the confined iodine has to face thermal treatments for the final storage in molten glass so that high stability of the confined form is demanded. As described in recent litterature,[11] two types of methods have been developed so far for the ^{129}I capture: caustic or acidic scrubbing solutions and chemisorptions on silver-based materials.

The scrubbing method is subdivided in different possible techniques. The already operating technique so far is the alkaline scrubbing where the out-gases are treated with NaOH solutions following the reaction in solution:

Reaction 1 - Scrubbing solution method.

$$3I_2 + 6OH^- \leftrightarrow 5I^- + IO_3^- + 3H_2O$$

The iodides and the iodates, obtained by a dismutation reaction, precipitate as NaI and $NaIO_3$. This system is already used in the Reprocessing Facility of La Hague in France, Rokkashoko Reprocessing Plant in Japan and in Windscale and the THORP (Thermal Oxide Reprocessing Plant) facility in the United Kingdom. The capture by this system allows the confinement of the elemental iodine, but not of the organic iodine CH_3I. Also, this system has concerns about the safety of the implants due to a high corrosiveness and a liquid waste is produced demanding special treatments. Alternative scrubbing methods, as the *Iodox process*, the *Mercurex process* and the fluorocarbon solvents, are currently used at pilot scale or applied only in laboratory. In the *Iodox process* tested by the Oak Ridge laboratory both elemental and organic iodines are dissolved with hyperazeotropic nitric acid leading to the formation of iodates, IO_3^-. The formation of the iodates occurred as follows:

Reaction 2 - Iodox Process.

$$2CH_3I + 4HNO_3 \leftrightarrow 2CH_3O_2 + I_2 + N_2O_4 + 2H_2O$$

$$I_2 + N_2O_4 + 4H_2O \leftrightarrow 2I^- + 2NO_3^- + 2H_2O$$
$$I^+ + 4HNO_3 \leftrightarrow IO_3^- + 2H^+ + 2N_2O_4 + H_2O$$

Iodates are then precipitated as stable HI_3O_8 or $BaIO_3$. The main drawback of this technique is the complexity of the process that demands several steps. The *Mercurex process* also allows dissolution of both molecular and organic forms of iodine with $Hg(NO_3)_2$ / HNO_3 solutions and aims to precipitate HgI_2, but the use of the highly toxic Hg^{2+} limited any possible application. The reaction for this method is reported:

Reaction 3 - Mercurex Process.

$$6I_2 + 6Hg(NO_3)_2 + H_2O \leftrightarrow 5HgI_2 + Hg(IO_3)_2 + 12HNO_3$$

Moreover, flurocarbon solvents such as $CH_2Cl_2F_2$ (known as R-12) are typically used for other radionuclides (Kr, Xe, CO_2) but they showed the ability to capture iodine as well. The main issue of this technique for the case of iodine is the selectivity, since NO_x and other elements are trapped as well.

A good alternative to scrubbing methods is the use of solid adsorbents, since they demand less maintenance and they do not produce liquid wastes. Different types of solid adsorbents have been proposed so far. Activated carbons were employed for the capture of ^{129}I but they have several disadvantages: the iodine desorption at relatively low temperatures, the low ignition temperature and the risks of explosive gases formation. Also, in the operating conditions of fuel reprocessing plants, the selected entrapment of the iodine is strongly reduced by the presence of water and the stability of the active carbon affected by the aggressive NO_x vapours. An improvement was achieved with macroreticular resins, like the Amberlite XAD series, which showed selectivity towards non-ionic species as I_2 and CH_3I. However, resins work efficiently only under 50 °C and the out-gases have generally a higher temperature around 80 °C. The most performing class of solid adsorbents so far has been the Ag-based materials that aim to the precipitation of the compound AgI, which is insoluble in water and stable up to 558 °C. The advantages of these materials are the efficiency and the high capacity of entrapment and the safety of the systems. Different forms of Ag-based materials have been tested so far, like silica or alumina supports impregnated with $Ag(NO_3)$ and Ag^+-exchanged zeolites.

Zeolites are a class of natural and synthetic microporous aluminosilicates SiO_2/Al_2O_3, that are used for their ability to exchange cations and to host H_2O or other small molecules in their micropores. Especially the zeolites of type faujasite and mordenite have attracted the attention of researchers for the capture of iodine in the AgI form. In order to charge the zeolites with Ag^+, typically a portion of Na^+ cations present in the structure is exchanged. The ability to exchange cations is higher when the $SiO_2 : Al_2O_3$ ratio is low, but at the same time a high $SiO_2 : Al_2O_3$ ratio is requested to have good mechanical stability and better compatibility to acidic conditions. A higher $SiO_2 : Al_2O_3$ ratio is found in mordenites, being more chemically resistant than faujasites.

Chapman *et al.* reported the preparation of a Ag^+-mordenite (Ag^+-MOR) obtained from the modification of a Na^+-mordenite LZM5-Na.[12] They were able to deposite 15 wt% of Ag^+. Further they reduced Ag^+ to Ag^0 with a flux of H_2 (Figure 2).

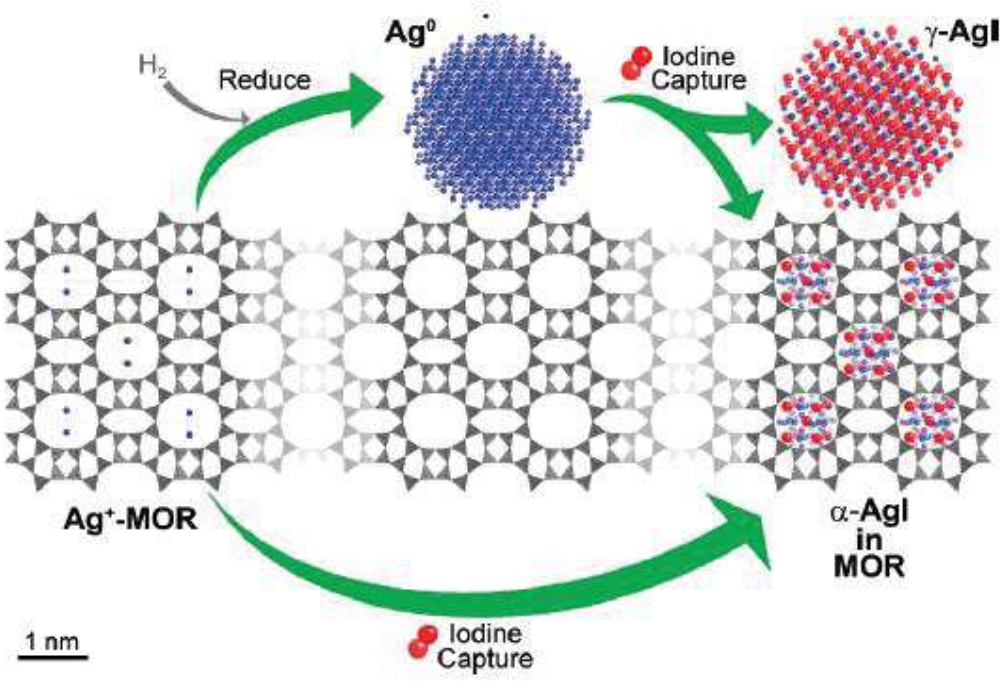

Figure 2 – Representation of the Ag^0-mordenites for the entrapment of I_2 by Chapman *et al.*[12]

The reduced Ag^0 moved from the pores to the surface and formed nanoparticles of size ≈ 3 nm. They treated both Ag^+-MOR and Ag^0-MOR with iodine at 95 °C for 12 hours and the results showed that the Ag^0 in metallic state was more efficient in iodine capture than the Ag^+ cation. The treatment with iodine brought to the precipitation of the γ-AgI phase on the surface and subnanoscale α-AgI phase in the pores (Figure 2). In the case of the Ag^+-MOR, only the formation of the intrapore α-AgI was observed and this was considered a more secure confinement, since the possibility to close the porosity could guarantee a long-term storage of the waste product. The possibility to regenerate the Ag-mordenites with a flux of H_2 and to transfer the iodine to cheaper supports was considered, but its feasibility have not been demonstrated yet. The main disadvantage for these Ag-based systems however is the high cost for the silver. Also, the selectivity can be reduced by the presence of a high humidity level and of NO_x species that precipitate as $AgNO_3$. Alternative zeolites containing other metals are found literature. For example, in the work of Doscocil *et al.* a zeolites containing Cs^+, Na^+ and K^+ was tested for the entrapment of iodine and formation of iodides was observed.[13] Investigations of reversibility of the confined iodine at 500 °C indicated that only the Na^+- and K^+-zeolite performed a good regeneration, whereas in the Cs^+-zeolite still a large quantity of CsI was retained. Further developments in the chemistry of zeolites have brought to novel structures with a larger variety of compositions. Lin *et al.* published in 2012 a new family of synthetic zeolites called *zeo-balls,* based on an exchange of O^{2-} anions with S^{2-} or Se^{2-}, as well as replacement of Si^{4+} with Ge^{4+}, by employing ionothermal methods to chalcogenidotetrelate precursors, resulting in a fullerene-like

structures with apertures in the range 5-8 Å, suitable for the insertion of iodine. *Zeo-balls* showed uptake of iodine in different media (vapours, cyclohexane, ethanol and water) with a possible maximal capture of 11 molecules of I_2 per cage.[14]

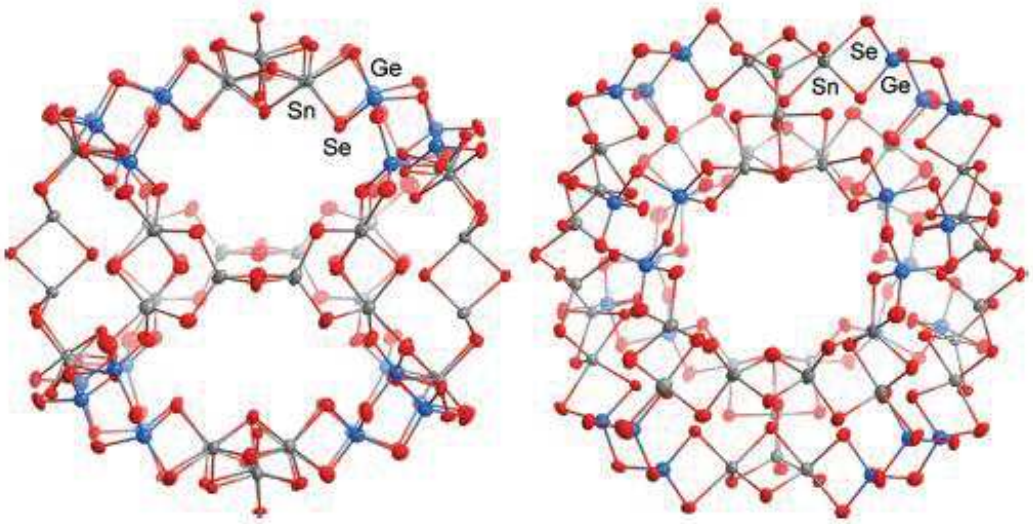

Figure 3 – Two orientation views of zeo-balls, image taken fro the work of Lin *et al.*[14]

Other very recent studies performed by Campayo *et al.* have proposed to use hydroxyapatites of formula $M_{10}(XO_4)_6Y_2$ (where M = Ca^{2+}, Sr^{2+}, Na^{2+}… XO_4 = PO_4^{3-}, CO_3^{2-}… Y = OH^-, F^-…), in order to precipitated the radionuclide ^{129}I as iodates.[15] [16] The iodates IO_3^- were detected inside the structure replacing groups as PO_4^- and OH^- and with a retention up to 550 °C.

In the last decade, researchers have investigated alternative methods in the field of the coordination chemistry, exploiting the extremely large variety of structures based on coordination of metal centers to organic or inorganic ligands. In the next paragraph, a proper introduction to the coordination compounds is reported.

Coordination chemistry and application in the nuclear industry

According to IUPAC definition,[17] a coordination compound is *"any compound that contains a coordination entity. A coordination entity is an ion or neutral molecule that is composed of a central atom, usually that of a metal, to which is attached a surrounding array of atoms or groups of atoms, each of which is called a ligand."* A *coordination compound* can also be described as a complex formed by a Lewis acid (electron acceptor) with a Lewis base (electron donor). The first use of the term *'coordination compound'* can be found in the work of Werner at the end of the 19th century in his work about the $[Co(en)_3]Cl_3$ and $[Pt(en)_2]Cl_2$ complexes.[18] Coordination compounds can be the building units for solid materials based on coordination bonds. In 1967, with the term *coordination polymers* (CPs), Bailar named the inorganic compounds which could be described as macromolecular structures arising from the repetition at least in one dimension of a simple unit.[19] Hystorically, Diesbach obtained the first synthetic *coordination polymer* in 1704, initially

used as colorant for dying and painting under the name of *Prussian Blue*. Only later in 1936 this compound was characterized by XRPD patterns by Keggin and Miles and it was recognized as the formula $Fe^{III}_4[Fe^{II}(CN)_6]_3$.[20] Especially in the last decades, coordination chemistry has largely developed with the characterization of 1-D, 2-D and 3-D structures. Apart the term *coordination polymer*, the term *Metal Organic Frameworks* (MOFs) has been employed since the 1990s to describe 1-D, 2-D or 3-D structures where a metallic centre is coordinated to rigid organic bridging ligands and the structure presents porosity and a high specific surface area.[21] Confusion about the terminology was matter of discussion in a paper by Biradha *et al.*, who indicated that the term *Metal Organic Frameworks* would be more suitable to describe 3-D networks, whereas coordination polymers would be more appropriate for 1-D and 2-D networks.[22] Alternatively, new terms have been coined so far to include all 1-D, 2-D and 3-D networks in one comprehensive family: *coordination-network solids* by Batten,[23] *porous coordination polymers* (PCPs) by Kitagawa[24] and *metal-organic rotaxane frameworks* (MORFs) by Loeb.[25] The materials commonly known as MOFs are the family that has received so far the major attention due to the possibility of tuning their pore size, the specific surface area and the internal surface properties, by playing with both inorganic and organic chemistry. MOFs have open new solutions to several applicative fields, *i.e.* adsorption of gaseous species, drug delivery, sensing, heterogeneous catalysis, employment of their optical, luminescent and ferroelectric properties.[26] Focusing on the entrapment of gases, several computational and experimental works have suggested solutions to the storage of specific gaseous molecules. Methane and hydrogen used as possible alternative fuels demand a safe and low volume storage, for instance. In order to quote some examples, the networks PCN-10 and PCN-11,[27] were proposed for the storage of methane, whereas the networks MIL-100(Al)/Pd,[28] the series IRMOFs[29] and the Cu/Zn-MOFs[30] have revealed good storage properties for the hydrogen. Sequestration of the carbon dioxide from the industrial outgases, deriving from combustion of coal and natural gas, is another field where MOFs have found a wide possible application: for instance, the structures DOBDC[31] or the IRMOFs series, already employed for H_2.[32] Other studies have also focused on the entrapment of hydrocarbons as methanol, ethanol and benzene, obtained high sorption values.[33] Suitable structures for the selective separation of gases, *i.e.* CO_2 from methane, have also been synthetized demonstrating the high tunable properties of MOFs.[34, 35, 36, 37] Recently, MOFs have attracted the interest of nuclear industry as well for the treatment of the exhausted outgases that contain radioactive volatile elements as ^{133}Xe, ^{85}Kr, ^{129}I.[11] For example, structures as the nickel coordinated dioxobenzenedicarboxylic acid (NiDOBDC) and copper benzene tri-carboxylic acid (Cu-BTC) showed selective capture of Kr and Xe from air,[38] thanks to the 1-D channels with tailored dimensions. Some few MOFs have been proposed so far for the capture of radioactive iodine as well, performing tests with the stable $^{127}I_2$. In 2011 Sava *et al.* initially studied the structure ZIF-8 where the tetrahedral Zn^{II} centre was coordinated with 2-methylimidazole.[39] In the ZIF-8 structure, the cages with diameters of 11.6 Å are connected *via* sixmembered-ring apertures whose diameter of 3.4 Å allows for the directional diffusion of iodine. Upon sorption in iodine vapours, Sava and coworkers detected a maximal capacity of 125 wt% corresponding to molar ratio I_2/Zn =

1.1. They also estimated that 25 wt% of iodine was bound weakly on the surface and the remaining 100 wt% was strongly confined in the sodalite-like cages up to the decomposition of the structure (300 °C).[40] The high retention was justified by the authors with the small size of the cages. The smaller pore lent itself to increase interaction between host and guest, in essence making the nature of the interaction more 3-D in character rather than a 2-D surface−guest interaction. The dependence on the pore size in the confinement process was already reported by previous thermochemical studies of confinement energetics between guest molecules and porous silica.[41] These studies indicated that the material with the smallest accessible cavity has the strongest host−guest stabilization interaction. The Rietveld refinement on the I_2-loaded ZIF-8 permitted to recognize two types of occupation sites (Figure 4).

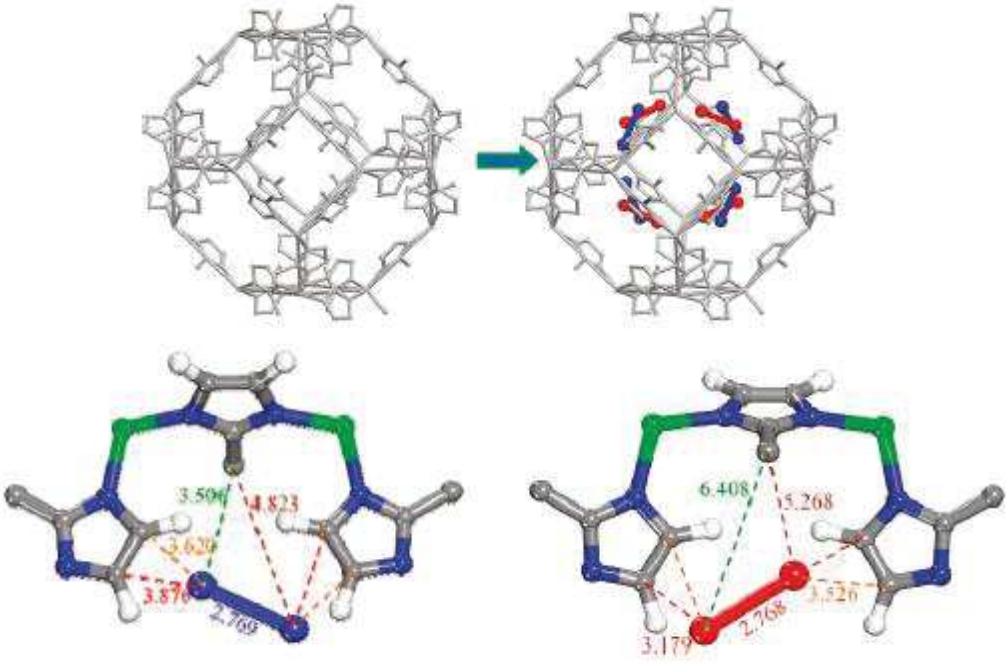

Figure 4 – Entrapment of I_2 with MOF ZIF-8 by Sava *et al.*[39]

Sava *et al.* proposed later the structure Cu-BTC that arises from coordination of divalent Cu centre with 1,3,5-tricarboxylate units and with triangular cavities of 5 Å and larger cavities of 11 Å.[42] They obtained maximal capacity of 125 wt% corresponded to molar ratio I_2/Cu = 1.5, which was higher than the capacity for the ZIF-8. Rietveld refinement performed on the I_2-loaded Cu-BTC permitted to solve the structure indicating that the iodine interacted preferentially with the carbonyl oxygen atoms. According to their discussion, the iodine was entrapped as I_2 molecule and it could be released thermically in the range 150-250 °C, with decomposition of the structure above 250 °C. Also, for both ZIF-8 and Cu-BTC, a small contraction of the structure was detected at increasing I_2 loading. Finally, they demonstrated that iodine could be selectively entrapped in water steam by Cu-BTC, even though the MOF structure was hydrophilic, probably because the apolar iodine acted as barrier to adsorption of water.

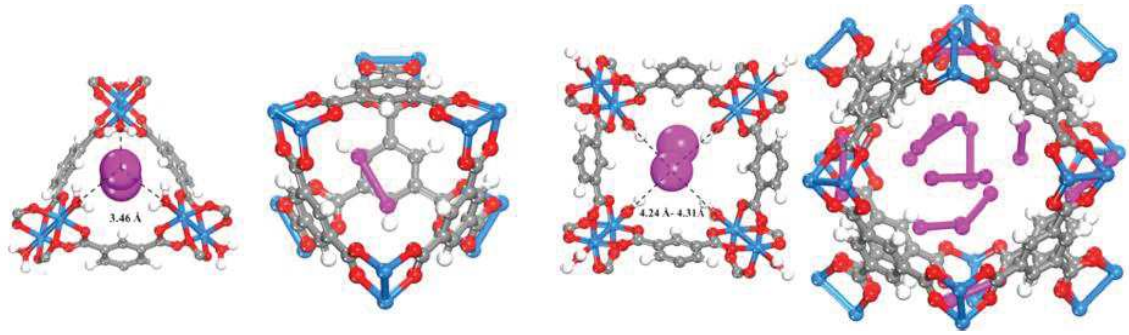

Figure 5 – Representation of the entrapment of I_2 with the MOF Cu-BTC by Sava *et al.*[42]

Alternative MOF structures were studied by Cui *et al.* who proposed the copper tetrazolate, $[Cu^{II}(btz)]_n$.[43] They captured the iodine by contact of $[Cu^{II}(btz)]_n$ crystals with a solution of I_2 in cyclohexane and they observed a maximal capture of 0.5 I_2 per $Cu^{II}(btz)$ unit. Thermal analyses detected retention of I_2 up to 135 °C. The structure showed a thermal stability up to 340 °C. In this work the authors also discussed the nature of the confined iodine, concluding that the molecular I_2 and not polyiodides was confined in the cages, due to the short distance I-I (2.68 Å) determined by resolution of the structure, and that iodine was stabilized by charge transfer with N atoms in the structure. However, the authors did not explain how the charge transfer to iodine could maintain an unperturbated bond length. Moreover, Falaise *et al.* studied the Al-metal-benzenedicarboxylate structure (MIL series) with several functional groups and they performed adsorption isotherms at room temperature in solutions of I_2 in cyclohexane (Figure 6).[44] They initially studied the I_2 adsorption with the structure MIL-53 which exhibited the highest BET surface area (up to 1140 $m^2.g^{-1}$), However, only 5% of the iodine was removed from the starting solution after 48 hours. These low values was interpreted as a negligible amount of adsorbed I_2 on the grain surface.

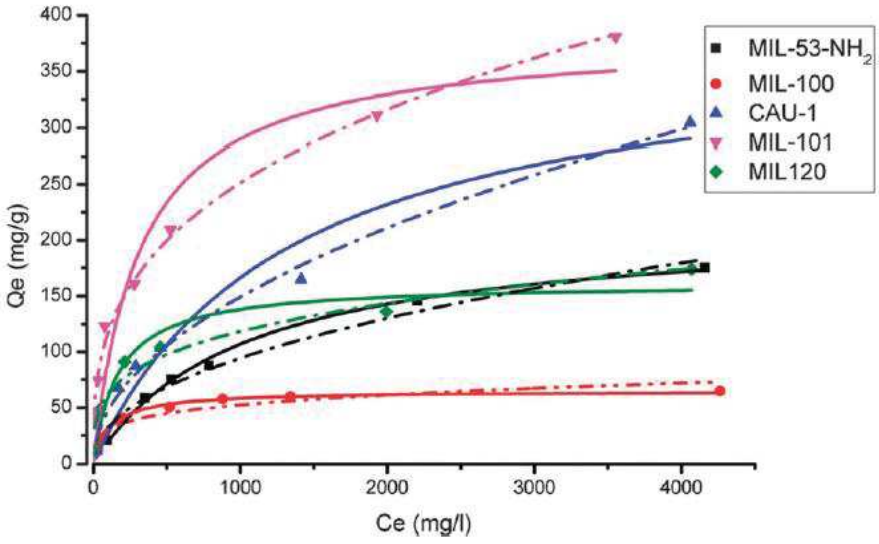

Figure 6 – I_2 adsorption isotherms in cyclohexane solutions for the family of MIL structures by Falaise *et al.*[44]

The functionalization of the porosity with –Cl, –NO_2, –COOH or –CH_3 moieties could improve the capacity, but the maximum removal efficiency remains lower than 20%. Higher values were detected with –$(COOH)_2$, –$(OH)_2$ or –Br groups, that permitted an adsorption percentage after 2 days of 34%, 46% and 47%, respectively. The best removal capacity was reached for MIL-53-NH_2 with a maximal efficiency of 60%. A further improvement was obtained with rigid structures as the MIL-101. The amino-functionalized MIL-101-NH_2 shows the best I_2 adsorption kinetics, with 90% of the initial molecular iodine removed after 30 hours. The entrapped amount corresponded to 0.3 wt% and molar ratio I_2/Al = 0.75. The second best sorbent was the structure CAU-1 (Al centres coordinated to terephthalic acid) which also contained –NH_2 groups. The non-reversibility in MIL structures was demonstrated by soaking the iodine-loaded materials in ethanol, with no iodine release in the solvent.

The MOFs reported in literature for the capture of iodine showed good capacity but low structural stability (200-300 °C). Coordination networks with pore size in the range 5-8 Å, based on stronger coordination linkers such as cyanides, may represent another alternative with improved stability and comparable iodine uptake. The next chapter presents and discusses the experimental work about the utilization of the *Hofmann-type structures* for the entrapment of the molecular iodine in solutions of cyclohexane and in gaseous phase at 80 °C. A history of this family of materials and discussion of the state of the art will introduce the experimental work.

Bibliography

[1] world-nuclear.org

[2] Businessweek.com: “The U.S. Nuclear Power Industry's Dim Future”, July 18, 2013

[3] Reuter.com : « French nuclear power here to stay, says industry minister », PARIS Mon Dec 9, 2013.

[4] Andrews A. *CRS Report Fo Congress: “Nuclear Fuel Reprocessing: U.S. Policy Development”* (2008)

[5] Wang Y., Gao H., Brinker C.J., Xiong Y., Holt K., Miller A., Pohl P., Ockwig N., Rodriquez M.A., Bencoe D.S., Tellez H., Kruichak J.N., Turnham R., Murphy A.W. *Sandia Report-5901* (2010).

[6] Häfner D.R., Tranter T.J., INL Report EXT-07-12299 (2007)

[7] IRSN Report, “Fichier Radionucléide Iode-129”.

[8] Van Liddlesworth L., Handl J., Johns P., *J. Radioanalytical Nucle. Chem.* (2000) 243, 2, 467.

[9] Berkeley Laboratories, Report NEN6548 « Iodine-129 : Handling Precautions ».

[10] Jubin R.T., Report ORNL/TM-10477, Oak Ridge National Laboratory (1988).

[11] Soelberg N.R., Garn T.G., Greenhalgh M.R., Law J.D., Jubin R., Strachan D.M., Thallapally P.K., *Science and Technology of Nuclear Installations* (2013) ID 702496, 12.

[12] Chapman, K. W.; Chupas, P. J.; Nenoff, T. M. *J. Am. Chem. Soc*. (2010) 132, 8897.

[13] Doskocil E.J., Bordawekar S.V., Kaye B.G., Davis R.J., *J. Phys. Chem. B* (1999) 103, 30.

[14] Lin, Y.; Massa, W.; Dehnen, S. *J. Am. Chem. Soc*. (2012) 51, 2303.

[15] Laurencin D., Vantelon D., Briois V., Gervais C., Coulon A., Grandjean A., Campayo L., *RSC Adv.* (2014) 4, 14700.

[16] Campayo L., Grandjean A., Coulon A., Delorme R., Vantelon D., Laurencin D. *J. Mater. Chem.* (2011) 21, 17609.

[17] Nomenclature of Inorganic Chemistry IUPAC Recommendations 2005, International Union of Pure and Applied Chemistry, ed. N. G. Connelly, T. Damhus, R. M. Hartshorn and A. T. Hutton, The Royal

[18] Ribas J. Coordination Chemistry, WIley-VCH

[19] Bailar J. C. Prep. Inorg. React. (1964) 1, 1-57

[20] Keggin J. E., Miles S., *Nature* (1936) 137, 577.

[21] Keeffe M., Yaghi O.M., *Chem.Rev.* (2012) 112, 675.

[22] Biradha K., Ramanan A., Vittal *J. J. Crystal Growth & Design* (2009) 9, 7, 2969.

[23] Batten S.R., *CrystEngComm,* (2012) 14, 3001.

[24] Kitagawa, S.; Matsuda, R., *Coord. Chem. Rev.* (2007) 251, 2490.

[25] Loeb, S. J. *Chem. Commun.(*2005) 1511.

[26] Zhou H., Long J.R., Yaghi O.M., *Chem. Rev.* (2012) 112, 673.

[27] Wang, X.-S.; Ma, S.; Rauch, K.; Simmons, J. M.; Yuan, D.; Wang, X.; Yildrim, T.; Cole, W. C.; Lopez, J. L.; Meijere, A. d.; Zhou, H.-C., *Chem. Mater.* (2008) 20, 3145.

[28] Zlotea C., Campesi R., Cuevas F., Leroy E., Dibandjo P., Volkringer C., Loiseau T., Férey G. and Latroche M., *J. Am. Chem. Soc.,* (2010) 132, 9, 2991.

[29] Jesse L. C. Rowsell and Omar M. Yaghi, *J. Am. Chem. Soc.,* (2006) 128, 1304.

[30] Ma, L.; Lee, J. Y.; Li, J.; Lin, W., *Inorg. Chem.* (2008) 47, 3955.

[31] Caskey, S. R.; Wong-Foy, A. G.; Matzger, A. J., *J. Am. Chem. Soc.* (2008) 130, 10870.

[32] Millward, A. R.; Yaghi, O. M. *J. Am. Chem. Soc.* (2005) 127, 17998.

[33] Lee, J. Y.; Olson, D. H.; Pan, L.; Emge, T. J.; Li, J. *Adv. Funct. Mater.* (2007) 17, 1255.

[34] Britt, D.; Furukawa, H.; Wang, B.; Glover, T. G.; Yaghi, O. M. *Proc. Nat. Acad. Sci.* (2009) 106, 20637.

[35] Kishan, M. R.; Tian, J.; Thallapally, P. K.; Fernandez, C. A.; Dalgarno, S. J.; Warren, J. E.; McGrail, B. P.; Atwood, J. L. *Chem. Comm.* (2010) 46, 538.

[36] Xu, Q.; Liu, D. H.; Yang, Q. Y.; Zhong, C. L.; Mi, J. G. *J. Mater. Chem.* (2010) 20, 706.

[37] : Llewellyn, P. L.; Bourrelly, S.; Serre, C.; Filinchuk, Y.; Ferey, G. *Angew. Chem., Int. Ed.* (2006) 45, 7751.

[38] Liu J, Thallapally P.K., Strachan D.M., *Langmuir* (2012) 28, 31, 11584.

[39] Sava, D. F.; Rodriguez, M. A.; Chapman, K. W.; Chupas, P. J.; Greathouse, J. A.; Crozier, P. S.; Nenoff T. M. *J. Am. Chem. Soc*. (2011) 133, 12398.

[40] Hughes, J. T.; Sava, D. F.; Nenoff, T. M.; Navrotsky, A. *J. Am. Chem. Soc*. (2013) 135, 16256.

[41] Wu, D.; Navrotsky, A. Geochim. *Cosmochim. Acta* (2013) 109, 38.

[42] Sava, D. F.; Chapman, K. W.; Rodriguez, M. A.; Greathouse, J. A.; Crozier, P. S.; Zhao, H.; Chupas, P. J.; Nenoff, T., *Chem. Mater.* (2013) 25, 2591.

[43] Cui, P.; Ren, L.; Chen, Z.; Hu, H.; Zhao, B.; Shi, W.; Cheng, P. *Inorg. Chem.* (2012) 51, 2303.

[44] Falaise C.; Volkringer C.; Facqueur J.; Bousquet T.; Gasnot L.; Loiseau T.; *Chem. Comm.* (2013) 49, 10320.

CHAPTER 1

-

Entrapment of the molecular iodine with the bulk Hofmann-type structures

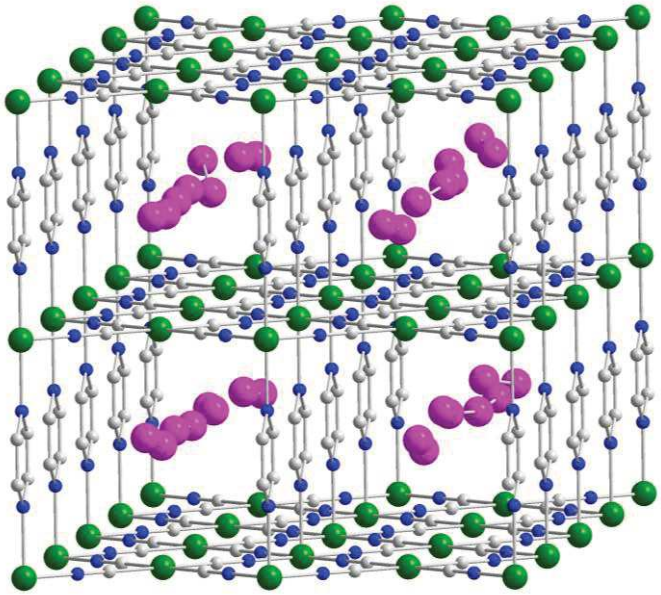

In this chapter the family of the Hofmann-type clathrates will be introduced and then the discussion about the entrapment of the molecular iodine with the Hofmann-type structures M'(L)[M''$(CN)_4$] (M' = NI^{II}, Co^{II}; L = pyrazine, 4,4'-bipyridine, 4,4'-azopyridine; M'' = Ni^{II}, Pd^{II}, Pt^{II}) will be developed.

Introduction to the Hofmann-type clathrates.

When a MOF or a zeolite hosts small-sized molecules such as H_2O, H_2 or CO_2, inside the porosity, it originates a *clathrate*. The term *clathrate* stems from Latin word *clathratus*[1] that means "enclosed or protected by the cross bars of a grating" and was introduced by Powell in 1948 for the compound $3C_6H_4(OH)_2 \bullet SO_2$.[2,3] The term was then extended to describe a larger class of synthetic materials, as well as some natural materials like the methane clathrate,[4] with the specific property of including guest molecules inside its own crystalline structure. First observations of such a property were actually carried out much earlier: in 1823 by Faraday and Davies for the chlorine hydrate compound,[5,6] in 1841 by Schafhäutl for graphite intercalate,[7] in 1859 by Wöhler about the β-quinol complexes with SO_2 [8] and in 1897 by Hofmann and Küspert, who reported the inclusion of benzene inside the nickel cyanide ammonia compound, obtaining the complex $Ni(CN)_2 \bullet NH_3 \bullet C_6H_6$.[9] Other phenomena of inclusion were reported as well at the beginning of the 20th century without a systematic study of the obtained compounds. [10, 11,12,13,14] Focusing about the work of Hofmann and Küspert, they precipitated their clathrate $Ni^{II}(CN)_2 \bullet NH_3 \bullet C_6H_6$ by addition of benzene to a solution of nickel cyanides in aqueous ammonia and containing acetic acid. They also remarked the formation of analogue compounds by inclusion of other small molecules as thiophene, furane, pyrrole, aniline or phenol,[15,16] but how the elements were arranged in the lattice was still unknown. Substituted benzenes with larger dimensions did not form any complex with nickel cyanide and ammonia. The possibility to capture only the small aromatic molecules by *enclathration* was later patented by Jones and Fay for the selective recovery of benzene from hydrocarbon stocks.[17] A first comprehension of the structure of clathrate compounds came many years later with the works of the crystallographer Powell. He was the first to understand that, in a clathrate compound, a precise stoichiometric ratio between the host structure and the guest molecule always existed and that the cage and its guest molecule could be taken as a unit cell.[18] Powell proposed a structure for the Hofmann's clathrates and pointed out that only the small group of molecules employed by Hofmann – *i.e.* benzene, thiophene, furane, pyrrole, aniline or phenol – fulfilled the conditions for the formation of the clathrate, since the lattice parameters of the cage formed by $Ni^{II}(CN)_2 \bullet NH_3$ had a very close size of the included molecules. From their XRPD patterns they found approximate parameters $a = b = 7.2$ Å and $c = 8.3$ Å for a unit cell of formula $Ni^{II}(NH_3)_2[Ni^{II}(CN)_4] \bullet 2G$, (G = guest molecule), which was the double of the formula reported by Hofmann. The structure was described as nickel cyanides forming a flat 2-D structure, where the square planar Ni^{2+} coordinated to four C from 4 CN^- ligands and the octahedral Ni^{2+} coordinated to four N from 4 CN^- ligands and 2 N from the NH_3 ligands in *trans*- position. The

parameter *a* and *b* in the Powell's analysis were given by $\sqrt{2} \cdot d$ where *d* is the distance of two cyanide-bridged Ni atoms next to each other and parameter *c* is given by 2 pillared ammonia groups. Due to the distance between the benzene molecule and the moieties of the host structure, it was suggested that no bonds were formed between the guest molecule and the host material and the molecule was simply trapped inside the cage. The representation of the unit cell of $Ni^{II}(CN)_2 \cdot NH_3 \cdot C_6H_6$ by Powell and a view of the plane (001) are reported in Figure 1.

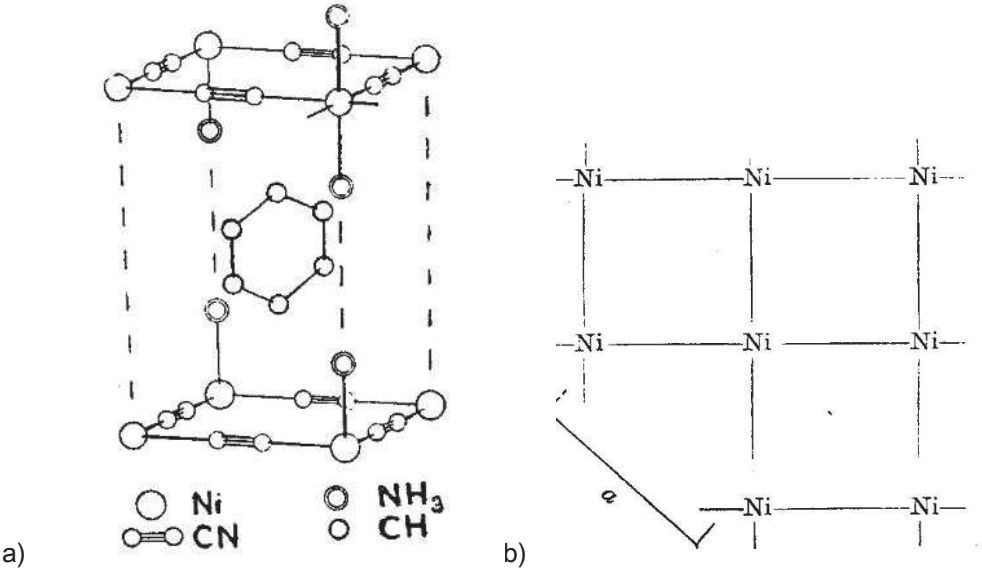

a) b)

Figure 1 – (a) Structure for the Hofmann's clathrate proposed by Powell and Rayner; (b) representation of $[Ni(CN)_4]^{2-}$ sheets or plane (001) from the work of Powell and Rayner[18].

The formation of the 2-D structure given by bridging cyanides was already proposed by Keggin and Miles in 1936 for the 3-D structure of the *Prussian Blue*, $Fe_4[Fe(CN)_6]_3 \cdot xH_2O$.[19] The IR active stretching mode of the bridging $\nu(C \equiv N)$ in the Hofmann's clathrate was measured by Bhatnagar and it was found at 2160 cm^{-1}.[20] Developments around the Hofmann's clathrates were continued especially by Iwamoto,[21] who proposed to name all the possible analogues of the Hofmann's first clathrate, with the novel term *Hofmann-type clathrates*. In the largest meaning of the term, *Hofmann-type clathrates* include all compound with general formula $M'(L)_n[M''(CN)_4] \cdot xG$ where M' is a bivalent cation with octahedral geometry, M'' is a bivalent cation with square planar geometry, L can be a monodentate ligand (if n = 2) or a bidentate linear ligand (if n = 1) and G is the guest molecule in molar ratio x : 1 with the host structure. All elements M', $[M''(CN)_4]^{2-}$, L and G can be modulated to obtain a large number of other clathrates. A detailed list of possible substitutions that are found in literature is now reported in separate paragraphs and a general chemical description of the building elements is treated as well in each paragraph.

Replacement of the octahedral metallic centre M' in $M'(L)_n[M''(CN)_4]\bullet xG$.

The octahedral symmetry, labelled with point group O_h, is the most stable geometry for the coordination number = 6 and also the most stable geometry for a large variety of metal centres. When M^{2+} is a free transition metallic cation, its 5 *d* orbitals are degenerate, but when coordination to a set of ligands occurs, a splitting always takes place due to electron repulsion between the σ orbitals of the ligands directed to the metal centre and the closer *d* orbitals of the cation. Limiting the discussion to σ orbitals in the metal-ligand complex of O_h symmetry (Figure 2-a), the d_{z^2} and $d_{x^2-y^2}$ orbitals from the cation move to higher energy with respect to the degenerate orbitals of the free cation, since the repulsion with the 6 ligands is higher, and form the anti-bonding orbital of the complex labelled e_g^*. The d_{xz}, d_{xy}, and d_{yz} orbitals do not participate to the σ bond and form the non-bonding orbital labelled t_{2g}.[22] However, they can participate in the π bond with the ligands, perpendicularly to the σ bond axis. The amount Δ_0 of the splitting between the two e_g^* and t_{2g} orbitals depends on the nature of the ligands. For example, π-acidic ligands as CN^- cause a larger splitting than π-basic ligands as NH_3 or pyridine (Figure 2-b). In the molecular diagram, the 12 electrons coming from the 6 ligands are located in the bonding orbitals at lower energy, whereas the *d* electrons of the metallic centre are located in the e_g^* and t_{2g} orbitals. The occupancy of the e_g^* orbitals with unpaired *d* electrons determines the high spin state of the metallic centre.

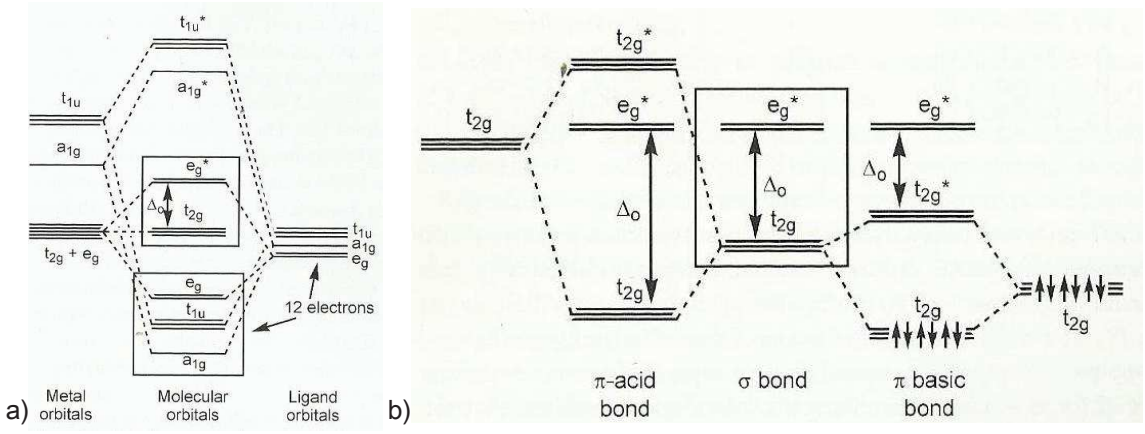

Figure 2 - MOs for the octahedral configuration: (a) σ bond and (b) π bond [22]

In the Hofmann's clathrate, the octahedral position surrounded by N atoms was occupied by Ni^{2+}. Since O_h geometry can be observed for several metals with different electron configurations, many possible substituents to Ni^{2+} are possible. A first attempt was carried out by Baur and Schwarzenbach,[23] who employed in the preparation for the Hofmann's clathrates the double cyanide $M'[Ni(CN)_4]$ where M' was Cd^{2+}, Cu^{2+} or Zn^{2+}. Crystallographic characterizations for analogues $M'^{I}(NH_3)_2[Ni^{II}(CN)_4]\bullet 2C_6H_6$ were then performed with M' = Mn^{2+}, Fe^{2+}, Cu^{2+}, Zn^{2+} or Cd^{2+} showing a tetragonal structure for all the materials. [24,25,26,27,28,29] The employment of cations Co^{2+} and Hg^{2+} was also considered later for different Hofmann-type clathrates as the M'(p-benzoquinone)$Ni(CN)_4\bullet 2G$ (M' = Mn, Co, Ni or Hg; G = aniline)[30] or in the structure

Co^{II}(propylendiammine)[$Ni^{II}(CN)_4$].[31] As show by the spectroscopic studies reported in these papers, the different employed cation M' for a specific clathrate influences especially the lattice parameters and the strength of the coordination with the bridging CN^- and the organic ligands. Other authors observed by IR spectroscopic analysis the modulation of the vibration mode ν(C≡N) or the modes for the organic ligands, when different metals were used, and they concluded that the shift to higher values for this modes followed the order of the second ionization potential of the cations: Cd^{2+} < Mn^{2+} < Fe^{2+} < Co^{2+} < Ni^{2+} < Zn^{2+} < Cu^{2+}.[32] [33] The use of Fe^{2+} have attracted the attention in the last decade due to the spin-cross over properties observed for the Hofmann-type clathrates with structure $Fe^{II}(L)[M''(CN)_4]\bullet nH_2O$ (with L = pyrazine, 4,4'-azopyridine or bipyridylacetylene and M'' = Ni^{2+}, Pd^{2+} or Pt^{2+}).[34] [35]

Replacement of the tetracyanometallate $[M''(CN)_4]^{2-}$ in $M'(L)_n[M''(CN)_4]\bullet xG$.

The second cation in the Hofmann-type clathrates has coordination number = 4 and it is surrounded by 4 CN^- ligands in a tetrahedral or square planar configuration. As reported in Figure 3, the tetrahedral configuration or T_d symmetry shows an inverted situation with respect to the octahedral symmetry: the σ orbitals of the ligands experience a higher repulsion towards the orbitals d_{xz}, d_{xy}, and d_{yz} which move to higher energy with respect to the degeneracy in the free cations and form the anti-bonding t_2 orbital of the metal-ligands complex. The d_{z^2} and $d_{x^2-y^2}$ orbitals do not participate to the σ bond and form the non-bonding e_g orbital in the complex (Figure 3-a).[22] The tetrahedral configuration is the most stable when 4 ligands surround a metal cation, anyway the square planar configuration, labelled D_{4h}, can be stabilized for a specific class of metal centres and ligands. Metallic cations with electron configuration d^8 as M'' = Ni^{2+}, Pd^{2+}, Pt^{2+} or Au^{3+} can originate stable square planar $[M''(CN)_4]^{2-}$ with π-acidic ligands with low steric hindrance as CN^-. As reported in Figure 3-b, for the D_{4h} symmetry the repulsion towards the orbital $d_{x^2-y^2}$ of the cation is the highest and thus it splits at higher energy forming the anti-bonding b_{1g} orbital of the complex. Splitting of other orbitals is due to formation of π orbitals of the complex.

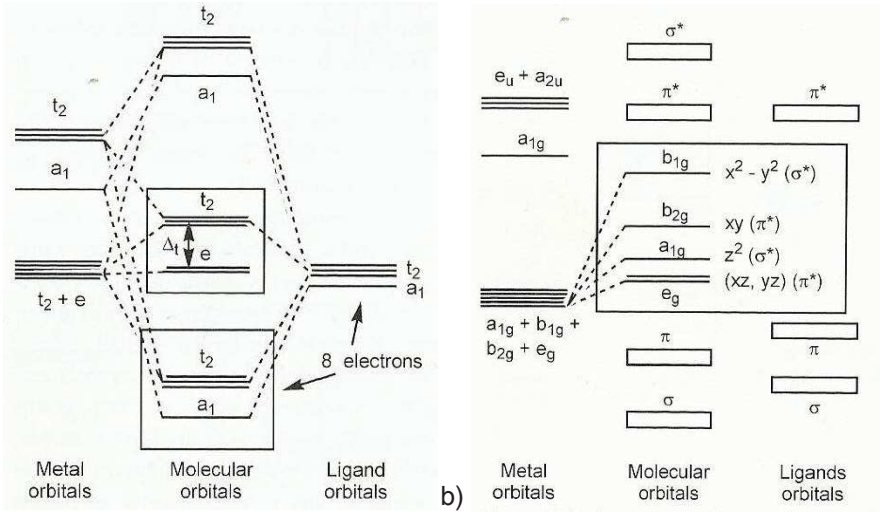

Figure 3 - MOs for (a) tetrahedral configuration and (b) square planar configuration.[22]

In the Hofmann's clathrate the Ni^{2+} occupied the square planar position, coordinated to 4 CN^-. From a chemical point of view, the CN^- ligands are bridging ligands since they connect the square planar centre to the octahedral centre to form the flat sheets of cyanometallates. The square planar Ni^{2+} cations coordinate to C by giving electron density from their *d* orbitals to the unoccupied π^* orbital of CN^- (back donation), whereas the octahedral Ni^{2+} coordinate on the N side of the cyanide ligand by taking electron density from the occupied σ^* orbital of CN^-.[36] In Figure 4 the MOs representation for a free CN^- ligand is reported.

Most of the Hofmann-type clathrates found in literature contained the square planar $[Ni^{II}(CN)_4]^{2-}$ building block but also the use of the square planar $Pd^{II}(CN)_4]^{2-}$ and $[Pt^{II}(CN)_4]^{2-}$ block are found. [37] [38] [39] Square planar building blocks typically give space groups P4/m, P4/mmm (tetragonal) or Pmma (orthorhombic), with rectangular porosities (α-type).[21] However, parallel studies characterized the modified family of Hofmann-T_d-type clathrates where tetrahedral $[M''(CN_4)]^{2-}$ building units with M'' = Cd^{2+} or Hg^{2+}. In this family, typical space groups are C2/c, C2/m (monoclinic) or Fd3m (cubic) and cavities assume both rectangular cavities (α-type) and twisted-prism cavities (β-type). [40,41,42,43] Coexistance of the same cation in the two positions of the host structure has been observed so far only for the Ni^{2+} (octahedral and square planar), as in the Hofmann's clathrate $Ni^{II}(NH_3)_2[Ni^{II}(CN)_4]\bullet 2C_6H_6$ and analogues, and for the Cd^{2+} (octahedral and tetrahedral) as in one of the first clathrates with $[Cd^{II}(CN)_4]^{2-}$ *i.e.* the $Cd^{II}(NH_3)_2[Cd^{II}(CN)_4]\bullet 2C_6H_6$.[40]

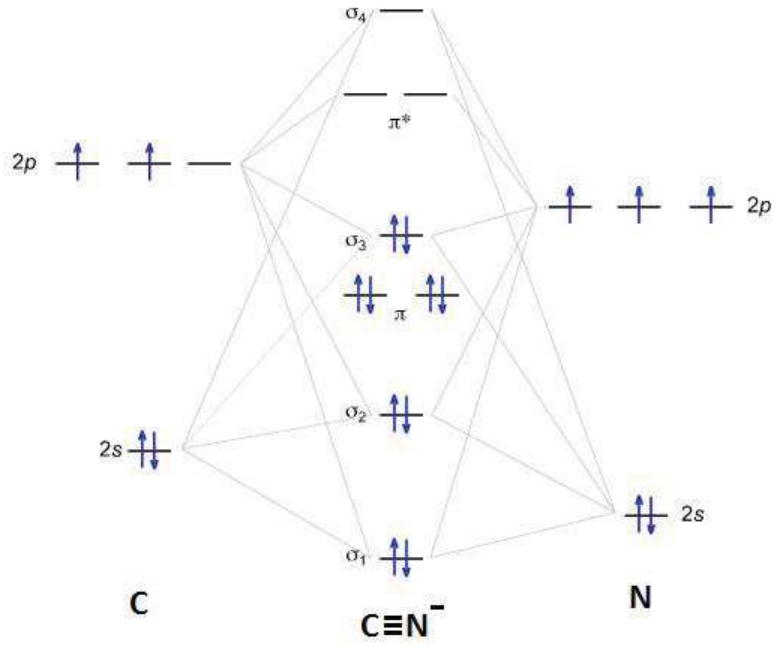

Figure 4 - MOs for the CN^- free ligand before coordination.

Replacement of the ligand L in $M'(L)_n[M''(CN)_4]\bullet xG$.

Concerning the linear ligand, a large list of possible molecules exists. We limit here to mention the most employed ligands that were used so far to replace the ammonia in the Hofmann-type clathrates. First of all, from a chemical point of view, the used organic ligands are typically neutral π-basic ligands where the lone pair of an electronegative atom as N, S or O in the molecular structure is given to the octahedral metallic centre. We will refer here to the different classes of ligands as *X-bonding* ligands, where X = N, S or O. Also, in order to pillar the $[Ni^{II}(CN)_4]^{2-}$ planes, the ligand must have a linear structure and two possibilities have been studies so far, giving different stoichiometries:

- $M'(L)_2[M''(CN)_4]\bullet xG$ – use of two monodentate ligands that coordinate respectively to one metal centre and bind to each other by Van der Waals forces;
- $M'(L)[M''(CN)_4]\bullet xG$ – use of one bidentate ligand that coordinates by covalent bonds to two metal centres, to bind the 2-D $[M'M''(CN)_4]_n$ structures.

For the monodentate N-bonding ligands, apart ammonia other ligands have been used so far: aromatic ligands as pyridine[44] and its derivatives,[45,46,47] imidazole,[48,49] piperidine[50] and its derivatives,[51] non-aromatic amines derivatives as dimethyl amine,[52] 2(1-cyclohexenyl)-ethylamine[53] or cycloheptylamine.[54] Monodentate O-bonding ligands as water molecules,[55] dioxana,[56] dimetylsulfoxide,[57] dimethylformamide,[58] and S-bonding ligands as dimethylthioformamide,[59] 1-propanethiol and n-propyl mercaptane,[60] or cyclohexanethiol[61] were used. About the bidentante ligands employed so far in the Hofmann-type clathrates, especially the following N-bonding ligands have been considered: rigid aromatic ligands as pyrazine,[42 62] 4-4'-bipyridine,[42 43 62] 4,4'-azopyridine,[63] 1,2-bis(4-pyridyl)ethane[64] or bipyridyl acetylene,[35] 1,4-bis(4-pyridylacetylene)benzene,[65] substituted ligands as the 2-methyl pyrazine,[66] flexible aromatic ligands as 1,2-bis(4-pyridyl)ethylene[67] non-aromatic ligands as ethylendiamine[68] or 1,9-diaminononane[69] or 1,10-diaminodecane.[70] S-bonding bridging ligands are also found in literature as the 1,2-ethanedithiol[71] or the 1,6- hexanedithiol.[72]

The main effect of changing the ligand L is the modulation of the pore size, since the length of ligand determines the distance between the $[M'M''(CN)_4]_n$ planes. For short ligands as ammonia, pyrazine or ethylendiamine a distance about 7-8 Å is obtained, whereas for longer ligands as 1,9-diaminononane or 1,4-bis(4-pyridylacetylene)benzene distance raises to 16-19 Å. Also, the use of certain ligands can create different effects as the *breathing effect* in the case of Ni^{II}(1,2-bis(4-pyridyl)ethylene)$[Ni^{II}(CN)_4]$ when the guest molecule CO_2 was introduced in the porosities due to flexibility of the ligand,[67] or *puckering effect* of the flat $[M'M''(CN)_4]_n$ structures as in the case of Cd(dimethymamine)$[Ni^{II}(CN)_4]\bullet xG$ (G = aniline or benzene). Finally, the pore size given by the ligand L allowed the introduction in the structure of larger guest molecules that could not enter in the Hofmann's clathrate as, for instance, the methyl xylene[73] or the dichlorobenzene.[21]

Replacement of the guest molecule G in $M'(L)_n[M''(CN)_4]\bullet xG$.

The final parameter that can be modulated is the nature of the guest molecule. Some examples have already been reported previously in this chapter for the first studies by Hofmann, as benzene9 and other small aromatic molecules like pyrrole, aniline, thiophene, furane and phenol.[15,16] The first clathrate of a non-aromatic compound was obtained with dioxane.[74] All prepared clathrates in early literature were precipitated in the presence of the guest molecule, a way that we could call *in-situ* preparation. For some clathrates, as for example the $Cd(pyrazine)[Cd(CN)_4]\bullet C_6H_6$, the guest molecule was necessary for the host structure to exist, and any attempts to prepare the host structure without the guest molecule, acting as a template, failed.[42] In some of the studies about the benzene clathrate carried out by Aynsley[75] and Bhatnagar,[76] it was reported that an evacuation of the guest molecules under vacuum was possible, with progressive change of the unit cell but still similar crystal lattice and molecular configuration. Direct preparations of compounds without the guest molecule were performed starting from the work of Rüegg and Ludi with the synthesis of the $Ni^{II}(en)_2[Pd^{II}(CN)_4]$,[37] followed by the works of Cemak and *et al.* about by the series $M'(en)_2[Ni^{II}(CN)_4]$ with M'' = Ni^{2+}, Cu^{2+}, Zn^{2+}.[77] [78] [79] An attempt to prepare a benzene clathrate starting from the empty host structure was performed for example by Kantarci *et al.*, who precipitated the structure $Co^{II}(cycloheptylamine)_2[Ni^{II}(CN)_4]$ and then followed by benzene insertion in the structure by adsorption of vapours.[54] They also observed the guest molecule release in air. Even though the reported works about the preparation of 'empty' $M'(L)_n[M''(CN)_4]$ did not mention it, it is reasonable to think that the precipitated structures in water actually contained H_2O molecules inside the cages. In the works of Niel *et al.* about the spin cross-over properties of the series $Fe^{II}(pyrazine)[M''(CN)_4].xH_2O$ (with M'' = Ni^{2+}, Pd^{2+}, Pt^{2+}) the amount of water inside the cages was estimated by TGA and was around 2 H_2O per unit cell for the specific studied series.[34] The also recognized a tetragonal lattice for the water-containing structure, with space group P4/m. In a development of this study by Bartal-Murgui *et al.* about the *spin cross-over properties* (SCO) of the compound $Fe^{II}(bpac)[M''(CN)_4]\bullet H_2O$ (where bpac = bipyridiyl acetylene), tests about the reversible desorption of water were included as well, showing that water left the structure upon heating till 120 °C and full rehydratation was observed in atmospheric air after 24 hours.[35] The possibility to prepare empty host structures in water, with desirable properties by modulating the building blocks, and to introduce different guest molecules has opened the possibility to the storage of small molecules as well as the already cited study about the *spin cross-over properties*. Focusing on the study of SCO properties, several guest molecules other than water were physisorbed inside empty structures containing Fe^{2+} and showed that the adsorption of guest molecules shifted the transition temperature from the high-spin to the low-spin states at the Fe^{II} sites. This interesting phenomenon was proposed as alternative technology to build sensing materials. Following the published work of Niel *et al.,*[34] the introduction of a large set of guest molecules inside the host structure $Fe^{II}(pz)[Ni^{II}(CN)_4]$ to stabilize a LS or HS state was also

performed by Southon *et al.*[80] They considered the adsorption and the desorption processes with gases as N_2, O_2, CO_2 and vapours as methanol, acetone, ethanol, toluene, acetonitrile. Dislike from what Niel *et al.* previously reported, Southon and coworkers assessed that for the majority of the obtained crystals of $Fe^{II}(pz)[Ni^{II}(CN)_4]\bullet 2H_2O$ they observed in reality an orthorhombic lattice with space group P/mmm, masked as a tetragonal lattice by pseudo-merohedral twinning (orthorhombic twin structures sharing the same reciprocal axes). By contrast, the tetragonal lattice (P4/m) was confirmed for the empty host structure. The representation for the water-filled clathrate is reported in Figure 5.

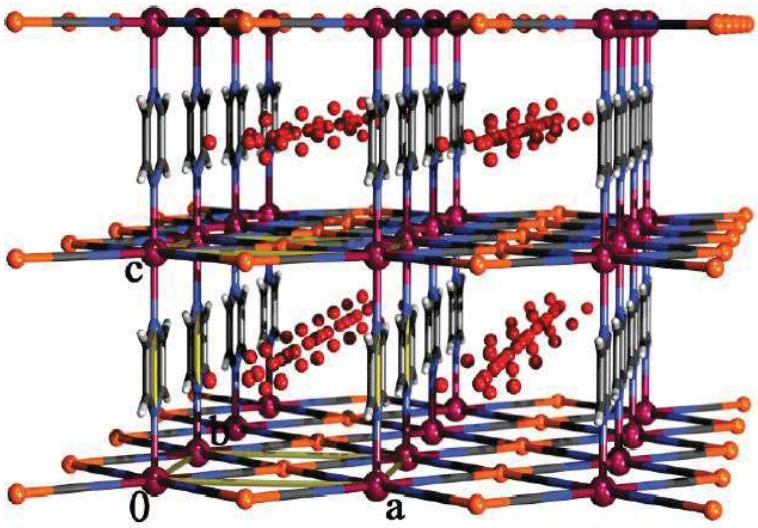

Figure 5 - Representation for $Fe^{II}(pz)[Ni^{II}(CN)_4].2H_2O$ by Southon *et al.*[80]

Also, they reported that the lattice parameters were in general influenced by the spin state, whose transition temperature depended on the presence of the guest molecules as well: the atomic distances between the Fe^{II} centres and the coordinated N atoms were around 1.9 Å in the LS compound and around 2.1 Å in the HS compound, since, in the HS state, occupancy of the anti-bonding orbital set e_g^* by unpaired electrons (Figure 6) increased the bong length. The measured adsorption isobars for O_2, N_2 and CO_2 indicated a hysteresis that arose from the structural modification connected with the spin transition. The adsorption capacities for N_2 and O_2 were higher in the HS structure than in the LS structure. The capacity for the adsorption of CO_2 turned out to be pressure dependent: at higher pressures, higher capacity was observed in the HS structure, similarly N_2 and O_2, but at lower pressures the LS structure exhibited a higher capacity. The adsorption isotherms for the vapours indicated following guest/host structure molar ratios: 1.6 for methanol, 1.5 for ethanol, 1.1 for acetone, 1.0 for acetonitrile, 0.8 for toluene. For all clathrates, the reversible desorption of the guest molecules with a *memory effect* of the structural features was observed.

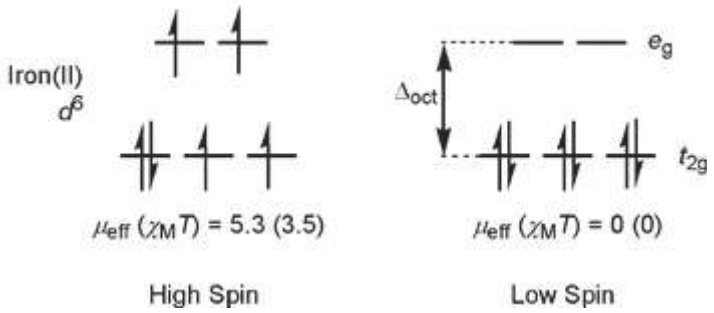

Figure 6 – Crystal field representation of the *d* orbitals for the Fe^{II} centres, showing spin transition.

Further studies focused on the analogue $Fe^{II}(pz)[Pt^{II}(CN)_4]$. The reversible physisorption of SO_2 in this structure was studied by Arcis-Castillo *et al.* One equivalent of SO_2 per unit cell was found located on the Pt^{II} site and physisorption occurred due to back donation from the HOMO of the Pt atom to the LUMO of SO_2 (Figure 7).[81]

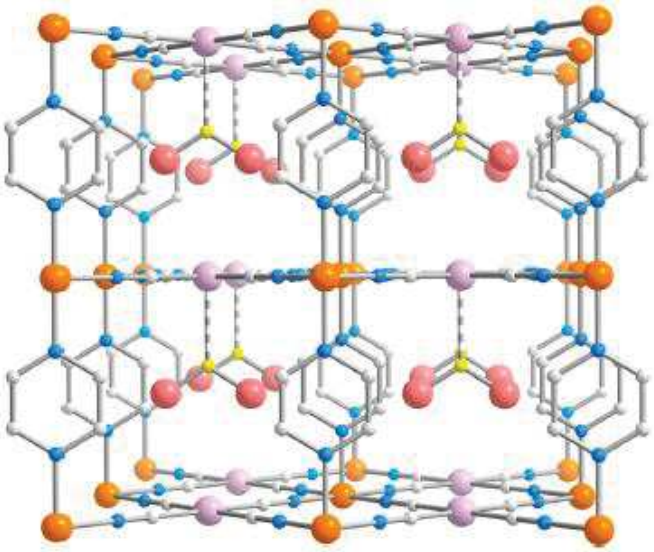

***Figure 7 – Representation of the $Fe^{II}(pz)[Pt^{II}(CN)_4]$ structure after SO_2 insertion, by Arcis-Castillo et al.*[81]**

In the same host structure, Ando *et al.* inserted one equivalent of CS_2 per unit cell and they observed a preferential interaction with the pyrazine rather than the metals(Figure 8).[82,83] Insertion of maleic acid in the $Fe^{II}(pz)Pt^{II}(CN)_4]$ structure by Bao *et al.* gave similar result with supposed location of the molecule between the pyrazines.[84]

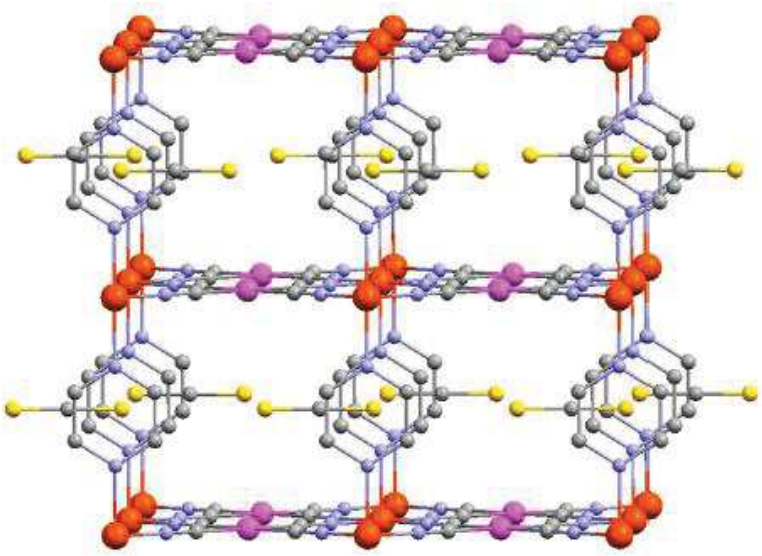

Figure 8 - *Representation of the $Fe^{II}(pz)[Pt^{II}(CN)_4]$ structure after CS_2 insertion, by Ando et al.*[82]

In the case of the $Fe^{II}(bpac)[M''(CN)_4]$ structure, pyridine and pyrazine were introduced in vapours by Bartal-Murgui *et al.* revealing a capacity per unit cell of 0.75 of pyridine and 0.45 of pyrazine. [35] Another interesting study about SCO properties of the $Fe^{II}(pz)Pt^{II}(CN)_4]$ structure, considered again an *in-situ* preparation where the guest molecule was iodine.[85] [86] The iodine clathrate precipitated by mixing a $K_2[Pt^{II}(CN)_4]$ solution with an ethanolic solution of I_2 and a solution of $Fe^{II}(NH_4)_2(SO_4)_2{\cdot}6H_2O$ and pyrazine (in presence of ascorbic acid to avoid oxidation of Fe^{2+}). The precipited material showed a formula per unit cell $Fe^{II}(pz)Pt^{II/IV}(CN)_4]{\bullet}I^-$, with iodides coordinated in *trans*-position on the Pt^{IV} sites (Figure 9). A fundamental difference between this clathrate and the common Hofmann-type clathrates is the interaction between the host structure and the guest molecules: in $Fe^{II}(pz)Pt^{II/IV}(CN)_4]{\bullet}I^-$ an oxidative addition occurred with formation of covalent bonds, whereas in common Hofmann-type clathrates the guest molecule does not interact strongly with the host structure. Ohtani and coworkers also tried to modulate the amount of iodine for a precise control of the transition temperature in the temperature range 300-400 K. They tried at first to introduce iodine in the gaseous phase inside the structure but they could not control the process. Finally they used a solid state reaction where the compounds $Fe^{II}(pz)Pt^{II/IV}(CN)_4]{\bullet}I^-$ and $Fe^{II}(pz)Pt^{II}(CN)_4]$ were mixed and heated to enhance the migration of the iodides through the porosities. This is so long the only reported example of post-synthetical introduction of the iodine in the Hofmann-type network.

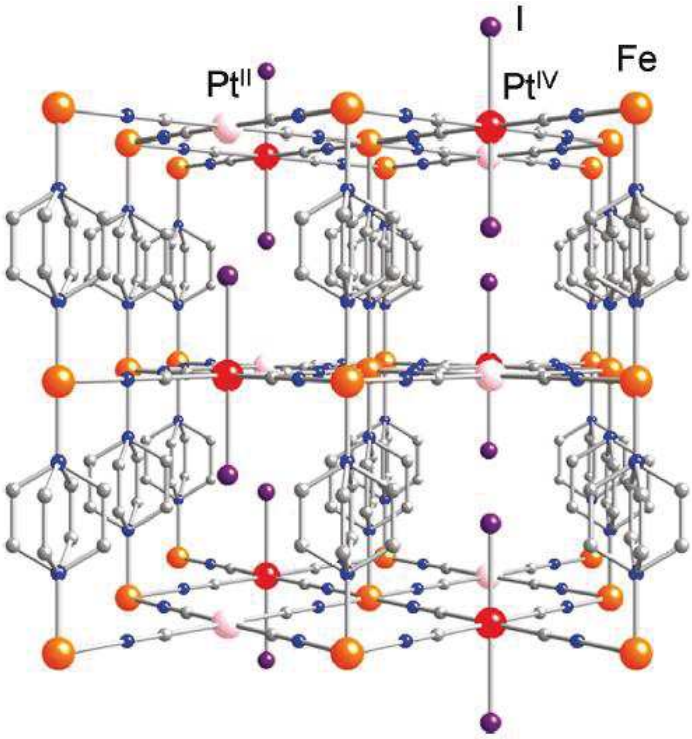

Figure 9 – Representation of $Fe^{II}(pz)[Pt^{II/IV}(CN)_4].I^-$ structure, obtained by an *in-situ* ptocess by Ohtani et al.[86]

In the field of the storage of gaseous compounds for the energy as H_2 or the sequestration of CO_2 from the industrial outgases, some studies already considered the Hofmann-type structures. The first study concerning the storage of hydrogen by Hofmann-type materials was published in 2007 by Li *et al.* [87] They studied the H_2 adsorption in cryogenic conditions (77 K) inside the structures $M'(L)[Ni^{II}(CN)_4]$ with M' = Fe^{II}, Co^{II}, Ni^{II} and they determined a maximal capacity around $M'(pz)[Ni^{II}(CN)_4]\bullet 2H_2$ for all structures. In 2008 Culp *et al.* extended the same study to a larger family, where M' = Co^{II} or Ni^{II}, L = pyrazine, 4,4'-bipyridine, or 4,4'-dipyridylacetylene, M'' =Ni^{II}, Pd^{II}, or Pt^{II}. [67] They evaluated the effect of the pore size on the adsorption: passing from pyrazine to bipyridine and dipyridylacetylene, the size of the pores (that are free spaces in the unit cells) progressively increased respectively from 7 to 11 and 13 Å. The adsorption isotherms showed that no actual improvement occurred and the storage density actually decreased by increasing the distance between planar cyanometallates. Culp and co-workers concluded that the smaller the size of the pores was, the higher was the adsorption heat (typically around 6-7 $kJ.mol^{-1}$ for H_2 inside coordination polymers and MOFs). Further studies about H_2 adsorption were continued by Rodriguez-Hernandez *et al.* and they focused on the reversible lattice structural transition on cooling the structures $M'(pz)[Ni^{II}(CN)_4]$ with M' = Co^{II} or Ni^{II}.[88] Culp *et al.* extended the work to the storage of other molecules, as CO_2 and N_2. For the CO_2 storage the *breathing structure* $Ni^{II}(bpene)[Ni^{II}(CN)_4]$ (where bpene = 1,2-bis(4-pyridyl)ethylene) permitted adsorption of about 14 CO_2 molecules per unit cell. [67] The breathing effect was given by the variation of the tilt angle of the pillared bpene molecules and consequent transition from a monoclinic to a tetragonal lattice, which was reversible on desorption of guest CO_2. As the authors reported, they encountered

some initial problem with the synthesis, since free bpene molecules remained trapped inside the cages and reduced the adsorption capacity. An improved method consisted in washing away the guest ligands with acetone.[89] Culp *et al.* extended this work for the series $Ni^{II}(L)[Ni^{II}(CN)_4]$ called *PICNICs* (Pillared Nickel Cyanides) where L was a large variety of 40 bidentate aromatic ligands.[65] They reported that, in contrast to the result with the flexible bpene ligand, the use of rigid ligands as bpac performed low capture of CO_2. The flexibility of Hofmann-type clathrates for the storage of different type of molecules opens to other possible applications. In the present work the first study about the entrapment of the molecular iodine in solution and in vapours with the Hofmann-type clathrates is presented as possible alternative to the current method of capture of the radioactive volatile iodine I^{129} produced in the nuclear power plants. A discussion about the preparation of supported $Ni^{II}(pz)[Ni^{II}(CN)_4]$ nanoparticles for the reversible capture of iodine will the one of the topics of the next section of this chapter.

1.1 – Characterization of the iodine adsorption with the Hofmann-type structures in solution and in vapours.

In part 1 of Chapter 1, the Hofmann-type structure $Ni^{II}(pz)[Ni^{II}(CN)_4]$ (Section 1.1.1) and the analogue structures obtained by modulating the different building elements (Sections 1.1.2, 1.1.3, 1.1.4 and 1.1.5) are experimentally studied for the entrapment of iodine in solutions of cyclohexane and in gaseous phase to investigate the affinity, the maximal capacity and the nature of the interactions.

1.1.1 - The Hofmann-type $Ni^{II}(pz)[Ni^{II}(CN)_4]$ and the capture of the molecular iodine.

The structure $Ni^{II}(pz)[Ni^{II}(CN)_4]$ was already reported in literature in the work of Culp *et al.* who precipitated the material by reaction of dehydrated $Ni[Ni(CN)_4]$ and pyrazine in xylene, under reflux conditions.[62] In the present work, we chose to prepare the structure as clathrate $Ni^{II}(pz)[Ni^{II}(CN)_4]\bullet 2H_2O$, with a slightly modified published procedure for $Fe^{II}(pz)[Pt^{II}(CN)_4]\bullet 2H_2O$.[85] This method did not need reflux conditions and the use of organic solvents and the material showed a relatively good crystallinity. The salt $Ni^{II}(NO_3)_2\bullet 6H_2O$ (3 mmol) was dissolved in a 50 vol% water / 50 vol% methanol solution, then 3 mmol of pyrazine was added; finally 3 mmol of $K_2[Ni^{II}(CN)_4]$ separately dissolved in water was added to the solution and instant precipitation of the solid occurred. For further details about the experimental preparation, see *Experimental Section*. The X-Ray Powder Diffraction pattern (XRPD) indicated that the precipitated $Ni^{II}(pz)[Ni^{II}(CN)_4]\bullet 2H_2O$ was isostructural to the previously reported $Fe^{II}(pz)[Pt^{II}(CN)_4]\bullet 2H_2O$ analogue, whose resolved structure was published in the work of Niel *et al.*,[34] as shown in Figure 10 for the most intense peaks (range 2θ = 10-26). The main peak was observed at 17.5° and it was related to the Miller plane (110). Since the powder was sieved to size 45µm in order to fill the 0.5 mm large capillary, the peaks were larger and they overlap sometimes. For example, the (100) peak was partially overlapped by the more intense (001) peak at around 12.5° and the (101) peak was completely covered by the (110) peak and not visible. LeBail analysis carried out to model the XRPD data (for the refined XRPD patterns with LeBail method, see *Annexes*) indicated that the material crystallized in a tetragonal *P4/m* space group with the cell parameters values $a = b$ = 7.1762(3) Å, c = 7.0316(5) Å, $\alpha = \beta = \gamma$ = 90.0°. With respect to the reference phase $Fe^{II}(pz)[Pt^{II}(CN)_4]\cdot 2H_2O$, the peaks were shifted to higher 2θ values due to the stronger coordination with Ni^{II} that gave smaller lattice parameters.

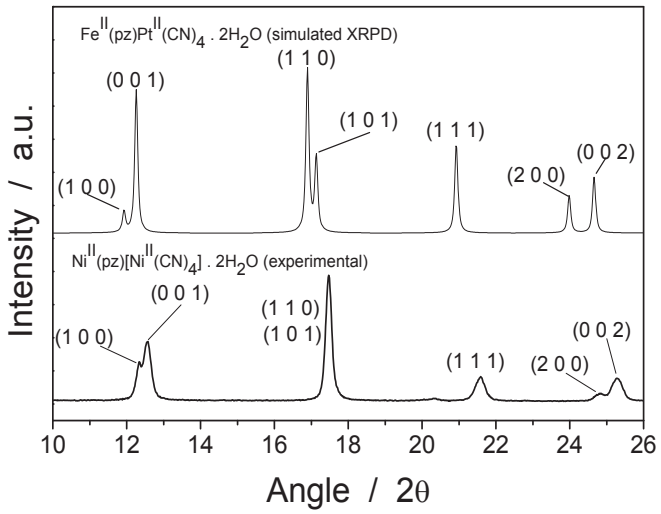

Figure 10 - Indexing of the phase $Ni^{II}(pz)[Ni^{II}CN)_4]\cdot 2H_2O$ with resolved isostructural $Fe^{II}(pz)[Pt^{II}CN)_4]\cdot 2H_2O$.

The thermogravimetric analysis (TGA), performed under air, showed a loss below 100 °C regarding water and traces of other solvents used in the synthesis (methanol) or in the washing step (acetone). Another weight loss of overall 38 wt% around 400 °C corresponded to one pyrazine and 4 CN^- (Figure 11). The residue consisted of metals that reacted with O_2 over 400 °C to give nickel oxide (final green powder).

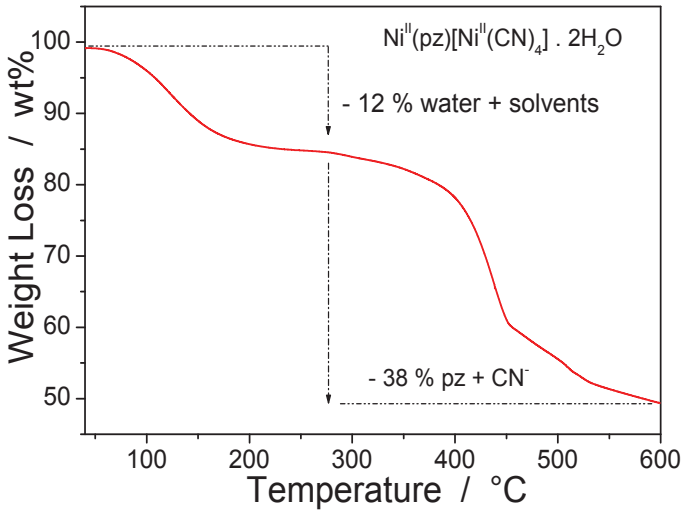

Figure 11 – TGA curve for $Ni^{II}(pz)[Ni^{II}CN)_4]\cdot 2H_2O$.

The FT-IR spectra for $Ni^{II}(pz)[Ni^{II}(CN)_4]$ were registered at room temperature in KBr matrix, in transmission configuration, in the range 400-3500 cm^{-1}. In order to identify all the bands the precursor $K_2Ni^{II}[(CN)_4]$, the pure crystalline pyrazine, the complex Ni^{II}-pyrazine as well as the complex $Ni^{II}[Ni^{II}(CN)_4]$ were also analyzed. The indexing of the bands for the pyrazine was carried out following the work of Breda *et al.* [90] and Ekici *et al.* [42] As complementary analysis, the Raman for the clathrate structure was also performed with laser D473 in the range 1500-3500 cm^{-1}. Table

1 compares the crystalline pyrazine with the coordinated ligand in order to associate the correct vibration modes. The typical vibration modes of the aromatic ring of pyrazine consist of: weak bands related to the stretching mode of aromatic C-H around 3100 cm^{-1} C-H in-plane and out of plane bending and vibrations of the overall ring in the range 1500-400 cm^{-1}. After coordination, a general shift to higher frequencies of most of the bands was detected as effect of coordination, as already observed previously for Hofmann-type clathrates containing pyrazine ligand (Table 1).[91] The pyrazine is a π-basic ligand that coordinates by transfer of electron density from an anti-bonding orbital π^* to the octahedral Ni centre. This makes the molecule vibrate at higher frequencies.

The stretching mode of cyanide, ν(C≡N), is typically observed at 2079 cm^{-1}, when the cyanide is a free ion,[92] but the coordination of the CN^- ligands to a metallic centre generally triggers an increase of the vibration mode. We report now the evolution of the free cyanides to the bridging cyanides in the Hofmann-type structure in terms of IR vibration modes. When four CN^- ligands were coordinated to a Ni^{II} centre in the square planar compound $K_2[Ni^{II}(CN)_4]$, where Ni^{II} was coordinated to cyanide on the side of C, a strong band was measured at 2121 cm^{-1}, with a weak band at 2084 cm^{-1}, for ν(C≡N) (Table 2). The increase in frequency with respect to the free CN^- was due to the compromise between a σ-bonding, where CN^- ligand gave electron density from anti-bonding orbital σ^* to the metallic centre, and a π-bonding, where CN^- ligand filled its anti-bonding orbitals π^* with electron density from a *d* orbital of the metal by *back donation*. When the cyanides were coordinated with two Ni^{II} in the bi-dimensional coordination polymer $Ni^{II}[Ni^{II}(CN)_4]$ (prepared as explained in the *Experimental Section*), a shift by 45 cm^{-1} to higher vibrations was observed. In this case, CN^- acted as a bridging ligand with a σ-bonding on the N side, in which the depopulation of the σ^* anti-bonding orbital of CN^- justified the higher vibration mode of ν(C≡N). Finally, when the tri-dimensional $Ni^{II}(pz)[Ni^{II}(CN)_4]\bullet 2H_2O$ with pyrazine was prepared, a further shift by 9 cm^{-1} occurred for the ν(C≡N) mode, with stronger band at 2174 cm^{-1}. CN^- ligands had actually other vibration modes but most of them were not detected due to very weak intensity as the stretching ν(Ni-C≡N) and the out-of-plane γ(Ni-C≡N), typically situated in the range 450-550 cm^{-1}.[93] By contrast, the vibration mode δ(Ni-C≡N) was strong and shifted largely due to coordination, passing from 416 cm^{-1} in $K_2[Ni^{II}(CN)_4]$ to 444 cm^{-1} in $Ni^{II}[Ni^{II}(CN)_4]$ and $Ni^{II}(pz)[Ni^{II}(CN)_4]\bullet 2H_2O$. As explained in literature,[60] this effect was due to mechanical coupling of the internal modes of $[Ni^{II}(CN)_4]^{2-}$ with the newly formed δ(Ni-N≡C) vibrations. Moreover, a new strong band at 485 cm^{-1} appeared in the low region. The spectrum recorded on the complex $Ni^{II}(NO_3)_2$/pyrazine (for the preparation, see *Experimental Section*) confirmed that this was for the band for the coordination Ni^{II}-pyrazine bond.

Table 1 - IR and Raman bands for crystalline and coordinated pyrazine.

(w = weak; s = strong; * = Raman and IR active; ** = only Raman active)

Vibration mode matching (ν = stretching; δ = bending; γ = out of plane)	Crystalline, non-coordinated Pyrazine	Coordinated Pyrazine in *Ni*^{II}(pz)[Ni^{II}(CN)$_4$]
ν(C-H)	3085 cm^{-1} (w)* 3064 cm^{-1} (w)	3119 cm^{-1} (w)
ν_{ring}	1540 cm^{-1} (w) 1492 cm^{-1} (s) 1419 cm^{-1} (s)	1550 cm^{-1} (w) 1494 cm^{-1} (w) 1423 cm^{-1} (s)
δ(C-H)	1343 cm^{-1} (w)	1355 cm^{-1} (w)
ν_{ring}	1176 cm^{-1} (w); 1147 cm^{-1} (s)	1162 cm^{-1} (s)
δ(C-H)	1123 cm^{-1} (s); 1110 cm^{-1} (s) 1068 cm^{-1}(s)	1129 cm^{-1} (s) 1090 cm^{-1} (s)
δ_{ring}	1024 cm^{-1} (s)	1057 cm^{-1} (s)
ν_{ring}	1011 cm^{-1} **	1034 cm^{-1} (s)**
γ(C-H)	796 cm^{-1} (s)	812 cm^{-1} (s)
δ(C-H)	701 cm^{-1} (w) **	699 cm^{-1} (s)**
γ_{ring}	597 cm^{-1} (w); 414 cm^{-1} (s)	559 cm^{-1} (w)

Table 2 – IR and Raman bands for cyanides and metal-ligand bands.

(vw = very weak; w =weak; s = strong; vs = very strong; * = Raman and IR active)

Vibration mode matching (ν = stretching; δ = bending)	ν(C≡N)	δ(Ni-C≡N)	ν(*Ni*-N$_{pz}$)
K$_2$[Ni^{II}(CN)$_4$]	2121 (vs), 2084 (w)	416 (s)	-
Ni^{II}[Ni^{II}(CN)$_4$]	2165 (vs), 2129 (w)	446 (s)	-
Ni^{II} (NO$_3$)$_2$ / pyrazine	-	-	480 cm^{-1}
Ni^{II}(pz)[Ni^{II}(CN)$_4$].2H$_2$O	2174 cm^{-1} (vs)*, 2130 (w)*	444 (s)	485 (s)*

The $Ni^{II}(pz)[Ni^{II}(CN)_4]\bullet 2H_2O$ was also analyzed using solid UV-VIS spectroscopy in reflectance mode. The reflectance spectrum in Kubelka-Munk units is reported in Figure 12, where two bands were detected. A band appears in the VIS region at 555 nm, which corresponds to *d-d** transition; the position of the band depends on the oxidation and the coordination of the metallic centres. A second band, very intense, was found in the UV region and it is due to both electronic transitions in cyanides and aromatic bonds of pyrazine.

Once we confirmed to have the good compound $Ni^{II}(pz)[Ni^{II}(CN)_4]\bullet 2H_2O$, it was considered for the capture of iodine. Since the structure forms a water clathrate, H_2O molecules must be previously desorbed in order to introduce I_2 molecules. To this purpose, a thermal treatment over 80 °C under primary vacuum was necessary in order to obtain the dehydrated $Ni^{II}(pz)[Ni^{II}(CN)_4]$.

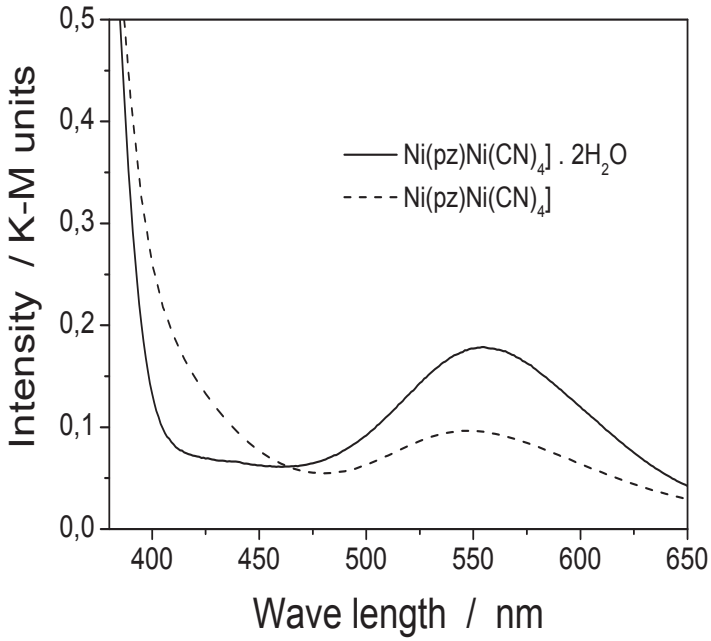

Figure 12 - UV-VIS spectra in reflectance mode for $Ni^{II}(pz)[Ni^{II}(CN)_4].2H_2O$ and $Ni^{II}(pz)[Ni^{II}(CN)_4]$.

A FT-IR spectrum was recorded for the dehydrated $Ni^{II}(pz)[Ni^{II}(CN)_4]$, pretreated under vacuum at 200 °C, and it was compared with the IR spectrum of the hydrated structure (Figure 13). The only difference between the spectra was the bands related to the adsorption of water (stretching mode, 4000-3000 cm^{-1}; bending mode 1630-1600 cm^{-1}), so that no significant structural modification after dehydration was detected. Further details about the adsorption of water are reported in Section 1.2.1. The dehydrated material however showed a change of colour from violet to grey. Ni^{2+} cations in octahedral configuration with 6 ligands can assume a large variety of colours depending on the nature of the ligands.[94] Since the change in colour is associated to the desorption of water, we could relate this change to the unsaturated Ni^{2+} cations on the surface that loose the coordinated H_2O molecules upon desorption. If the desorbed material was left in contact with air, a quite rapid rehydration of the surface occurred with subsequent change in colour. UV-VIS spectroscopy in reflectance mode was performed after desorption, attempting to

minimize the times of contact with air and a slightly lower band to 545 nm was detected, as sign of the change in coordination of Ni^{2+} cations probably on the surface.

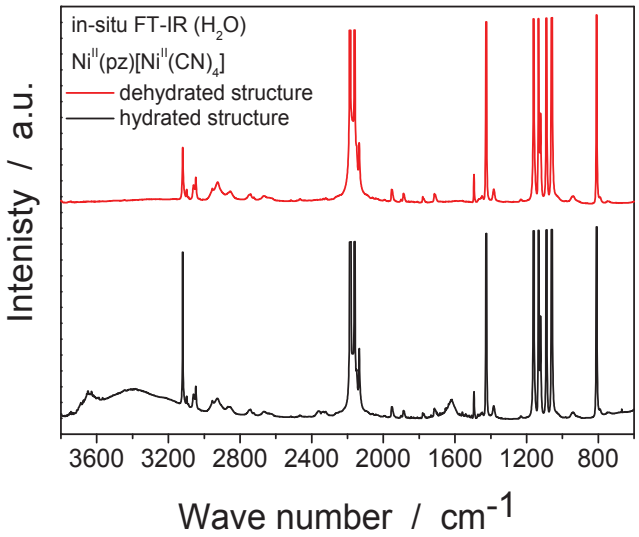

Figure 13 - FT-IR spectra for dehyrated $Ni^{II}(pz)[Ni^{II}(CN)_4]$ recorded under vacuum and hydrated NiII(pz)[Ni(CN)4].

Once the host structure $Ni^{II}(pz)[Ni^{II}(CN)_4]$ was prepared, the entrapment of iodine was evaluated in different conditions:

- in solutions of iodine in cyclohexane, since iodine has a high solubility in apolar solvents and does not interact giving ionic species;
- in vapours of iodine at 80 °C, in order to evaluate the entrapment of the gaseous phase;
- in vapours of iodine and in the presence of water at 80 °C, to study the selectivity that is demanded for a good efficiency in operating conditions. The results about the selectivity tests will be discussed in the dedicated section 1.2.1.

Entrapment of I_2 with the $Ni^{II}(pz)[Ni^{II}(CN)_4]$ structure.

The entrapment of the iodine can be described as an adsorption process inside the microporosity of the clathrate system. An adsorption process can be studied as an equilibrium reaction:

Equation 1 – General expression for an adsorption

$$[\boldsymbol{A}] + [\boldsymbol{S}] \leftrightarrow [\boldsymbol{S} \cdot \boldsymbol{A}]$$

where [A] is the concentration of adsorbate (or its pressure in the case of the gaseous phase), [S] is the concentration of the bare sites on the solid and [S•A] is the concentration of sites occupied by the adsorbate. An equilibrium constant K for this process can be written as:

Equation 2 – Equilibrium constant for an adsorption

$$K = \frac{[S \cdot A]}{[A][S]}$$

The value of K gives information about the affinity between the adsorbate and the adsorbent: the higher it is, the better the affinity is. Adsorption processes are generally studied by tracing an isotherm, *i.e.* the variation of adsorbed amount as function of the equilibrium concentration, at constant temperature. From the isotherm it is possible to estimate the maximal entrapment and the constant equilibrium. A systematic study of the adsorption of iodine was performed preferentially in a solution of cyclohexane, since the variation in concentration of iodine before and after the entrapment can be easily controlled with a UV-VIS spectrometer. Molecular iodine absorbs in the VIS region at 525 nm and its molar extinction coefficient in cyclohexane at room temperature (929.61 $L.mol^{-1}.cm^{-1}$) was obtained experimentally (for full description of the Beer-Lambert Law and the used technique, see the section *Annexes*). Before tracing the isotherm, the equilibrium time must be determined with a kinetic study. A kinetic curve was obtained by measuring the iodine entrapment after different times as shown in Figure 14. The absorbance of the iodine solution decreased rapidly and became constant after 2 hours, indicating that the equilibrium was reached. This indicated that a rapid entrapment occurred due to the high affinity for iodine. The curve were fitted with a good approximation with a pseudo-second order kinetic (for a full description of the model, see Annexes), meaning that the sorption rate followed the relationship:

Equation 3 – Pseudo-second order kinetics

$$r = k[Q_e - Q]^2$$

where Q_e is the entrapped amount at equilibrium and infinite time, Q is the entrapped amount at time t and k is the kinetic constant whose value for the $Ni^{II}(pz)[Ni^{II}(CN)_4]$ was $k = 0.18\ mmol.g^{-1}.min^{-1}$.

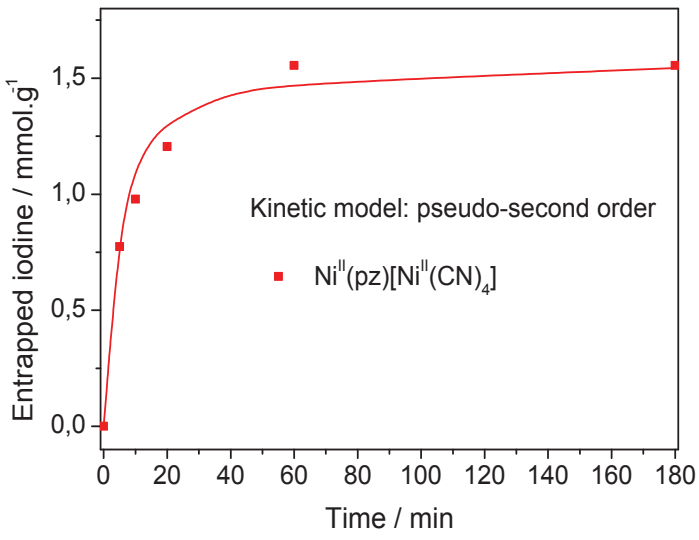

Figure 14 - Kinetics of sorption of I_2 by $Ni^{II}(pz)[Ni^{II}(CN)_4]$.

The isotherm for $Ni^{II}(pz)[Ni^{II}(CN)_4]$ was obtained by plotting the amounts of entrapped iodine at corresponding equilibrium concentrations (Figure 15). The curve is concave to the concentration

axis, which indicated that the adsorption is thermodynamically favoured and reflects the ability of the materials for the I_2 sorption in a wide range of concentration.

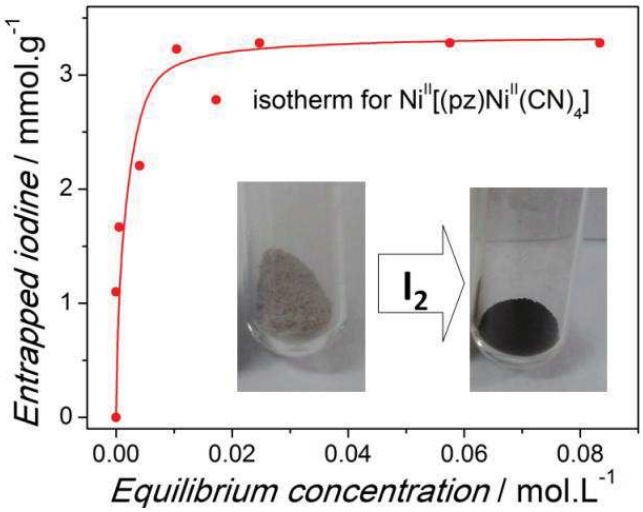

Figure 15 - Iodine adsorption isotherm in a cyclohexane solution for $Ni^{II}(pz)[Ni^{II}(CN)_4]$ Inset: from left to right, photographs of thermally activated powders before and after contact with iodine.

According to the IUPAC classification of isotherms, this is a *I type* isotherm (for the IUPAC classification of isotherms, see *Annexes*), which means that the adsorption is limited to the formation of a monolayer. The material changed its colour depending on the iodine concentration, ranging from yellow at very low concentration to dark brown after I_2 filling at maximal storage capacity (Inset Figure 15). The maximum adsorption capacity (Q_{max}), which is indicative of the efficiency of the materials to capture I_2, was determined from the plateau of the isotherm and it was equal to 3.28 ± 0.1 mmol.g^{-1}, corresponding to the adsorption of about 1 mole of I_2 per mole of the host structure. The experimental data were fitted with the Langmuir isotherm which is described by the following relationship (for a full description, see *Annexes*):

Equation 4: Langmuir isotherm.

$$Q = Q_{max}\frac{KC}{1+KC}$$

where Q are the entrapped amounts at related equilibrium concentrations C and K is the Langmuir constant. Even though we were still far from ideal conditions of application of the Langmuir model, a linear regression with R = 0.99 was obtained. The model approximated the curve since the adsorption was arrested to the formation of a monolayer i.e. only one I_2 per cage was adsorbed and no condensation of the adsorbate was observed. From the linear equation of the Langmuir model the following parameters were found: maximal capacity Q_{max} = 3.34 mmol.g^{-1} and Langmuir constant K = 1506 L.mol^{-1}. The parameters obtained from Langmuir linearized model were employed in the following relationship to estimate the free energy:

Equation 5 – Free energy.

$$\Delta G = -RTln(Q_{max}K)$$

with R = 8.314 $J.K^{-1}.mol^{-1}$ (gas constant) and temperature T = 300 K. Free energy value obtained with this formula had a negative value, which was consistent with the spontaneous observed adsorption. The maximal entrapped amount of iodine was confirmed by the TGA curve at rate 5°C.min^{-1} (Figure 16, blue curve), indicating a loss of 41 wt%. It was calculated a molar ratio iodine/host structure of 1.01 ± 0.03, which corresponded to one mole of iodine per mole of clathrate (for the quantification by TGA, see *Annexes*). The transformation associated to the release of I_2 was between 150 and 250 °C and the first derivative of the TGA curve indicated the inflection point (point with the highest desorption rate) around 180 °C.

The iodine capture by the dehydrated clathrate $Ni^{II}(pz)[Ni^{II}(CN)_4]$ was also investigated in gaseous phase at 80 °C, since this is the temperature of out-gases in real operating conditions. The powder was kept inside a hermetically closed glass container where a saturated atmosphere of iodine was created by sublimation at 80 °C (pressure around 1 kPa). The entrapment in vapours demanded a longer time of at least 3 days in order to have a homogeneous iodine-loaded material. Diffusion was indeed slower than in the solution test. The surplus of iodine that deposited on the powder without entering the structure was washed away with an apolar solvent like pentane or cyclohexane, so as to keep just the iodine inside the pores. The I_2 uptake from vapours determined from TGA curve a capture of 2.32 $mmol.g^{-1}$. The amount corresponded to final formula $Ni^{II}(pz)[Ni^{II}(CN)_4]$•0.7 I_2 (Figure 16).

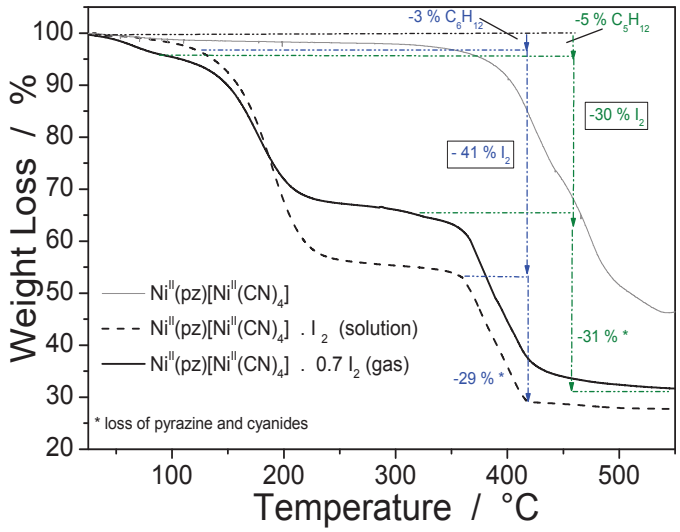

Figure 16 - Thermogravimetric analyses performed for $Ni^{II}(pz)[Ni^{II}(CN)_4]$•$2H_2O$ before and after iodine uptake in the gaseous phase and in solution.

An adsorption is always an exothermal process ($\Delta H < 0$) since the variation of the entropy is negative, $\Delta S < 0$. Hence, an increase in temperature decreases the equilibrium constant following the Van't Hoff relationship:

Equation 6

$$K(T) = K_0 exp\left(-\frac{\Delta H}{RT}\right)$$

where R is the gas constant, T the temperature and K_0 the equilibrium constant at T = 0 K. TGA associated with mass spectroscopy analyses (Figure 17) showed that, independently from the way the iodine was captured, it was released from the structure at 150 °C and was completely removed at 200 °C. The low temperature for a complete desorption suggested that the iodine was physisorbed. Also, the iodine was removed before the decomposition of the host structure around 400 °C indicating the possibility to regenerate the host structure and the cycling ability (see Section 1.1.2 for more details).

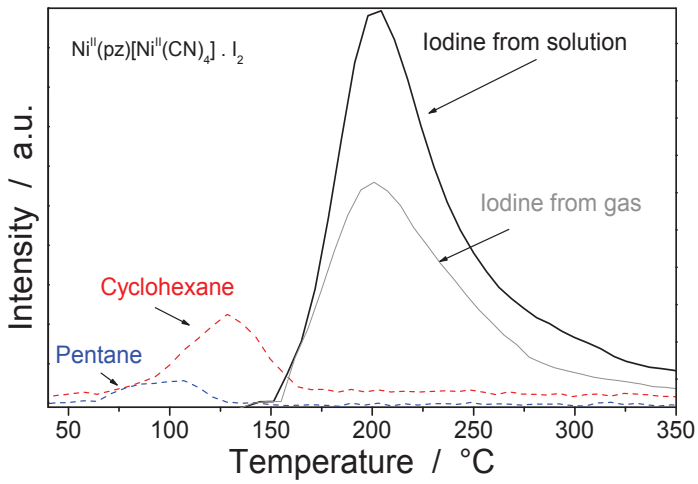

Figure 17 - Mass-spectroscopy associated to TGA indicating initial decomposition temperatures for iodine and solvents for the uptake in solution and vapours.

In order to better understand how the insertion of the iodine affects the structure of the clathrate and in which form the iodine was entrapped, XRPD analyses as well as different spectroscopic analyses (FT-IR, Raman, solid UV-VIS and XPS) were carried out.

Perturbation of the host structure.

XRPD patterns after the entrapment in solution were registered for the clathrates at different contents of iodine with formulas $Ni^{II}(pz)[Ni^{II}(CN)_4]\bullet x\ I_2$ where x = 0.2, 0.6 and 1. A XRPD pattern was also registered for the clathrate $Ni^{II}(pz)[Ni^{II}(CN)_4]\bullet I_2$ after a desorption treatment at 200 °C under primary vacuum (Figure 18). We reported as well the indexed Miller planes (hkl) for the P4/m structure of $Ni^{II}(pz)[Ni^{II}(CN)_4]$. With increasing content of iodine a gradual modification of specific Miller planes took place. The peaks related to the planes (100) and (200) and, thus, to the lattice parameters *a* and *b* gradually shifted to lower angles and their intensity increased. In parallel, the peaks related to the planes (001) and (002) and to the third parameter *c* slightly shifted to higher angles and its intensity decreased. The peak for the plane (001) almost became undetectable. No appearance of new peaks suggested that the geometry of the tetragonal lattice did not change after the entrapment.

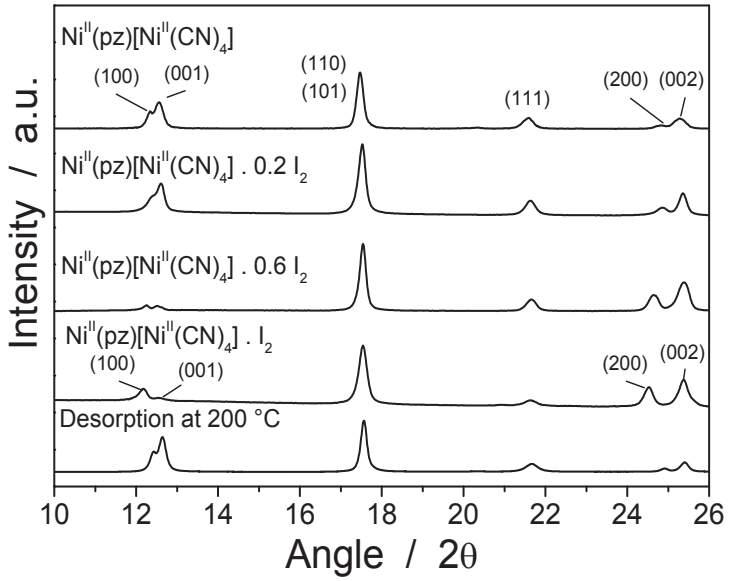

Figure 18 – XRPD for $Ni(pz)[Ni(CN)_4]\bullet x\ I_2$ where x = 0 or 0.2, 0.6 and 1 after entrapment in solution and XRPD after desorption of iodine.

Since the diffraction angle is bound to the atomic distance of the diffracting planes, a rough estimation of new lattice parameters could be performed with the formula:

Equation 7

$$\frac{1}{d^2} = \frac{h^2}{a^2} + \frac{k^2}{b^2} + \frac{l^2}{c^2}$$

where *d* is the atomic distance, *h*, *k* and *l* are the Miller indices and *a*, *b* and *c* are the lattice parameters. The use of this formula (for details, see *Annexes*) indicated that parameters *a* and *b* increased uniformly and *c* decreased slightly. The change in intensities was due to a change in the scattering power of the planes, which meant a modification of their electronic density.[95] Since the (100) peak, which was related to the distance between two pyrazines, became progressively more intense than the (001) peak with iodine loading, the iodine was supposed located in the space between the pyrazines rather than inside the tetracyanonickelates planes. LeBail refinement was performed on the structure at maximal content in order to find with a good precision the new lattice parameters (for details, see *Annexes*). $Ni^{II}(pz)[Ni^{II}(CN)_4]\bullet I_2$ showed a *P4/m* space group with cell parameters $a = b =$ 7.2605(6) Å, $c =$ 7.0072(5) Å, $\alpha = \beta = \gamma =$ 90.0°. The slight increase of the *a* and *b* cell parameters is by 0.084 Å. The final volume obtained by multiplication of the lattice parameters was 369.3(8) $Å^3$, which was slightly bigger (by 2%) than the initial volume before iodine uptake, 362.1(1) $Å^3$. The XRPD pattern on the desorbed structure at 200 °C shows a fully reversible process, giving same peak positions as the unfilled clathrate. For the entrapment in vapours, XRPD patterns were registered at maximal obtained capacity and after desorption at 200 °C under primary vacuum (Figure 19). The same trend as the entrapment

in solution as well as a full reversibility were detected. In the XRPD pattern of the I_2-loaded structure, we can still clearly distinguish the peaks (001) and (100) at low angles.

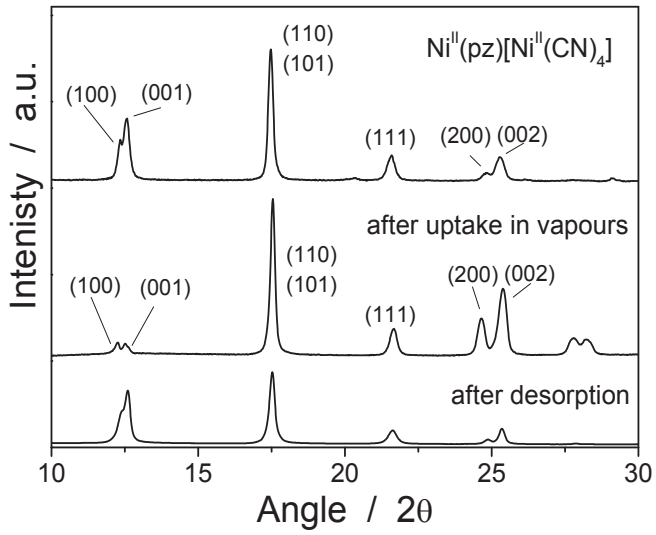

Figure 19 – XRPD for $Ni(pz)[Ni(CN)_4]$ before and after entrapment in vapours and deorption.

FT-IR spectra of the samples after maximal iodine loading in solution or in gas conditions show small shifts of the bands related to the pyrazine ligand (Table 3) and an appeareance of a more weak band at 1106 cm^{-1} not clearly detected for $Ni(pz)[Ni(CN)_4].2H_2O$, but visible in the free pyrazine spectrum (1110 cm^{-1}). This effect is justified by a weak interaction with the iodine inside the porosity.

Table 3 – Changes in FT-IR bands related to the pyrazine vibtrations, before and after uptake inside the structure $Ni^{II}(pz)[Ni^{II}(CN)_4]$.

Vibration mode matching (ν = stretching; δ = bending; γ = out of plane)	Pyrazine in $Ni^{II}(pz)[Ni^{II}(CN)_4]$	Pyrazine in $Ni^{II}(pz)[Ni^{II}(CN)_4].I_2$
ν_{ring}	1162 cm^{-1} (s)	1165 cm^{-1} (s)
δ(C-H)	1129 cm^{-1} (s); 1090 cm^{-1} (s)	1135 cm^{-1} (s); 1106 cm^{-1} (w); 1082 cm^{-1}(s)
γ(C-H)	812 cm^{-1} (s)	800 cm^{-1} (s)

In addition, the cyanide stretching vibration shifts from 2174 to 2165 cm^{-1}. Also, a little shift of the band for $\nu(Ni\text{-}N_{pyrazine})$ from 485 to 481 cm^{-1} is detected, indicating a weak effect on the coordination with the pyrazine. No bands for I-I bonds were observed at FT-IR spectroscopy, as a result of the symmetry selection rules.[96] Both materials loaded with I_2 in solution and gas were analysed after desorption at 200 °C as well. As already observed by XRPD, a full regeneration of

the host structure was observed by FT-IR with bond vibrations back to the same values as before capture, as Figure 21 and Figure 21 show.

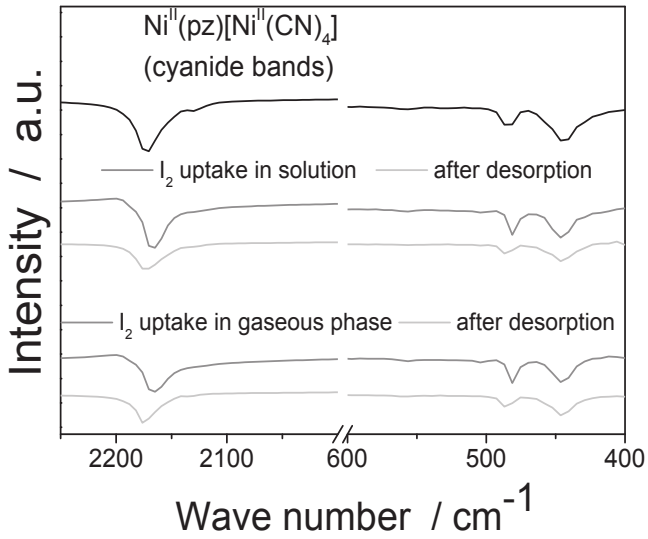

Figure 20 - FT-IR spectra for cyanides after uptake in solution or vapours and related desorptions.

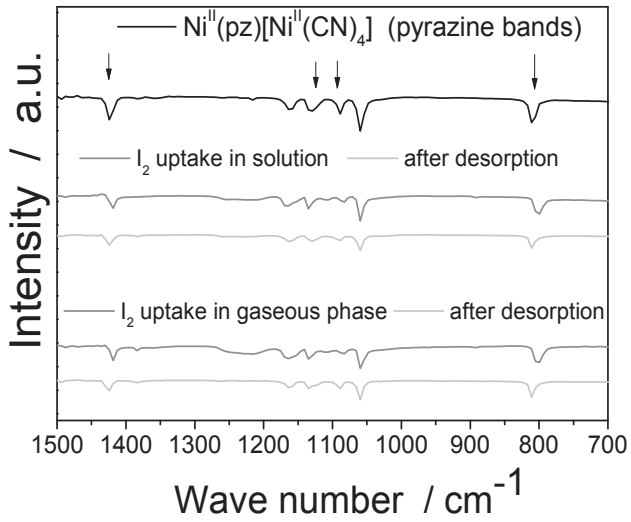

Figure 21 – FT-IR spectra for pyrazine after uptake in solution or vapours and related desorptions.

Besides, XPS analysis was also performed to see if oxidation state of Ni is affected after insertion of iodine. No change for the bands related to Ni 2p (bind energies 855 and 873 eV) was detected, that means that no redox reaction occurred.

Perturbation of the guest molecule (iodine).

As the TGA curves couple with mass spectroscopy showed, entrapment of iodine inside the clathrate was a reversible process indicating the presence of a weak interaction. The interaction did not only affect the structural stability of the host structure. We report now a further investigation concerning the nature of the confined iodine. The binding energy for iodine I 3d5

detected at XPS was 217 eV but, as XPS database of NIST showed,[97] there is no clear distinction between iodides and iodine for this technique. By contrast, Raman and UV-VIS spectroscopy are powerful means in order to characterize the electronic state and the perturbation of iodine both in solution and in the solid state. At this point of the discussion, it is important to remind some relevant chemical properties of the molecule I_2 before treating the techniques and related experimental data.

The molecular iodine I_2 (electron configuration [Kr] $4d^{10}\ 5s^2\ 5p^5$) is well known to be a Lewis acid acceptor, since it can interact with polar solvents or chemical species that expose electrons giving complexes donor-acceptor. This properties were studied since the '40s in the work of Hildebrand *et al.*[98] and further studies about interactions with hydrocarbons[99], or compounds with basic properties, such as pyridinium[100] or amines. [101] [102] [103] The acceptor capacity is due to the empty anti-bonding molecular orbital σ* as shown in Figure 22.

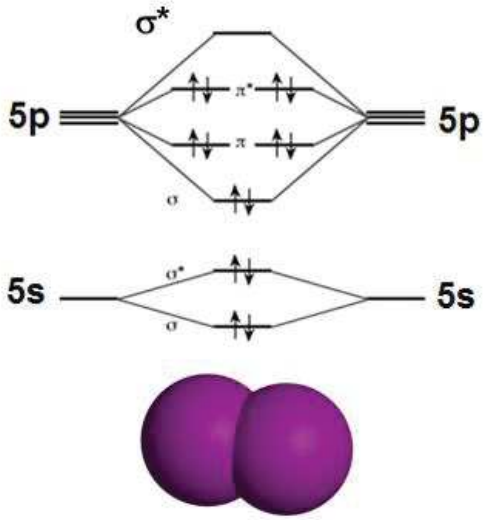

Figure 22 – M.O. for the molecule I_2.

Charge transfer from a π-donor to the σ^* anti-bonding orbital triggers a weakening effect on I-I bond which is 2.69 Å long in the free molecule. With a strong enough charge transfer, the bond I-I can be broken so as to form I^+ and iodide I^-. Since the iodide I^- is a donor, it typically exists in a strong interaction with I_2 (acceptor) giving I_3^-. Following this mechanism ionic species with higher molecular weight (polyiodides) can be formed, especially in the solid state depending on the I^-/I_2 ratio, as I_5^- , I_7^- or I_{12}^{2-} .[104] All these ionic species are not singular entities but are complexes of I_3^- and x I_2 molecules (x = 1, 2, 3 …) in interaction. In the coordination complexes, I^- is a typical π-basic ligand, however some rare cases of coordination complexes containing I_2 as ligand are also found in literature.[105] For instance, I_2 acts both as acceptor in the Van Koten complex (Figure 23-a), or as a donor in the $[(CF_3)\cdot Rh_2(O_2CCF_3)_4\cdot(I_2)]$ complex (Figure 23-b). In the Van Koten complex, I_2 and the metallic centre Pt^{II} coordinate by back donation: electron density from Pt^{II} orbital d_{z^2} is transferred to the anti-bonding orbital σ* of iodine. An occupation of the orbital σ* brings to an elongation of the I-I bond from 2.69 Å to 2.82 Å, without dissociation of I_2. Note that I_3^- typically has a bond length around 2.91 Å in the symmetric configuration.[106] By contrast, in the

case of the Rh-complex, I_2 acts as a donor and transfers to the metal the electron density from the anti-bonding orbitals π^*. The bond length of iodine in this interaction results unchanged and still at 2.69 Å.

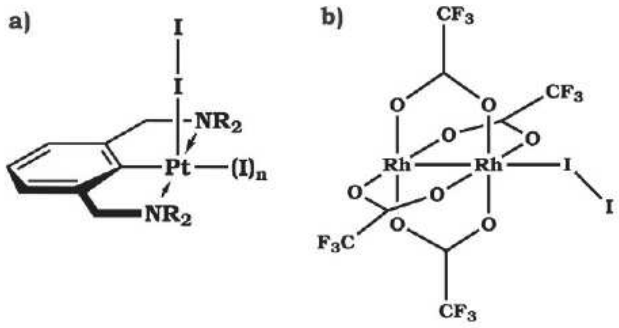

Figure 23 - Complexes with ligand I_2 as acceptor (a) and donor (b) [105]

These studies showed that I_2 as acceptor always undergoes a weakening of the bond, which is not observed when I_2 is a donor. Raman and UV-VIS spectroscopy generally give elucidations about the electronic state of the iodine and the intensity of the charge transfer. In the present work, according to the reported considerations from literature and the experimental spectra, interpretations about the nature of the interaction of I_2 with the host structure $Ni^{II}(pz)[Ni^{II}(CN)_4]$, as well as with the analogue structures treated in the next sections, were made. It is worth at first to explain how typically iodine is recognised with the used techniques. By UV-VIS spectroscopy, the absorption at λ = 525 nm for the molecular iodine is related to the gap between the HOMO (Highest Occupied Molecular Orbital) and the LUMO (Lowest Unoccupied Molecular Orbital). When the charge transfer occurs, this gap increases[107] and a blue shift to lower wavelengths in the UV-VIS spectrum is observed. The stronger is the donor, the larger is the shift. For weak charge transfers – *i.e.* with free pyrazine[108] - when iodine is perturbed but the dissociation does not occurs yet, absorption in the range 400-500 nm is observed, with a second band detected in the UV region around 200 nm. The wavelength 400 nm is reported in literature as the absorption for the pre-dissociation complex $[I_2]^-$ and thus represents a limit to the absorption range of I_2.[109] When the triodide, I_3^-, is formed due to dissociation, the UV-VIS spectrum shows typically 2 bands with maxima at 297 and 350-370 nm.[110] [111] Solid state UV-VIS spectroscopy in reflectance mode was performed for the characterization of the iodine entrapped in solution by the host structure $Ni^{II}(pz)[Ni^{II}(CN)_4]$ at different concentrations and it gave the spectra reported in Figure 24. At very low content of iodine, *i.e.* $Ni^{II}(pz)[Ni^{II}(CN)_4]\bullet 0.01\ I_2$, the clathrate was yellow and the confined iodine absorbed towards 400 nm overlapping partially with the UV band of the host structure. Even though the exact maximal absorption for this band cannot be seen, it was assumed lower than 400 nm and related to the presence of I_3^-. At increasing iodine content (from 0.1 I_2 per unit cell), a second band appears at 470 nm ans it was associated to the confined I_2. The material with composition $Ni^{II}(pz)[Ni^{II}(CN)_4]\bullet I_2$ at maximal capacity showed a sort of convolution of the bands observed at lower capacities with maximum around 430 nm. After desorption at 200 °C, still a

weak absorption could be recognized in the triiodide region (around 400 nm), estimated by EDX around 0.02 I_2 per unit cell.

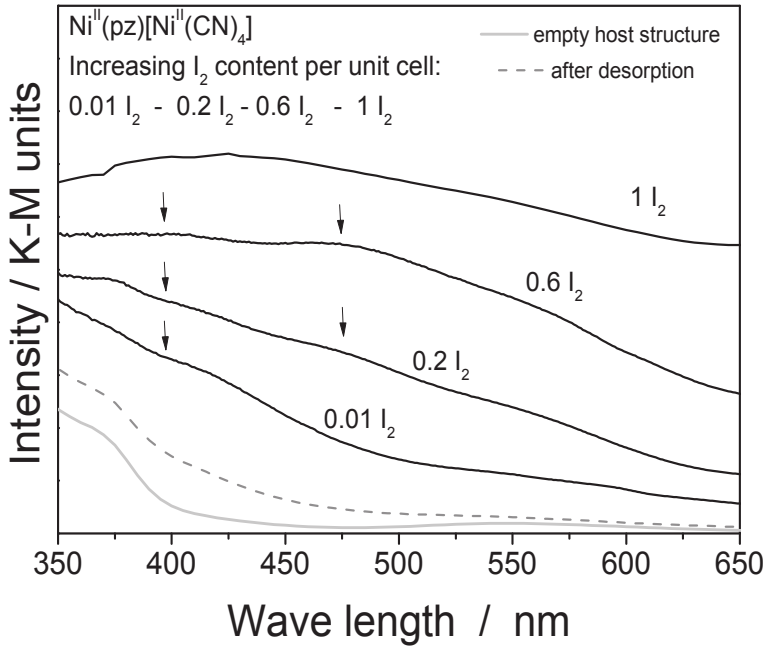

Figure 24 - Solid UV-VIS spectroscopy in reflectance mode for Ni^{II}(pz)[Ni^{II}(CN)$_4$] and clathrate at different iodine loading after entrapment in solution.

The UV-VIS spectrum in reflectance mode registered for the material after iodine entrapment in vapours showed a similarity with the iodine clathrate Ni^{II}(pz)[Ni^{II}(CN)$_4$]•I_2 prepared in solution, as reported in Figure 25.

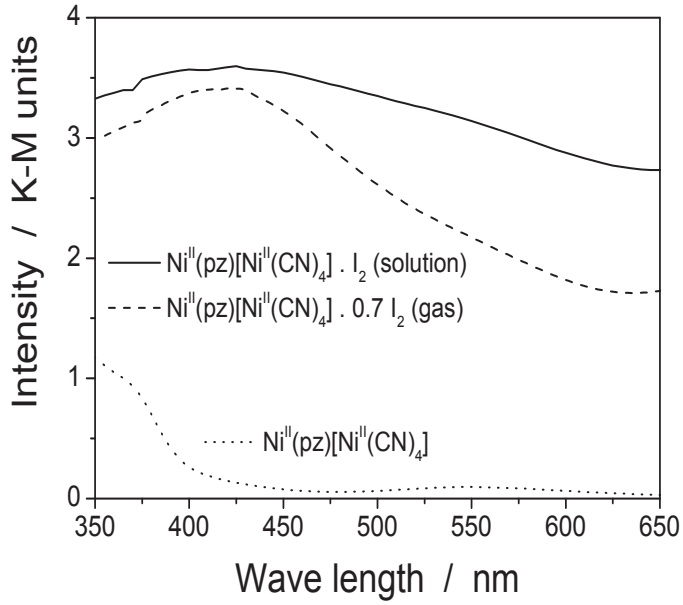

Figure 25 - Comparison of the materials at highest loading obteined after cpture in solution and vapours.

Relative intensities are not correlated to amount ratios I_3^- / I_2 since the molar extinction coefficient for I_3^- is always much higher than I_2.[112] Thus, I_3^- is expected to be in a minor quantity with respect to I_2. In support to the UV-VIS spectra, Raman spectra were registered as well. The Raman-active stretching mode ν(I-I) for the free gaseous iodine is at 213 cm^{-1}, as reported in literature.[113] The vibration mode can be lower depending on the phase of iodine, decreasing to 200 cm^{-1} for solutions in apolar solvents and to 180 cm^{-1} for solid iodine.[114] When a charge transfer occurs, the stronger it is, the weaker the vibration mode is. Noteworthy, the complex PVP-I_2, largely employed as bactericide, gives a Raman band at 170 cm^{-1} for interacting and non-dissociated iodine.[115] For stronger interactions giving dissociation and formation of I_3^-, two bands appear since the triiodide I-I-I has a symmetric mode, detected typically in the range 100-120 cm^{-1} and a (weaker) asymmetric mode, found typically in the range 130-150 cm^{-1}.[116,117,118] In some published works, the vibration at 160 cm^{-1} is associated to formation of I_5^-.[119,120] Raman performed on the $Ni^{II}(pz)[Ni^{II}(CN)_4]$ after capture of iodine in solution and in vapours indicated the presence of 3 bands for the iodine (Figure 26): 105 (s), 165 (s) and 205 (w) cm^{-1}. The band at 205 cm^{-1} was associated to traces of iodine dissolved in the washing solution with cyclohexane (or pentane for the test in gas). The band at 165 cm^{-1} correlated with the UV-VIS band at 470 nm for the confined molecular iodine, I_2, whereas the band 105 cm^{-1} (asymmetric mode) correlated with the band around 400 nm at UV-VIS spectra and it was associated to the presence of I_3^-. The weak shoulder at 150 cm^{-1} was related to the asymmetric stretching mode of the triiodides.

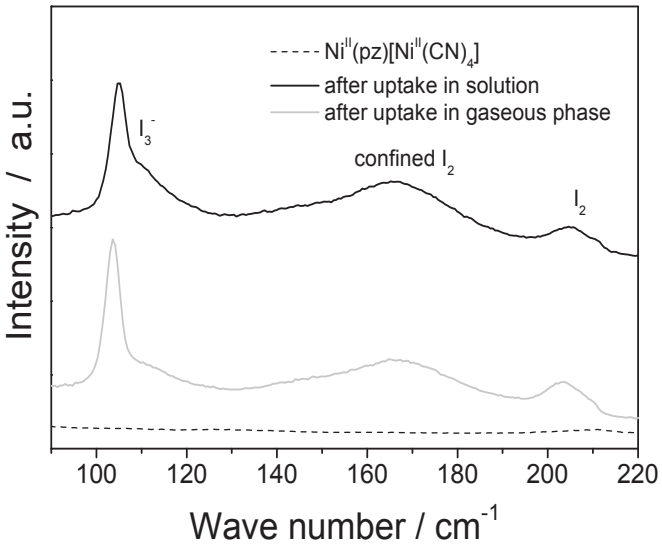

Figure 26 – Raman spectra (lasers HeNe) for the $Ni^{II}(pz)[Ni^{II}(CN)_4]$ and clathrate loaded in solution and vapours (range 50-220 cm^{-1}).

Since the spectra (recorded with laser HeNe) reported a very intense signal for the triodides, we carried out an attempt to correlate, at different loadings, the relative intensities between the triodides signal and the host structure signal. We chose as reference the peak at 700 cm^{-1} related to the Raman-active vibration mode δ(C-H) of the pyrazine ligand that was not perturbated by the introduction of the iodine in the cages. The normalized Raman spectrum at very low loading, *i.e.*

0.01 I_2 pr unit cell, already indicated an intense band for the triiodides (10 units) and a weaker band for the asymmetric stretching (150 cm^{-1}). At this loading, as discussed for the UV-VIS spectra, no confined molecular iodine was detectable. After increasing by 100 times the total amount of iodine in the clathrate, the relative Raman intensity of the triiodides only increased by 2.3 times, wherease the band for the confined iodine at 165 cm^{-1} became very intense (Figure 27). Because of these facts, we can state that the response of the triiodides at Raman spectroscopy was very intense and, at the maximal storage capacity, this signal could be associated to nearly 2 % of the overall adsorbed amount of iodine. The molar ratio I_3^- / I_2 was thus far from the right stoichiometry to form, for instance, I_5^- as main species.

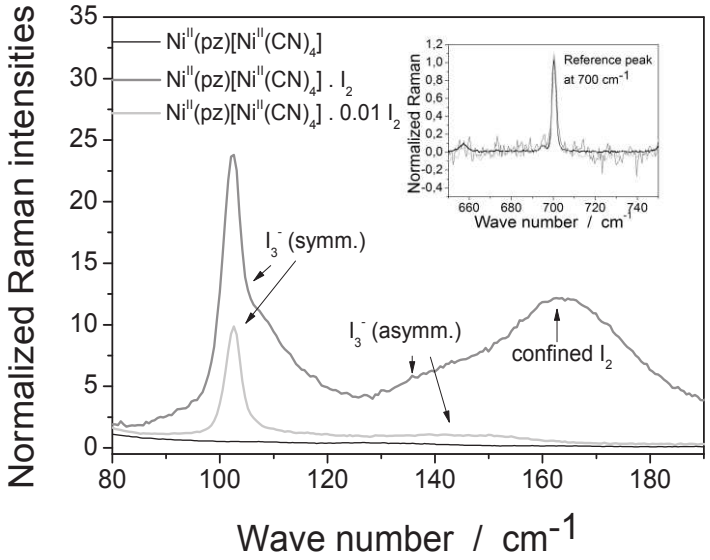

Figure 27 - Normalized Raman spectra for the clathrate at different iodine loadings.

At this point, it was clear that the confinement of the molecular iodine I_2, interacting weakly with the host structure, had to be the main mechanism of entrapment and the responsible agent for the change in lattice parameters as well as for the change in FT-IR vibration modes for the clathrate system. The lowering of the ν(C≡N) mode, from 2174 cm^{-1} in the empty host structure to 2165 cm^{-1} in the iodine clathrate, could be interpreted (in a speculative way) according to the presented argumentations. Since confined I_2 had to be an acceptor due to the observed blue-shift in UV-VIS and Raman spectroscopies, electron density could be weakly given by the π orbitals of the CN^- ligands and this would explain the weakening of vibration mode ν(C≡N). Adsorption of iodine was experimentally tested as well on the $Ni^{II}[Ni^{II}(CN)_4]$ complex, to see if the only presence of 2-D tetracyanonickelates would be enough for the retention of iodine. However, on this kind of complex only traces of I_3^- were adsorbed. Hence, the presence of the pyrazine ligand played an important role in the confinement as well. First of all, the organic ligand is responsible for the formation of the cage with suitable dimensions (close to the iodine molecule). Also, IR spectra showed a perturbation of the pyrazine ligand ligand suggesting that a charge transfer from the aromaticity of the ring to iodine could occur as well. Further considerations about the interaction

with the ligand will be reported in the Section 1.2.3 that includes the analysis of the dielectric relaxation of the pyrazine ligand at different I_2-loadings.

Once interpreted the state of the confined I_2, the nature of I_3^- formation needs some considerations. As explained previously in this paragraph, only electrophilic moieties with significant basic properties can dissociate I_2 to the couple I^+/I^- with subsequent formation of polyiodides. In the clathrate system $Ni^{II}(pz)[Ni^{II}(CN)_4]$, the only possibility of dissociative charge transfer with iodine should come from the electron rich N atoms in $[Ni(CN)_4]^{2-}$ and the pyrazine that are not strongly coordinated to the metallic centre and are available to give acid-base adducts. According to this description, we should have indeed structural defects as vacant metallic centres or surface defects. No I_3^- formation was detected by adding free pyrazine to a solution of iodine in cyclohexane indicating the the N atoms in the pyrazine are too weak to trigger the dissociation. Further tests were performed with precursors $[Ni^{II}(pz)]^{2+}$ and $[Ni(CN)_4]^{2-}$ in order to understand if building blocks can complex alone the iodine. Firstly, aqueous solutions $\approx 10^{-4}$ M of $[Ni^{II}(pz)]^{2+}$ (blue solution) and $[Ni(CN)_4]^{2-}$ (yellow solution) were prepared and then separately kept in dynamic contact with solutions of iodine in cyclohexane ($\approx 10^{-4}$ M, violet). After agitation of the biphasic systems, only the solution containing the $[Ni^{II}(CN)_4]^{2-}$ completely discoloured the iodine solution, whereas no I_2 extraction occurred with $[Ni^{II}(pz)]^{2+}$. The capture test was repeated with 1 mmol of $K_2[Ni^{II}(CN)_4]$ dissolved in water and a more concentrated solution of iodine in cyclohexane $7 \cdot 10^{-2}$ M (20 ml, 1.4 mmol). The agitation of the biphasic system brought to complete discolouration of the iodine solution, indicating a capture of more than one equivalent of I_2. We can write the possible charge transfer for the complex I_2 / CN^- , where CN^- is one of the four terminal cyanide ligands of $[Ni(CN)_4]^{2-}$, as follow:

Reaction 1 – Proposition for the formation of the triiodides.

$$2\ I_2 + CN^- \rightarrow CN\text{-}I^+ + I_3^-$$

so that a $[Ni(CN)_4]^{2-}$ unit was supposed to have a capacity of 8 I_2 per mole. Secondly, the solution containing $[Ni^{II}(CN)_4]^{2-}$ and I^+/I_3^- was used in an *in-situ* preparation for $Ni^{II}(pz)[Ni^{II}(CN)_4]$, that reminded the synthesis of the complex $Fe^{II}(pz)[Pt^{II/IV}(CN)_4] \cdot I^-$, performed in the works of Ohtani *et al.*, where the host structure $Fe^{II}(pz)[Pt^{II}(CN)_4]$ was precipitated in presence of I_2/I_3^- in a water-methanol solution.[86] In the present work, a second solution of $Ni(NO_3)_2$/pyrazine (1 mmol of each precursors) was added to the previous $[Ni(CN)_4]^{2-}/I_3^-$ solution, with instantaneous precipitation of a yellow compound. XRPD and FT-IR analyses gave overlapping spectra with $Ni^{II}(pz)[Ni^{II}(CN)_4]$ structure, indicating that coordination of the terminal cyanides to the Ni^{2+} cations occurred anyway. We report as example the comparison of the XRPD patterns for $Ni^{II}(pz)[Ni^{II}(CN)_4]$ precipitated without iodine and $Ni^{II}(pz)[Ni^{II}(CN)_4]$ precipitated in presence of iodine in Figure 28. SEM/EDX analyses indicated that only 0.05 I_2 (or equivalently 0.025 I^+/I_3^-) was retained per unit cell, in the precipitation of the complex. UV-VIS spectrum in reflectance mode indicated one intense band at 400 nm. The curve is compared in Figure 29 with two different loadings after entrapment in cyclohexane: spectrum for $Ni^{II}(pz)[Ni^{II}(CN)_4] \cdot 0.01\ I_2$ where only one band at 400 nm was detected as well and spectrum for $Ni^{II}(pz)[Ni^{II}(CN)_4] \cdot 0.6\ I_2$ where we could distinguish clearly

the band at 470 nm and the band at 400 nm. The comparison shows that the iodine at very low content after capture in solution has the same nature as the retained iodine in the *in-situ* precipitated compound and in both cases this are supposed to be the I_3^- species formed on the lattice defects. In the *in-situ* synthesis, indeed, not all the I_3^- in the $[Ni(CN)_4]^{2-}$ / I_3^- solution were retained by the precipitated compound, but only the I_3^- that were not substituted by the Ni^{2+} cations in the coordination with the terminal CN^- ligands.

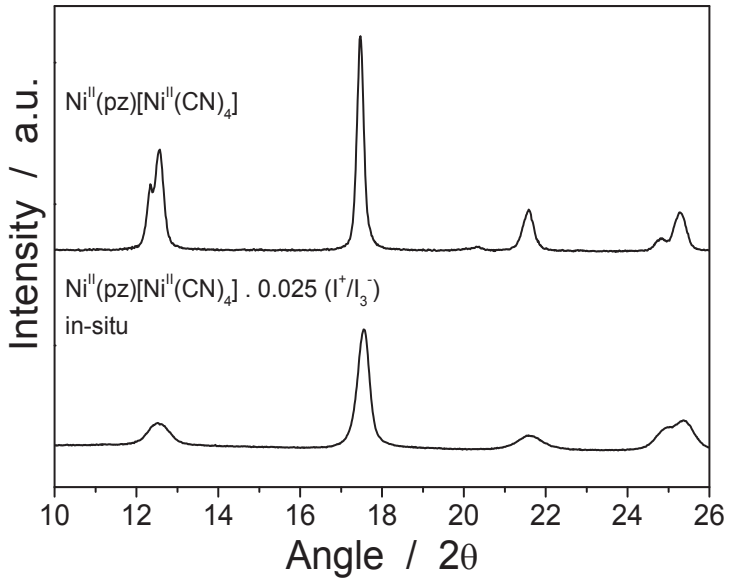

Figure 28 - Comparison between $Ni^{II}(pz)[Ni^{II}(CN)_4]$ without I_2 and $Ni^{II}(pz)[Ni^{II}(CN)_4]$ precipitated with I_2

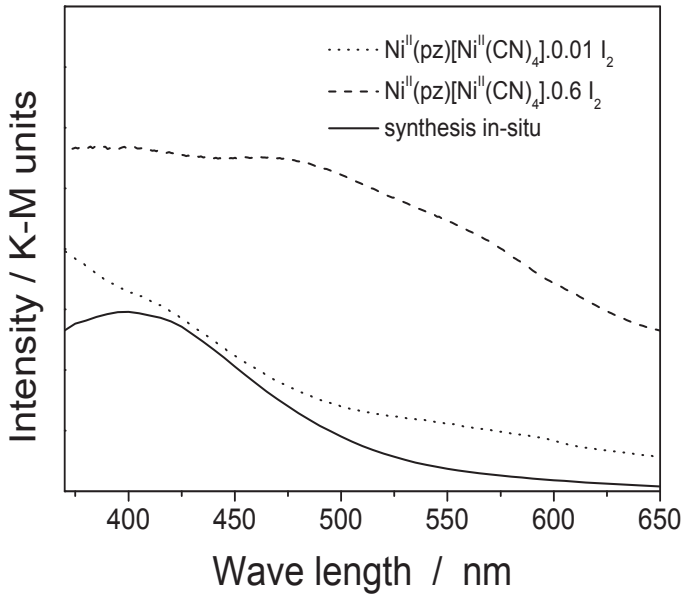

Figure 29 – UV-VIS spectra of *in-situ* prepared compound and comparison with $Ni^{II}(pz)[Ni^{II}(CN)_4]$ at different loadings after captures in solution.

Raman spectra registered on the *in-situ* compound also showed the typical bands for I_3^- with the intense symmetric stretching mode at 105 cm^{-1} and the weak asymmetric stretching mode around at 140 cm^{-1}. Comparison of the spectrum with fully loaded $Ni^{II}(pz)[Ni^{II}(CN)_4]\bullet I_2$ showed indeed a correspondence of the bands for I_3^- and no band for confined I_2 in the compound obtained *in-situ* (Figure 30).

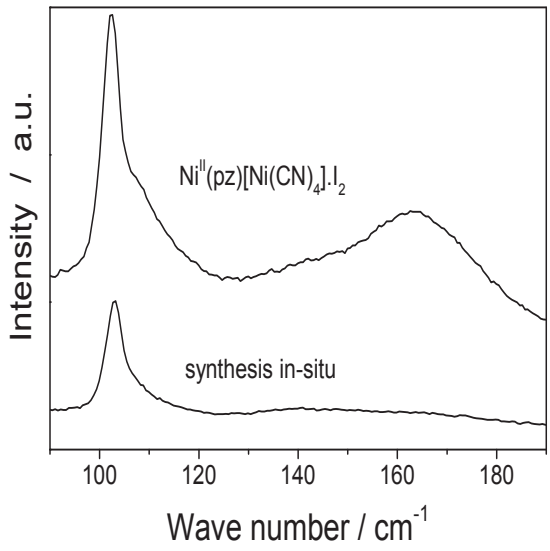

Figure 30 – Raman *in-situ* prepared compound and comparison with $Ni^{II}(pz)[Ni^{II}(CN)_4]$ at maximal content after capture in solution.

No direct observation of the defects with other methods was possible. Tests for detecting defects with *in-situ* FT-IR spectroscopy by sending acidic probe molecule (pyrrole) to the desorbed clathrate actually failed, most probably because concentration of defects was too small to be quantified. In conclusion, lattice defects can be considered the reason for formation of I_3^-, without excluding eventual formation of small quantities of I_5^- as well. According to this thesis, a GCMC modeling was carried out considering the introduction of uniquely molecular iodine inside the system $Ni^{II}(pz)[Ni^{II}(CN)_4]$ with a good matching to experimental data. A full description of the modelling will be treated in the dedicated section 1.2.2. The promising results about the efficient entrapment of the molecular iodine with the structure $Ni^{II}(pz)[Ni^{II}(CN)_4]$ motivated the extension of the work to the I_2 adsorption with analogue structures, where only one element of the unit cell was replaced to see the effect on the performance. In the general structure M'(L)[M''$(CN)_4$] the 3 different elements M', M'' and L can be modulated without changing the space group, provided that M' is an octahedral metal (symmetry O_h) as Fe^{2+}, Ni^{2+} or Co^{2+}; [M''$(CN)_4]^{2-}$ has a square planar geometry as $[Ni(CN)_4]^{2-}$, $[Pd(CN)_4]^{2-}$ or $[Pt(CN)_4]^{2-}$ and L is a bidentate linear ligand as pyrazine (pz), 4,4'-bipyridine (bpy) or 4,4'-azopyridine (azpy). In the next sections, the study about the insertion of iodine (in solution or in gaseous phase) performed for $Ni^{II}(pz)[Ni^{II}(CN)_4]$ is extended for the analogue structures $Co^{II}(pz)[Ni^{II}(CN)_4]$, $Ni^{II}(pz)[Pd^{II}(CN)_4]$, $Ni^{II}(pz)[Pt^{II}(CN)_4]$, $Ni^{II}(bpy)[Ni^{II}(CN)_4]$ and $Ni^{II}(azpy)[Ni^{II}(CN)_4]$.

1.1.2 Replacement of the square planar centre M'': series $Ni^{II}(pz)[M''(CN)_4]$ (M'' = Ni^{II}, Pd^{II}, Pt^{II}).

A series of Hoffman-type clathrates can be prepared by replacing the square planar metallic cation. Generally, when the coordination number of a metallic center is n = 4, square planar geometry is less favored than tetrahedral geometry. Cyanides can form very stable square planar complexes due to their low steric hindrance and their π-acidic characteristics.[22] Stable tetracyanometallates are formed with cations that have electronic configuration d^8, for instance, Ni^{2+}, Pd^{2+} and Pt^{2+}. Hence, the precursor $K_2[Ni^{II}(CN)_4]$ in the synthesis for $Ni^{II}(pz)[Ni^{II}(CN)_4]\bullet 2H_2O$ was replaced by $K_2[Pd^{II}(CN)_4]$ or $K_2[Pt^{II}(CN)_4]$. Both resulted clathrates $Ni^{II}(pz)[Pd^{II}(CN)_4]\bullet 2H_2O$ and $Ni^{II}(pz)[Pt^{II}(CN)_4]\bullet 2H_2O$ were precipitated as bright violet microcrystalline powders. Elemental analyses indicated a good agreements with expected compositions (see *Experimental Section).* The two Hofmann-type structures were isostructural to the published $Fe^{II}(pz)[Pt^{II}(CN)_4]\bullet 2H_2O$ as reported in Figure 31. LeBail refinement found almost identical lattice parameters for both structures, *i.e.* $a = b = 7.3384(2)$ Å, $c = 7.0325(3)$ Å ($V = 378.7(1)$ Å^3) for the $Ni^{II}(pz)[Pd^{II}(CN)_4]\bullet 2H_2O$ and $a = b = 7.3310(3)$ Å, $c = 7.0299(8)$ Å ($V = 377.8(1)$ Å^3) for the $Ni^{II}(pz)[Pt^{II}(CN)_4]\bullet 2H_2O$ (space group P4/m).

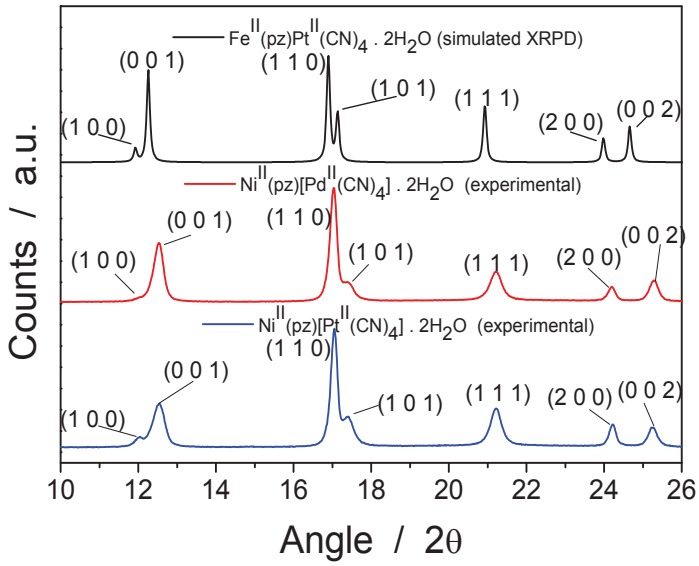

Figure 31 – XRPD for $Ni^{II}(pz)[Pd^{II}(CN)_4]\bullet 2H_2O$ and $Ni^{II}(pz)[Pt^{II}(CN)_4]\bullet 2H_2O$

The IR spectra of the materials revealed for the vibration mode ν(C≡N) values 2188 cm^{-1} for the $Ni^{II}(pz)[Pd^{II}(CN)_4]\bullet 2H_2O$ and 2184 cm^{-1} for $Ni^{II}(pz)[Pt^{II}(CN)_4]\bullet 2H_2O$. These values were higher than the ν(C≡N) mode in $Ni^{II}(pz)[Ni^{II}(CN)_4]\bullet 2H_2O$ at 2174 cm^{-1}, due to probably a lower back donation when Pt^{II} and Pd^{II} were in the square planar position. The ν(C≡N) mode at 2134 cm^{-1} in both $K_2[Pd^{II}(CN)_4]$ and $K_2[Pt^{II}(CN)_4]$ results increased after coordination with the cation Ni^{2+} on the N side. The bending mode δ(M-C≡N) of the precursors is assigned according to literature.[121-122] After

coordination, the δ(M-C≡N) mode of $[Pd^{II}(CN)_4]^{2-}$ increased due to formation of bridging cyanides and it moved from ≈400 cm^{-1} to 428 cm^{-1}. Similarly, for $[Pt^{II}(CN)_4]^{2-}$ it is shifted from 406 cm^{-1} to 471 cm^{-1}. The stretching mode ν(Ni-N_{pz}) of the bond Ni^{II}-pyrazine showed the value 485 cm^{-1} for all the series $Ni^{II}(pz)[M''(CN)_4]\bullet 2H_2O$ with M'' = Ni^{II}, Pd^{II} and Pt^{II}. Also, bands related to the pyrazine ligand in the 3 analogue structures did not change. A difference between the analogues was detected for the thermal stability. TGA curves indicated that the host structure $Ni^{II}(pz)[Pd^{II}(CN)_4]$ decomposed at 425 °C, whereas $Ni^{II}(pz)[Pt^{II}(CN)_4]$ was decomposed at 450 °C (Figure 32). Both temperatures were higher than the decomposition of $Ni^{II}(pz)[Ni^{II}(CN)_4]$ (400 °C). Therefore, thermal stability followed the order Ni^{II} < Pd^{II} < Pt^{II}. The TGA curve steps detected below 100 °C were related to the loss of water and traces of other used solvents (Figure 32). Eventual increase of weight after decomposition was due to formation of metal oxides.

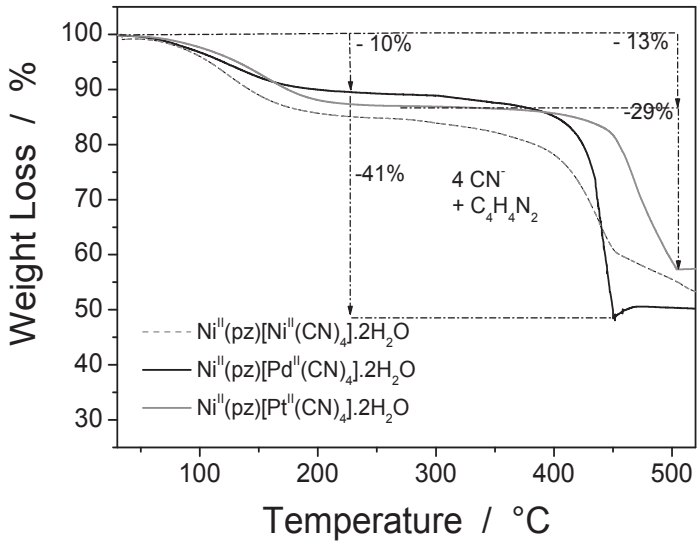

Figure 32 - TGAs for $Ni^{II}(pz)[M''(CN)_4].2H_2O$, M'' = Ni^{II}, Pd^{II}, Pt^{II}.

The two analogues show the same UV-VIS spectrum in reflectance mode, with a band at 550 nm for the d-d* transitions and a band in the UV region for the electronic transitions in the cyanides and pyrazine ligands. The dehydrated $Ni^{II}(pz)[Pd^{II}(CN)_4]$ and $Ni^{II}(pz)[Pt^{II}(CN)_4]$ were also obtained by heating at 80 °C under primary vacuum. For these structures just a minor change in color after removal of water is observed, from bright violet to pale violet. The adsorption of iodine in solution of cyclohexane and in gaseous phase, performed as previously explained for the other clathrates, actually gave drastically different results for the 2 structures, so that they will be treated separately.

Iodine entrapment with $Ni^{II}(pz)[Pd^{II}(CN)_4]$.

The kinetic study in a solution of iodine $3 \bullet 10^{-3}$ M showed an equilibrium time at 2 hours which was comparable to the observed time for $Ni^{II}(pz)[Ni^{II}(CN)_4]$ (Figure 33). The curve was fitted with the pseudo-second order model with kinetic constant k = 0.18 $mmol.g^{-1}.min^{-1}$.

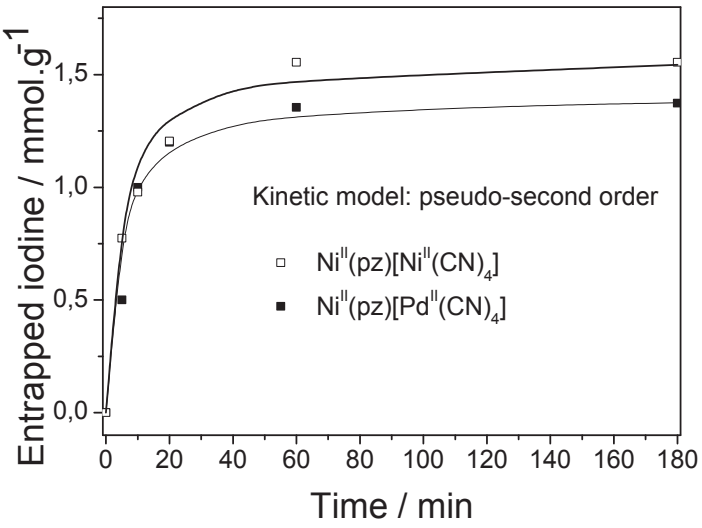

Figure 33 - Kinetic curves for $Ni^{II}(pz)[M''(CN)_4]$, M'' = Ni, Pd.

The isotherm of adsorption in cyclohexane, performed at room temperature, is shown in Figure 34 and compared with the isotherm of the analogue. A maximal capacity of 2.97 ± 01 $mmol.g^{-1}$ was observed, with saturation achieved for concentrations over 10^{-2} M. The maximal amount corresponded to one mole of I_2 per unit cell, which was the same maximal capacity for $Ni^{II}(pz)[Ni^{II}(CN)_4]$. The isotherm was fitted with the Langmuir model, with parameters k = 1100 $L.mol^{-1}$ and Q_{max} = 3.0 $mmol.g^{-1}$. TGA indicated a loss of iodine in the range 130-200 cm^{-1}, which corresponded nearly to 1 equivalent of I_2 per unit cell (Figure 35), with highest desorption rate around 154 °C according to the first derivative. The entrapment in gaseous phase indicated that the maximal capacity could be easily achieved in these conditions as well (Figure 35). The samples at maximal capacity obtained in solution and in gaseous phase, both with formula $Ni^{II}(pz)[Pd^{II}(CN)_4] \bullet I_2$, were analyzed at FT-IR spectroscopy, revealing a similar tendency to the analogue $Ni^{II}(pz)[Ni^{II}(CN)_4] \bullet I_2$. As in the case of the analogue structure, a modest overall perturbation was observed, except for the vibration mode of cyanides ν(C≡N) which decreased after insertion of iodine as reported in Table 4. We could interpret the decrease of the ν(C≡N) mode the same way as for $Ni^{II}(pz)[Ni^{II}(CN)_4] \bullet I_2$, *i.e.* a donation of electron density from π-bonding orbitals of the CN^- ligand to the σ^* anti-bonding orbital of iodine.

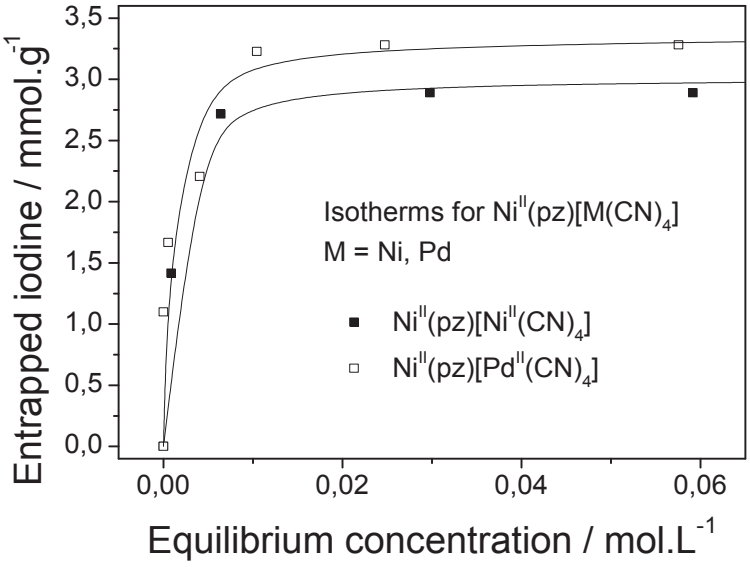

Figure 34 – RT isotherms for $Ni^{II}(pz)[M''(CN)_4]$, M'' = Ni, Pd.

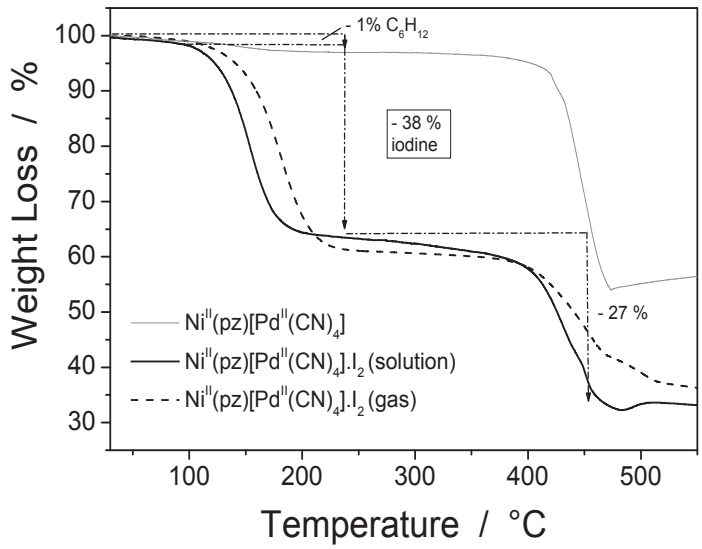

Figure 35 – TGA curves for $Ni^{II}(pz)[Pd^{II}(CN)_4]$ before and after iodine uptake in solution and gaseous phase.

Table 4 – IR vibration modes of $Ni^{II}(pz)[Pd^{II}(CN)_4]$ and $Ni^{II}(pz)[Pd^{II}(CN)_4].I_2$ (solution), s = strong band; vs = very strong band.

	$Ni^{II}(pz)[Pd^{II}(CN)_4]$	$Ni^{II}(pz)[Pd^{II}(CN)_4]\bullet I_2$
Pyrazine bands (strong bands)	1426, 1215, 1161, 1132, 1090, 1060, 809	1420, 1214, 1162, 1130, 1089, 1060, 809
ν(C≡N)	2188 (vs)	2177 (vs)
$\nu(Ni\text{-}N_{pz})$	485 (s)	481 (s)
ν(M-C≡N) where M = Ni, Pd	428 (s)	428 (s)

XRPD patterns recorded on both iodine clathrates (obtained from solution and from vapours) at maximal capacity indicated anyway a different evolution of the diffraction pattern, as shown in Figure 36. Again, the (001) peak decreased and become almost undetectable after entrapment, whereas the (100) peak increased and shifted to smaller 2θ angles due to an increase of the parameter *a*. In the range 2θ = 23°-26°, three peaks were detected instead of the expected two peaks (200) and (002) indexed in the empty host structure. The third peak could be explained as a change in lattice symmetry that brought parameters *a* and *b*, which always have the same length in the tetragonal lattice, not to evolve in an isotropic way after insertion of iodine in the structure. Using the Bragg's relationship (see *Annexes*), the peak at 2θ = 23.95 corresponded to d ≈ 7.43 Å, as well as the peak (100), so that it was assigned to the Miller plane (200). The peak at 2θ = 25.29° did not shift significantly after iodine insertion and it was assigned to (002) as before iodine insertion. The intermediate weaker peak at 2θ = 24.55° was then associated to newly formed plane (020) related to parameter *b* and it corresponded to a distance *d* ≈ 7.22 Å. LeBail refinement confirmed that the lattice after entrapment was orthorhombic (space group *P c m m*) with lattice parameters a = 7.4310(5) Å, *b* = 7.2319(7) Å, *c* = 7.0382(7) Å and V = 378.2(3) $Å^3$. The volume of the unit cell only decreased by ≈ 0.1%, so that we could state, that it actually maintained the initial volume. The change of symmetry could be justified as a different adaptation to the insertion of iodine, due to different coordination strength in the clathrate lattice. It could also considered a confirmation of the thesis by Southon *et al.*[80] They reported that, dislike from previous works,[34] the tetragonal structure $Fe^{II}(pz)[Ni^{II}(CN)_4]$ become orthorhombic upon adsorption of guest molecules, but that due to *pseudo-merohedry* the lattice could be confused as tetragonal. *Pseudo-merohedry* occurs when two separate twin crystals (where *twin crystals* means that they share some of the crystal lattice points) also share the reciprocal axes. Due to this phenomenon, the lattice parameters *a* and *b* of the tetragonal *superlattice* were actually an average value for the orthorhombic lattice. About $Ni^{II}(pz)[Pd^{II}(CN)_4]\bullet I_2$, anyway, we could state that there was no pseudo-merohedry masking the orthorhombic lattice after insertion of the guest molecule. The orthorhombic lattice however was not recognized when H_2O was the guest molecule, for any of the studied structures.

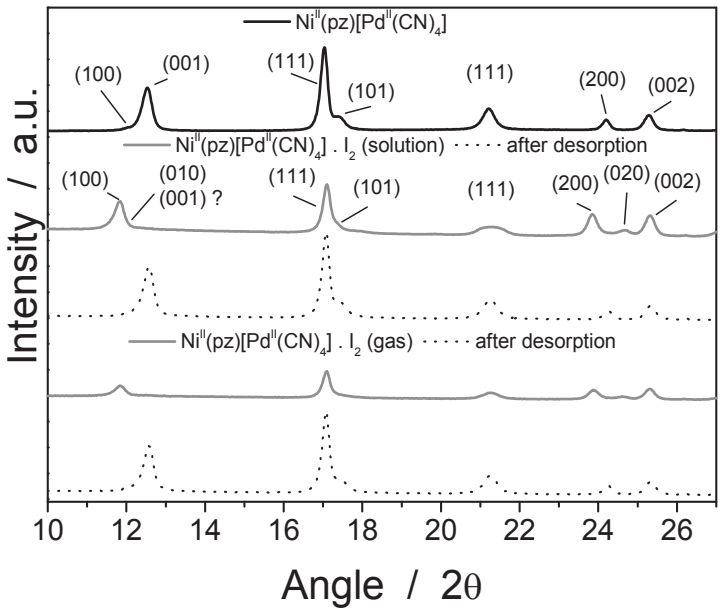

Figure 36 – XRPD patterns for unfilled $Ni^{II}(pz)[Pd^{II}(CN)_4]$ and $Ni^{II}(pz)[Pd^{II}(CN)_4]\bullet I_2$ from solution and vapours and desorbed structures.

Also, thermal desorption of iodine confirmed that the (020) peak disappeared when all iodine was thermally removed. Desorption was performed at 200 °C, since TGA curves clearly indicated a complete removal of iodine at this temperature. Moreover, the regeneration of the structure was confirmed by FT-IR spectra, after desorption from both iodine clathrates (solution and vapours) at maximal capacity (Figure 37 and Figure 38).

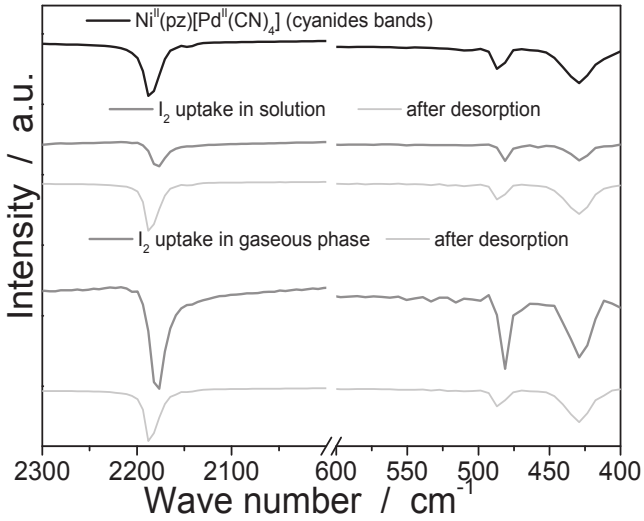

Figure 37 -FT-IR spectra in the intervals 2300-2000 cm^{-1} (cyanide stretching) and 600-400 cm^{-1} for $Ni^{II}(pz)[Pd^{II}(CN)_4]$, for $Ni^{II}(pz)[Pd^{II}(CN)_4].I_2$ from solution and vapours adsorption and respective desorbed structures.

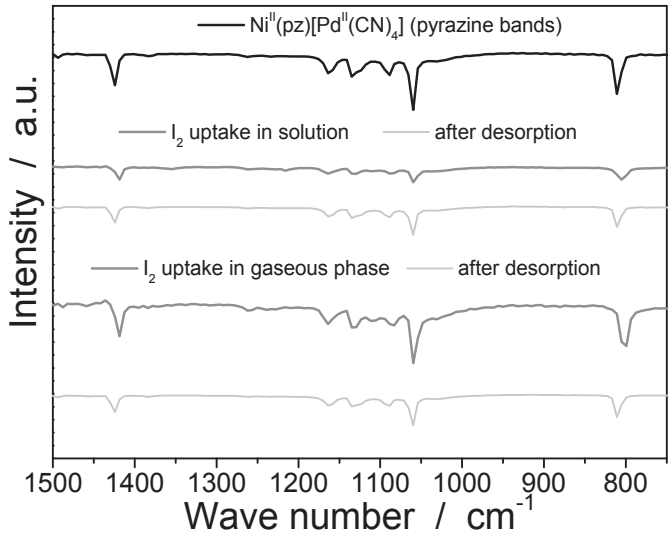

Figure 38 – FT-IR spectra of the pyrazine ligand in $Ni^{II}(pz)[Pd^{II}(CN)_4]$, $Ni^{II}(pz)[Pd^{II}(CN)_4].I_2$ from solution and vapours adsorption and respective desorbed structures.

Thermal desorption was also checked by using mass spectroscopy to determine at which temperature iodine started desorbing out of host structure. Data indicated a desorption from 140 °C, slightly lower than desorption occurring from $Ni^{II}(pz)[Ni^{II}(CN)_4]$ which started at 150 °C (Figure 39). We could justify this difference, since the volume of the unit cell for $Ni^{II}(pz)[Pd^{II}(CN)_4]\bullet I_2$ was 378.2(3) Å^3 *i.e.* higher than the respective value for $Ni^{II}(pz)[Ni^{II}(CN)_4]\bullet I_2$ (369.3 Å^3). Visibly, a smaller unit cell guaranteed the iodine retention to higher temperatures in the case of $Ni^{II}(pz)[Ni^{II}(CN)_4]\bullet I_2$.

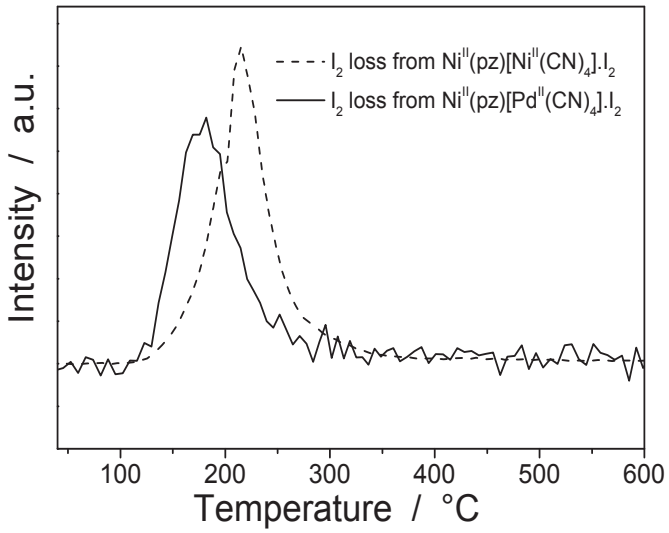

Figure 39 - Mass spectroscopy for the series $Ni^{II}(pz)[M''(CN)_4]$, M'' = Ni, Pd.

Subsequently, the nature of the confined iodine inside $Ni^{II}(pz)[Pd^{II}(CN)_4]$ was analyzed by solid state UV-VIS and Raman spectroscopy. Again, a resemblance with iodine confirmed in the $Ni^{II}(pz)[Ni^{II}(CN)_4]$ was detected. No differences were detected between the iodine clathrate obtained in solution and the one in vapours. Formation of polyiodides was observed due to the presence of the symmetric ν(I-I) mode at 114 cm^{-1} in the Raman spectra. The respective band in $Ni^{II}(pz)[Ni^{II}(CN)_4]\bullet I_2$ was visible at lower value, 105 cm^{-1}: as it will further discussed in the section 1.1.4, the symmetric ν(I-I) mode of triiodidides seems to be related to the employed tetracyanometallate. The higher Raman band at 167 cm^{-1} was correlated to the already discussed band for $Ni^{II}(pz)[Ni^{II}(CN)_4]$ at 165 cm^{-1} and it was associated to perturbed ν(I-I) mode of the confined I_2. A third band at 208 cm^{-1} was related to residual solution of iodine in cyclohexane (or washing solution in the case of the sample obtained from gaseous uptake).

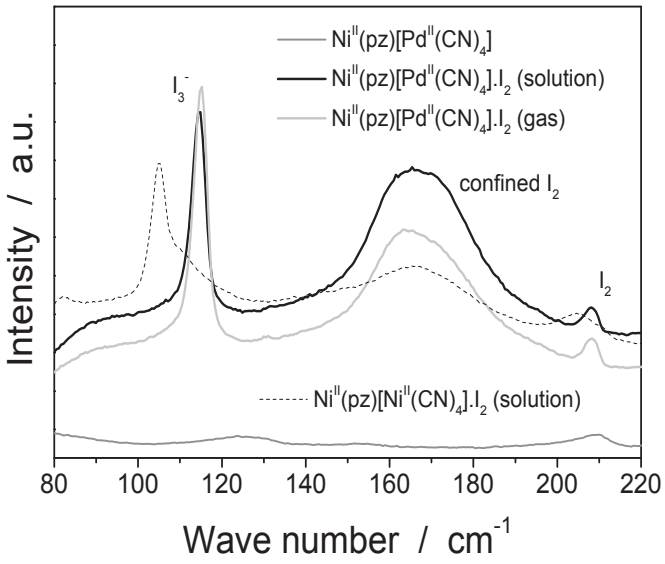

Figure 40 - Raman spectra, for for $Ni^{II}(pz)[Pd^{II}(CN)_4]$ before and after iodine adsorptio in solution and in gaseous phase and comparison with $Ni^{II}(pz)[Ni^{II}(CN)_4]\bullet I_2$.

The blue-shift of the ν(I-I) mode of confined I_2 suggested that the I_2 was behaving as a weak acceptor. The interacting donor species were identified in a first place as CN^- ligands due to the decrease of ν(C≡N) discussed previously. As reported in the previous section, the 2-D structure of a tetracyanometallate was not enough to retain large amounts of iodine, so that the pyrazine ligand had to play an important role in the confinement (formation of cages). The perturbation of the pyrazine in IR spectra indicated as well an interaction with the organic ligand. Finally, the formation of I_3^- was justified with the presence of defects as terminal cyanides. However, as discussed in the of $Ni^{II}(pz)[Ni^{II}(CN)_4]\bullet I_2$, I_3^- were expected to form in very small quantities. In parallel, the solid-state UV-VIS spectra in reflectance mode were registered for the clathrates $Ni^{II}(pz)[Pd^{II}(CN)_4]\bullet I_2$ which exhibited a black coloration (Figure 41). By subtracting the spectrum for $Ni^{II}(pz)[Pd^{II}(CN)_4]\bullet I_2$ (solution) with the spectrum of $Ni^{II}(pz)[Pd^{II}(CN)_4]$, a qualitative description of the iodine bands could be done. The substraction curve reported in Figure 41 showed a band

at 395 nm, which indicated the presence of the I_3^-, and a larger band that covered the region 450-500 nm as well due to the confined I_2.

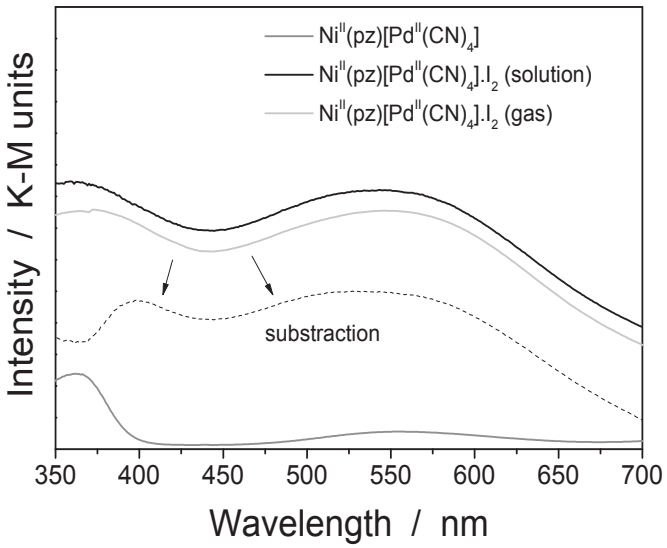

Figure 41 - solid state UV-VIS spectra for for Ni^{II}(pz)[Pd^{II}(CN)$_4$] before and after insertion of iodine in solution and vapours (reflectance mode).

The analysis of the introduction of I_2 inside the structure Ni^{II}(pz)[Pd^{II}(CN)$_4$] finally revealed the same confinement mechanism as Ni^{II}(pz)[Ni^{II}(CN)$_4$], with a different lattice adaptation that resulted in a weaker retention of iodine upon heating. In the next paragraph, the capture of iodine with the structure Ni^{II}(pz)[Pt^{II}(CN)$_4$] will be discussed.

Iodine entrapment with Ni^{II}(pz)[Pt^{II}(CN)$_4$].

The characterization of iodine as host molecule inside the clathrate-type structure where Pt^{2+} occupies the square planar position was already studied in the work of Agusti and Ohtani,[85] since the spin transition temperature of the host structure could be shifted due to an introduction of guest molecules. The complex obtained in their works was prepared with an *in-situ* process where crystals of solid I_2 were added to a methanolic solution of $K_2[Pt(CN)_4]$, then this solution was mixed with a solution of $Fe^{II}(NO_3)_2$•$6H_2O$/pyrazine and a yellow compound precipitated. Raman spectroscopy performed by Ohtani *et al.* showed a band at 129 cm^{-1}, characteristic for the platinum iodide bond ν(Pt-I). The explanation for the formation of the iodide is that an oxidative addition between I_2 and $[Pt^{II}(CN)_4]^{2-}$ occurred as reported in Equation 8 :

Equation 8 – Oxidative addition.

$$red)\ \ I_2 + 2e^- \rightarrow 2I^-$$
$$ox)\ \ [Pt^{II}(CN)_4]^{2-} \rightarrow 2e^- + \ [Pt^{IV}(CN)_4]^0$$

$$I_2 + \ [Pt^{II}(CN)_4]^{2-} \rightarrow \ [Pt^{IV}(CN)_4(I)_2]^{2-}$$

where the iodides I^- are placed in *trans*-position on the Pt^{IV} site, in a octahedral configuration, stabilizing the higher oxidation state of Pt^{IV} (Figure 42). Reported TGA curves in their work showed that the iodide decomposed after 250 °C. Also, a maximal capacity of $M^{II}(pz)[Pt^{II/IV}(CN)_4]\bullet I^-$ was detected, where only a halft of the Pt^{II} site oxidized to Pt^{IV}. We report in Figure 42 the resolved structure for the complex $Fe^{I}(pz)[Pt^{II/IV}(CN)_4]\bullet I^-$, already shown in the introduction to this chapter.

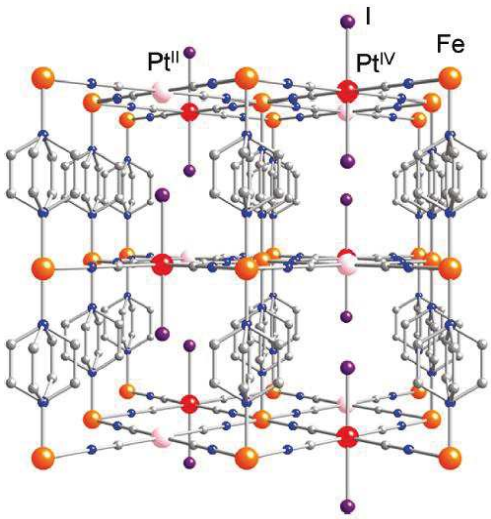

Figure 42 – Illustration of the complex $Fe^{II}(pz)[Pt^{II/IV}(CN)_4].I^-$ from the work of Ohtani et al.

Ohtani and coworkers also tried to introduce the iodine in vapours in order to obtain complexes at increasing amount of iodine, but apart mentioning this method in their work no further data were furnished. By contrast, they reported the obtained $Fe^{II}(pz)[Pt^{II/IV}(CN)_4]\bullet xI^-$ at different iodine-loadings x by solid state diffusion. Figure 43 shows the evolution of the XRPD patterns at different loadings.

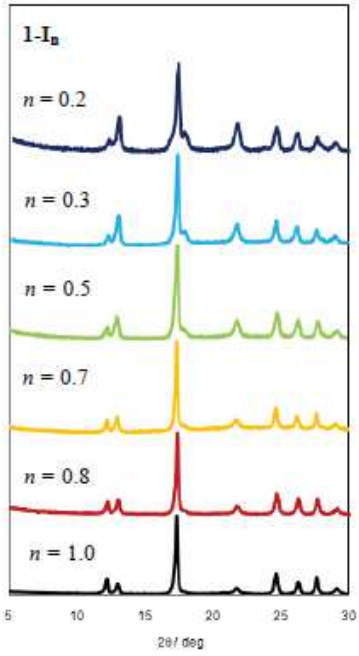

Figure 43 – XRPD patterns for $Fe^{II}(pz)[Pt^{II}(CN)_4]$ at different contents of I^- by Ohtani *et al.*

In the present work, the iodine was introduced in solution and in vapours after the preparation of the thermally activated $Ni^{II}(pz)[Pt^{II}(CN)_4]$ and the final clathrates were fully characterized. The purpose for this study was to check as well if different preparation methods could bring to substantial differences in the final product. First, the kinetic curve obtained in a solution of iodine $3 \cdot 10^{-3}$ M indicated an equilibrium time at 12 hours which is longer than the equilibrium time at 2 hours found for $Ni^{II}(pz)[M''(CN)_4]$ with M'' = Ni or Pd, as shown in Figure 54. The curve was fitted with the pseudo-second order model, with kinetic constant k = 0.04 $mmol.g^{-1}.min^{-1}$.

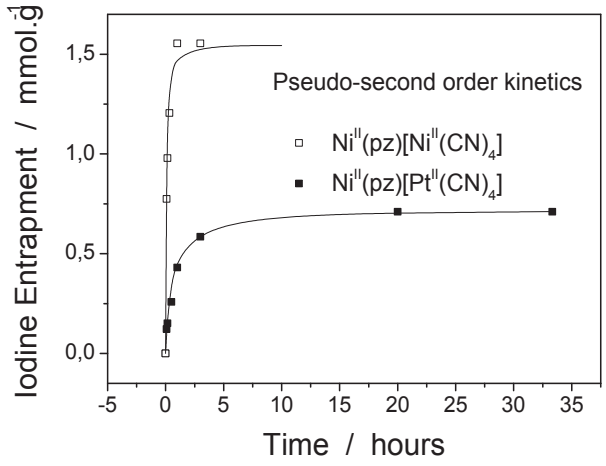

Figure 44 - Kinetic curved for $Ni^{II}(pz)[M''(CN)_4]$, M'' = Ni, Pd

The isotherm obtained at room temperature indicated a maximal capacity of 1.14 ± 0.05 $mmol.g^{-1}$ which corresponded to ≈ 0.5 I_2 per unit cell. This was the same capacity reported in the works of Agusti and Ohtani. The isotherm was fitted with the Langmuir model, with constant K = 550 $L.mol^{-1}$ (Figure 45).

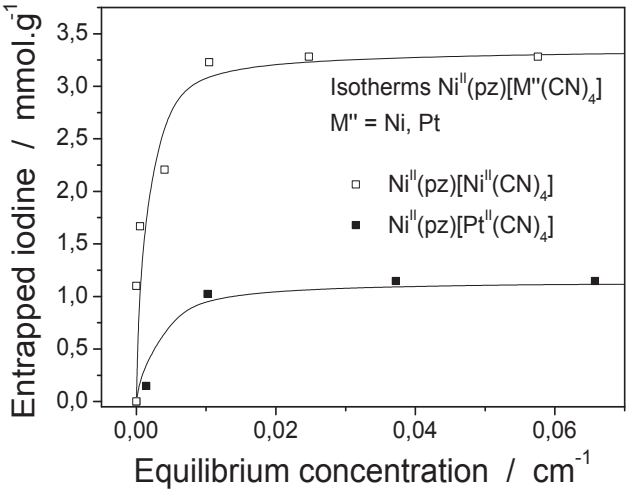

Figure 45 - Isotherms for $Ni^{II}(pz)[M''(CN)_4]$, M'' = Ni^{II}, Pt^{II}.

The same maximal capacity was observed when iodine was captured in I_2 vapours at 80 °C, as TGA curves show in Figure 46. Iodine was removed in the temperature range 250-

400 °C, as mass spectroscopy confirmed (Figure 47). This demonstrated that iodine was effectively retained up to 250 °C, which was higher by 100 °C than the desorption temperature for the analogues $Ni^{II}(pz)[M'' (CN)_4]$ with M'' = Ni^{II} or Pd^{II} (Figure 47).

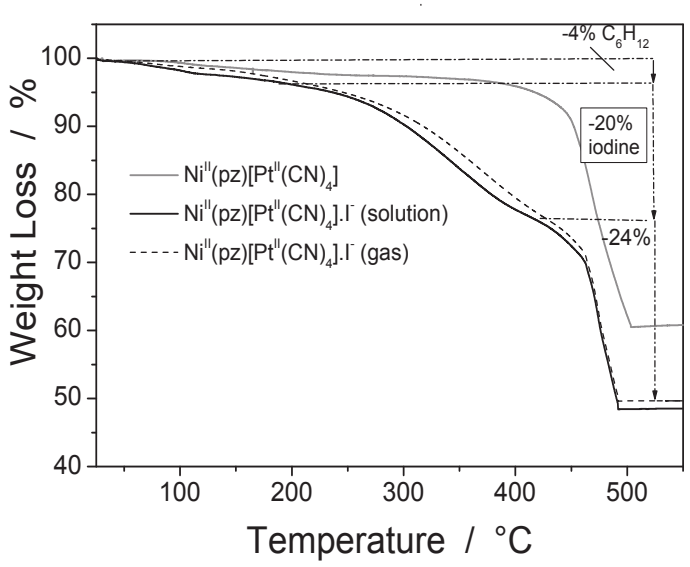

Figure 46 – TGA curves for $Ni^{II}(pz)[Pt^{II}(CN)_4]$ and $Ni^{II}(pz)[Pt^{II}(CN)_4].I^-$ after entrapment in solution and gaseous phase.

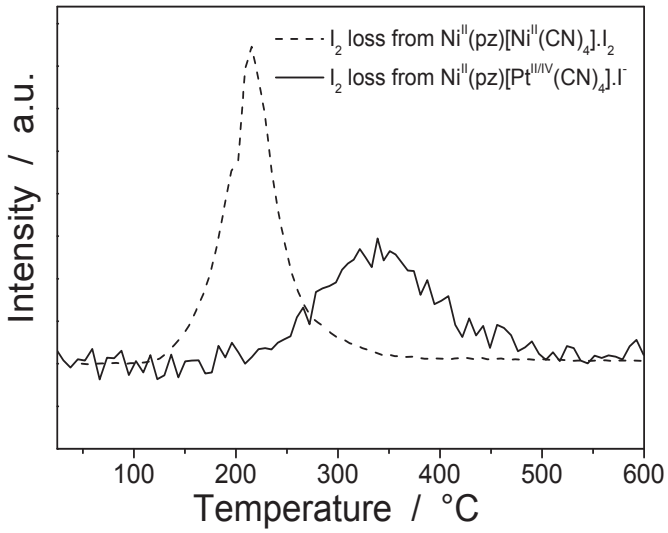

Figure 47 - Mass spectroscopy for the series $Ni^{II}(pz)[M''(CN)_4]$, M'' = Ni^{II}, Pt^{II}.

XPPD patterns recorded for the samples after entrapment showed that the diffraction peaks (100) and (200) shift to higher 2θ values suggesting a reduction of lattice parameters *a* and *b* (Figure 48). The same evolution of the XRPD patterns was studied by Ohtani and coworkers who analyzed the materials at increasing amount of iodide. LeBail refinement gave new lattice parameters *a* = *b* = 7.1775(3) Å and *c* = 6.9789(4) with group space P 4/m and V = 359.5(2) $Å^3$. A volume reduction of the unit cell by ≈5 % was observed.

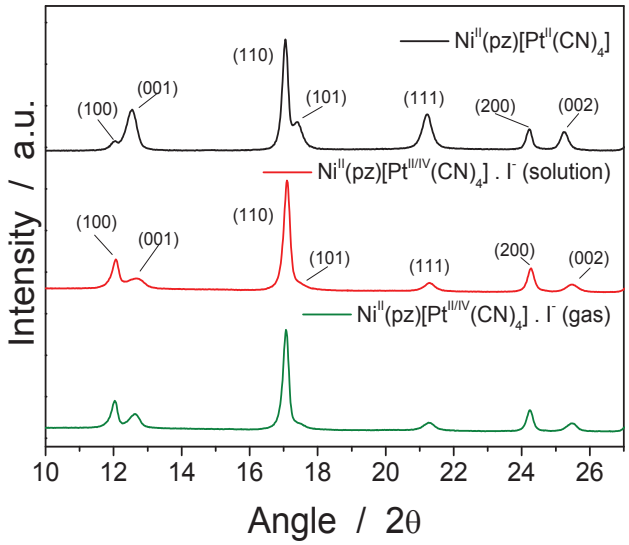

Figure 48 – XRPD for Ni^{II}(pz)[Pt^{II}(CN)$_4$], for the samples Ni^{II}(pz)[Pt$^{II/IV}$CN)$_4$].I$^-$ from solution and vapors and respective desorbed structures.

The FT-IR spectra after insertion of iodine showed a small perturbation of the overall structure, except for the cyanide bands. The values for the sample obtained in solutions are reported in Table 5. The initial intense band for ν(C≡N) at 2184 cm^{-1} did not change significantly, but a second cyanide band with comparable intensity appeared at 2216 cm^{-1}. The band at 2216 cm^{-1} was associated to the oxidized Pt^{IV} centers. Indeed, when the oxidation state of the metal centre increases, the lower electron density on the metal reduces the $d \rightarrow \pi^*$ back donation to the cyanide and the carbon-to-metal σ-bonding becomes the main contribution increasing the ν(C≡N) mode. The coexistence of the Pt^{II} and Pt^{IV} was present because the oxidative addition occurred only on the 50 % of the initial Pt^{II} sites.

Table 5 - IR vibration modes of Ni^{II}(pz)[Pt^{II}(CN)$_4$] and Ni^{II}(pz)[Pt^{II}(CN)$_4$].I$^-$ (solution)

	Ni^{II}(pz)[Pt^{II}(CN)$_4$]	Ni^{II}(pz)[Pt$^{II/IV}$(CN)$_4$].I$^-$
Pyrazine bands (strong bands)	1420, 1215, 1161, 1129, 1088, 1060, 809	1425, 1232, 1166, 1129, 1092, 1063, 803
ν(C≡N)	2184 (vs), 2146 (w)	2216 (vs), 2281 (vs), 2145 (w)
δ(Ni-N$_{pz}$)	485 (s)	486 (s)
ν(M-C≡N) where M = Ni, Pt	471 (s)	469 (s)

Moreover, the iodine clathrates prepared in solution and in vapours had a yellow coloration that absorbed at 430 nm, as the UV-VIS spectra registered in reflectance mode showed (Figure 49).

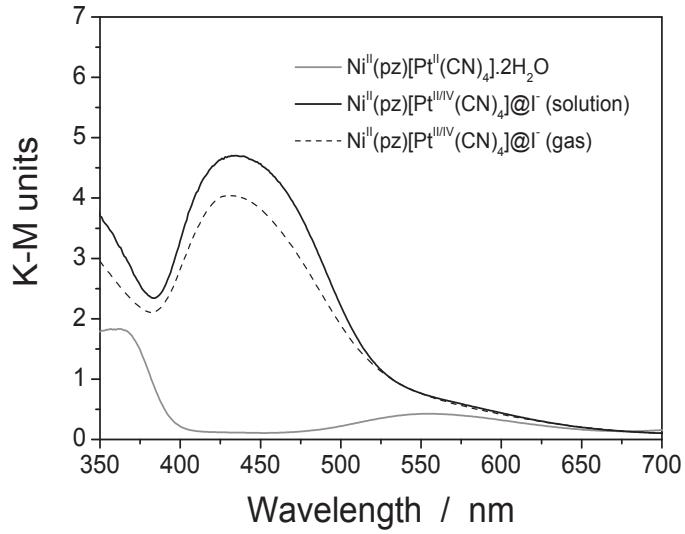

Figure 49 - Solid state UV-VIS spectra for for $Ni^{II}(pz)[Pt^{II}(CN)_4]$ before and after insertion of iodine in solution and vapours.

Ohtani *et al.* measured as well the absorption of the complex at low spin and they found similar spectrum with a large band between 400 and 500 nm. The Raman signal on both iodine clathrates $Ni^{II}(pz)[Pt^{II/IV}(CN)_4]\bullet I^-$ was a very intense band at 129 cm^{-1} that matched with the $\nu(Pt^{IV}$-I) mode discussed in literature (Figure 50).

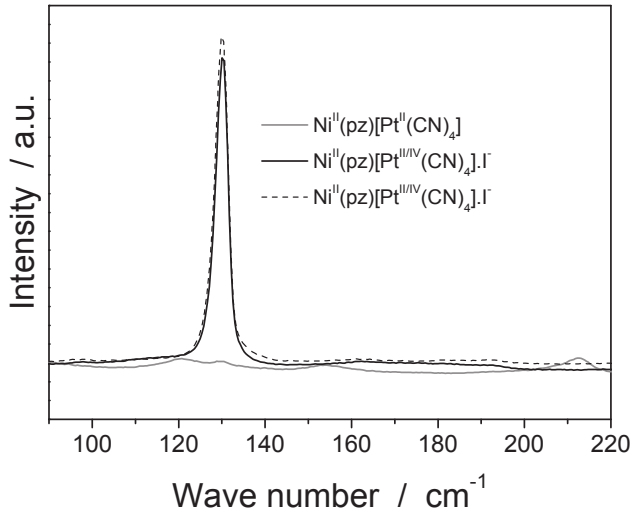

Figure 50 - Raman spectra for $Ni^{II}(pz)[Pt^{II}(CN)_4]$ before and after insertion of iodine in solution and vapors.

The $\nu(Pt^{IV}$-I) mode was so intense that the host structure signals became undetectable. Also, probably for the same reason, presence of other species of iodine was not detected either in the interval 100-200 cm^{-1}. Finally, thermal reversibility was tested for $Ni^{II}(pz)[Pt^{IV}(CN)_4\bullet I^-$. The first derivative indicated a large band centred around 350 °C, for the partial decomposition of the iodides. Anyway, the high stability of the iodides did not allow to find a temperature range where the clathrate was still thermally stable after full desorption. Even long heating programs at 350 °C

did not work. Thus, the $Ni^{II}(pz)[Pt^{II}(CN)_4]$ after entrapment of iodine cannot be regenerated due to the different nature of interaction between the iodine and the host structure.

Cycling ability for the series $Ni^{II}(pz)[M''(CN)_4]$, M'' = Ni^{II}, Pd^{II}.

The possibility of thermic regeneration of the host structure was further evaluated for the class $Ni^{II}(pz)[M''(CN)_4]$ to the structural resistance and the capacity upon cycling. As discussed in the previous paragraph, when Pt^{II} occupied the square planar position the redox reaction did not allow a complete desorption of the iodine off the host structure so that no cycling was possible for $Ni^{II}(pz)[Pt^{II}(CN)_4]$. The analogue dehydrated structures $Ni^{II}(pz)[Ni^{II}(CN)_4]$ and $Ni^{II}(pz)[Pd^{II}(CN)_4]$ were tested at cycling by repeating the adsorption/desorption process for 3 times overall. The adsorption step consisted both in the uptake in solutions of iodine in cyclohexane $7 \bullet 10^{-2}$ M and in the uptake in I_2 vapours at 80 °C. The amounts of the entrapped iodine was quantified by TGA. After the third uptake in solution, both $Ni^{II}(pz)[Ni^{II}(CN)_4]$ and $Ni^{II}(pz)[Pd^{II}(CN)_4]$ still indicated maximal capacity of 1 I_2 per unit cell, respectively 3.32 ± 0.1 $mmol.g^{-1}$ and 3.0 ± 0.1 $mmol.g^{-1}$. After the third uptake in gaseous phase, $Ni^{II}(pz)[Pd^{II}(CN)_4]$ still showed comparable capacity (3.0 ± 0.1 $mmol.g^{-1}$) whereas $Ni^{II}(pz)[Ni^{II}(CN)_4]$ entrapped around 0.8 equivalents of I_2 (or 2.8 ± 0.1 $mmol.g^{-1}$). At the third cycle in I_2 vapours, $Ni^{II}(pz)[Ni^{II}(CN)_4]$ showed actually an improved capacity with respect the first cycle (2.3 ± 0.1 $mmol.g^{-1}$ or about 0.7 equivalents of I_2). This fact suggested that it was possible to get closer to the maximal theorical capacity and that the desorption-adsorption processes probably enhanced the capacity.

XRPD patterns were registered to check the structural stability after the third cycle (in solution and in gaseous phase) and after the third desorption process, in order to check the structural stability of the host structure upon cycling. The XRPD patterns are reported in Figure 51 for $Ni^{II}(pz)[Ni^{II}(CN)_4]$ and in Figure 52 for $Ni^{II}(pz)[Pd^{II}(CN)_4]$. Final desorbed structures still showed a high crystallinity and the same pattern as the initial structures. The same structural adaptations to iodine insertion, observed after the first cycle in solution or gaseous phase for both Hofmann-type structures, were visible after the third cycle as well. For instance, $Ni^{II}(pz)[Pd^{II}(CN)_4]$ always showed the appearance of the (020) Miller plane at 2θ = 24.7° that was justified as a change of space group from P4/m (tetragonal) to Pcmm (orthorhombic).

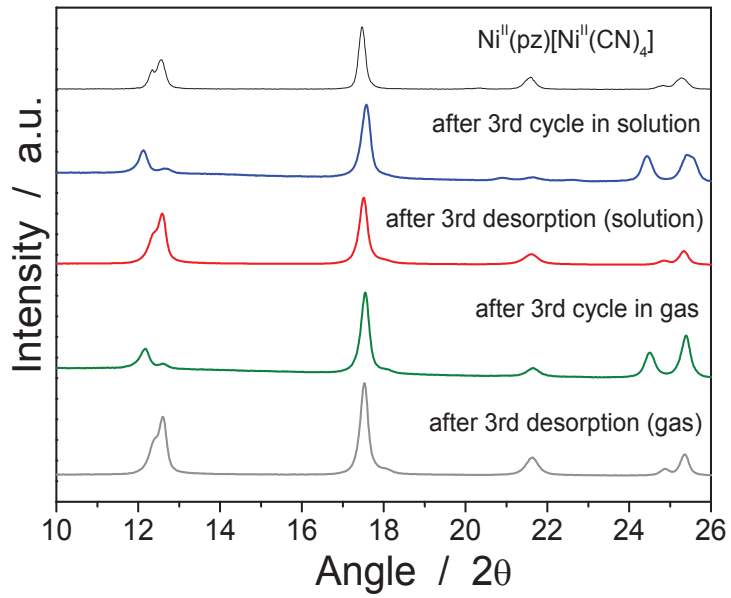

Figure 51 – XRPD for $Ni^{II}(pz)[Ni^{II}(CN)_4]$ after 3rd cycles in solution and gaseous phase and desorptions.

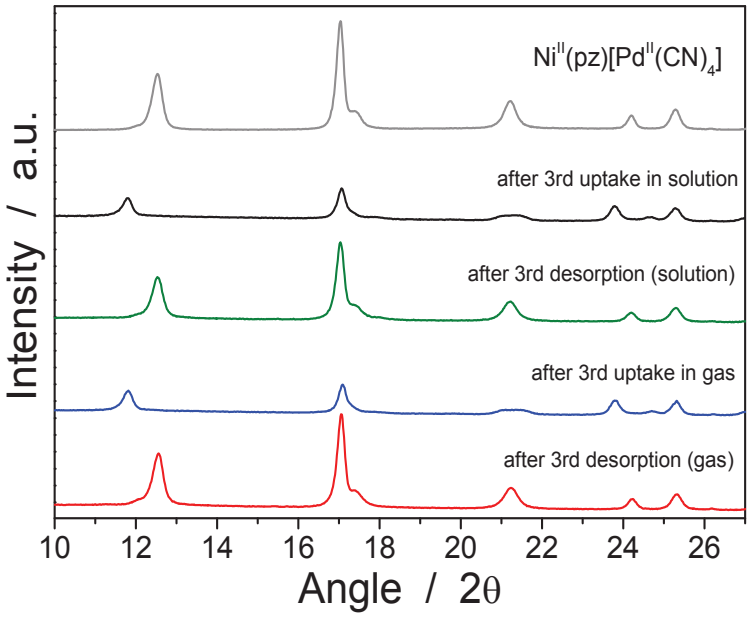

Figure 52 - XRPD for $Ni^{II}(pz)[Pd^{II}(CN)_4]$ after 3rd cycles in solution and gaseous phase and desorptions.

1.1.3 - Replacement of the octahedral metal M': M'(pz)[$Ni^{II}(CN)_4$] series (M' = Ni^{II}, Co^{II}).

Octahedral geometry can be observed for a large series of metallic ions and it is the most stable geometry for a metallic cation surrounded by 6 ligands. Hofmann-like clathrates with formula $M^{II}(pz)[Ni^{II}(CN)_4]\bullet xH_2O$ were obtained with salts $M'(BF_4)_2$ or $M'(NO_3)_2$ of a bivalent metal like M' = Mn^{2+}, Fe^{2+}, Co^{2+}, Zn^{2+} or Cu^{2+}, by adapting the synthesis for $Ni^{II}(pz)[Ni^{II}(CN)_4]\bullet 2H_2O$. A series of microcrystalline compounds was obtained and X-ray Powder Diffraction patterns for each of them were registered (Figure 53). The compounds precipitated with cations Mn^{2+}, Cu^{2+} and Zn^{2+} did not show the same pattern than $Ni^{II}(pz)[Ni^{II}(CN)_4]\bullet 2H_2O$. SEM/EDX analyses found molar ratios Mn/Ni ≈ 1, Zn/Ni ≈ 1 but Cu/Ni ≈ 2. Cation Cu^{2+} probably preferred a tetragonal arrangement but no further investigation was carried out. The precipitated compound with Fe^{2+} demanded inert conditions to minimize the oxidation of Fe^{2+} to Fe^{3+}. However the final compound was partially amorphous, with weak crystalline peaks. It was supposed to be $Fe^{II}(pz)[Ni^{II}(CN)_4]$ by comparisons with studies about this compound.[80]

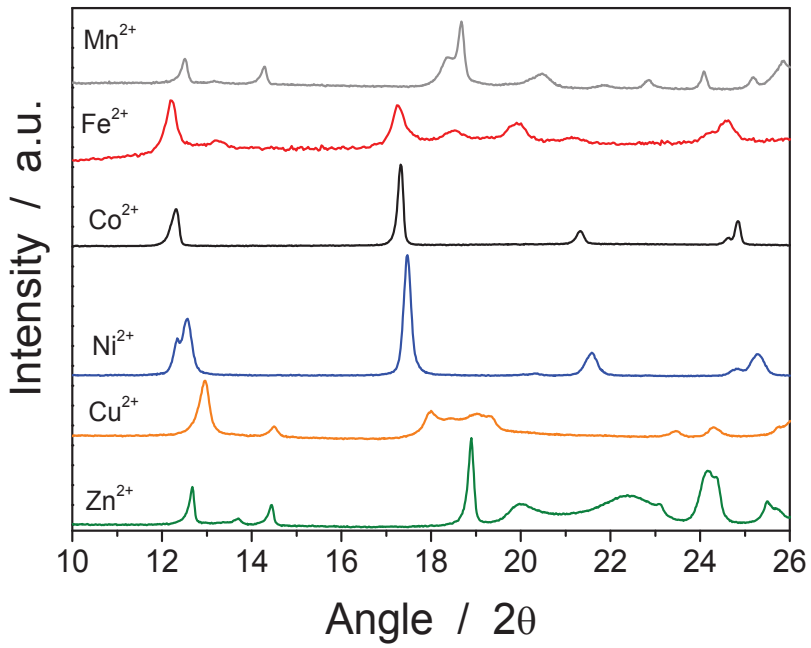

Figure 53 – XRPD patterns for the series M^{2+} / $(pz)[Ni^{II}(CN)_4]^{2-}$ where M = Mn, Fe, Co, Ni, Cu, Zn.

The compound obtained with Co^{2+}, with expected composition $Co^{II}(pz)[Ni^{II}(CN)_4]\bullet 2H_2O$ (x = 1 or 2), was the best candidate for further investigations in the present work, since it showed a high crystallinity and the XRPD pattern close to $Ni^{II}(pz)[Ni^{II}(CN)_4]$. Elemental analysis indicated a good agreement with the expected composition with a molar ratio Co/Ni ≈ 1. The XRPD pattern was compared with the simulated powder pattern for $Fe^{II}(pz)[Pt^{II}(CN)_4]\bullet 2H_2O$ (referenced solved structure) as showed in Figure 54. Indexation of almost all main peaks was possible, indicating

that $Co^{II}(pz)[Ni^{II}(CN)_4]\bullet 2H_2O$ is isostructural to the reference structure as well as to the series $Ni^{II}(pz[M''(CN)_4]\bullet 2H_2O$ with M'' = Ni^{II}, Pd^{II} or Pt^{II}. As in the case of $Ni^{II}(pz[Ni^{II}(CN)_4]\bullet 2H_2O$, full identification of the planes with correct Miller indexes was not possible since (100) and (001) overlapped partially and also (110) and (101) planes were too close to be distinguished.

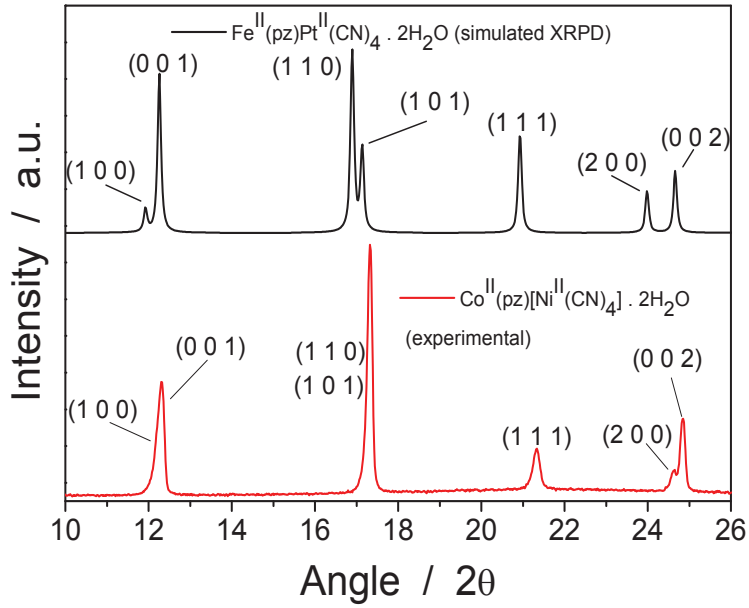

Figure 54 – Indexing of peaks for $Co^{II}(pz)[Ni^{II}(CN)_4]$.

LeBail refinement on the structure $Co^{II}(pz)[Ni^{II}(CN)_4]\bullet 2H_2O$ revealed lattice parameters $a = b =$ 7.2262(7) Å, and c = 7.1594(9) Å (space group P4/m), thus a volume of the unit cell of 373.8(5) $Å^3$. FT-IR spectra showed that the stretching ν(C≡N) was located at 2166 cm^{-1} with a weaker band at 2147 cm^{-1}, whereas the δ(M-N≡C) mode was at 442 cm^{-1} (where M = Co, Ni). The vibration $\nu(Co\text{-}N_{pz})$ was found at 474 cm^{-1} which was the same value found experimentally in the complex $Co^{II}(pz)(NO_3)_2$. For the analogue structure $Ni^{II}(pz)[Ni^{II}(CN)_4]\bullet 2H_2O$, the ν(C≡N) mode was at 2174 cm^{-1} and the $\nu(Ni\text{-}N_{pz})$ mode was at 485 cm^{-1}, indicating that Ni^{II} cation gave a stronger coordination with the ligands. The higher vibration modes for $Ni^{II}(pz)[Ni^{II}(CN)_4]\bullet 2H_2O$ with respect $Co^{II}(pz)[Ni^{II}(CN)_4]\bullet 2H_2O$ were justified since they followed the order for the second ionization potential Ni^{2+} > Co^{2+}. TGA analyses showed that $Co^{II}(pz)[Ni^{II}(CN)_4]\bullet 2H_2O$ was stable up to 350 °C, a possible reflection of the weaker coordination of Co^{2+}. The decomposition below 100 °C was again associated to the loss of water and other solvents used in the preparation.

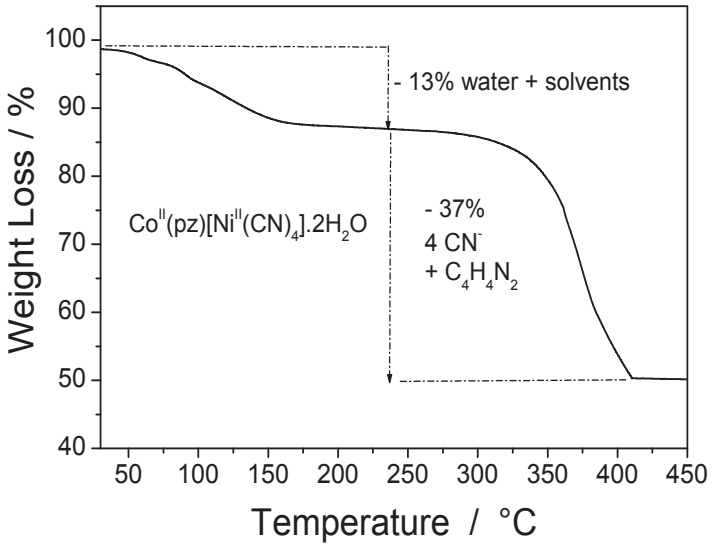

Figure 55 – TGA for $Co^{II}(pz)[Ni^{II}(CN)_4].2H_2O$.

The hydrated $Co^{II}(pz)[Ni^{II}(CN)_4]\bullet 2H_2O$ has a pink colouration and its UV-VIS spectrum showed an absorption band at 480 nm, related to the *d-d** electronic transitions (Figure 56). When the dehydrated $Co^{II}(pz)[Ni^{II}(CN)_4]$ was obtained, by heating at 80 °C under primary vacuum for 8 hours, the color of the compound turned to blue-violet. The UV-VIS spectrum of the dehydrated compound showed the appearance of a new band at 600 nm, which can be assigned to the spin-allowed *d–d** transitions of the Co(II) centres in a tetrahedral coordination environment,[123] so that the spectrum of dehydrated $Co^{II}(pz)[Ni^{II}(CN)_4]$ showed the presence of both octahedral and tetrahedral Co^{2+}. Since the spectra were measured in reflectance mode, we can expect a major response of the surface where we can locate unsaturated Co^{2+} centres that lost water molecules on desorption. By the rest, since water desorption did not affect the XRPD pattern and the FT-IR spectrum, we excluded a change in geometry of the bulk Co^{2+}.

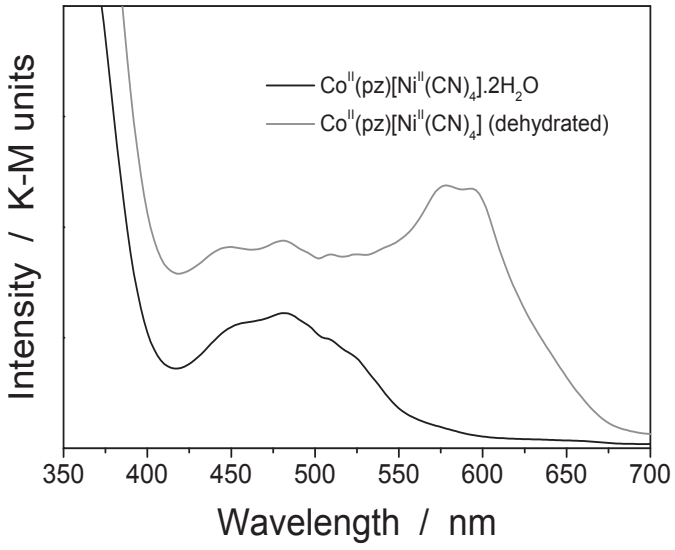

Figure 56 - UV-VIS for hydrated $Co^{II}(pz)[Ni^{II}(CN)_4].2H_2O$ and dehydrated $Co^{II}(pz)[Ni^{II}(CN)_4]$.

Following the same protocol described in the previous section, the entrapment of iodine in solution and in vapours were performed for the dehydrated structure $Co^{II}(pz)[Ni^{II}(CN)_4]$. The kinetic curve traced at iodine concentration $3.\bullet10^{-3}$ M in cyclohexane shows the same equilibrium time as $Ni^{II}(pz)[Ni^{II}(CN)_4]$, as Figure 57 shows. The curve was fitted with the pseudo-second order model with kinetic constant k = 0.28 $mmol.g^{-1}.min^{-1}$.

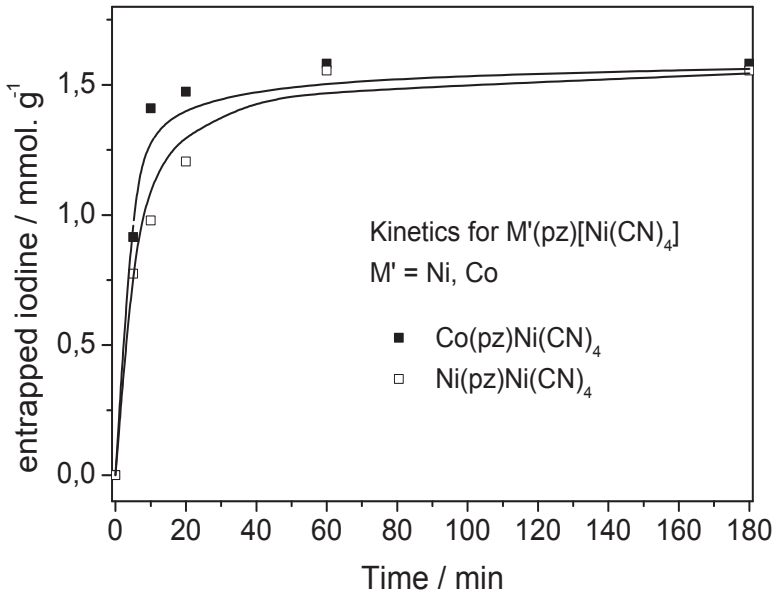

Figure 57 - kinetics of iodine adsorption for the group M'(pz)[Ni(CN)4], M' = Ni^{II}, Co^{II}.

The isotherm performed at different concentration of iodine indicated a maximal iodine capacity of 3.32 ± 0.1 $mmol.g^{-1}$, that corresponded to the adsorption of about 1 I_2 per unit cell. The experimental curve was then fitted with the Langmuir model using a Langmuir constant (or adsorption energy) K = 2946 $L.mol^{-1}$. This constant was higher than the one for $Ni^{II}(pz)[Ni^{II}(CN)_4]$ (K = 1506 $L.mol^{-1}$), indicating that the affinity of $Co^{II}(pz)[Ni^{II}(CN)_4]$ to iodine is slightly higher than $Ni^{II}(pz)[Ni^{II}(CN)_4]$. The maximal amount was confirmed by TGA, where a loss in the interval 150 and 250 °C was detected (Figure 61). First derivative indicated the highest desorption rate around 225 °C. The iodine entrapment in gaseous phase did not show any decrease in the maximal capacity and TGA showed a iodine/host structure molar ratio close to 1, meaning one I_2 per unit cell, so that for both conditions of capture we obtained a clathrate of formula $Co^{II}(pz)[Ni^{II}(CN)_4]\bullet I_2$. The iodine uptake in gaseous phase indicated that it was easier for $Co^{II}(pz)[Ni^{II}(CN)_4]$ to reach the maximal capacity than for the analogue structure $Ni^{II}(pz)[Ni^{II}(CN)_4]$, whose capacity in vapours was about 0.7-0.8 I_2 per unit cell. Further discussion about this difference in performance will be reported in the section 1.2.1.

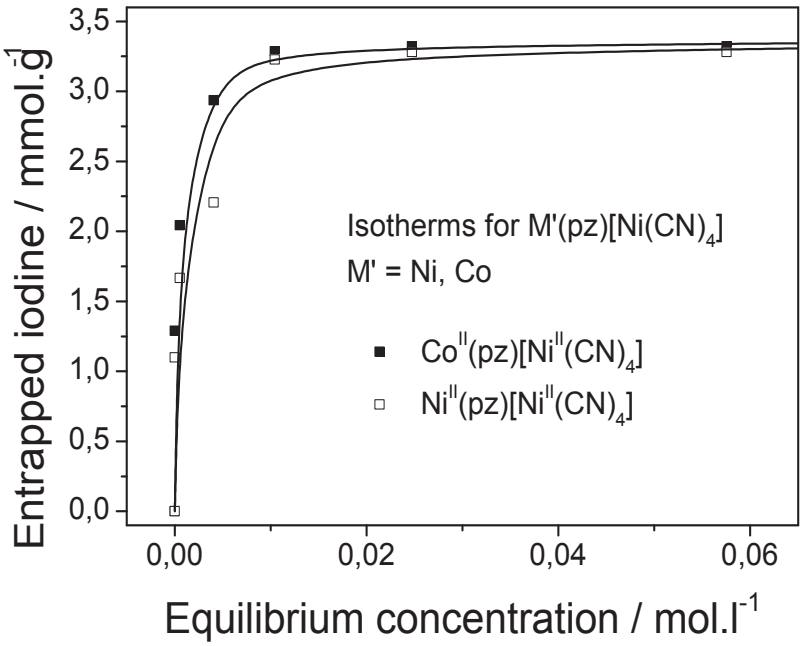

Figure 58 – Isotherms of iodine adsorption for the group M'(pz)[Ni(CN)4] M' = Ni^{II}, Co^{II}

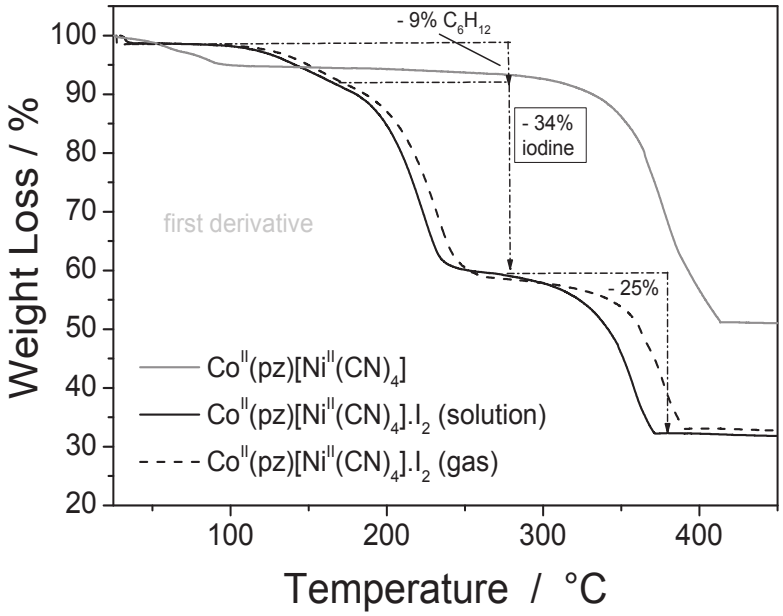

Figure 59 - TGA curves for $Co^{II}(pz)[Ni^{II}(CN)_4]\bullet I_2$ obtained in solution and in gaseous phase

In the infrared spectrum of the material at maximal capacity, the bands of pyrazine were perturbated by the presence of the iodine suggesting a blocking effect to the free rotation of the ligand. Interestingly, the ν(C≡N) mode shifted to higher frequencies (2177 cm^{-1}, with a shoulder at 2186 cm^{-1}) compared to the initial value 2167 cm^{-1}. By contrast, in the case of $Ni^{II}(pz)[Ni^{II}(CN)_4]$, the initial ν(C≡N) mode at 2174 cm^{-1} decreased to 2165 cm^{-1}. Other specific features for the IR spectrum of the clathrate $Co^{II}(pz)[Ni^{II}(CN)_4]\bullet I_2$ were remarked as the evident blue-shift of the modes ν(Co-N_{pz}) and ν(M-C≡N) occurred, whereas no significant shift for the corresponding bands occurred for $Ni^{II}(pz)[Ni^{II}(CN)_4]\bullet I_2$. The evolution of IR bands after iodine entrapment in solution is reported in Table 6. Before discussing the possible reason for these shifts, it is important to have an overall view of all characterizations.

Table 6 – IR bands for $Co^{II}(pz)[Ni^{II}(CN)_4]$ before and after the adsorption of iodine, w = weak; s = strong; vs = very strong.

	$Co^{II}(pz)[Ni^{II}(CN)_4]$	$Co^{II}(pz)[Ni^{II}(CN)_4]\bullet I_2$
Pyrazine bands (strong bands)	3115 (w), 1417 (s), 1160 (s), 1130 (s), 1086 (s), 1055 (s), 1030 (s), 806 (s)	3120 (w), 1420 (s), 1172 (s), 1131 (s), 1121 (s), 1106 (w), 1085 (w), 1071 (s), 1057 (s), 799 (s)
ν(C≡N)	2167 (vs), 2147 (shoulder)	2177 (s), 2186 (shoulder)
ν(Co-N_{pz})	474 (s)	502 (s)
ν(M-C≡N) where M = Co, Ni	442 (s)	465 (s)

XRPD patterns indicated how the lattice of $Co^{II}(pz)[Ni^{II}(CN)_4]$ responded to the insertion of I_2. The (100) and (200) Miller planes diffracted at lower angles after insertion of iodine at maximal capacity, as well as the (001) and (002) planes, indicating an overall decrease of the lattice parameters due to a stronger interaction. In Figure 60 the evolution of the XRPD pattern after entrapment in solution is reported. The perturbation of the lattice parameters was even more visible than for $Ni^{II}(pz)[Ni^{II}(CN)_4]\bullet I_2$, with considerable shifts for the (110) and (111) peaks. Identical evolution was observed for the sample obtained by adsorption in gaseous phase as Figure 60 shows. The LeBail refinement performed on the XRPD pattern for the clathrate $Co^{II}(pz)[Ni^{II}(CN)_4]\bullet I_2$ gave the lattice parameters $a = b = 7.1593(5)$ Å, $c = 6.8942(5)$ Å.

The volume of the unit cell after entrapment was 353.3(6) $Å^3$, which meant a volume reduction by 5% upon uptake. By contrast, the volume of the unit cell of $Ni^{II}(pz)[Ni^{II}(CN)_4]\bullet I_2$ after entrapment was 369.3(8) $Å^3$ which was slightly bigger than $Co^{II}(pz)[Ni^{II}(CN)_4]$. Thus, we could expect a better confinement of iodine by $Co^{II}(pz)[Ni^{II}(CN)_4]$. TGA coupled with mass spectroscopy revealed indeed a desorption temperature around 180 °C, as Figure 61 shows, which was higher by 30 °C with respect to the analogue clathrate $Ni^{II}(pz)[Ni^{II}(CN)_4]\bullet I_2$. Mass spectroscopy also indicated that the loss of iodine was finished around 250 °C (at the heating rate of the analysis, 5°C.min^{-1}),

which was below the structural decomposition by at least 100 °C. Complete desorption was attained by heating at 200 °C for 1 hour. As Figure 60 reports, diffraction peaks after desorption were identical to the ones before entrapment for both entrapment in solution and in gaseous phase.

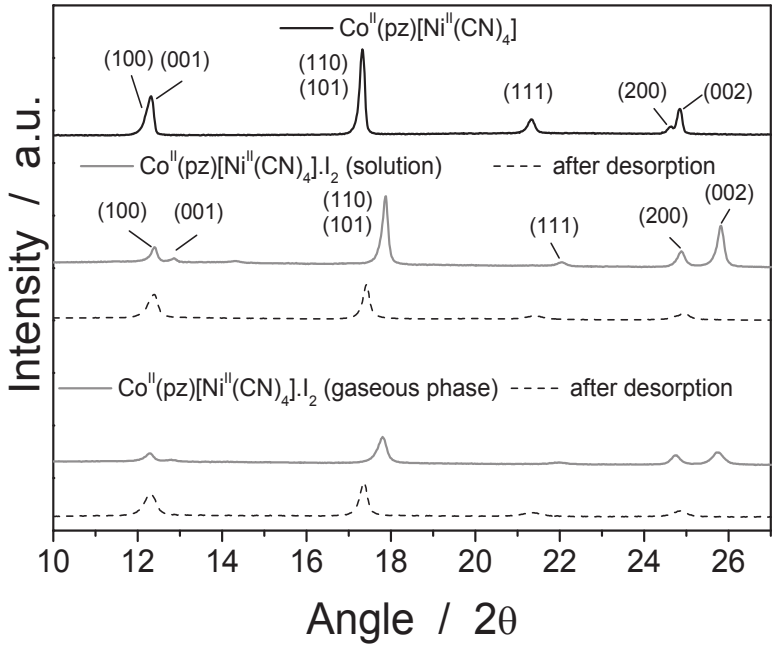

Figure 60 – XRPD for $Co^{II}(pz)[Ni^{II}(CN)_4].2H_2O$, iodine-loaded structures and related desorptions.

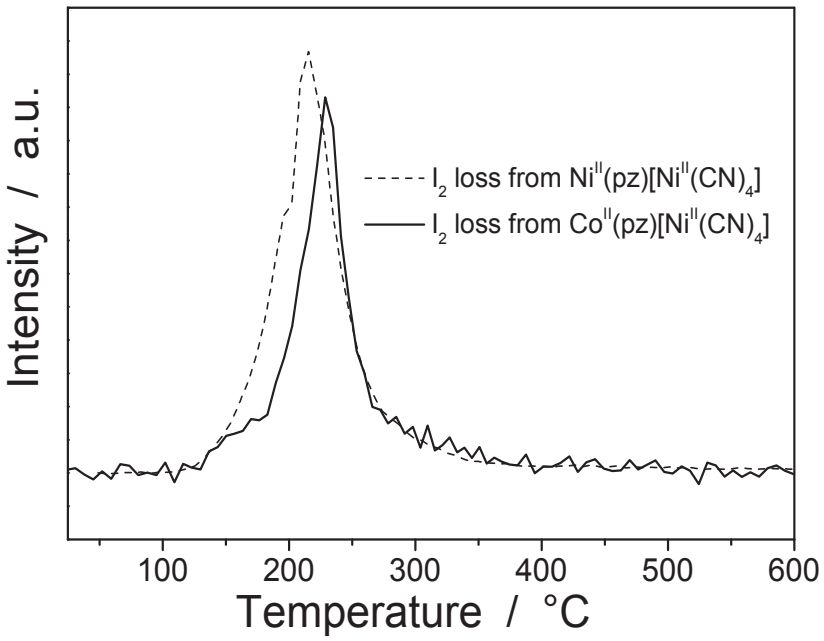

Figure 61 – Mass spectroscopy for the series $M'(pz)[Ni(CN)_4]$ with M' = Ni or Co.

After desorption, IR vibration modes of pyrazine (Figure 62), as well as cyanide bands (Figure 63) assumed same unperturbated values of the unfilled host structure indicating a full reversibility. Again, no difference between the sample obtained in solution and the one obtained in gaseous phase was encountered. The reversibility indicated that the interaction with the iodine was weak and that the guest molecules did not destroy the coordination with cyanides and pyrazine.

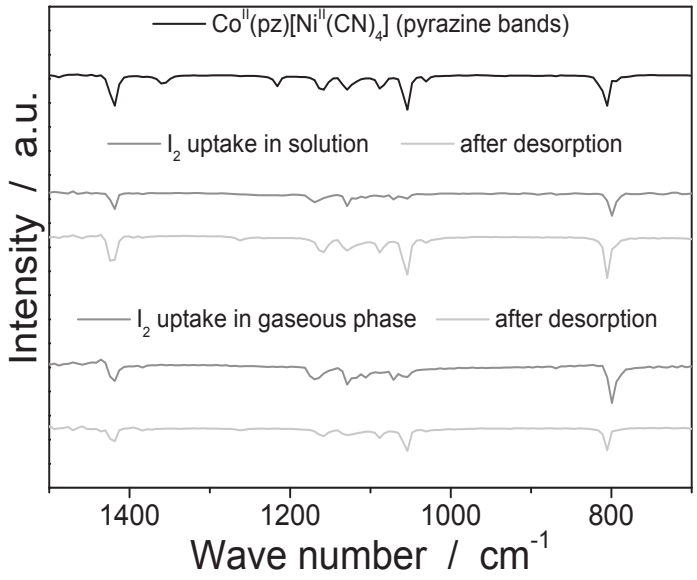

Figure 62 - IR bands (pyrazine) for $Co^{II}(pz)[Ni(CN)_4]\bullet I_2$ and after desorption.

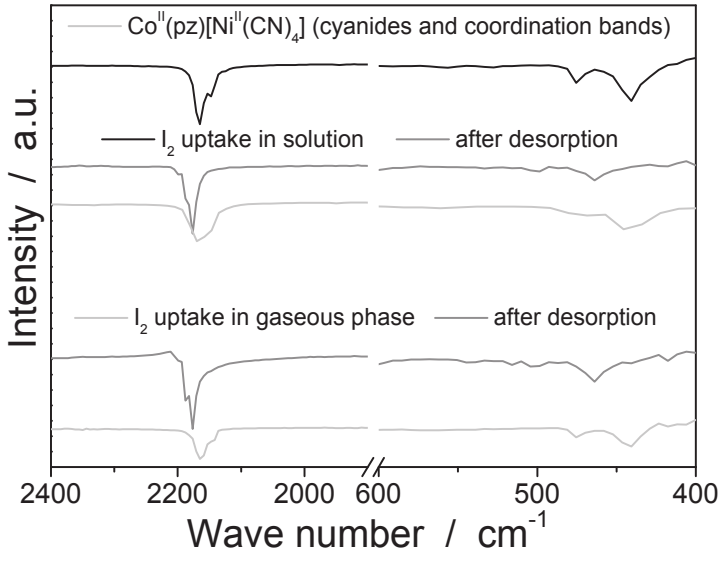

Figure 63 – IR bands (cyanide bands) for $Co^{II}(pz)[Ni(CN)_4]\bullet I_2$ and after desorption.

For a better insight of the nature of the confined iodine, UV-VIS spectra in reflectance mode on the solid samples were performed for both samples at maximal capacity. Figure 65 reports the spectra for the host structure before and after the iodine insertion in solution and vapours. Note

that the iodine clathrates exhibited a black colouration. A main UV-VIS band with maximum around 460 nm was detected for both clathrates and it was associated to the confined I_2 interacting with the host structure.

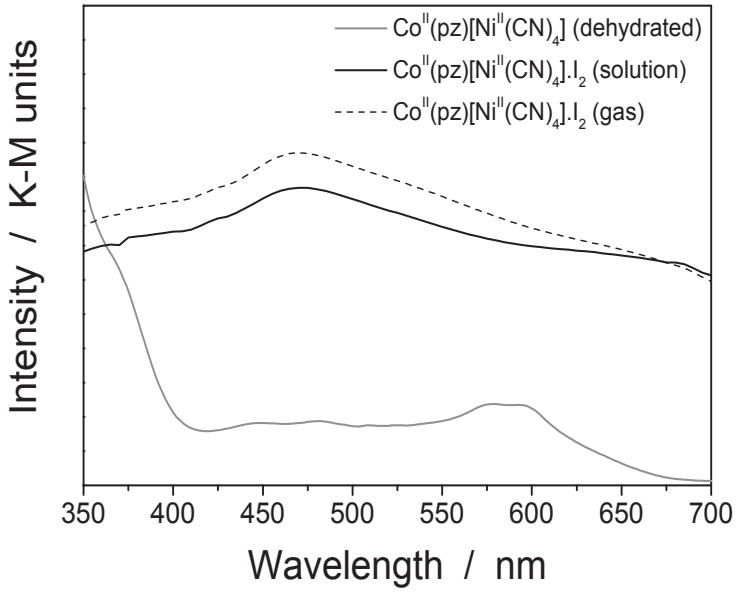

Figure 64 – UV-VIS spectra for for $Co^{II}(pz)[Ni^{II}(CN)_4]$ before and after uptake in solution and vapours.

Raman spectra showed almost the same profile already observed for the $Ni^{II}(pz)[Ni^{II}(CN)_4]\bullet I_2$ (Figure 65). The band at 108 cm^{-1} is characteristic for the triiodides formation onto the lattice defected in $Co^{II}(pz)[Ni^{II}(CN)_4]\bullet I_2$. The large band with maximum at 160 cm^{-1} was associated to the confined I_2. The slightly lower ν(I-I) mode of the interacting mode with respect to the value in the clathrate $Ni^{II}(pz)[Ni^{II}(CN)4]\bullet I_2$ (maximum at 165 cm^{-1}) was correlated with the stronger interaction deduced from the other analyses.

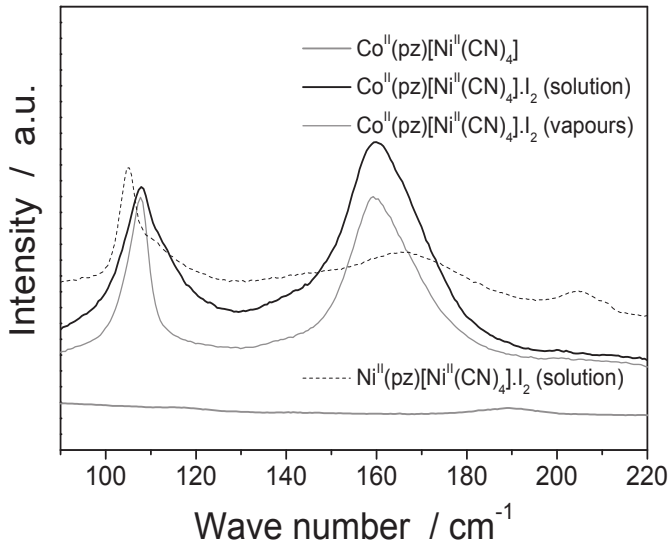

Figure 65 – Raman spectra for for $Co^{II}(pz)[Ni^{II}(CN)_4]$ before and after iodine uptake in solution and vapours.

We can now attempt an interpretation of the overall view given by the different analyses. If we reconsider the shifts in the IR spectra reported in Table 6, an increase of the ν(C≡N) mode was reported. Generally, an increase in frequencies for ν(C≡N) can occur due to a decrease in back donation due to an oxidative addition, as it happened in the case of the complex $Ni^{II}(pz)[Pt^{II/IV}(CN)_4]\bullet I^-$ or due to a stronger coordination on the N side of the CN^- ligands. According to literature,[124] complexes of Co^{II} with tetradentate macrocyclic ligands, the 4,7,11,14-tetrazacyclotetradecane, can undergo oxidation by reaction with a halogen as Br_2 or I_2, as reported by Heckerman *et al.*[124] The oxidation of Co^{II} to Co^{III} is accompanied by formation of coordinated iodide ligands I^- and reformation of molecular iodine I_2. Note that in these complex, the Co^{II} centres disposes of two unsaturated octahedral sites, on which the oxidative addition can occurs. Upon oxidation to Co^{III}, the complex becomes, indeed, square pyramidal.

Reaction 2 – Oxidative addition between iodine and $Co([14]aneN_4)^{2+}$ reported by Heckerman *et al.*[124]

$$Co^{II} + I_2 \rightarrow Co^{III}{-}I^- + I\cdot \quad \textit{For two redox reactions:} \quad 2I\cdot \rightarrow I_2$$

Even though a partial oxidation of Co^{II} to Co^{III} could not be excluded *a priori*, since it would explain the general trend of the IR bands for $Co^{II}(pz)[Ni^{II}(CN)_4]\bullet I_2$ and subsequently the reduction of the unit cell, some relevant point would discard this type of interaction. Firstly, XPS analysis on $Co^{II}(pz)[Ni^{II}(CN)_4]$ performed before and after the introduction of iodine showed the same peak for the Co 2p at 780 eV, with a shoulder at 785 eV due to the satellites configurations. This was the same values reported by other XPS studies, performed on the oxides of bivalent cobalt CoO.[125] Secondly, the Co^{II} sites are supposed to have all six saturated octahedral sites (two pyrazines and four cyanides ligands), so that further ligand addition should increase the coordination number. Moreover, the iodine desorption tests clearly indicated that that host lattice was preserved upon iodine insertion and no decoordination of the ligands in the Co^{II} centre occurred either. Thirdly, the Raman spectra did not show any band that could be associated to $\nu(Co^{III}\text{-}I)$, as it was possible for $\nu(Pt^{IV}\text{-}I)$ in the characterization of $Ni^{II}(pz)[Pt^{II/IV}(CN)_4]\bullet I^-$. Raman spectra for $Co^{II}(pz)[Ni^{II}(CN)_4]\bullet I_2$ were, indeed, comparable to spectra for $Ni^{II}(pz)[Ni^{II}(CN)_4]\bullet I_2$ and $Ni^{II}(pz)[Pd^{II}(CN)_4]\bullet I_2$ where the eventual oxidation of Ni^{II} was excluded since there was no shift to higher frequencies for the vibration modes ν(C≡N), δ(Ni-CN) and $\nu(Ni\text{-}N_{pz})$. Alternatively, we could think of a *back donation* where the t_{2g} orbitals in the O_h configuration weakly interacted with the σ^* anti-bonding orbital of I_2, which acted as an acceptor of electron density. This fact would explain the perturbation of the confined molecular iodine observed by Raman and UV-VIS spectroscopy. A partial removal of charge from the metallic centre by I_2 would increase the splitting Δ_o and the ligand-to-metal charge transfer for the six surrounding electron-rich ligands (four CN^- and 2 pyrazine). This fact would explain the blue-shift of the cyanide bands and the reduction of the unit cell. However, only further DFT calculations may eventually clear up if this kind of interaction could take place and why we should observe this type of interaction for octahedral Co^{II} and not for Ni^{II} centres.

In the next section, the analogue structure $Co^{II}(pz)[Pd^{II}(CN)_4]$ will be characterized in order to evaluate the effect of replacing both octahedral and square planar metals in the system $Ni^{II}(pz)[Ni^{II}(CN)_4]$.

1.1.4 - Combined effects with concurrent replacement of both metallic centres.

The purpose of this study was to verify if the different responses of the host structures to the insertion of iodine were effectively connected to the specific replaced building elements. The $Co^{II}(pz)[Pd^{II}(CN)_4]\bullet 2H_2O$ compound was precipitated using $Co^{II}(NO_3)_2\bullet 6H_2O$, pyrazine and $K_2[Pd^{II}(CN)_4]$ as precursors. EDX analyses confirmed a molar ratio Co/Pd ≈ 1. The colour of the hydrated compound was pink as for the analogue $Co^{II}(pz)[Ni^{II}(CN)_4]\bullet 2H_2O$ and it turned to blue-violet upon dehydration, indicating the transition of unsaturated Co^{2+} from octahedral to tetrahedral geometry, located most probably on the grain surfaces. The iodine clathrate was prepared by dynamic contact of the dehydrated $Co^{II}(pz)[Pd^{II}(CN)_4]$ with a cyclohexane solution $\approx 7\bullet 10^{-2}$ M for 24 hours. It was supposed an identical equilibrium time as the analogue host structures $Co^{II}(pz)[Ni^{II}(CN)_4]$ and $Ni^{II}(pz)[Pd^{II}(CN)_4]$. TGA also indicated a loss of one equivalent of I_2 on the interval 150-250 °C, so that final formula for the clathrate was $Co^{II}(pz)[Pd^{II}(CN)_4]\bullet I_2$. First derivative indicated the higher decomposition rate at 200 °C, but the transformation starting around 160 °C. The Raman spectrum registered with laser NeHe indicated two bands, at 114 cm^{-1} and at 164 cm^{-1}, similarly to the analogue clathrates where iodine was confined as interacting I_2 and a minor quantity of polyiodides. A comparison of the Raman spectra for the iodine clathrates prepared in solution is reported in Figure 66. It was noticed that the lower band related to the symmetric ν(I-I) mode of I_3^- was found at lower values (100-110 cm^{-1}) for structures containing the building block $[Ni^{II}(CN)_4]^{2-}$ and it was found around 115 cm^{-1} for structures containing the building block $[Pd^{II}(CN)_4]^{2-}$. This fact supported the hypothesis about the formation of I_3^- on terminal tetracyanometallates (or defects).

Focusing on the FT-IR spectra for the CN^- ligands, the stretching mode ν(C≡N) for the unfilled host structure was at 2179 cm^{-1}. After iodine uptake, the band shifted to 2183 cm^{-1}. The intensification of the ν(C≡N) mode followed the trend observed for the clathrate $Co^{II}(pz)[Ni^{II}(CN)_4]\bullet I_2$ even though the shift to higher frequencies was less pronounced. In the region at low frequencies, $Co^{II}(pz)[Pd^{II}(CN)_4]$ showed a band at 471 cm^{-1} corresponding to ν(Co-N_{pz}) and a band at 422 cm^{-1} associated to δ(M-CN). After entrapment, actually 3 bands appeared: 502, 457 and 428 cm^{-1}. Even though no clear association was possible, the values indicated an increase in frequencies for δ(M-CN) and ν(Co-N_{pz}) upon I_2 adsorption as observed for $Co^{II}(pz)[Ni^{II}(CN)_4]\bullet I_2$. FT-IR spectrum registered after desorption at 200 °C confirmed the full reversibility for this host structure, too. The lattice adaptation was checked by X-ray diffraction on $Co^{II}(pz)[Pd^{II}(CN)_4]$ and $Co^{II}(pz)[Pd^{II}(CN)_4]\bullet I_2$ (Figure 67). The observed tendency was intermediate between adaptations observed for $Co^{II}(pz)[Ni^{II}(CN)_4]$ and $Ni^{II}(pz)[Pd^{II}(CN)_4]$.

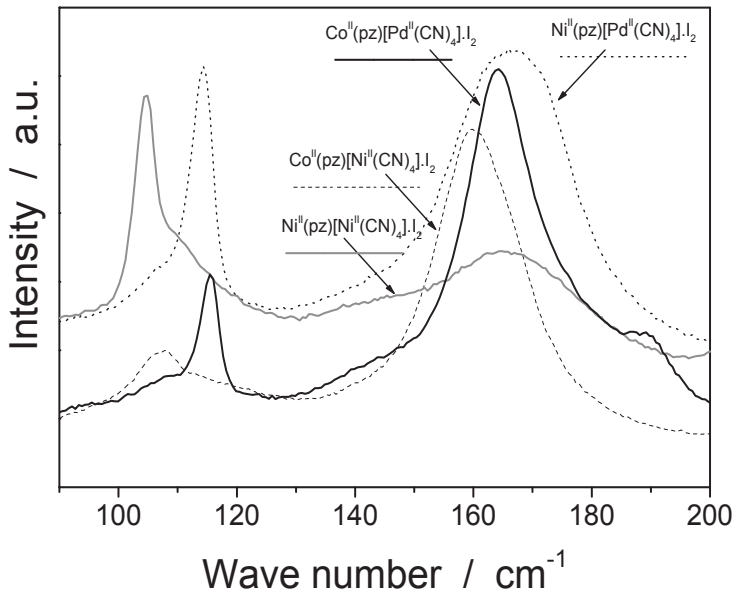

Figure 66 - Raman spectra for M'(pz)[M"(CN)$_4$].I$_2$ with M' = Co^{II} or Ni^{II} and M" = Ni^{II} or Pd^{II}.

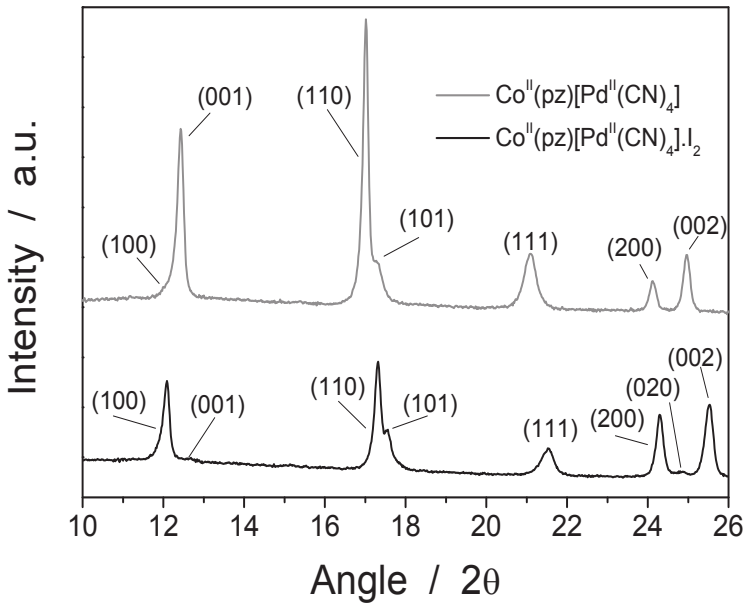

Figure 67 - XRPD for Co^{II}(pz)[Pd^{II}(CN)$_4$] and Co^{II}(pz)[Pd^{II}(CN)$_4$].I$_2$.

By using the Bragg's relationship, on the peaks (002) and (200) we found lattice parameters for the unfilled host structure a = b ≈ 7.36 Å and c ≈ 7.11 Å (V ≈ 385,1 Å^3). After iodine uptake, a general decrease of the lattice parameters occurred as observed in the clathrate Co^{II}(pz)[Ni^{II}(CN)$_4$]•I$_2$. Also, a new peak at 2θ = 24.8 appeared similarly to the case Ni^{II}(pz)[Pd^{II}(CN)$_4$]•I$_2$ and it was associated to the new plane (020) due to change of symmetry. Rough estimation of the lattice parameters gave a ≈ 7.31 Å, b ≈ 7.14 Å and c ≈ 6.96 Å (V ≈ 363.2 Å^3) for an orthorhombic lattice. By comparing the volumes, a reduction by ≈ 5% occurred upon

iodine insertion, similarly to the case $Co^{II}(pz)[Ni^{II}(CN)_4]\bullet I_2$. By the study of the $Co^{II}(pz)[Pd^{II}(CN)_4]$, it was confirmed that, in general:

- when Co^{II} occupied the octahedral position, a stronger interaction with I_2 with respect to octahedral Ni^{II} and a diminution by 5% of the unit cell was observed;
- when Ni^{II} occupied the octahedral position (with Ni^{II} or Pd^{II} in the square planar position), an increase of the lattice parameter *a* was always detected instead of a decrease;
- when Pd^{II} occupied the square planar position, a new diffraction peak appeared around 2θ = 24°-25° in the XRPD patterns indicating a change of symmetry from P4/m to Pcmm.
- when Ni^{II} occupied the square planar position the group space did not change upon iodine uptake.

The starting desorption temperatures, determined by mass spectroscopy, and the temperature with highest desorption rate, determined by first derivative of the TGA curve, were plotted as a function of the unit cell volume for each iodine clathrate (Figure 68). Nearly linear relationships were found. On the same graph, also, Raman values for ν(I-I) of interacting I_2 were plotted, indicating an almost linear relationship as well. For bigger unit cells, indeed, I_2 was retained up to higher temperatures and a more important blue-shift in Raman spectra was detected due to stronger interaction.

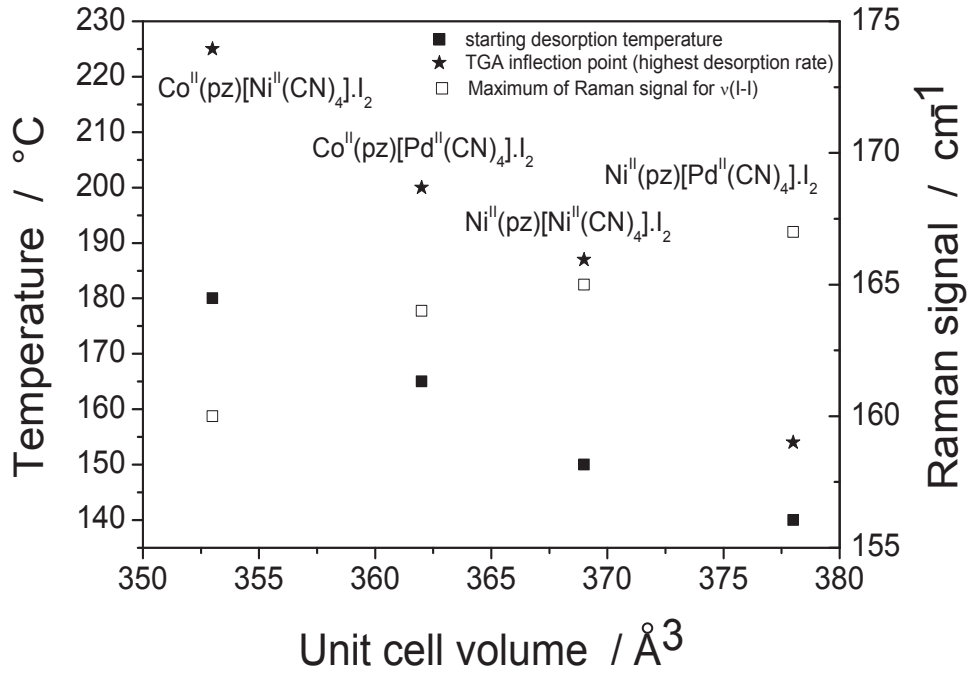

Figure 68 - Plotting of desorption temperatures and Raman stretching mode of the confined iodine as function of the unit cell volume at maximal capacity.

The next section will conclude the first part of Chapter 1 and it will focus on the replacement of the organic bidentate ligand in the host structure and consequences on the adsorption of iodine.

1.1.5 - Remplacement of the bidentate ligand L: $Ni^{II}(L)[Ni^{II}(CN)_4]$ series.

Another element that can be modulated in the host structure is the organic bridging ligand. The ligand must have a linear geometry and has the role to pillar the planar tetracyanonickelates by coordination on the O_h metal, defining the distance between them and consequently the dimension of the microporosity. An exhaustive study about the series $Ni^{II}(L)[Ni^{II}(CN)_4]$, called PICNICs (Pillared cyano-nickelates), was performed by Culp *et al.* [62] [65] [67] The chosen ligands could generate cages with size between ≈7 Å, when pyrazine was used, to ≈19 Å, when the 1,4 bis(4-pyridylacetylene)benzene was used. Some examples of used ligands for PICNICs are shown in Figure 69. Substituted ligands can contain as well functionalized groups, as amino- or fluoro- groups, to enhance interactions with the guest molecules. Anyway, tests performed so far for N_2 and CO_2 adsorption revealed that a decrease in efficiency occurred when the ligand was functionalized, since the functional group occupied the free space. In the case of H_2 adsorption, a shorter ligand as pyrazine gave a better confinement efficiency due to a better packing effect of H_2.[62]

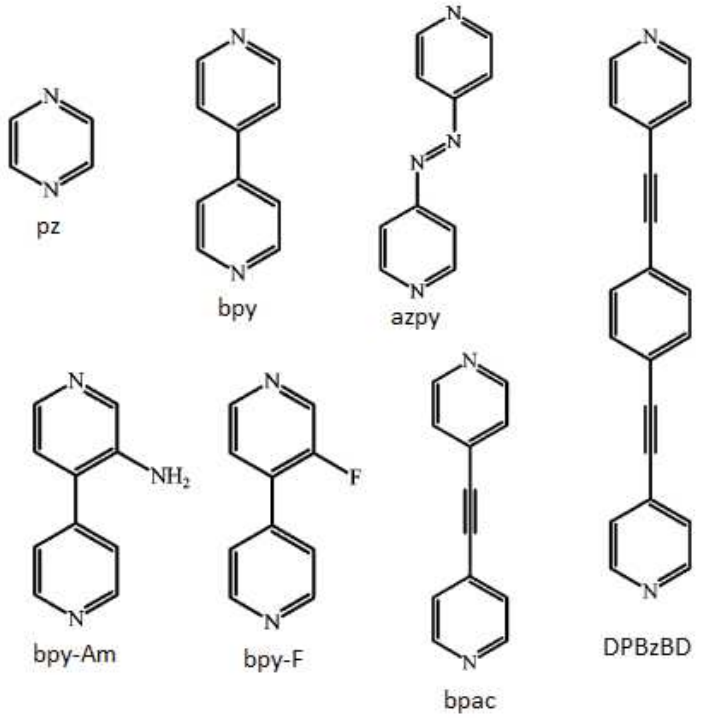

Figure 69 – Examples of ligands for the series PICNICs studied by Culp *et al.*[65]

The different flexibility of ligands was also studied: for example, about CO_2 adsorption by Culp *et al.*,[67] the more flexible 4-bipyridyl ethylene was preferred to the more rigid 1,2-bis(4-pyridyl)acetylene, since it induced a better adaptation (*breathing effect*) of the lattice under CO_2 adsorption. No real structure resolution of this class of host structures containing Ni in both *Oh*

and D_{4h} positions have been achieved yet, since it is difficult to obtain an enough good crystallization. However, for several PICNICs XRPD indicated an isostructural tetragonal lattice.
The entrapment of iodine with the $Ni^{II}(pz)[Ni^{II}(CN)_4]$, pz = pyrazine, performed in the present work showed an outstanding efficiency and a very high density occupation in the free space of the lattice. As explained previously, the iodine interacted with both the tetracyanickelates moieties and the pyrazine. Interaction with the ligands was assumed especially from the shifts in the IR spectra after capture. Free rotation of pyrazine was blocked by the presence of the guest iodine, as the decrease of the γ(C-H) mode suggested, and the ring stretching slightly increased. For the clathrate $Ni^{II}(pz)[Ni^{II}(CN)_4]\bullet I_2$, the charge transfer of π-electrons from the aromaticity of pyrazine to the σ^* anti-bonding orbital of iodine was considered as possible contribution to confinement. We initially assumed that organic bridging ligand as 4,4'-bipyridine or 4,4'-azopyridine which contain two aromatic rings should improve the entrapment. The enhancement could come as well from a bigger cage, given by a larger *c* parameter of the unit cell. The ligands 4,4'-bipyridine and 4,4'-azopyridine were supposed to give respectively $c \approx 11$ Å and $c \approx 13$ Å. On the other side, an increase in pore dimension should decrease the confinement, as observed for the H_2 adsorption, since the distancing of the tetracyanonickelates reduced the confining effect of Van der Waals interactions giving a lower density occupation inside the cages. To verify this point, entrapment of iodine was performed by replacing the pyrazine ligand in the network $Ni^{II}(pz)[Ni^{II}(CN)_4]$ with 4,4'-bipyridine (bpy) and 4,4'-azopyridine (azpy).

Preparation of $Ni^{II}(bpy)[Ni^{II}(CN)_4]$ and $Ni^{II}(azpy)[Ni^{II}(CN)_4]$.

The material $Ni^{II}(bpy)[Ni^{II}(CN)_4]\bullet H_2O$ was obtained, by adapting the synthesis for $Ni^{II}(pz)[Ni^{II}(CN)_4]\bullet H_2O$, where the ligand pyrazine was replaced by the 4,4'-bipyridine (see Experimental Section). As a result, a microcrystalline green powder was precipitated. Elemental analyses indicated that no relevant excess of ligand molecules remained trapped in the cages, since the detected amounts 42.7 wt% of C and of 21.9 wt% of N were very close to the theorical values of 42.48 wt% C and 21.24 wt% N for $Ni^{II}(bpy)[Ni^{II}(CN)_4]\bullet H_2O$. The material underwent the loss of the ligands between 400 and 600 °C (Figure 70). The XRPD pattern showed a highly crystalline material with main peak $2\theta = 18.7°$ that corresponded to the experimental XPRD pattern published by Culp for the same material shown in Figure 71. No real *Crystallographic Information File* (CIF) for this structure or analogues ones is available yet, anyway J. Culp was able to build from supposed lattice parameters a "hand-made" CIFs for the series $Ni^{II}(bpy)[M(CN)_4]$, where M = Ni^{II} or Pd^{II}. He obtained a good matching with th experimental XRPD pattern for the $Ni^{II}(bpy)[Pd^{II}(CN)_4]$.

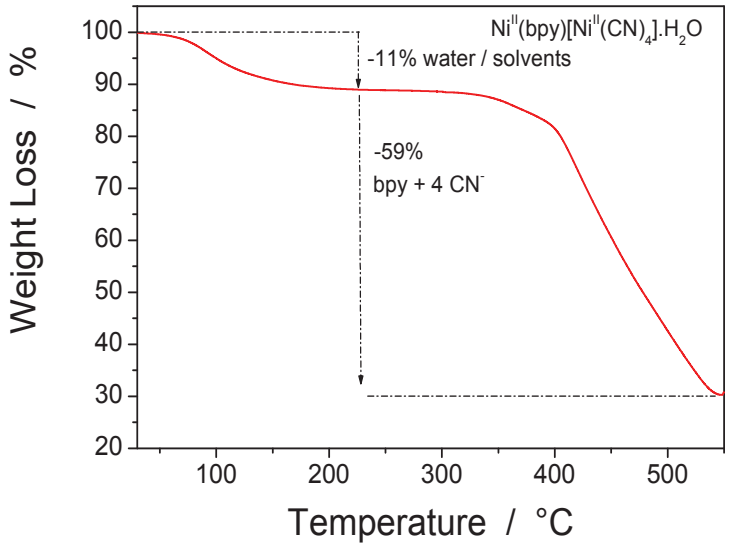

Figure 70 – TGA curve for $Ni^{II}(bpy)[Ni^{II}(CN)_4]•H_2O$.

As showed in Figure 72, the XRPD obtained in the present work for $Ni^{II}(bpy)[Ni^{II}(CN)_4]•H_2O$ did not have a high correspondence to the simulated pattern, especially for the intensity of the peaks and some not indexed peak. Culp justified the same observation, by considering a corrugation of the cyanometallates in the real material. LeBail refinement indicated the lattice parameters $a = b =$ 7.2772 Å, c = 11.2788 Å with $\alpha = \beta = \gamma = 90.0°$ (space group P4/mmm) which corresponds to the published parameters.[62] Then the material was checked at the FT-IR spectrometer. For the indexing of the IR active bands, the paper of Bayari *et al.* has been used as reference for all spectra.[126] In Table 7 the FT-IR bands for the free 4,4'-bipyridine and the coordinated 4,4'-bipyridine in $Ni^{II}(bpy)[Ni^{II}(CN)_4].H_2O$ are summarized. An overall moderate shift of the bands was detected upon coordination, with the same trends as reported in the paper of Bayari, where IR bands for the clathrate $Cd(bpy)[Hg(CN)_4]•2C_6H_6$ were reported. As shown in Table 8, the stretching mode of cyanide ν(C≡N) was found at 2163 cm^{-1} and the δ(Ni-CN) was observed at 440 cm^{-1}. Both values were higher than the related bands in the precursor $K_2[Ni^{II}(CN)_4]$, due to bridging coordination on the N-side of the cyanides to Ni^{II} (charge transfer from the filled anti-bonding $\sigma*$ orbital of the cyanides to the cation). The other IR active modes ν(Ni-CN) and γ(Ni-CN) were not detected and supposed to be very weak. A weak band for the $\nu(Ni\text{-}N_{bpy})$ mode was recognized at 486 cm^{-1}, since the same band was experimentally measured for the complex $Ni^{II}(NO_3)_2$/bypridine.

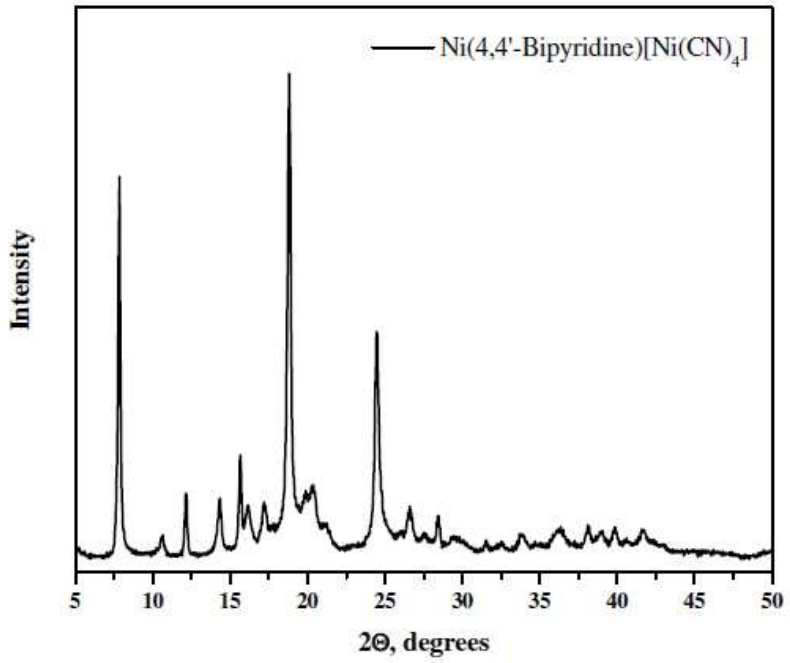

Figure 71 - Experimental XRPD for $Ni^{II}(bpy)[Ni^{II}(CN)_4]\cdot H_2O$ by Culp *et al.*[62]

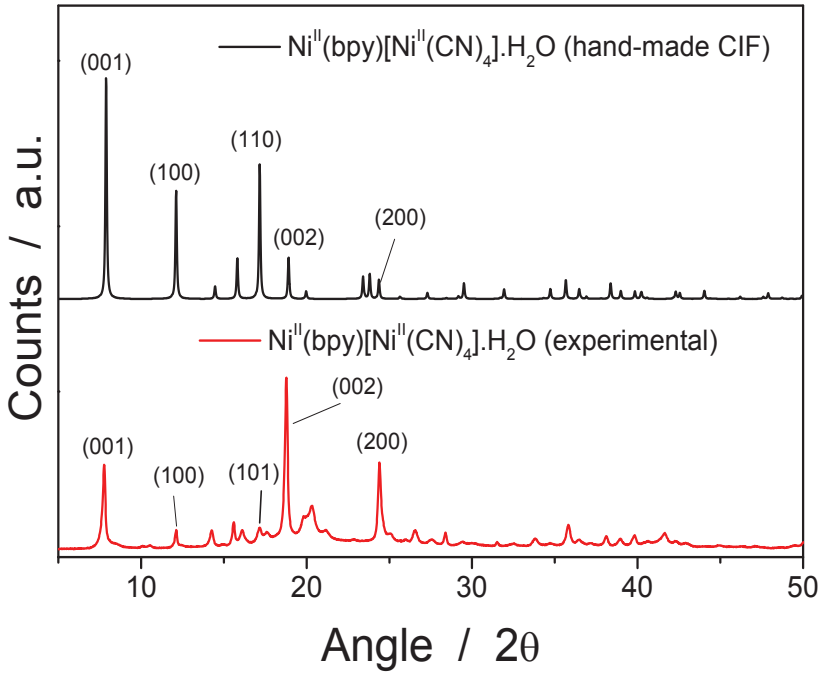

Figure 72 – XRPD for $Ni^{II}(bpy)[Ni^{II}(CN)_4]\cdot H_2O$ and simulated pattern.[62]

Table 7 – FT-IR bands for free 4,4'-bipyridine and coordinated 4,4'-bipyridine in $Ni^{II}(bpy)[Ni^{II}(CN)_4].H_2O$. w = weak; s = strong.

Vibration Mode	Free 4,4'-bipyridine	Coordinated 4,4'-bipyridine in $Ni^{II}(bpy)[Ni^{II}(CN)_4].H_2O$
ν(C-H)	3072 (w) 3026 (w)	3097 (vw) 3078 (vw)
ν_{ring}	1530 (s) 1487 (s) 1406 (s)	1534 (s) 1488 (s) 1411 (s)
δ(C-H)	1323 (w) 1220 (s)	1318 (w) 1218 (s)
ν_{ring}	1077 (s)	1064 (s)
δ(C-H)	1036 (s)	1045 (w)
ν_{ring}	990 (s) 962 (w)	994 (w) 965 (w)
γ(C-H)	860 (w) 810 (s) 732 (s)	855 (w) 805 (s) 730 (w)
δ(C-H)	672 (w) 630 (w) 615 (s)	675 (w) 635 (w) 612 (w)
γ_{ring}	496 (s)	not detected

Table 8 – IR values in intervals 2200-2000 cm^{-1} and 600-400 cm^{-1}. s = strong; vs = very strong; w = weak

Vibration mode	$K_2[Ni^{II}(CN)_4]$	$Ni^{II}(bpy)[Ni^{II}(CN)_4]$	$Ni^{II}(bpy)(NO_3)_2$
ν(C≡N)	2121 (vs) 2084 (w)	2163 (vs) 2124 (w)	-
δ(Ni-C≡N)	416 (s)	440 (s)	-
$\nu(Ni\text{-}N_{pz})$	-	486 (w)	486 (w)

This material was then tested for the entrapment of the molecular iodine in solutions of cyclohexane and in vapours. The clathrate $Ni^{II}(bpy)[Ni^{II}(CN)_4]\bullet H_2O$ was previously treated at 80 °C under vacuum to obtain the empty host structure $Ni^{II}(bpy)[Ni^{II}(CN)_4]$, which exhibited a blue-grey colour. According to the same hypothesis made for structures $Ni^{II}(pz)[Ni^{II}(CN)_4]$ and $Co^{II}(pz)[Ni^{II}(CN)_4]$, the change in colour was due to the removal of the water molecules, which were probably coordinated on Ni^{2+} cations with empty coordination sites particularly at the surface. The material maintained its structure upon dehydration, as observed for the pyrazine-containing analoges. UV-VIS spectra, registered in reflectance mode, for the hydrated and

dehydrated structures are reported. The band related to the *d-d** electronic transitions in Ni^{2+} at 580 nm slightly shifted to lower values of 570 nm when water was removed (Figure 73).

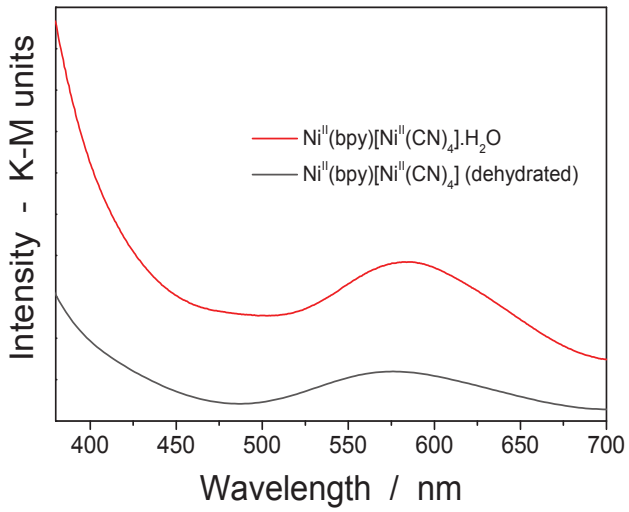

Figure 73 – UV-VIS spectra for $Ni^{II}(bpy)[Ni^{II}(CN)_4]\bullet H_2O$ and $Ni^{II}(bpy)[Ni^{II}(CN)_4]$.

The other organic ligand that was considerated was the commercially available 4,4'-azopyridine. The precipitation of the analogue $Ni^{II}(azpy)[Ni^{II}(CN)_4]\bullet H_2O$ is carried out by adapting the synthesis for $Ni^{II}(pz)[Ni^{II}(CN)_4]\bullet 2H_2O$, where pyrazine was replaced by 4,4'-azopyridine. Thus, the final material presented an orange color given by the azo-group N=N of the bidentate ligand. The Rietveld refinement for the analogue structure $Fe^{II}(azpy)[Pt^{II}(CN)_4]\bullet H_2O$ was carried out by Agusti *et al.* [63] and it was used as reference pattern for the X-Ray Diffraction patterns. A representation of the resolved structure containing water molecules is reported in Figure 74.

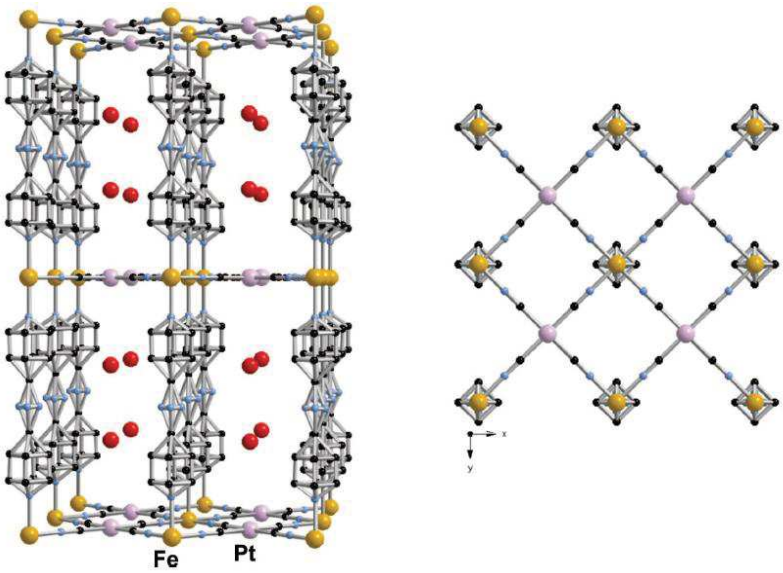

Figure 74 - Representation of $Fe^{II}(azpy)[Pt^{II}(CN)_4].H_2O$ by Agusti *et al.*[63]

As the authors of the CIF observed, the precipitated $Fe^{II}(azpy)[Pt^{II}(CN)_4]\bullet H_2O$ compound did not match exactly with the simulated XRPD pattern and an attempt to grow single crystals in H tubes was necessary. In the present work, our attempts to obtain $Ni^{II}(azpy)[Ni^{II}(CN)_4]\bullet H_2O$ single crystals actually failed since powder precipitated in H tubes, but the slower crystallization allowed a better indexation for most of the peaks and the recognition of the right compound. On the other side, the $Ni^{II}(azpy)[Ni^{II}(CN)_4]\bullet H_2O$ compounds obtained by instantaneous precipitation did not crystallize very well. Different Ni^{2+} salts were employed as well – $Ni^{II}(BF_4)_2$, $Ni^{II}(NO_3)_2$ and $Ni^{II}Cl_2$ - to see if modulating the counter-anions could have a beneficial effect on crystallization. When $Ni^{II}(BF_4)_2$ was used, for instance, the peak (001) was found at $2\theta = 7°$, giving ≈ 13 Å that was closer to the expected lattice parameter *c*, whereas with other salts the parameter *c* was slightly lower. Crystallization in H tube was performed as well with $Ni^{II}(BF_4)_2$, in a water-methanol solution, and after few weeks precipitation of powder occurred. The results for some batches obtained by instantaneous precipitation (nicknamed IP batches) and the slowly crystallized compound (nicknamed SC batch) are reported in Figure 75, in comparison with the simulated reference pattern for $Fe^{II}(azpy)[Pt^{II}(CN)_4]\bullet H_2O$.

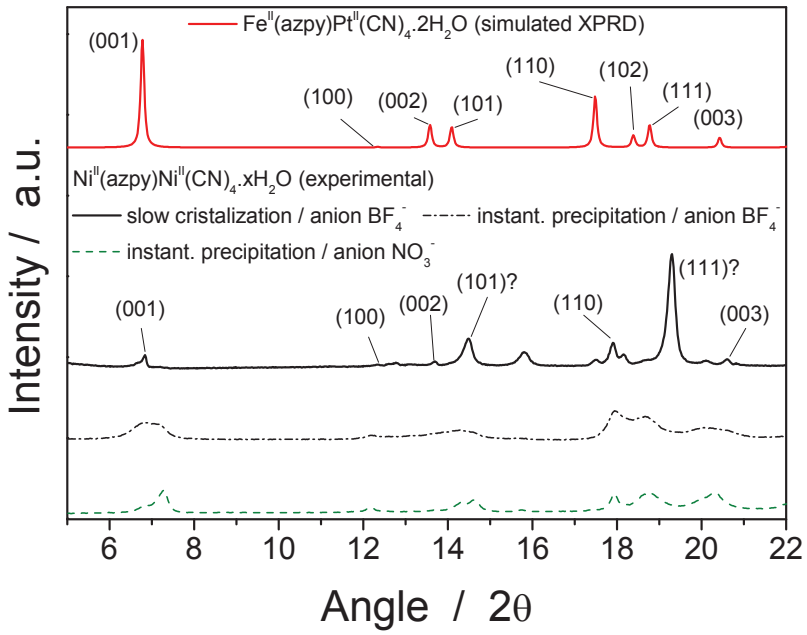

Figure 75 – Indexing of peaks for simulated XRPD of $Fe^{II}(azpy[Pt^{II}(CN)_4].H_2O$ and experimental XRPD patterns for $Ni^{II}(azpy)\{Ni^{II}(CN)_4\}\bullet H_2O$.

The peaks (001), (100), (002), (110) and (003) were recognized for the slowly crystallized compound. The presence of (001) around $2\theta = 7°$ for all batches indicated that in any case the $[Ni^{II}(CN)_4]^{2+}{}_n$ sheets were pillared by the bidentate ligand. Corrugation of the cyanonickelates could explain the difference with the reference pattern. LeBail refinement was possible only on XRPD pattern of the slowly crystalized batch. Lattice parameters $a = b = 6.969(2)$ Å and $c = 13.213(6)$ Å were found, which match with expected parameters. Also, elemental analyses

indicated amounts 39.7 wt% of C and 26.8 wt% for N that were very close to expected values 39.6 wt% of C and 26.4 wt% of N for composition $Ni^{II}(azpy)[Ni^{II}(CN)_4]\bullet H_2O$. As seen with the TGA analysis, the material had a weight loss of 11% due to the loss of water and traces of solvents (methanol and acetone) and later the decomposition of the ligand cyanides and 4,4'-azopyridine between 400 and 600 °C. The loss of water actually consisted of two contributions, as it can be seen in Figure 80: a loss by about 7% under 100 °C and a loss by 4% over 100 °C, corresponding to 1 H_2O equivalent. The lower loss could be related to physisorbed water on the surface and traces of other solvents, whereas the higher loss could be associated to the water inside the cages in interaction by H-bonding with the N=N groups. Infrared spectra were performed for IP(BF_4^-) batch and the SC batch indexation of the peaks was carried out according to previous FT-IR spectroscopic studies of the free and the coordinated ligand.[127,128] Table 9 shows that small shifts occurred upon coordination.

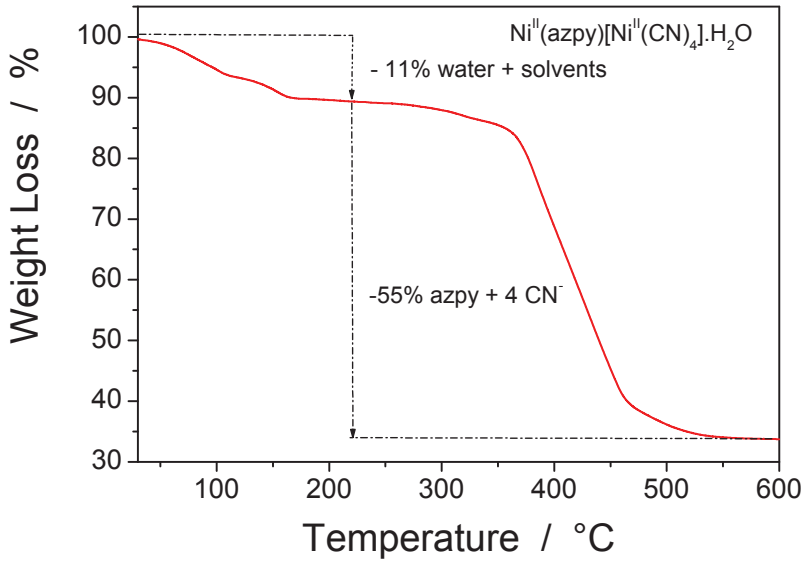

Figure 76 – TGA for $Ni^{II}(azpy)[Ni^{II}(CN)_4].H_2O$ IP(BF_4^-) batch.

Table 9 – free and coordinated 4,4'-azopyridine vibration modes. vw = very weak, w = weak, s = strong

Vibration Modes	4,4'-azopyridine	Coordinated ligand (SC batch)	Coordinated ligand (IP batch)
ν(C-H), ν(C-N_{azo})	3049 (vw)	3055 (vw)	3082 (vw)
ν(C-C), ν(C-N_{azo})	1586 (s)	overlapped with δ(O-H)	1584 (w)
ν(C-C), ν(C-N)	1564 (s)	1570	1568 (w)
ν(N=N)	(1510)**	not visible	1506 (vw)
ν(C-C), ν(C-N), δ(C-H)	1489 (s)	1473 (s)	1489 (s)
δ(C-H), ν(C-C)	1414 (s) 1322 (s)	1411 (s) 1322 (w)	1411 (s) 1321 (w)
ν(C-H), ν(C-N_{azo}), δ(C-C)	1223 (s)	1226 (s)	1227 (s)
ν(C-H), ν(C-C), δ(C-N)	1092 (w) 1053 (s)	1091 (w) 1057 (s)	1091 (w) 1046 (s)
ν_{ring}	989 (s)	1019 (s)	1018 (s)
γ(C-H)	832 (s)	839 (s)	839 (s)
γ(C-H), γ(C-C), γ(C-N)	734 (w)	Not visible	739 (w)
δ(C-C-C)	657 (w)	Not visible	668 (w)
γ(C-C), γ(C-N)	565 (s)	Not visible	569 (s)
δ(C-C-C), δ(C-N-C)	529 (w)	524 (w)	526 (w)

Table 10 - Cyanides bands for $Ni^{II}(azpy)[Ni^{II}(CN)_4]\bullet H_2O$

	ν(C≡N)	δ(Ni-C≡N)
$K_2[Ni^{II}(CN)_4]$	2121 (vs); 2084 (w)	416 (s)
Ni^{II} $[Ni^{II}(CN)_4]$	2165 (vs); 2129 (w)	446 (s)
IP batch	2165 (vs); 2130 (w)	442 (s)
SC batch	2164 (vs)	442 (s)

Entrapment of the iodine with $Ni^{II}(bpy)[Ni^{II}(CN)_4]$ and $Ni^{II}(azpy)[Ni^{II}(CN)_4]$.

Both materials were treated at 200 °C under vacuum to desorb all the water and traces of other solvents and to obtain the dehydrated host structures $Ni^{II}(bpy)[Ni^{II}(CN)_4]$ and $Ni^{II}(azpy)[Ni^{II}(CN)_4]$. In the case of $Ni^{II}(azpy)[Ni^{II}(CN)_4]$, due to a problem of quantities, full characterization for the iodine capture was performed on the IP(BF_4^-) batch, for which good reproducibility of the results was possible. For the small amount extracted out of the H tubes, an entrapment in solution at maximal concentration was performed for a comparison. The kinetic curves were carried out in a solution $3 \cdot 10^{-3}$ M (Figure 77). Both curves for $Ni^{II}(bpy)[Ni^{II}(CN)_4]$ and $Ni^{II}(azpy)[Ni^{II}(CN)_4]$ followed a second order model, with respectively $k = 0.056$ mmol.g^{-1}.min^{-1} and $k = 0.027$ mmol.g^{-1}.min^{-1}. The equilibrium was estimated around 12 hours and it was higher than the time for $Ni^{II}(pz)[Ni^{II}(CN)_4]$ (2 hours), due to the larger pores.

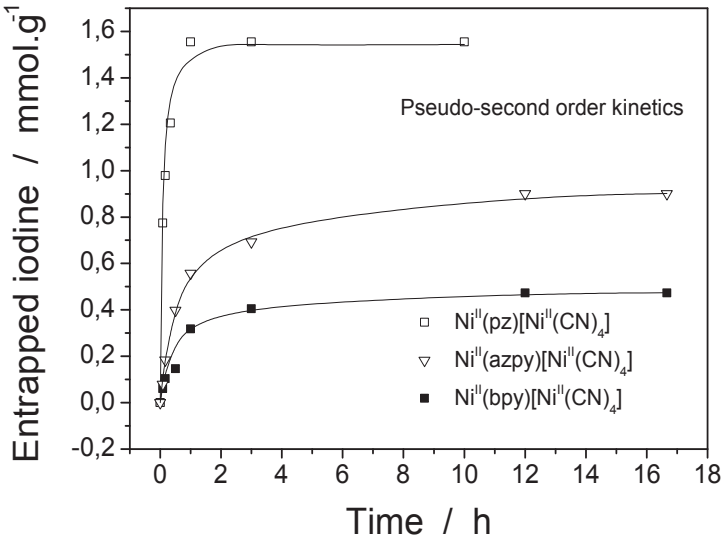

Figure 77 – Kinetic curve for $Ni^{II}(L)[Ni^{II}(CN)_4]$, L = pz, bpy, azpy.

Then the isotherms at room temperature were plotted considering concentrations of iodine in cyclohexane in the range 10^{-4} M - $7 \cdot 10^{-2}$ M. Comparison with $Ni^{II}(pz)[Ni^{II}(CN)_4]$ indicated a dramatic decrease in efficiency for both analogues (Figure 78). Both curves for $Ni^{II}(bpy)[Ni^{II}(CN)_4]$, and $Ni^{II}(azpy)[Ni^{II}(CN)_4]$ were succefully fitted with the Langmuir model, using respectively $K = 3448$ mol.g^{-1} and $K = 2385$ mol.g^{-1}. In the case of $Ni^{II}(bpy)[Ni^{II}(CN)_4]$, a maximal capacity of 0.7 ± 0.1 mmol.g^{-1} was found, that corresponded to 0.25 I_2 per unit cell. Even the entrapment in vapours of iodine at 80 °C gave a very close maximal capacity as the TGA curves show in Figure 79. For $Ni^{II}(azpy)[Ni^{II}(CN)_4]$ it was found a maximal storage capacity of 1.45 ± 0.1 mmol.g^{-1}, corresponding to 0.5 I_2 per unit cell. Again, the amount was confirmed by TGA curve where a loss of iodine by 21% between 150 and 250 °C was observed and the entrapment in vapours on the same IP batch indicated reproducibility of the maximal entrapment (Figure 80).

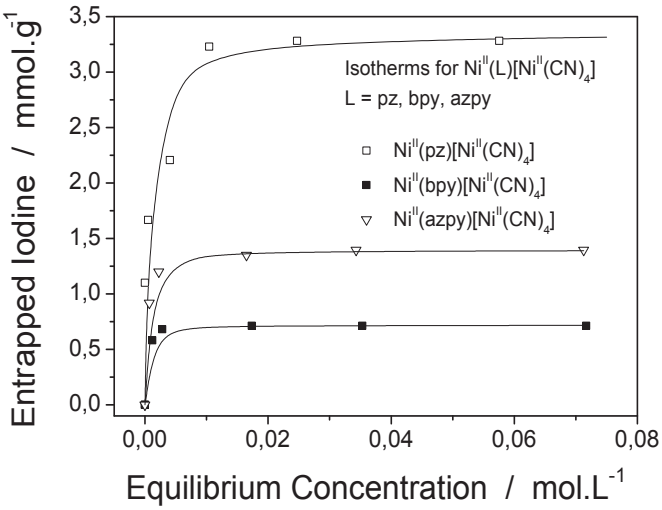

Figure 78 – Isotherm for $Ni^{II}(L)[Ni^{II}(CN)_4]$, L = pz, bpy, azpy.

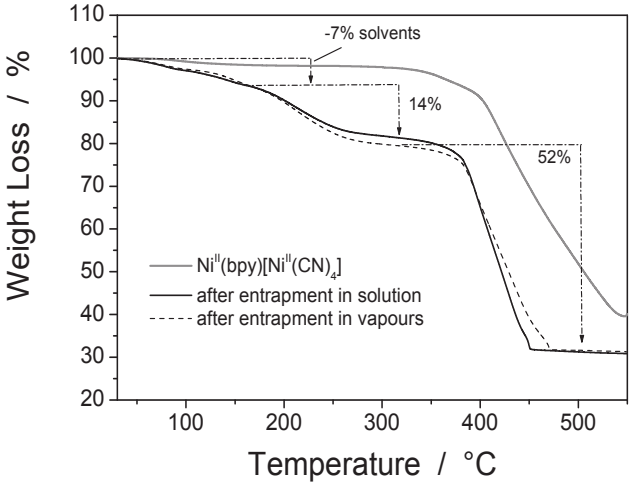

Figure 79 – TGA curves for $Ni^{II}(bpy)[Ni^{II}(CN)_4]$ after entrapment in solution and gaseous phase.

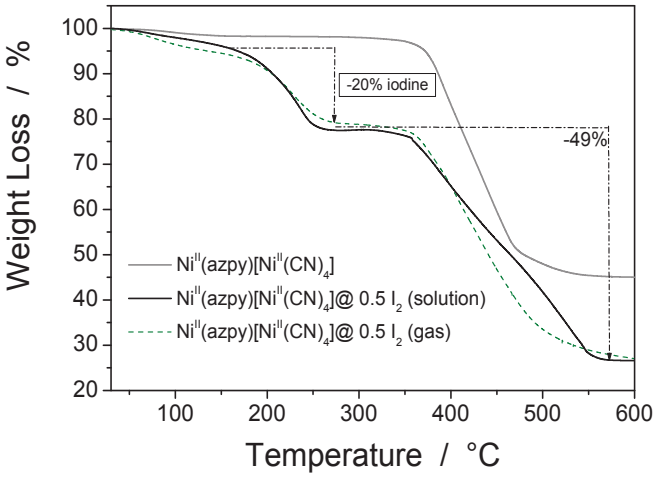

Figure 80 - TGA curves for $Ni^{II}(azpy)[Ni^{II}(CN)_4]$ after entrapment in solution and gaseous phase.

Since the hypothesis that the free space in the host structure could be occupied by other species as free ligand molecules was discarded by the elemental analyses, we could justify the strong decrease in the maximal capacity with the pore size. Also, the capacity did not increased by doubling the aromatic rings, with respect to $Ni^{II}(pz)[Ni^{II}(CN)_4]\bullet I_2$, so that the confined iodine was supposed to be especially in interaction with the cyanonickelates. However, as discussed in the previous sections, the entrapment tests with 2-D structure $Ni^{II}[Ni^{II}(CN)_4]$ did not show any relevant uptake of I_2 in solution. This suggested that the bidentate ligands played a role as well in retaining the iodine, due to formation of the cage. The improvement of capacity by using the azopyridine ligand with respect to the bipyridine ligand can be justified by an interaction between the iodine and the azo-group. The interactions that retained the smaller amount of iodine could eventually be stronger than the confinement inside $Ni^{II}(pz)[Ni^{II}(CN)_4]$. This was suggested by mass spectroscopy performed on both clathrates $Ni^{II}(bpy)[Ni^{II}(CN)_4]\bullet 0.25\ I_2$ and $Ni^{II}(pz)[Ni^{II}(CN)_4]\bullet 0.5\ I_2$. The analysis, shown in Figure 81, indicated that the desorption starts at 175 °C which was slightly higher with respect to the confined iodine in $Ni^{II}(pz)[Ni^{II}(CN)_4]$ (150 °C).

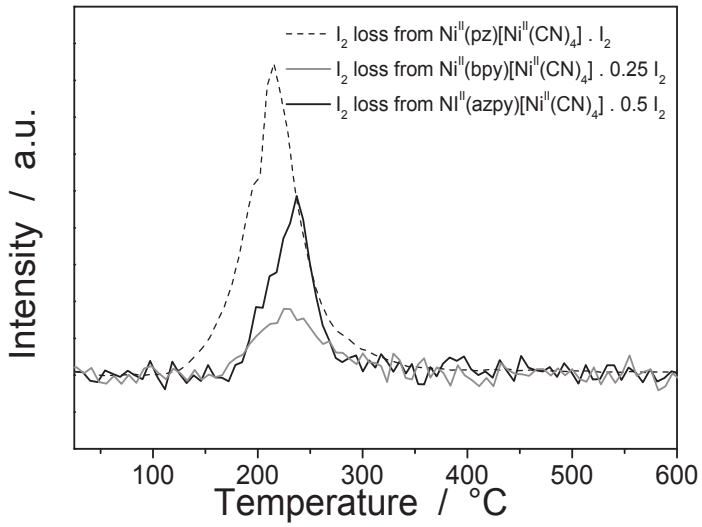

Figure 81 - Mass spectroscopy for $Ni^{II}(L)[Ni^{II}(CN)_4]$, where L = pz, bpy, azpy.

XRPD patterns recorded for $Ni^{II}(bpy)[Ni^{II}(CN)_4]\bullet 0.25\ I_2$ (Figure 82) and $Ni^{II}(azpy)[Ni^{II}(CN)_4]\bullet 0.5\ I_2$ (SC batch, Figure 83) did not point any relevant modification in structures with respect to the unfilled structures. For the bipyridine-containing structure, the only small change concerned the (111) peak that slightly moved after entrapment to lower 2θ values and it was reversibly back after iodine desorption at 200 °C. LeBail refinement and FT-IR spectra after entrapment in solution and gas were identical to the analyses before entrapment, confirming no substantial modification of both structures.

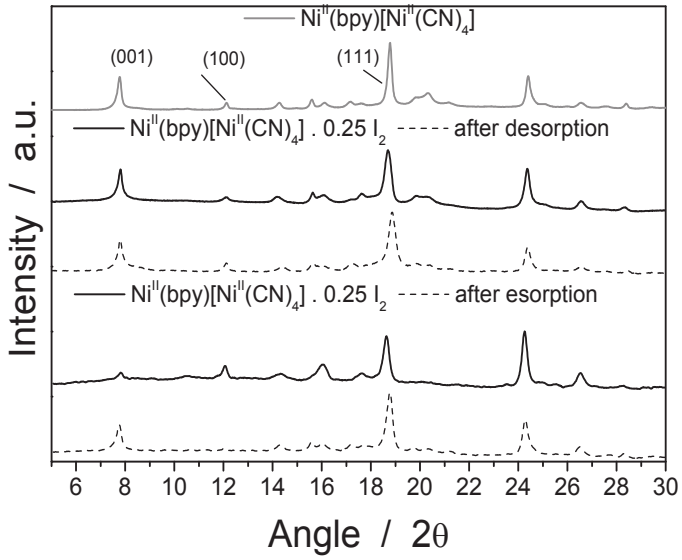

Figure 82 – XRPD for Ni^{II}(bpy)[Ni^{II}(CN)$_4$] after entrapment in solution and gaseous phase and related desorbed structures.

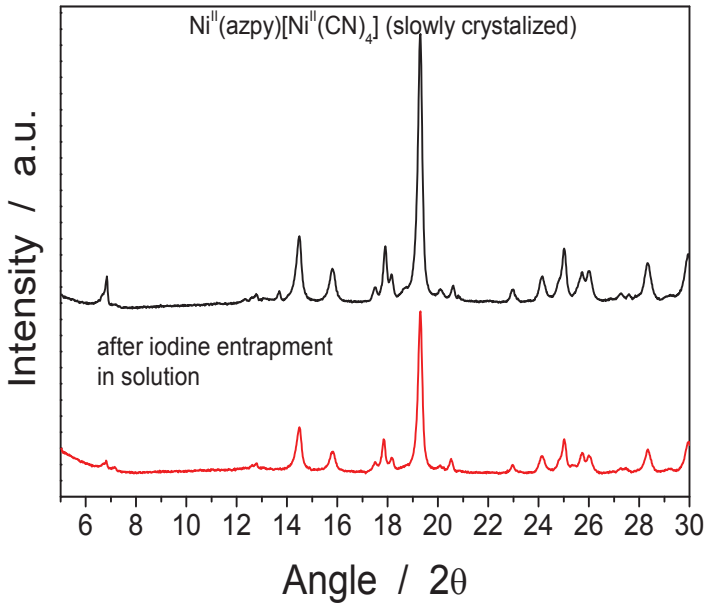

Figure 83 – XRPD for slowly crystalized (SC) Ni^{II}(azpy)[Ni^{II}(CN)$_4$] batch before and after I$_2$ entrapment.

The materials after entrapment were analyzed then by reflectance UV-VIS and Raman spectroscopy. The confined iodine in Ni^{II}(bpy)[Ni^{II}(CN)$_4$]•0.25 I$_2$ gave a large absorption band with a maximum around 420 nm (Figure 84). An easy interpretation was not possible for this value, since molecular iodine typically absorbs at higher wavelength and triiodides always absorb under 400 nm, as discussed in the previous section. In the case of Ni^{II}(azpy)[Ni^{II}(CN)$_4$]•0.5 I$_2$ (IP batch), for both capture in solution and in vapours iodine absorbed in a large range with maximum around 435 nm, higher than the maximum for Ni^{II}(bpy)[Ni^{II}(CN)$_4$]•0.25 I$_2$ (Figure 85). We could assume the shift to higher values with respect to Ni^{II}(bpy)[Ni^{II}(CN)$_4$] was due to charge transfer with the

azo (N=N) groups of the bidentate ligand. Azo-groups are responsible for the reflected orange colour of the unfilled structure and they absorb around 450 nm. This iodine-azo interaction was assumed but no experimental evidence was possible. Interactions with tetracyanonickelates anyway were not excluded and cooperation of both moieties should be responsible for the confinement. Also, UV band in the polyiodides region suggests that I_3^- species were formed as well, most probably on the terminal cyanides. Since XRPD and FT-IR spectra for this series of analogues did not significantly change after I_2 uptake, a UV-VIS spectrum of the desorbed structure at 200 °C was carried out (Figure 84 and Figure 85, dotted curve). The large band of iodine disappeared, with just some visible traces around 400 nm and below, due to the chemisorbed polyiodides. Further, in support to UV-VIS spectra, Raman spectra showed a similar situation for both $Ni^{II}(bpy)[Ni^{II}(CN)_4]$•0.25 I_2 (Figure 86) and $Ni^{II}(azpy)[Ni^{II}(CN)_4]$•0.5 I_2 (Figure 87): a large band for the ν(I-I) mode of the confined I_2 with a maximum at 165 cm^{-1} and a shoulder around 175 cm^{-1} and the symmetry ν(I-I) mode for I_3^- at 108 cm^{-1}. We can eventually associate the value 175 cm^{-1} to the iodine confined by the cage effect since the cage was larger than the pyrazine-containing structures, whearas the main band at 165 cm^{-1} is related to charge transfers of different nature, as the specific bidentate ligands.

In conclusion, the change of the bidentate ligand indicated through a different way that the size of the cage was an important parameter to efficiently confine iodine. The host structures that were built with the pyrazine ligand showed a more suitable pore size to stabilize a large amount of iodine inside the cages. Firstly, the kinetic studies showed that the sorption process was faster for the small cages of $Ni^{II}(pz)[Ni^{II}(CN)_4]$ (2 hours), whereas it took 12 hours for the adsorption by $Ni^{II}(bpy)[Ni^{II}(CN)_4]$ and $Ni^{II}(azpy)[Ni^{II}(CN)_4]$ to reach equilibrium. The effect of the cage, however, was visible since a certain amount of iodine was retained. However, the stronger retention in temperature indicated an further contribution given by the interaction with the bidentate ligands and the tetracyanonickelates. For instance, the higher capacity of the clathrate $Ni^{II}(azpy)[Ni^{II}(CN)_4]$•0.5 I_2 with respect to $Ni^{II}(bpy)[Ni^{II}(CN)_4]$•0.25 I_2, had to be related to the type of employed organic ligand.

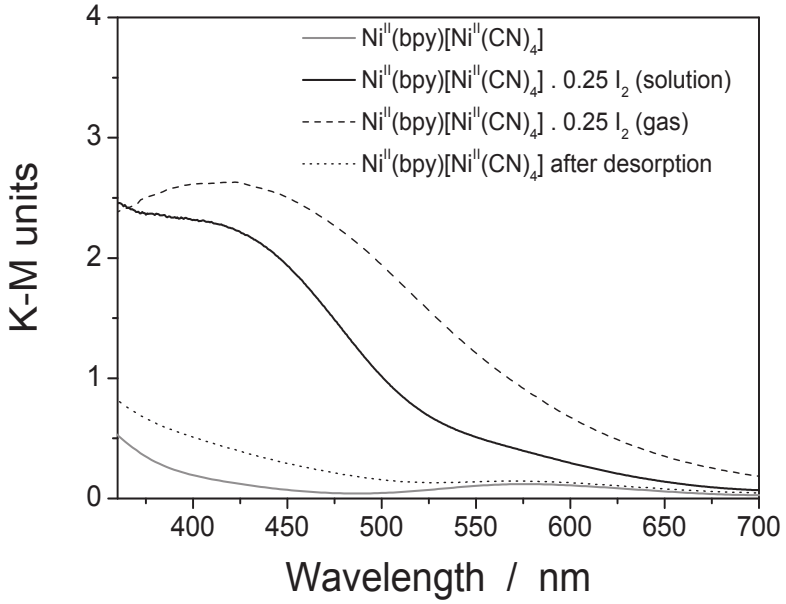

Figure 84 – reflectance mode UV-VIS spectra for $Ni^{II}(bpy)[Ni^{II}(CN)_4]$ after entrapment in solution and gaseous phase and the desorbed structure.

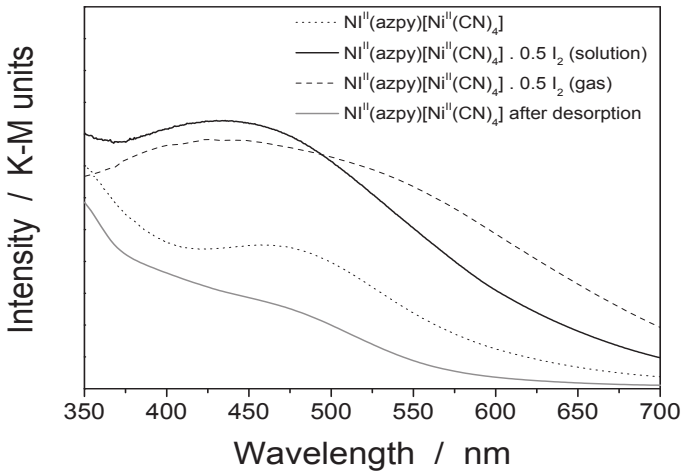

Figure 85 – reflectance mode UV-VIS spectra for $Ni^{II}(azpy)[Ni^{II}(CN)_4]$, before and after entrapments and after desorption.

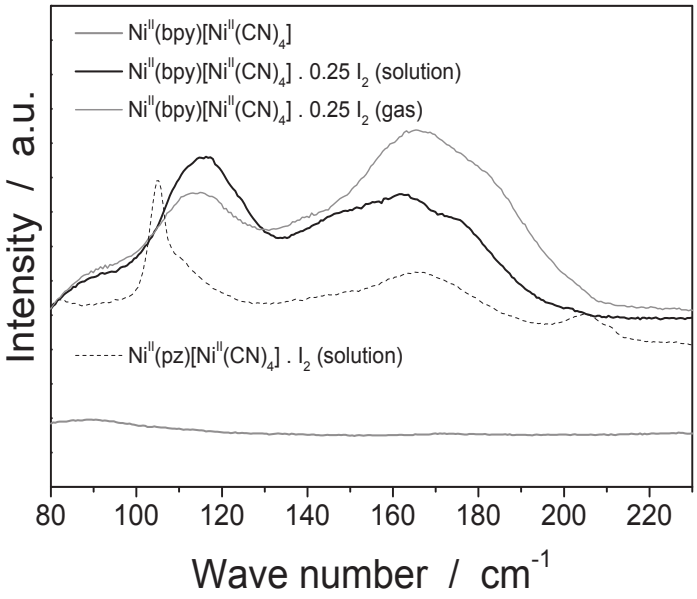

Figure 86 – Raman spectra for Ni^{II}(bpy)[Ni^{II}(CN)$_4$] after entrapment in solution and gaseous phase.

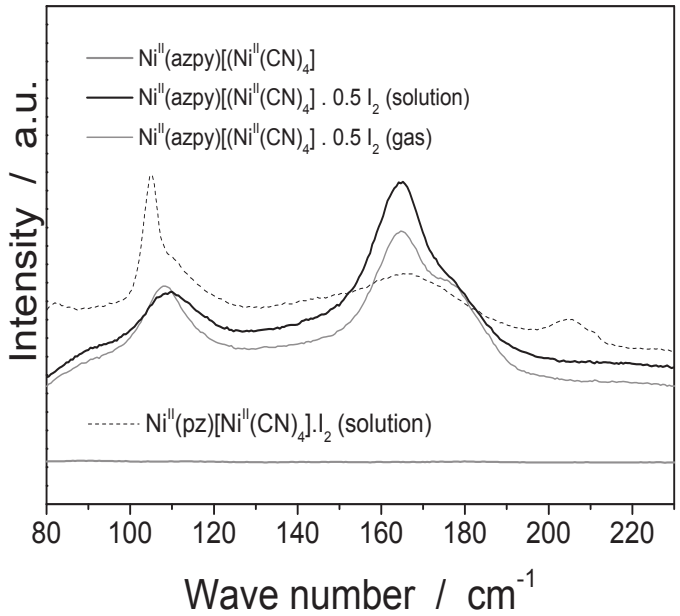

Figure 87 – Raman spectra for Ni^{II}(azpy)[Ni^{II}(CN)$_4$], before and after entrapments.

1.2 – Supplementary studies

The second part of Chapter 1 includes three distinct works, of different nature, related to the adsorption of iodine by the bulk Hofmann-type structures. These works are mainly the results of the collaborations that contributed to the present thesis project. Even though some technical details will be reported as well, the following sections are mainly intended to discuss the meaning of the results of the presented data, with respect to the previously reported experimental work. Section 1.2.1 is dedicated to the selective capture of iodine in presence of water steam by the Hofmann-type structures that exhibited the highest capacity and it includes a collaboration with Prof. Barbara Onida of the Technical University of Turin. Section 1.2.2 will focus on the Grand Canonical Monte-Carlo simulations, performed in the collaboration with Prof. Guillaume Maurin of the Institut Charles Gerhardt of Montpellier (team DAMP). Section 1.2.3 will be about the measurements of Dielectric Relaxation Spectorscopy (DRS) and Complex Impedence Spectroscopy (CIS) carried out on the solid saples by Dr. Sabine Devautour-Vinot of the Institut Charles Gerhardt of Montpellier (team DAMP).

1.2.1 – Selective entrapment of iodine in water vapours by the Hofmann-type structures.

In the operative conditions, molecular iodine is released in water vapours that contain NO_x and traces of other halogens. Water is the most abundant species in the out-gases and it is important to entrap selectively the iodine against this molecule. The captures performed in vapours of iodine already indicated that the maximal capacity was easily reached for $Ni^{II}(pz)[Pd^{II}(CN)_4]$ and $Co^{II}(pz)[Ni^{II}(CN)_4]$ (one I_2 per unit cell). For $Ni^{II}(pz)[Ni^{II}(CN)_4]$, by contrast, the tests of entrapment in vapours only reached a capacity around $Ni^{II}(pz)[Ni^{II}(CN)_4]$•0.7-0.8 I_2. It was assumed that other molecules in air, as water steam, could be physisorbed affecting the maximal capacity. A new series of entrapments was performed for the host structures $Ni^{II}(pz)[Ni^{II}(CN)_4]$, $Ni^{II}(pz)[Pd^{II}(CN)_4]$ and $Co^{II}(pz)[Ni^{II}(CN)_4]$. In hermetical containers, 100 mg of a dehydrated Hofmann-type structure and 800 mg of iodine were placed in separated open flasks and 10 ml of distilled water were added in the containers. The operating temperature was 80 °C and the tests were stopped after one week. A representation of the geometry of the system is reported in the *Experimental Section.* Then the clathrates were dried in air and TGA curves, FT-IR and Raman spectra were registered. TGA curves after the entrapments in vapours of I_2 only and in vapours of I_2 / H_2O for $Ni^{II}(pz)[Ni^{II}(CN)_4$, $Ni^{II}(pz)[Pd^{II}(CN)_4]$ and $Co^{II}(pz)[Ni^{II}(CN)_4]$ are reported prespectively in Figure 88, in Figure 89 and in Figure 90.

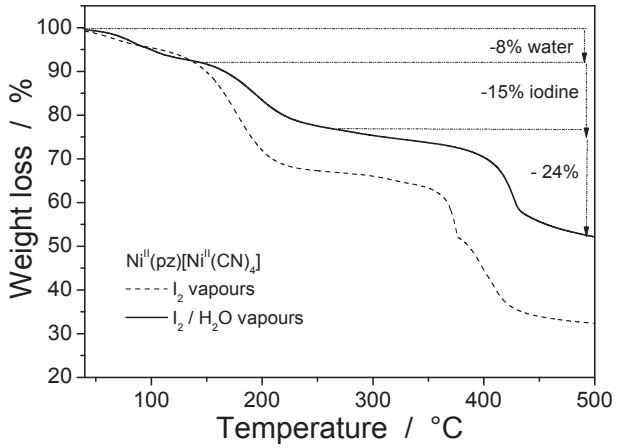

Figure 88 - TGA for the selectivity test with $Ni^{II}(pz)[Ni^{II}(CN)_4]$.

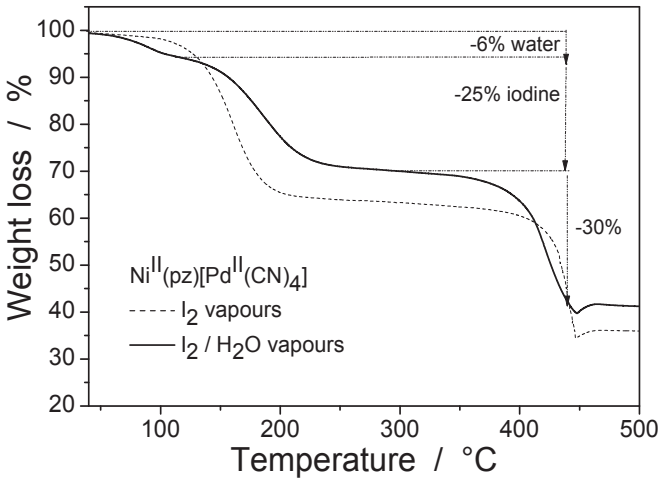

Figure 89 - TGA for the selectivity test with $Ni^{II}(pz)[Pd^{II}(CN)_4]$.

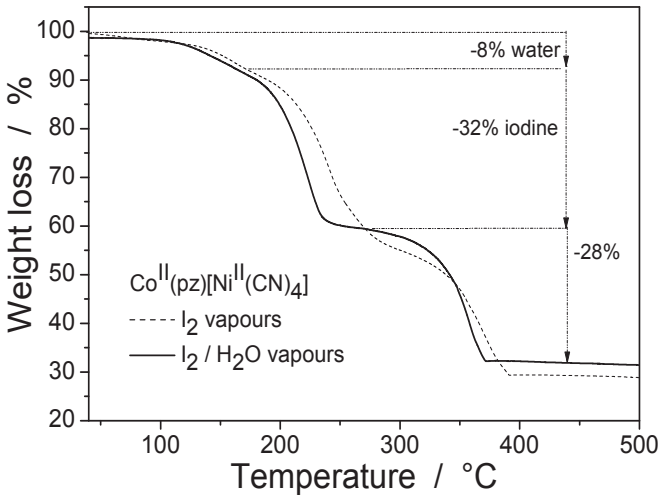

Figure 90 - TGA for the selectivity test with $Co^{II}(pz)[Ni^{II}(CN)_4]$.

Direct observations of TGA curves already suggested that the iodine entrapment with $Co^{II}(pz)[Ni^{II}(CN)_4]$ was not largely affected by the presence of water vapours, whereas for the other two structures a more significant reduction of the maximal capacity was clearly visible. The mechanism of entrapment in these conditions was slowed down by the fact that water initially condensed in the flask of the (still cold) powder and iodine had to diffuse through the water. However, the low solubility of iodine at room temperature became much higher at 80 °C and this allowed iodine to reach the host structure. After the capture, no liquid water was found in the flask of the powder, probably because, when the powder reached the temperature 80 °C, water preferentially condensed on the container walls. The residual water inside the container after the capture was dark brown indicating that a significant amount of iodine dissolved in the water as well. The entrapped amounts in these conditions with the three selected materials, were quantified by TGA (for the method, see *Annexes*). The entrapped amount was expressed as I_2 molecules per unit cell of host structure. A comparison with the entrapment in solution and in vapours without excess of water is reported in Table 11.

Table 11 - I_2 equivalents per unit cell after different conditions of entrapment.

Host structure	C_6H_{12} solution	I_2 vapours	I_2/H_2O vapours
$Ni^{II}(pz)[Ni^{II}(CN)_4]$	1 I_2	0.7-0.8 I_2	0.5 I_2
$Ni^{II}(pz)[Pd^{II}(CN)_4]$	1 I_2	1 I_2	0.6 I_2
$Co^{II}(pz)[Ni^{II}(CN)_4]$	1 I_2	1 I_2	0.8 I_2

In the case of $Ni^{II}(pz)[Ni^{II}(CN)_4]$, the detrimental effect of water was more important. According to the entrapment tests performed in I_2 vapours without excess of water already indicated a difficulty for $Ni^{II}(pz)[Ni^{II}(CN)_4]$ to reach the highest capacity during the entrapment in gaseous phase. The capacity of the structure $Ni^{II}(pz)[Pd^{II}(CN)_4]$ was also affected by the presence of water, decreasing by 40%. On the other side, $Co^{II}(pz)[Ni^{II}(CN)_4]$ still showed a good capacity even though a decrease by 20% was observed.

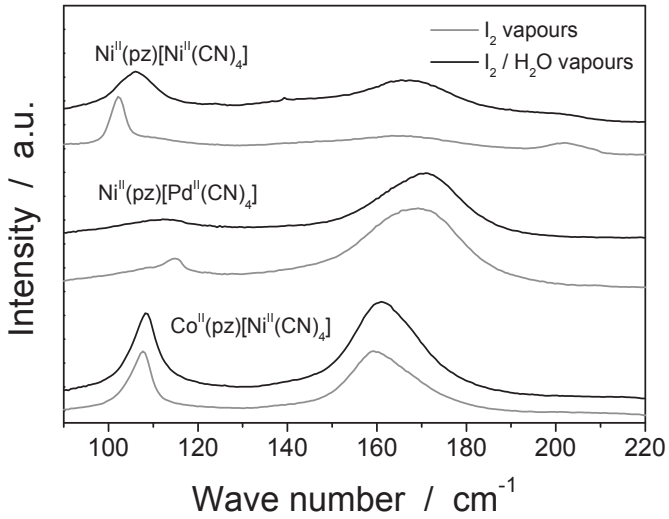

Figure 91 - Raman spectra for the clathrates prepared in gaseous phase, with and without water steam.

The nature of the confined iodine was checked by Raman spectroscopy. The spectra for the capture in I_2/H_2O vapours were comparable to the spectra for the capture in I_2 vapours, proving that the presence of water did not change the nature of the confined iodine (Figure 91).

The reason why the selectivity of $Co^{II}(pz)[Ni^{II}(CN)_4]$ was higher than the analogue structures must be related to the different affinity to water or *hydrophilicity* of the structures. A good technique that allows an evaluation of the interaction with water is the *in-situ* FT-IR spectroscopy. The analyses were carried out in the laboratories of the Technical University of Turin, inside the collaboration with Prof. Barbara Onida. The measurements were performed on the dehydrated structures $M'(pz)[Ni^{II}(CN)_4]$, where cation M' was Ni^{II} or Co^{II}, in order to evaluate how the change of the cation M' could affect the affinity to water. To perform the adsorptions of water, we prepared the samples as thin tablets without diluting the products in any matrix. The tablets had to be fine enough to allow the recording of a transmission spectrum. We dehydrated the samples at 200 °C under primary vacuum inside a specific vacuum tube for FT-IR analyses. This tube consisted of a stopcock valve on one side, to branch to the vacuum line, and of an IR cell in KBr for the measurements on the other side. Then we recorded the spectra of the desorbed samples in the interval 3800-1500 cm^{-1} to check that no residual water remained after the thermal treatment. Subsequently, we closed the vacuum line and we sent through a different branch a small quantity of distilled water by controlling the pressure with an electronic barometer. When the pressure reached equilibrium after the adsorption of a small water quantity on the sample, a spectrum was registered and we performed the following adsorption. This process was repeated up to an equilibrium pressure close to 18 mbar (saturation). Then, the pressure was gradually decreased by opening larger sections of the line. Finally the water was desorbed from the sample under primary vacuum for 1 hour, at room temperature. Spectra during the desorption process were registered as well. For a correct interpretation of the FT-IR spectra, a short remind of the FT-IR active band for the free H_2O and interacting H_2O is necessary. Since the shifts in IR-active bands for H_2O are related to the strength of the interaction with the Lewis acid (or base), this type of spectroscopic studies were largely exploited to investigate the surfaces of metal oxides and nanoporous aluminosilicates as zeolites. [129] [130] [131] The stretching mode ν(O-H) of free water is typically detected in higher region 3800-3700 cm^{-1} as a narrow band, but when water forms H-bonds with other oxygens of other H_2O molecules, typically another larger band appears due to Fermi resonance and it is located around 3400 cm^{-1} for the liquid state and around 3200 cm^{-1} for the tetrahedrically coordinated water.[132] The bending mode δ(O-H) of water is typically situated around 1600 cm^{-1}, with asymmetric shape, and it increases upon stronger H-bonding (for instance, 1630 cm^{-1} in liquid water). A decrease of δ(O-H) to 1580-1590 cm^{-1} can occur as well, for the coordinated water on a Lewis acid (*i.e.* metallic cations) where H_2O interacts through the lone pairs of the oxygens.[131]

The spectra for the H_2O adsorption on $Ni^{II}(pz)[Ni^{II}(CN)_4]$ and $Co^{II}(pz)[Ni^{II}(CN)_4]$ are reported in Figure 92 (stretching region) and Figure 93 (bending region). Concerning the stretching region (Figure 92), we distinguished three bands gradually appearing at increasing H_2O pressures. At

low pressures, the narrow band for the free O-H appeared alone at 3650 cm^{-1} (labelled with one star *), due to water vapours in the IR cell. Upon following water adsorptions, the large band for interacting O-H was visible around 3400 cm^{-1} (labelled with two stars **), indicating probable condensation of liquid water on the sample. The interaction of O-H bonds could be with other electron donor species as well, like terminal CN^- or aromatic rings of pyrazine. The resulting large bands on both samples may be the results of different contributions. The maximum of these large bands showed slightly different values on the two samples, *i.e.* 3376 cm^{-1} for $Co^{II}(pz)[Ni^{II}(CN)_4]$ and 3398 cm^{-1} for $Ni^{II}(pz)[Ni^{II}(CN)_4]$, but no clear explanation for this was found due to the large variety of possible interactions (CN^-, H_2O or pyrazine). At higher pressures, when large water condensation occurred on the samples, a shoulder at 3200 cm^{-1} finally appeared in both spectra due to H-bond between the H of one water molecule with the O atom of another. On desorption, however, all three stretching bands for O-H disappeared on both samples.

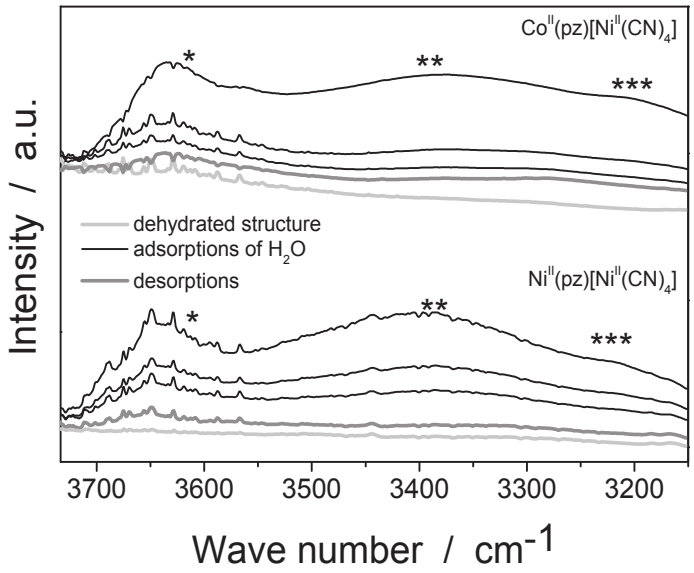

Figure 92 - Adsorptions of water on Hofmann-type structures (stretching region).

Interesting information also came from the region of the bending (Figure 93). On both samples the first layer of adsorbed water showed a bending mode at 1598 cm^{-1} for $Ni^{II}(pz)[Ni^{II}(CN)_4]$ and at 1601 cm^{-1} for $Co^{II}(pz)[Ni^{II}(CN)_4]$. These low values suggested that the first adsorbed water was coordinated on Lewis acid sites as Ni^{2+} and Co^{2+}. We could situate these sites on the surface of the samples where it was more probable to find metallic centres with non-saturated coordination sites. At higher pressures of water, the bending underwent a blue-shift to 1612 cm^{-1} for $Co^{II}(pz)[Ni^{II}(CN)_4]$ and to 1620 cm^{-1} for $Ni^{II}(pz)[Ni^{II}(CN)_4]$. These values were still low for the typical bending mode of condensed water (1630 cm^{-1}) so that they suggested the formation of water clusters inside or outside the Hofmann-type structures. We could state that generally the value of δ(O-H) for the clusters is related to their dimensions: the bigger the cluster, the higher the δ(O-H) mode. For instance, measurements of the δ(O-H) mode for clusters $(H_2O)_n$ in gaseous phase reported in literature[133] indicated the following values: 1595 cm^{-1} for n = 1; 1600 cm^{-1} for n = 2;

1610 cm^{-1} for n = 3; 1630 cm^{-1} for n = 4. Bending modes at high pressures on both Hofmann-type structures were very large with a more symmetric shape for $Ni^{II}(pz)[Ni^{II}(CN)_4]$, so that clusters of different size had to be present on both samples. However, the higher δ(O-H) mode on $Ni^{II}(pz)[Ni^{II}(CN)_4]$ suggested a larger amount of bigger clusters. On desorption at room temperature a relevant difference between the two samples was detected. Gradual decrease of water pressure immediately desorbed all the water off the $Co^{II}(pz)[Ni^{II}(CN)_4]$ sample and after one hour under primary vacuum no δ(O-H) mode was not visible anymore. By contrast, after one hour of primary vacuum on $Ni^{II}(pz)[Ni^{II}(CN)_4]$, the δ(O-H) mode for water clusters disappeared but the band at 1598 cm^{-1} related to the coordinated water on Lewis acid sites Ni^{2+} was still visible.

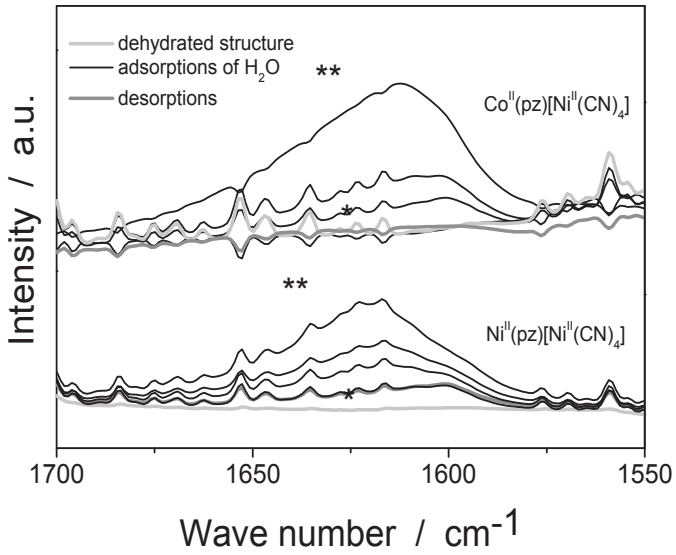

Figure 93 - Adsorptions of water on Hofmann'type structures (bending region).

Data indicated the formation of more stable complexes with water on the surface of $Ni^{II}(pz)[Ni^{II}(CN)_4]$. On the other side, the complexes formed on the surface of $Co^{II}(pz)[Ni^{II}(CN)_4]$ were easily destabilized and destroyed by reducing the pressure at room temperature. These data correlated with some experimental observations about the rehydration process of the two materials. As reported in the previous sections, when the dehydrated $Ni^{II}(pz)[Ni^{II}(CN)_4]$ (grey powder) was exposed to air, it rapidly adsorbed water molecules on the surface, exhibiting again the violet colour of the hydrated structure. By contrast, the dehydrated $Co^{II}(pz)[Ni^{II}(CN)_4]$ (blue powder) recovered very slowly the pink colouration of the hydrated structure. We could expect that the rehydration may be partially due to the sorption inside the cages as well. However, the dehydrated 2-D structures $Ni^{II}[Ni^{II}(CN)_4]$ (brown powder) and $Co^{II}[Ni^{II}(CN)_4]$ (blue powder) were as well exposed to air, and only the $Ni^{II}[Ni^{II}(CN)_4]$ recovered the green colour of the related hydrated structure $Ni^{II}(H_2O)_2[Ni^{II}(CN)_4]\bullet xH_2O$, indicating clearly a higher affinity to water for the Ni^{2+} cation.
This higher affinity on Ni^{2+} sites was then correlated with the higher decrease in capacity during the entrapment of I_2 in water vapours. In the case of $Ni^{II}(pz)[Ni^{II}(CN)_4]$, the effect was the highest since Ni^{2+} is in both octahedral and square planar position. Square planar Ni^{II} seemed anyway to

have a minor role in decreasing the capacity, since $Co^{II}(pz)[Ni^{II}(CN)_4]$ maintained a higher capacity with respect $Ni^{II}(pz)[Pd^{II}(CN)_4]$ as discussed previously. We can finally formulate the hypothesis that when unsaturated Ni^{2+} cations were present on the grain surface, stable water complexes formed rapidly and the diffusion of I_2 was partially hindered by water since the molecular I_2 and H_2O have opposite polarities. Hence, the structure $Co^{II}(pz)[Ni^{II}(CN)_4]$ exhibited a better selectivity due to formation of less stable complexes with water.

1.2.2 – Grand Canonical Monte-Carlo modelling of the entrapment of iodine with Hofmann-type structures.

In support of the experimental characterisations, a computational approach based on an energy minimization procedure was used to determine a plausible crystal structure of the fully loaded $Ni^{II}(pz)[Ni^{II}(CN)_4]\bullet I_2$ and analogue structures $M'(pz)[M''(CN)_4]\bullet I_2$ with M' = Ni^{II} or Co^{II}, pz =pyrazine, M'' = Ni^{II}, Pd^{II} and Pt^{II}. The calculations were carried out by Prof. Guillaume Maurin of the Institut Charles Gerhardt of Montpellier (team DAMP). The structure of the network $Ni^{II}(pz)[Ni^{II}(CN)_4]$ in its unfilled state was constructed from the crystal structure of $Fe^{II}(pz)[Ni^{II}(CN)_4]$, previously reported by Southon *et al.*,[80] by initially substituting Fe by Ni atom and imposing the unit cell parameters obtained by LeBail refinement of the XRPD pattern ($a = b =$ 7.2605(6) Å, $c =$ 7.0072(5) Å, $\alpha = \beta = \gamma$ = 90.0°). This structure model was energy minimized with the classical Universal Force Field (UFF)[134] to describe the van der Waals parameters and the charge equilibration qEq method[135] was employed to calculate the partial charges. The Ewald summation was employed to evaluate the electrostatic interactions in the long range, while the van der Waals interactions beyond 14 Å were neglected. The Van der Waals interactions were represented by the classical 12-6 Lennard-Jones potential reported in Equation 9:

Equation 9 - Equation for the repulsion-dispersion 12-6 Lennard-Jones (LJ) potential.

$$V(r) = 4\varepsilon\left[\left(\frac{\sigma}{r}\right)^{12} - \left(\frac{\sigma}{r}\right)^{6}\right]$$

Where ε is the depth of the potential well; σ is the distance for $V = 0$ and r is the distance between two atoms. The resulting structure was then geometry-optimized at the Density Functional Theory level to provide finally a plausible crystal structure. For the fully iodine-loaded material, we started from the so-built empty structure and the computational assisted structure determination approach described above was further performed by maintaining fixed the experimental unit cell parameters in order to propose a plausible structure model. The absolute iodine adsorption isotherm for the so-built loaded structure was computed up to 1 bar at 25°C by means of Grand Canonical Monte Carlo (GCMC) simulations. The iodine molecule was represented by a diatomic uncharged model (I-I bond remaining fixed at 2.66 Å), while the atoms of the framework were described by the UFF force field. The iodine-framework interactions consisted only of a repulsion-dispersion 12-6 Lennard Jones (LJ) term. The corresponding LJ parameters were calculated using the mixing Lorentz-Berthelot combination rules. A simulation box of 64 ($4 \times 4 \times 4$) rigid unit

cells with typically 2 × 108 Monte Carlo steps were considered in these calculations. In addition to the adsorption isotherm reported in Figure 94, the adsorption enthalpy was also calculated in the whole range of loading using the revised Widom's test particle method.[136] It was calculated a value of 48.1 kJ/mol at low coverage and a gradual increase with the loading from 48.1 to 53.9 kJ/mol. The shape of the simulated isotherm corresponded with the *type I* profile (adsorption of a monolayer), observed experimentally as well.

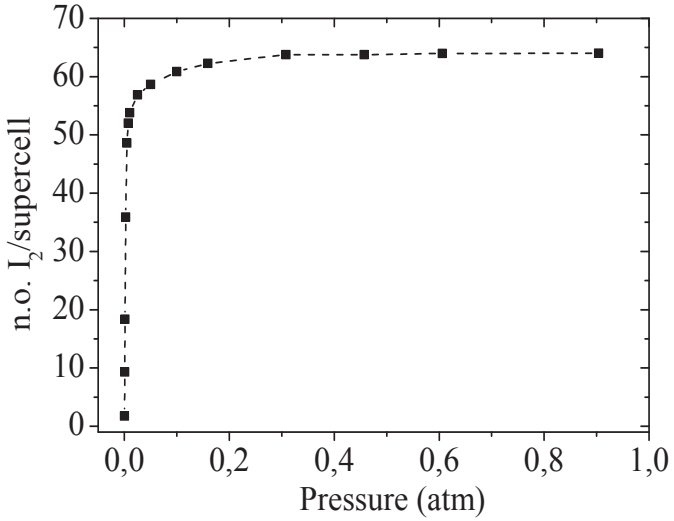

Figure 94 – I_2 adsorption isotherm for $Ni^{II}(pz)[Ni^{II}(CN)_4]$ calculated with Grand Canonical Monte Carlo simulation

The calculations revealed that the optimal maximal uptake was 1 mole of I_2 by unit cell, confirming the experimentally achieved saturation capacity of the material in solution. Also, the steep increase at low temperature indicated a high affinity with the host structure. The analysis of the preferential arrangements of iodine issued from these simulations evidenced that the iodine molecules: (*i*) interacted with both the Ni^{2+} ion of the $[Ni(CN)_4]^{2-}$ moiety (distances ranging from 3.32 to 3.71 Å) and the pyrazine (3.52-3.74 Å) already from low loadings, in agreement with the experimental observation reported in Section 1.1.1, and (*ii*) tended to orientate along the direction of the tunnel with distances separating each other over 4 Å. In Figure 95(a-d), screen shots for the different loadings are reported to show the arrangement of the guest molecules inside the lattice: a) low loading; b) and c) intermediate loading and d) saturation. Also, Grand Canonical Monte-Carlo (GCMC) simulations were carried out for the adsorption of I_2 inside the networks $Ni^{II}(pz)[Pd^{II}(CN)_4]$ and $Co^{II}(pz)[Ni^{II}(CN)_4]$ in order to observe the impact of the nature of the metal. The simulated isotherms matched with the experimental isotherms concerning the maximal capacities *i.e.* $Co^{II}(pz)[Ni^{II}(CN)_4]\bullet I_2$ and $Ni^{II}(pz)[Pd^{II}(CN)_4]\ \bullet I_2$. However they showed similar adsorption enthalpies at low coverage (Figure 96) and isotherm slopes (Figure 96, inset). Hence, by considering exclusively the Van der Waals contributions no impact of the nature of the metal on the strength of the host/guest interactions and on the adsorption mechanism was detected. Experimental data however indicated that a slightly different affinity in the order $Ni^{II}(pz)[Pd^{II}(CN)_4]$

< $Ni^{II}(pz)[Ni^{II}(CN)_4]$ < $(Co^{II}(pz)[Ni^{II}(CN)_4]$ occurred, due to electronic effects that the GCMC modeling did not take into account. For a better insight, further DFT simulations will be demanded in the future to confirm (or discard) the proposed hypotheses about the charge transfers iodine-host structure.

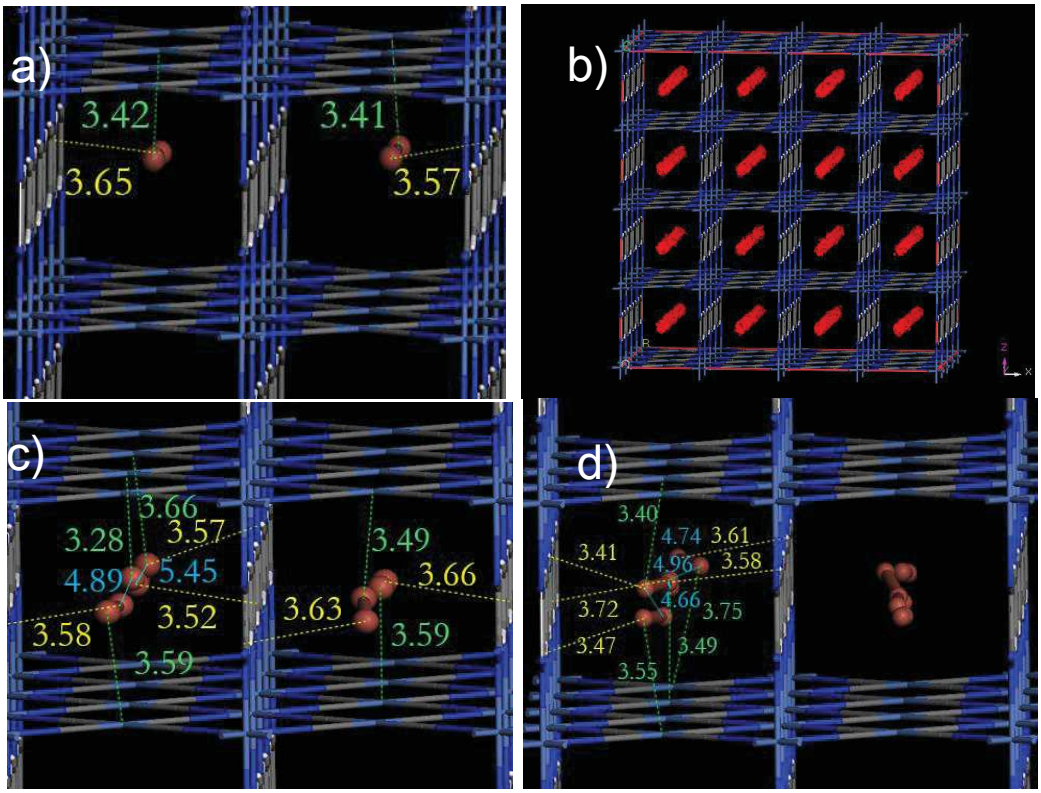

Figure 95 - Screenshots for different loading of iodine in the $Ni^{II}(pz)[Ni^{II}(CN)_4]$: a) low loading; b) and c) intermediated loading; d) saturation.

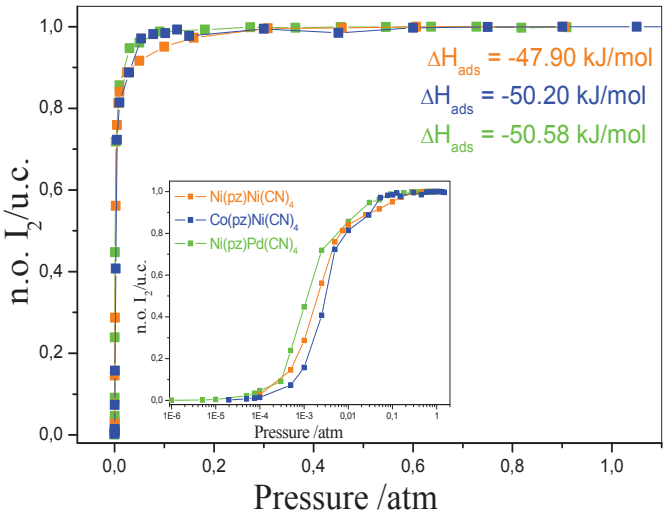

Figure 96 - GCMC simulation of I_2 adsorption on Hofmann-type analogues.

1.2.3 - Electrical properties of the Hofmann-type structures.

The electrical properties for the iodine-loaded materials were investigated inside the collaboration with Dr. Sabine Devatour-Vinot of the Institut Charles Gerhardt of Montpeller (team DAMP) who carried out the measurements on the samples. The ionic conductivity properties of the samples were studied by recording the global conductivity, $\sigma_{ac}(f, T)$ at fixed temperature as a function of the frequency f of the applied electric field. For many common non-metallic materials, the alternate current (*ac*) conductivity $\sigma_{ac}(f)$ measured at fixed temperature is usually expressed as:

Equation 10 - Alternate current conductivity

$$\sigma_{ac}(f) = \sigma_{dc} + \sigma'(f)$$

which results from the combination of the steady state or direct current (*dc*) conductivity σ_{dc} and the purely dispersive component or polarization conductivity $\sigma'(f)$. Basically, the *dc* conductivity corresponds to long-range redistribution of charges, *i.e.* ionic or electronic transport, while the polarization contribution arises from local rearrangement of charges or dipoles causing dipolar reorientation or dielectric relaxation and thus resulting in the intrinsic bulk polarization. Noteworthy, in insulators, $\sigma_{dc} \approx 0$, and so that only the polarization conductivity is detectable. Measurements of Complex Impedence Spectroscopy (CIS) indicated that the void structure $Ni^{II}(pz)[Ni^{II}(CN)_4]$ turned out to be an insulator, since the component σ_{cd} was absent and σ_{ac} was low. The evolution of the conductivity for the progressive adsorption of iodine at different loadings is reported in Figure 95 (left). At very low content of iodine, conductivity remained low since there was no propagation of charges. As comparison, for very low iodine loadings (0.01-0.02 I_2 per unit cell) the UV-VIS spectra recorded in solid state showed especially the absorption bands of the triiodides (formed very probably on the terminal cyanides), that were probably isolated and strongly chemisorbed and they could not propagate the charge. An increase in conductivity was detected for higher iodine loadings, up to 5 magnitude orders higher than the empty structure. The increase was justified by the presence of ionic species as triiodides, but also for the aligned arrangement of the iodine molecules in the network tunnels, calculated by the GCMG simulations, that allowed the creation of conductive paths for the charge propagation. The CIS measurements were performed as well on the structures $Co^{II}(pz)[Ni^{II}(CN)_4]$, $Ni^{II}(pz)[Pd^{II}(CN)_4]$ and $Ni^{II}(pz)[Pt^{II}(CN)_4]$ at high iodine loadings, to investigate the changes in the electric behaviour by modulation of the metallic centres (Figure 95, right). All empty structures were initially insulators as the analogue $Ni^{II}(pz)[Ni^{II}(CN)_4]$. After insertion of iodine, $Co^{II}(pz)[Ni^{II}(CN)_4]$ and $Ni^{II}(pz)[Pd^{II}(CN)_4]$ showed an increase in conductivity by five order of magnitude, indicating the same electric behaviour and a similar host/guest and guest/guest interactions with respect to $Ni^{II}(pz)[Ni^{II}(CN)_4]$. Both GCMC simulations and experimental adsorption isotherms, kinetic studies, TGA and Raman measurements supported the similarity of the confinement of

iodine inside the structures $Ni^{II}(pz)[Ni^{II}(CN)_4]$, $Ni^{II}(pz)[Pd^{II}(CN)_4]$ and $Co^{II}(pz)[Ni^{II}(CN)_4]$. A different case was represented by $Ni^{II}(pz)[Pt^{II}(CN)_4]$, since the iodine-loaded structure did not significantly increase the conductivity with respect to the empty structure. This was indeed a consequence of the reduction of I_2 to iodide I^- and the oxidative addition of the I^- ligand on Pt^{IV} occurred. Since the charged species were strongly blocked on the Pt^{IV} sites, no high charge propagation was possible in the complex $Ni^{II}(pz)[Pt^{II}(CN)_4]\bullet I^-$.

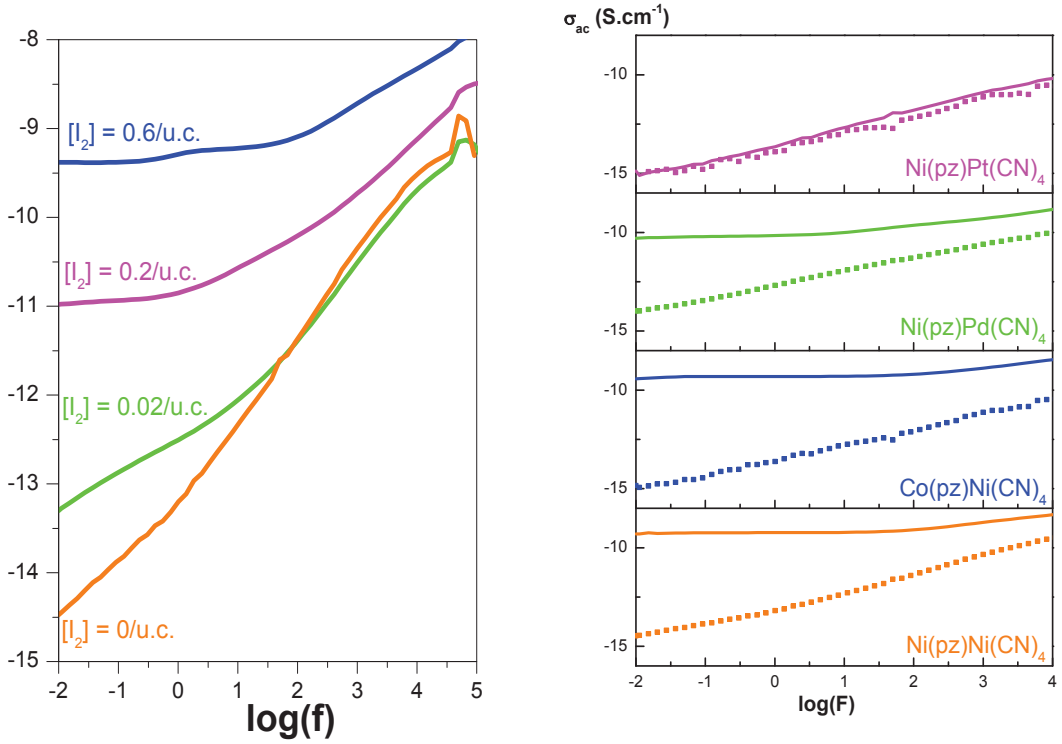

Figure 97 – CIS measurements for (left) $Ni^{II}(pz)[Ni^{II}(CN)_4]$ at different loadings and (right) analogue structures in the empty and filled state.

As parallel study, the molecular mobility of the bidentate organic ligand (free rotation) was investigated by measurements of the dielectric relaxation properties with the Dielectric Relaxation Spectroscopy (DRS).[137] The dielectric relaxation properties of the samples in terms of the dielectric loss ε" were deduced from the measurement of the complex dielectric function, $\varepsilon^*(f,T) = \varepsilon'(f,T) - i\varepsilon''(f,T)$, at different fixed frequencies under non-isothermal conditions, with a constant and slow heating rate (0.5 °C.min^{-1}). We checked that during the measurements performed at a given frequency and under linear heating conditions, the fluctuation of the temperature was very limited, so that the isothermal conditions can be considered to be attained. For both types of experiments, the crystalline powder was introduced into a specific cell similar that is generally used for liquids. About 75 mg of the powder sample was poured on the lower electrode of the cell, and then very gently pressed by the upper metallic electrode. The empty $Ni^{II}(pz)[Ni^{II}(CN)_4]$ network was *in situ* treated at 200 °C for 2 hours under dried nitrogen flux, in order to ensure that the residual water molecules are fully removed. For the iodine loaded materials $Ni^{II}(pz)[Ni^{II}(CN)_4]\bullet xI_2$ with x = 0.02,

0.2 and 0.6, according to TGA analysis, the *in situ* treatment was performed at 80°C in order to remove residual water and solvent molecules while avoiding any departure of the iodine guest. To analyse the dielectric relaxation peak, the Arrhenius model is employed. In that case, the relaxation rate $1/\tau$, characterizing the dielectric relaxation process, is expressed as follows:

Equation 11 – Dielectric relaxation time

$$\frac{1}{\tau} = \frac{1}{\tau_0} \exp\left(-\frac{\Delta E}{kT}\right)$$

where k corresponds to the Boltzmann's constant, T the temperature, ΔE the energy barrier characterizing the relaxation process and τ_0 the pre-exponential factor.[14] According to Equation 11, the Arrhenius plot issued from the temperature and frequency data recorded for the relaxation process, for which $\omega\tau = 1$ with ω being the electrical field angular frequency, allows us to estimate the values of ΔE and τ_0. The measurement performed on the empty $Ni^{II}(pz)[Ni^{II}(CN)_4]$ detected a flat signal with negligible values. The absence of response indicated that the pyrazine ligands in the empty structure were apolar and symmetric. The evolution of the dielectric peak at different iodine loadings is reported in Figure 98. At low iodine loading, a dielectric signal appeared at low temperature, indicating a dipole on the pyrazine ligand. We interpreted this signal as the result of the interactions iodine-pyrazine. The dielectric peak corresponded to $\tau_0 \approx 10^{-23}$ s which was consistent with a correlated a dynamic involving the guest molecule and the host structure.[138] As confirmed by the GCMC simulation, at low loading (0.02 I_2 per unit cell) the guest iodine interacted preferentially with the host structure moieities due to high affinity, rather than with other iodine molecules. The increase of the iodine loading (0.2 I_2 per unit cell) did not shift the dielectric peak and did not have any influence on the values for ΔE and τ_0, meaning that the dynamic did not change. The peak disappeared at higher loadings (0.6 I_2 per unit cell) since the larger amount of iodine acted as steric hindrance to the rotation of the pyrazine. These results could be correlated with the perturbation of the IR-active vibration modes of the pyrazine ligand after insertion of the iodine. Since iodine is a π-acceptor, it can indeed interact with the π-electrons of the aromatic rings as well. The calculated distance iodine-pyrazine in the GCMC simulations was around 3.6 Å that was consistent with an attractive force. The iodine-cyanides distance, however, was slightly lower (about 3.4 Å) suggesting that interaction with the cyanides had to be stronger.

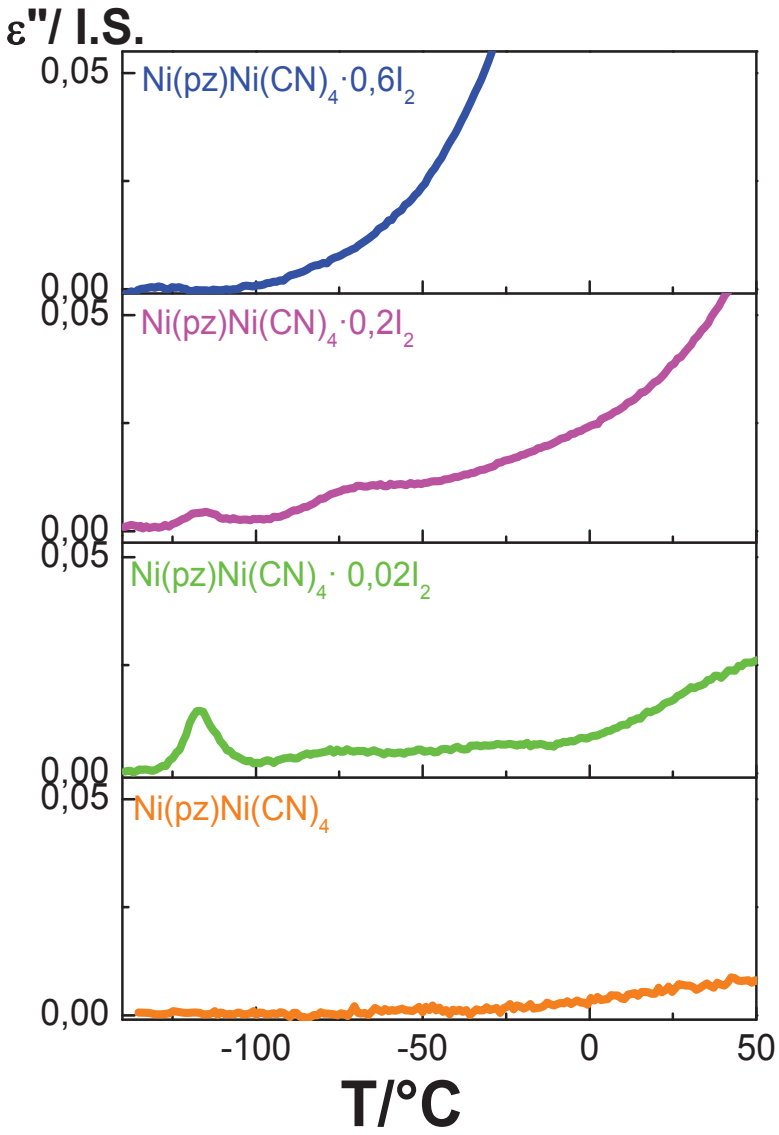

Figure 98 – Dielectric Relaxation Spectroscopy on the $Ni^{II}(pz)[Ni^{II}(CN)_4]$ at different iodine loadings.

Conclusion.

In Chapter 1 we have presented the adsorption of the molecular iodine in solution and in gasous phase with the Hofmann-type structure $Ni^{II}(pz)[Ni^{II}(CN)_4]$ (tetragonal, P4/m) and with the isostructural networks $M'(L)[M''(CN)_4]$ (where M' = Ni^{II}, Co^{II}; pz = pyrazine; M'' = Ni^{II}, Pd^{II}, Pt^{II}; L = pyrazine, 4,4'-bipyridine or 4,4'-azopyridine) and we discussed the mechanisms of the iodine confinement. For a better comparison of the different achieved storage capacities, the iodine adsorption isotherms for the fully characterized structures are reported in Figure 99, where the storage capacity is expressed in moles of iodine per moles of the host structures. All isotherms exhibited a steep increase at low concentrations and a plateau at maximal capacity, indicating an excellent affinity and a *type I* profile (adsorption of a monolayer).

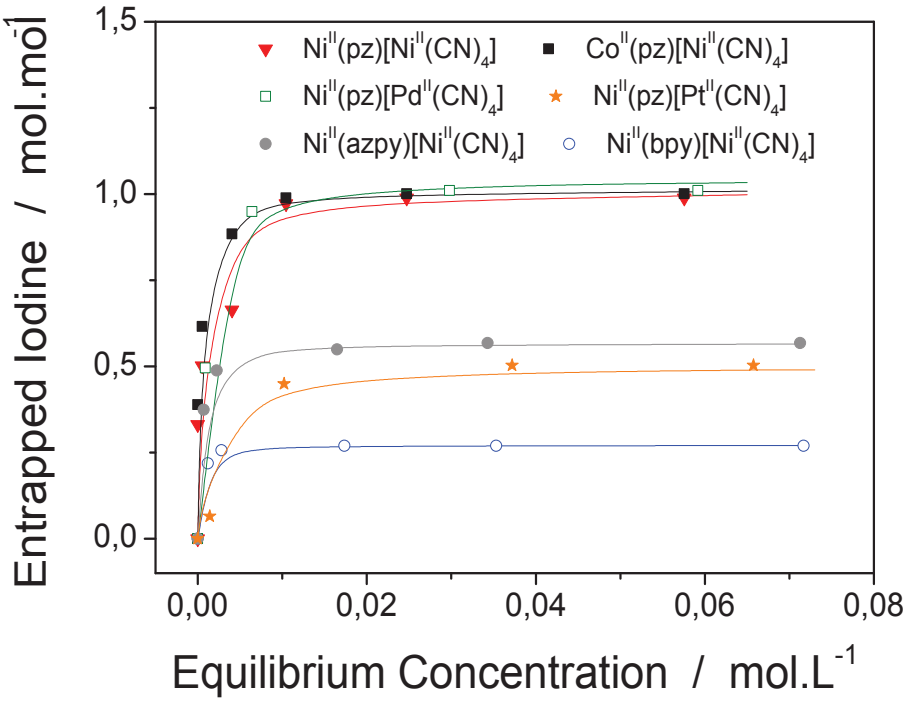

Figure 99 - Room temperature adsorption isothotherms for the Hofmann-type analogues.

When Ni^{II} or Pd^{II} occupied the square planar position and pyrazine was the bidentate organic ligand, iodine was entrapped up to one equivalent of I_2 per unit cell. Also, the UV-VIS and Raman spectra recorded on the solid samples showed that the confined iodine was mainly physisorbed and released between 130 and 250 °C (according to the compositions) before the decomposition of the host structures. The study of the desorption process indicated that a full regeneration by thermal treatment of the structures was achieved and that the structures performed a good resistance to cycling processes with a good maintainability of the high sorption capacity. A minor amount of iodine was found chemisorbed as polyiodides and that was justified by the experimental data with formation of I_3^- on lattice defects, *i.e.* the terminal CN^- ligands that did not

bridge the metallic cations. The adaptation of the lattice upon the insertion of iodine was different according to the employed building blocks and this influenced the starting desorption temperature of I_2 out of the host structure. In the structure $Ni^{II}(pz)[Ni^{II}(CN)_4]$ the small adaptation of the unit cell was interpreted as the effect of a weak electrostatic interaction with the cyanides and with the pyrazine ligands as well, as the GCMC modeling and the dielectric relaxation properties of the pyrazine ligands indicated. For this structure, iodine was successfully confined up to 150 °C (at atmosphere pressure). The use of $[Pd^{II}(CN)_4]^{2-}$ in $Ni^{II}(pz)[M''(CN)_4]$ triggered a change of space group from P4/m (tetragonal to P/mmm (orthorhombic). The volume of the unit cell however did not significantly change after insertion of iodine and the iodine desorption started at the lowest observed temperature *i.e.* 140 °C due to weaker confinement. The used of Co^{II} in the octahedral position gave a stronger interaction bringing to a relevant reduction of the unit cell. The nature of this interaction was interpreted as a relatively weak charge transfer between the guest iodine and the metal but further DFT calculations will elucidate the mechanism. $Co^{II}(pz)[Ni^{II}(CN)_4]$ at maximal storage capacity exhibited the smallest unit cell and iodine was desorbed at 180 °C, *i.e.* at higher temperature with respect to the analogue structures containing physisorbed iodine. The opposing effects of using Pd^{2+} and Co^{2+} on the lattice adaptation could be concurrently observed for the case of $Co^{II}(pz)[Pd^{II}(CN)_4]$: the ability of this structure to confine iodine was very close to $Ni^{II}(pz)[Ni^{II}(CN)_4]$. A summary of the specific features for each structures in reported in the table of page 122. No general differences where observed for the clathrates prepared in gaseous phase with respect to the ones prepared in solution, with only exception for $Ni^{II}(pz)[Ni^{II}(CN)_4]$ for which approaching to the maximal capacity in gaseous phase was more difficult. The large presence of water steam had a detrimental effect on the storage capacity especially for the structures containing Ni^{2+} cations, rather than Co^{2+}. It was indeed detected by spectroscopic analyses that the Ni^{2+}-containing structures formed more stable complexes with adsorbed water than the Co^{2+}-containing structures. Hence, the $Co^{II}(pz)[Ni^{II}(CN)_4]$ was finally recognized as the best candidate for the selective entrapment of iodine.

A totally different mechanism was observed for $Ni^{II}(pz)[Pt^{II}(CN)_4]$ that underwent an oxidative addition with iodine. The characterization of the complex $Ni^{II}(pz)[Pt^{II/IV}(CN)_4]\bullet I^-$ matched with the published data about the $Fe^{II}(pz)[Pt^{II/IV}(CN)_4]\bullet I^-$ prepared with an *in-situ* synthesis (or by solid state diffusion), indicating that the preparation did not influenced the final product. The replacement of the pyrazine ligand with 4,4'-bipyridine and 4,4'-azopyirdine decreased the maximal storage capacity, confirming that for a better confinement a small unit cell with dimensions close to the molecule I_2 was necessary in order to maximize the host-guest interactions. However, the $Ni^{II}(azpy)[Ni^{II}(CN)_4]$ exhibited a maximal storage capacity around 0.5 I_2 per unit cell, against the 0.25 I_2 per unit cell of $Ni^{II}(azpy)[Ni^{II}(CN)_4]$, suggesting that the azo-group of the azopyridine could stabilize a larger amount of iodine.

For the nuclear application, we can consider $Co^{II}(pz)[Ni^{II}(CN)_4]$ the best candidate, since: 1) it does not contain expensive metals; 2) it exhibits an enhanced selective capture of iodine against water with respect the $Ni^{II}(pz)[Ni^{II}(CN)_4]$; 3) it exhibits the same maximal capacity of $Co^{II}(pz)[Ni^{II}(CN)_4]\bullet I_2$ as well as the analogues with cations Ni^{II} or Pd^{II} in the square planar

configuration. If it the If we compare the iodine capture observed for this chosen materials with respect to the other studied Metal Organic Frameworks[139,140,141,142,143], we can observe similar stoichiometries at maximal storage capacity (Table 12).

Table 12 – Comparison of different coordination polymers (or MOFs) for the confinement of iodine.

MOF	Stoichiometry with metallic centres	Weight ratio $[\frac{mass\ I_2}{mass\ MOF} \cdot 100]$	Iodine retention in temperature
$Co^{II}(pz)[Ni^{II}(CN)_4]$	$I_2/Co = 1$ $I_2/Ni = 1$	85 wt%	< 180 °C
Cu-BTC	$I_2/Cu = 1.5$	175 wt%	< 150 °C
ZIF-8	$I_2/Zn = 0.76$	100 wt%	< 300 °C
MIL-101(Al)	$I_2/Al = 0.71$	35 wt%	not reported

The retention in temperature varies according to the type of employed structure. The Cu-BTC retains iodine up to 150 °C, *i.e.* at the same temperature as the $Ni^{II}(pz)[Ni^{II}(CN)_4]$. In both materials the iodine is physisorbed and it is relased at relatively low temperatures. However, the stronger interaction in $Co^{II}(pz)[Ni^{II}(CN)_4]$ allows a retention of iodine to a higher temperature (180 °C). The ZIF-8 is the most performing decontaminant, since it can retain the iodine up to 300 °C (*i.e.* up to decomposition of the structure). It is also known to have the best resistance to hydrolysis (up to 50% of humidity) which is generally the main limit in the use of organic linker containing MOFs. This stability, however, was revealed to be only due to kinetic reasons, since after few months even this structure decomposes in contact with water.[144] The Hofmann-type structures, by contrast, show a real chemical stability to hydrolysis due to the insoluble metal-cyanide bonds. Also, they exhibit resistance to cycling (for the series $M'(L)[M''(CN)_4$ with $M'' = Ni^{II}$ or Pd^{II}) and possibilty to fully regenerate the structure, if this property may eventually be required for the selective I_2 capture in the nuclear plants.

Focusing on the application, beside the use of the bulk decontaminant material, we considered the preparation of Hofmman-type supported nanoparticles, to study the feasability for a such nanocomposite and the eventual advantage in using such materials. Thus, in the next chapter, another possible modulation of the reference structure $Ni^{II}(pz)[Ni^{II}(CN)_4]$ will be treated, *i.e.* the particle size. The preparation of supported nanoparticles of $Ni^{II}(pz)[Ni^{II}(CN)_4]$ will be discussed in the part 2.1.

Summary table for the bulk Hofmann-type structures before (1) and after (2) iodine adsorption (in solution).

	$Ni^{II}(pz)[Ni^{II}(CN)_4]$	$Ni^{II}(pz)[Pd^{II}(CN)_4]$	$Co^{II}(pz)[Ni^{II}(CN)_4]$	$Co^{II}(pz)[Pd^{II}(CN)_4]$	$Ni^{II}(bpy)[Ni^{II}(CN)_4]$	$Ni^{II}(azpy)[Ni^{II}(CN)_4]$	$Ni^{II}(pz)[Pt^{II}(CN)_4]$
Maximal capacity per unit cell	1 I_2	1 I_2	1 I_2	1 I_2	0.25 I_2	0.5 I_2	1 I^- (*i.e.* 0.5 I_2)
Equilibrium time [hours]	2	2	2	2	12	12	12
ν(C≡N) 1 [cm^{-1}]	2174	2188	2167	2179	2163	2163	2186
ν(C≡N) 2 [cm^{-1}]	2165	2178	2178	2183	2163	2163	2186; 2200
δ(M-C≡N) 1 [cm^{-1}]	444	428	442	422	440	442	471
δ(M-C≡N) 2 [cm^{-1}]	442	428	465	428	440	442	469
ν(I-I) [cm^{-1}]	165	167	160	164	165; 175	165; 175	*ν(Pt^{IV}-I) 129*
$V_{unitcell}$ 1 [$Å^3$]	362.1	378.7	373.8	385.1	605.5	641	377.8
$V_{unitcell}$ 2 [$Å^3$]	369.3	378.2	353.3	363.1	601.7	641	358.9
Change in volume	+2%	negligible	-5%	-5%	negligible	negligible	-5%
Desorption [°C]	150	140	180	160	175	175	250

Bibliography

[1] Davies E. *Journal of Inclusion Phenomena and Molecular Recognition in Chemistry* (1998) 32, 499.

[2] Powell H.M. *J. Chem. Soc.* (1948) 61.

[3] Powell H.M. *J. Chem. Soc.* (1947) 208.

[4] Hoffmann R., *American Scientist* (2006) 94, 16.

[5] Faraday M., *Quart. J. Sci.*, (1823) 15, 71.

[6] Davy H., Philos. *Trans. R. Soc. London* (1811) 101, 1.

[7] Schafhäutl C. *J. Prakt. Chem.*, (1841) 21, 129.

[8] Wöhler F. *Liebigs Ann. Chem.*, (1849) 69, 297.

[9] Hofmann K.A. and Küspert F., *Z. Anorg. Allg. Chem.* (1897) 15, 204.

[10] Hartley H., Thomas N.G., *J. Chem. Soc.* (1906) 1013.

[11] Wieland H. and Sorge H., *Z. Physiol. Chem.* (1916) 97, 1.

[12] Terres E. and Vollmer W., *Z. Petroleum* (1935) 31, 1.

[13] Bengen M.F., German Patent Application OZ 123438 (March 18 1940).

[14] Mikus F.F., Hixon R.M., Rundle R.E., *J. Am. Chem. Soc.* (1946) 63, 1115.

[15] Hofmann K. A., Höchtlen F., *Ber.* (1903) 36, 1149.

[16] Hofmann K. A., Arnoldi H., *Ber.* (1906) 39, 339.

[17] Jones A. L., Fay P. S., U.S. 2732413, January 24, 1956. C.A.

[18] Powell H.M., Rayner J. H. *Nature* (1949) 163, 566-567.

[19] Keggin J. E., Miles S., *Nature* (1936) 137, 577.

[20] Bhatnagar V. M., *Z. Anorg. Allgem. Chem.* (1968), 363, 318-320

[21] Iwamoto T., *Journal of Incl. Phen. Mol. Recogn. in Chem.* (1996) 24, 61-132.

[22] Ribas J. « Coordination Chemistry » Wiley.

[23] Baur R., Schwarzenbach G., *Helv. Chim. Acta*, (1960) 403, 842.

[24] R. Kuroda and Y. Sasaki: *Acta Crystallogr.* B (1974) 30, 687.

[25] Kitazawa T., Sato Y., Takahashi M. and Takeda M., *J. Phys. Chem. Solids* (1996) 57, 1073-1078.

[26] Miyoshi T., Iwamoto T. and Sasaki Y., *Inorg. Chim. Aeta* (1973) 7, 97.

[27] Bittner H.G., Kearley G.J., Howard C.J. and Fillaux F., *Aeta Crystallogr. Sect B,* (1994) 50, 431.

[28] Sasaki Y., *Bull. Chem. Soe. Jpn.* (1969) 42, 2412.

[29] Nishikiori S., Kitazawa T., Kuroda R., Iwamoto T., *J. Inclusion Phenom. Mol. Reeognit. Chem.* (1989) 7, 369.

[30] Kartal Z., *Journal of Molecular Structure* (2009) 938, 70.

[31] Bayrak C., Kasap E., Kantarci Z., *ARI* (1998) 50, 214.

[32] Güllüoglu M.T., Yurdakul S., *Journal of Molecular Structure* (2002) 641, 93.

[33] Akyuz S., *Vibrational Spectroscopy* (2000) 22, 49.

[34] Niel, V.; Martinez-Agudo, J. M.; Munoz, M. C.; Gaspar, A. B.; Real, *J. A. Inorg. Chem.* (2001), 40, 3838.

[35] Bartual-Murgui, C.; Salmon, L.; Akou, A.; Ortega-Villar, N. A.; Shepherd, H. J.; Munoz, M. C.; Molnar, G.; Real, J. A.; Bousseksou, A. *Chem. Eur. J.* (2012), 18, 507.

[36] Riffith W. P., Q. Rev. *Chem. Soc.* (1962) 16, 188.

[37] Ruegg M., Ludi A., *Theoret. Chim. Acta* (1971), 20, 193.

[38] Suziki S., Orville-Thomas W.J., Sopkova A., Skorsepa J., *J. of Mol. Struct.* (1979) 54, 1.

[39] Ansell M.A., Zeppenfeld A.C., Ham W.K. Page C.J. *MRS Proceedings* (1994), 351, 171.

[40] Kantarci Z., Kasap E., *J. INcl. Phenom. Molec. Recogn. In Chem.* (1995) 20, 33.
[41] Iwamoto T., Kiyoki M., Ohtsu Y., Takeshige-Kato Y. *Bull. Of Chem. Soc. Of Japan* (1978) 51, 2, 488.
[42] Ekici N., Kantarci Z., Akyüz S., *J. Incl.Phenom. and Mol. Rec. Chem.* (1991) 10, 9.
[43] Bayari S., Kantarci Z., Akyuz S. *J. of Incl. Phenom. Mol. Rec. Chem.* (1994) 17, 291.
[44] Akyüz S., Depster A.B., Morehous R.L., Suzuki S. *J. Mol. Struct.* (1973) 105.
[45] Akyüz S., Davies J.E.D., Demir Y., Varman N., *J. Mol. Struct.* (1982) 79, 267.
[46] Agustslu S., Akyüz S., Davies J.E.D., *J. Mol. Struct.* (1984) 114, 437.
[47] Martinez V., Gaspar A. B., Munoz M. C., Ballesteros R., Ortega-Villar N., Ugalde-Saldivar V. M., Moreno-Esparza R., Real J. A. Eur. *J. Inorg. Chem.* (2009) 303.
[48] Tufan Y., Karacan N., Davies J.E.D., *Vibrational Sectroscopy* (2000), 23, 51.
[49] Tufan Y., Karacan N., Davies J.E.D *Journal of Inclusion Phenomena and Macrocyclic Chemistry* (1999) 33, 149.
[50] Güllüoglu M.T.,Yurdakul S. *Journal of Molecular Structure* (2002), 641, 93.
[51] Parlak C., Spectrochimica Acta Part A (2012) 99, 12.
[52] Nishikiori Sh., Iwamoto T. *Journal of Structural Chemistry* (1999) 40, 5.
[53] Izgi T., Parlak C., Aytekin T., Senyel M., *Journal of Molecular Structure* (2008) 892, 311.
[54] Kantarci Z., Gümüs Z., Öwisik H. *J. Incl. Phenom. and Macroc. Chem.* (2005) 53, 219.
[55] Drago R.S., Kwan J.T., Archer R.D., *J. Am. Chem. Soc.* (1958) 80, 2667.
[56] Depster A.B., Uslu H., *Spectrochim. Acta Part A* (1978) 34, 71.
[57] Bayari S., Kantarci Z., Akyüz S., *J. Mol. Struct.* (1995) 351, 19.
[58] Senyel M., *Bull. Of Pure and Appl. Sci.* (2001) 20, 61.
[59] Senyel M., Kürkçüoglu G.S., *J. Appl. Spec.* (2001) 68, 5862.
[60] Kartal Z., Türköz D., Bahceli S., *Acta Physica Slovaca* (2004) 54, 2, 97.
[61] Kartal Z. Sayin E., *Journal of Molecular Structure* (2011) 994, 170.
[62] Culp J. T., Natesakhawat S., Smith M. R., Bittner E., Matranga C., Bockrath B., *J. Phys Chem. C* (2008), 112, 7079.
[63] Agusti G., Cobo S., Gaspar A. B., Molnàr G., Moussa N. O., Szilàgyi P. A., Pàlfi V., Vieu C., Munoz M. C., Real J. A., Boussekou A., *Chem. Mater.* (2008) 20, 6721.
[64] Tufan Y., Karacan N., Davies J.E.D *J. Incl. Phenom. and Macr. Chem.* (2001) 40, 275.
[65] Culp J. T., Madden C., Kauffman K., Shi F., Matranga C., *Inorg. Chem.* (2013) 52, 4205.
[66] Kürkçüoglu G.S., Yesilel O.Z., Kavlak I., Büyükgüngör O., *Struct. Chem.* (2008), 19, 879.
[67] Culp J.T, Smith M.R., Bittner E., Bockrath B., *J. Am. Chem. Soc.* (2008) 130, 12427.
[68] Kitazawa T., Mizushima Y., Shiraha J., Taguchi R., Katoh A., Hasagawa T., Nishikiori Sh., Iwamoto T., *J. Incl. Phenom. and Mol. Recogn. in Chem.* (1991) 10, 29.
[69] Hashimoto M., Hasegawa T., Ichida H., Iwamoto T., *Chem. Lett.* (1989) 18, 8, 1387.
[70] Sertbakan T. R., Semran Saglam S., Kasap E., Kantarci Z., *Vibrational Spectroscopy* (2000) 24, 249.
[71] Uygun Ü.M., Öztürk N.,Cirak C., Türköw D., Bahceli S., *J. Incl. Phenom. and Macr. Chem.* (2006) 54, 187.
[72] Kartal Z., Türk T., *Journal of Molecular Structure* (2012) 1014, 74.
[73] Tufan Y., Karacan N., Özdemir Ü. *J. Incl. Phenom. and Macr. Chem.* (2001) 40, 275.
[74] Yuge H., Kim C., Iwamoto T., Kitazawa T. *Inorganica Chimica Acta* (1997) 257, 217.
[75] Aynsley E. E., Campbell W. A., Dodd R. E., *Proc. Chem. Soc. London* (1957) 210.
[76] Bhatnagar V. M., *Defence Sci. New Dehli* (1964), 14, 667.
[77] Cernak J., Chomic J., Maloghova D., Dunaj-Jurco M., *Acta Crystallgr. Sect C* (1988) 44, 1902.

[78] Cernak J., Potocnak I., Chomic J., Dunaj-Jurco M., *Acta Crystallgr. Sect. C* (1990) 46, 1098.

[79] Lokaj J., Gyerova A., Sopkova A., Sivy J., Kettmann V., Vrabel V., *Acta Crystallogr. Sect. C* (1991) 47, 2447.

[80] Southon P. D., Liu L., Fellows E. A., Price D. J., Halder G. J., Chapman K. W., Moubaraki B., Murray K. S., Létard J., Kepert C. J. *J. Am. Chem. Soc.* (2009) 131, 10998.

[81] Arcis-Castillo, Z.; Munoz-Lara, F. J.; Munoz, M. C.; Aravena, D.; Gaspar, A. B.; Sanchez-Royo, J. F.; Ruiz, E.; Ohba, M.; Matsuda, R.; Kitagawa, S.; Real, *J. A. Inorg. Chem.* (2013) 52, 12777.

[82] Ando H., Nakao Y., Sato H., Ohba M., Kitagawa S., Sakaki S., *Chemical Physics Letters* (2011) 511, 399.

[83] Ohba, M.; Yoneda, K.; Agusti, G.; Munoz, M. C.; Gaspar, A. B.; Real, J. A.; Yamasaki, M.; Ando, H.; Nakao, Y.; Sakaki, S.; Kitagawa, S. *Angew. Chem. Int. Ed.* (2009) 48, 4767.

[84] Bao, X.; Shepherd, H. J.; Salmon, L.; Molnar, G.; Tong, M.-L.; Bousseksou, A. *Angew. Chem. Int. Ed.* (2013) 52, 1198.

[85] Agusti, G.; Ohtani, R.; Yoneda, K.; Gaspar, A. B.; Ohba, M.; Sanchez-Royo, J. F.; Munoz, M. C.; Kitagawa, S.; Real, J. A. *Angew. Chem. Int. Ed.* (2009) 48, 8944.

[86] Ohtani R., Yoneda K., Horkie N., Kitagawa S., Gaspar A. B., Munoz M. C., Real J. A., Masaaki O., *J. Am. Chem. Soc.* (2011) 133, 8600.

[87] Li Y., Liu Y., Wang Y., Leng Y., Xie L., Li X., Inter. *J. Of Hydr. Chem.* (2007) 32, 3411.

[88] Rodriguez-Hernandez J., Lemus-Santana A.A., Ortiz-Lopez J., Jiménez-Sandoval S., Reguera E., *J. Sol. St. Chem.* (2010) 183, 105.

[89] W. Wong-Ng,a Culp J. T., Chen Y. S., Zavalij P., Espinal L., Siderius D. W., Allen A. J., Scheinsd S., Matrangab C., *Cryst. Eng. Comm.* (2013) 15, 4684.

[90] Breda S., *Journal of Molecular Structure* (2006) 786, 193.

[91] Kantarci Z., Davarcioglu B., Bayrak C., *J. Incl. Phenom. Macr. Chem*. (2001) 39, 115.

[92] Yoshikawa S., David H. O'Keeffe, Winslow S. Caughey J. *Biol. Chem.,* (1985) 260, 351.

[93] Kartal Z., Türköz D., Bahçeli S., acta physica slovaca, (2000) 54, 2, 97.

[94] L. R. Summerlin, C. L. Borgford, and J. B. Ealy, *Chemical Demonstrations: A Source Book for Teachers*, (1987) vol. 2, 73.

[95] Rohrer G., "Structure and Bonding in Crystalline Materials", 2001, Cambridge University Press.

[96] Andersson, A.; Sun, T. S. *Chem. Phys. Lett.* (1970), *6*, 611.

[97] srdata.nist.gov/xps

[98] Benesi A., Hildebrand J.H. , *J. Am. Chem. Soc.,* (1949) 71, 2703.

[99] Cvetanovic R. J., Duncan F. J., Faloner, Sunder W. A. *J. Am. Chem. Soc.* (1966) 88, 8.

[100] Kosower E.M. *J. Am. Chem. Soc.* (1955) 77, 3883.

[101] Kobinata S., Nagakura S., *J. Am. Chem. Soc.* (1966) 88, 17.

[102] Nandy P., B. Bhowmik B.B., *Chemistry and Physics of Lipids* (1986) 42, 303.

[103] Southwick P.L., Christman D.R. *J. Am. Chem. Soc.* (1953) 75, 3, 629.

[104] Groessl M., Fei Z., Dyson P. J., Katsyuba S., Vikse K.L., McIndoe *J. S. Inorg.Chem.* (2011) 50, 9728.

[105] Rogachev A.Y., Hoffmann *R. J. Am. Chem. Soc.*, (2013) 135, 8, 3262.

[106] Hongshan H. and Andrew G. Sykes *Acta Cryst.* (2011) E67, 434.

[107] Camarota B., Goto Y., Inagaki S., Garrone E., Onida B. *J. Phys. Chem.* 2009, 113, 20396.

[108] Bailey R. *Acta Cryst.* (1992) C48, 2259.

[109] Slifkin M.A., *Nature* (1963) 198, 1301.

[110] Li N., Shi L., Wang X., Guo F., Yan C. *Int J Anal Chem* (2011), 130102.

[111] Chang J., Ohno M., Esumi K., Meguro K. *J. Am. Chem. Soc.*, (1998) 65, 10, 1664.

[112] Palmet D., Ramette, R. Mesner R., *Journal of Solution Chemistry*, (1984), 13, 9.

[113] Klaboe, P. *J. Am. Chem. Soc.* (1967) 89, 15, 3667.

[114] Svensson H. Kloo L. *Chemical Reviews* (2003) 103, 5, 1649.

[115] Robert B. Login, John J. Merianos, patent US5002763 A (26 mars 1991).

[116] Deplano P., Ferraro J.R., Mercuri M.L., Trogu E.F. *Coord. Chem. Rev.* (1999) 188, 71.

[117] Moulay S., *J Polym Eng* (2013) 33, 5, 389.

[118] Chorro M., Kane G., Alvarez L., Cambedouzou J., Paineau E., Rossberg A., Kociak M., Aznar R. Pascarelli S., Launois P., Bantignies J. L. *Carbon* (2013), 100.

[119] Ye J. T., Iwasa Y., and Tang Z. K., *Phys. Rev. B* (2011) 83, 193409.

[120] Pei C., Ben T., Xu S., Qiu S. *J. Mat. Chem. A* (2014), 2, 7179.

[121] Kurkcuoglu AM., Yesilel G.S, Buyukgungor O. Z., *J. of Mol. Struct.* (2014) 1059, 101.

[122] Muhle C., Peters E., Jansen M., *Verlag der Zeitschrift für Naturforschung* (2009), 111.

[123] Diring S., Wang D. O., Kim C., Kondo M., Chen Y., Kitagawa S., kamei K., Furikawa S., *Nature Comm,* 4.

[124] Heckman R.A., Espenson J.H., *Inorg. Chem.* (1979) 18, 1.

[125] Hassel M., Freund H., *Surface Science Spectra* (1996) 4, 3, 273.

[126] Bayari S., Kantarci Z., Akyuz S., *J. of Incl. Phenom. Mol. Rec. Chem.* (2004) 17, 291.

[127] Grzeskowiak R., Whatley C., Goldstein M., *Spectrochimics Acta* (1976) 21A, 1577.

128 Zhuang Z., Cheng J., Wang X., Yin Y., Chen G, Zhao B. *Journal of Molecular Structure* (2006), 794, 77.

[129] Bordiga S., Regli L., Lamberti C., Zecchina A., Bjørgen M., *J. Phys. Chem. B* (2005) 109, 7724.

[130] Zecchina A., Coluccia S., Guglielminotti E., Ghiotti G. *The Journal of Physical Chemistry*, (1971) 76, 18.

[131] Zecchina A., Coluccia S., Guglielminotti E., Ghiotti G., *J. Phys. Chem.*, 1971, *75* (18), 2774.

[132] Abramczyk H., Brozek-Pluska B., Surmacki J., Jablonska-Gajewicz J., Kordek R., *Journal of Biophysical Chemistry 2* (2011) 158.

[133] Paul J.B., Provencal R. A., Chapo C., Roth K., Casaes R., and Saykally R. J. *J. Phys. Chem. A* (1999), 103, 2972.

[134] Rappe A. K., Casewit C. J., Colwell K. S., Goddard W. A., Skiff W. M., *J. Am. Chem. Soc.*, (1992) 114, 10024.

[135] Rappe A.K., Goddard W.A., *J. Phys. Chem.,* 1991, 95, 3358.

[136] Blugt T. J. H., Garcia-Perez E., Dubbekdam D., Ban S., Calero S., *J. Chem. Theory Comput.,* (2008) 4, 1107.

[137] Devautour-Vinot S. *J. Phys. Chem. C* (2013) 117, 11654.

[138] Devautour-Vinot S., *Chem. Mater.* (2012), 24, 2168.

[139] Sava, D. F.; Rodriguez, M. A.; Chapman, K. W.; Chupas, P. J.; Greathouse, J. A.; Crozier, P. S.; Nenoff T. M. *J. Am. Chem. Soc.* (2011) 133, 12398.

[140] Hughes, J. T.; Sava, D. F.; Nenoff, T. M.; Navrotsky, A. *J. Am. Chem. Soc.* (2013) 135, 16256.
Wu, D.; Navrotsky, A. Geochim. *Cosmochim. Acta* (2013) 109, 38.

[141] Sava, D. F.; Chapman, K. W.; Rodriguez, M. A.; Chupas, P. J.; Nenoff, T., *Chem. Mater.* (2013) 25, 2591.

[142] Cui, P.; Ren, L.; Chen, Z.; Hu, H.; Zhao, B.; Shi, W.; Cheng, P. *Inorg. Chem.* (2012) 51, 2303.

[143] Falaise C.; Volkringer C.; Facqueur J.; Bousquet T.; Gasnot L.; Loiseau T.; *Chem. Comm.* (2013) 49, 10320.

[144] Cychosz K. A., Matzger A. J., *Langmuir* (2010) 26, 17198.

CHAPTER 2

-

Supported nanoparticles for the entrapment of mobile radioactive elements

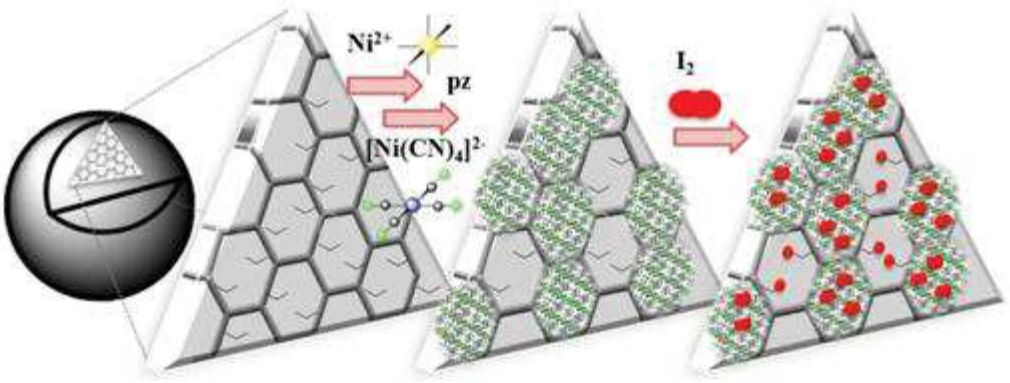

Introduction to the supported nanoparticles of coordination polymers.

Nuclear industry has recently considered the use of mesoporous materials to improve the systems of decontamination and the storage of the radionuclides from the out-gases and the effluents. The US Department of Energy considered the employment of functionalized mesoporous materials for the waste disposal in a report of 2006,[1] since they are supposed to exhibit a better resistance to radiation due to self-healing mechanisms and the large presence of interfaces that act as sinks for the irradiation-induced point defects (even though no real observation of such phenomena have been published yet). For the waste disposal, they can perform a higher storage capacity with respect to nowadays methods such as the incorporation in bitumen matrices, the cementification process or the use of borosilicate glasses.[2] Another advantage of mesoporous supports is the possibility to seal the pores after the material was used for the decontamination, by a sintering process at 900 °C or by reaction with ammonia vapours.

The term “mesoporous” refers to materials with porosity in the range 2-50 nm. The first mesoporous structures, specifically silica-based materials, were patented in the late 60s – early 70s. For instance, in the patent by Chiola *et al.* in 1971, they prepared a low-density silica by hydrolysis of a tetralkylsilicate with a cationic surfactant that acts as template for the mesopores.[3] However, only 20 years later, new studies caused an exponential development in this field, notably the works of Beck *et al.* about the preparation of MCM-41 silicas by a hydrothermal process and an ionic surfactant (hexadecyl-trimethyl-amino-bromide)[4] and the preparation of SBA-15 by Zhao *et al.* with non-ionic tri-block co-polymers.[5] [6]

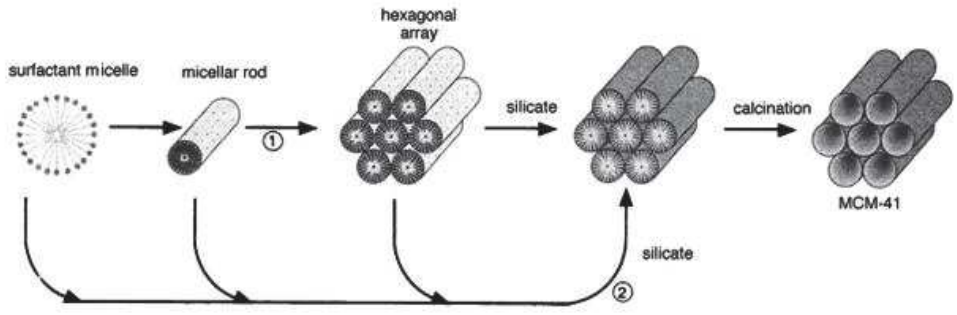

Figure 1 – Exemplification for the preparation of a mesoporous silica of type MCM-41.

In this type of synthesis the organic surfactant has the role of *template* for the final size of the mesopores, since it organizes in micelles with geometry depending on physical and chemical parameters (temperature, pressure, concentration, pH). In MCM-41 and SBA-15, micelles form elongated structures stacked in a hexagonal geometry. Condensation of a

silica precursor, typically the tetraethoxysilane (TEOS), is triggered by different methods as a hydrothermal process or evaporation of the solvent. Finally, calcination of the product eliminates the organic phase and liberates the mesopores. Typically, mesoporous silicas prepared by this method expose a specific surface area between 500 and 1000 $m^2.g^{-1}$ with pores between 2-15 nm. The modulation of these features is achieved by choosing the surfactant as well as by introducing in the synthesis specific organic molecules as mesytilene (or 1,2,3-trimethyl benzene) in order to grow larger pores (10-20 nm in the case of mesytilene).[7] Mesoporous silicas can be the starting support to build more complex, functionalized materials at nanoscale with tunable properties. For instance, the family of coordination polymers called Pussian Blue's analogues have been considered in the last years for the functionalization of mesoporous silicas for different applications. As brief historical remind about the application fields for the Prussian Blue $Fe^{III}_4[Fe^{II}(CN)_6]_3$ and its analogues, in the 20th century researchers found several potential applications for this class of materials due to their microporosity (≈5 Å), for instance: the building of molecular sieves,[8] catalytic processes,[9] the removal of heavy metal ions in wine production,[10] the electrochemical applications as battery building,[11] the electronic switching and electrochromic devices.[12] This was as well the first kind of coordination compound to find an application connected to nuclear decontamination, for the sorption of $^{137}Cs^+$ in waste nuclear solutions.[13] In this last application, the use of supported nanoparticles instead of the bulk compound can improve the storage capacity, since nanoparticles have a higher surface-to-volume ratio. Further, due to their small size, faster diffusion processes can be expected compared to the curse, bulk materials. Preparation of Prussian Blue-analogues nanoparticles originally concerned studies about the specific magnetic properties consisting in superparamagnetic behaviour with a slow relaxation of the magnetisation. For this purpose, size-controlled nanoparticles of 2-5 nm were prepared in ionic liquids,[14] reverse micelle media,[15] organic phase synthesis with oleic acid and trialkylamines as stabilizers.[16] In the context of the magnetic studies, in 2005 Larionova *et al.* prepared for the first time nanoparticles of Prussian Blue analogues $M^{n+}[M(CN)_m]$ (with $M^{n+} = Fe^{2+}$, Ni^{2+}, Fe^{3+}; M'' = Fe^{3+} with m = 6 or Mo^{5+} with m = 8) inside a pyridine-functionalized mesoporous silica, by using the mesopores of size 7.5 nm as nanoreactors.[17] The building process of these functionalized materials took inspiration from the *click chemistry* introduced in 2001 by Sharpless *et al.*,[18] who proposed to introduce in chemistry the new idea, inspired by the natural synthetic processes, of building complex structures from simple and small molecules in a rapid and easy way. The anchoring of the building elements to the pore surface was possible thanks to coordination of the cations M^{n+} to the pyridine-type grafting, otherwise consecutive cycles of infiltration would have washed away the deposited precursors. The silica matrix was grafted in distilled toluene under reflux conditions with functionalized triethoxysilane, that react with the silanol groups on the surface Si-OH with release of ethanol as by-product and formation of Si-O-Si bonds. The growth of nanoparticles was possible by a *step-by-step* process where the functionalized silica was

repeatedly infiltrated with a methanolic solution of M^{n+} and then with a methanolic solution of $[N(C_4H_9)_4]_3[M(CN)_m]$. They performed in total 3 cycles obtaining finally nanoparticles of size 5 nm and an occupation of 56% of the initial free space in the mesopores. TEM images confirmed that the mesostructure of the silica was not affected by the infiltration cycles.

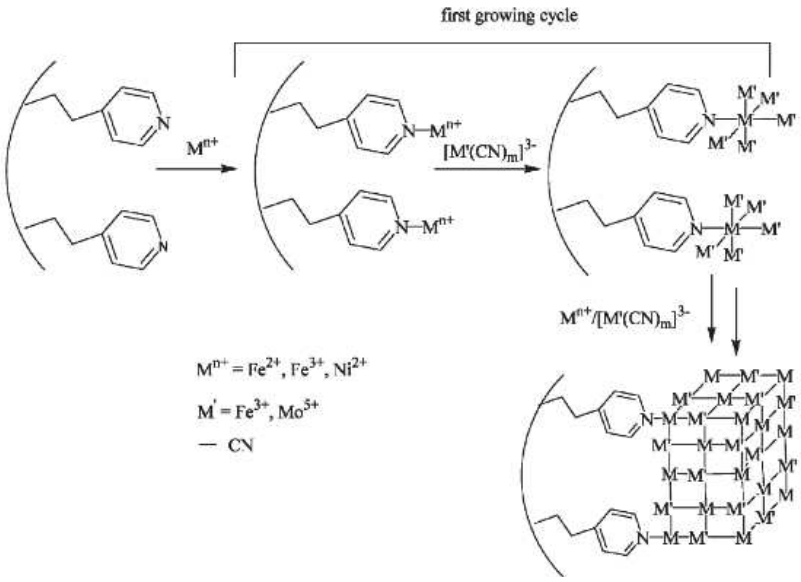

Figure 2 - Illustrated preparation for the hybride Prussian Blue-silica materials.[17]

The process described for the hybrid materials was further adapted for the preparation of analogue materials by changing the grafting agent, the composition of the nanoparticles or the ceramic support. Concerning the grafting agent, the use of a chelating grating agent was reported in the work of Sangvanich *et al.*, who used 2-aminethyl-3-aminopropyl-trimethoxysilane (Figure 3-a).[19] In the paper by Turgis *et al.* they used instead the grafting agent 3-azidopropyltriethoxysilane. In this reaction, the Cu catalyzed the triazole ring formation, then the ring acted as a chelator, immobilizing the copper inside the silica matrix thanks to its aromatic N and OH groups (Figure 3-b).[20] Using a bidentate (or chelating) grafting guaranteed a better anchoring to the silica walls.

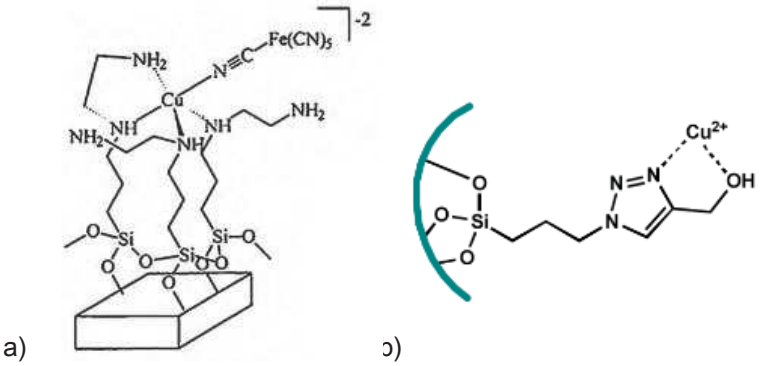

a) c)

Figure 3 - Examples from litterature of bidentate grafting agents to complex precursors of Prussian Blue analogues.[19, 20]

Different supports were also considered. For instance, in the paper of Causse *et al.* nanoparticles of Prussian Blue were incorporated in a monolith silica.[21] Delchet *et al.* used glass beads (Vitrabio®) of size ≈200 µm, with mean pore size of 30 nm and specific surface area of 150 $m^2.g^{-1}$.[22] Published studies for the sorption of Cs^+ and Tl^+ with their family of hybrid materials based on Prussian Blue analogues reported that the supported nanoparticles clearly showed a higher capacity per gram of decontaminant material with respect to the related bulk Prussian Blue analogue (Table 1).

Table 1 - Capacities per gram of Prussian Blue reported in wroks by Delchet *et al.* [22] and Sanvanich *et al.* [19] (NPs = nanoparticles).

	Cs^+	Tl^+
Supported $Co_3[Fe(CN)_6]_2$-NPs [22]	1.3 $mmol.g^{-1}$	-
Bulk $Co_3[Fe(CN)_6]_2$ [22]	0.4 $mmol.g^{-1}$	-
Supported $Cu_3[Fe(CN)_6]_2$-NPs [19]	0.13 $mmol.g^{-1}$	0.14 $mmol.g^{-1}$
Bulk $Cu_3[Fe(CN)_6]_2$ [19]	0.09 $mmol.g^{-1}$	0.03 $mmol.g^{-1}$

In a recent work (not published yet) by Larionova *et al.* the synthesis was adapted for the infiltration of insoluble chitosan beads, an organic polymer obtained by crabs' shells which is largely used in the *green chemistry*. A previous work of the team considered as well chitosan beads as supports for nanoparticles of Hofmann-type structure $Fe^{II}(pz)[Pt^{II}(CN)_4]$ (mean size 3 nm) to investigate the spin cross-over properties at the nanoscale.[23] In an earlier paper, the same type of nanoparticles were prepared by reverse microemulsion and then embedded in a silica matrix by Raza *et al.* to investigate magnetic properties as well.[24] However, there are no published works so far about the preparation of Hofmann-type nanoparticles by infiltration of a mesoporous silica.

In this chapter we will treat the preparation of nanocomposites for the entrapment of specific elements (I_2 and Co^{2+}) and their performance in the selective entrapment. The first part is a development of the previous chapter and considers the growth of nanoparticles of the Hofmann's structure $Ni^{II}(pz)[Ni^{II}(CN)_4]$ inside mesoporous silicas and the entrapment of molecular iodine in solution (materials labelled as Sil@NP and Glass@NP). The second part will include a different study which focuses on the entrapment of Co^{2+} in aqueous solutions with supported Prussian Blue nanoparticles (materials labelled as 1-Ni and 5-Fe). The two projects are included in the same chapter due to the similarities in the synthesis of the decontaminant materials and the more applicative aspect with respect to the previous chapter.

2.1 - Supported $Ni^{II}(pz)[Ni^{II}(CN)_4]$ nanoparticles for the reversible capture of the molecular iodine.

In the first part of Chapter 2, the preparation and the characterization of the supported $Ni^{II}(pz)[Ni^{II}(CN)_4]$ nanoparticles onto different ceramic supports is reported. The materials are also used for the entrapment of molecular iodine in solutions of cyclohexane, performed following the same protocol as for the bulk materials. A study of the reversible desorption is then performed. Two different ceramic supports were employed for the fabrication of the nanocomposites: a mesoporous silica and commercial porous glass beads. In both cases, the synthesis of the hybrid nanocomposites supporting $Ni^{II}(pz)[Ni^{II}(CN)_4]$ nanoparticles was performed by a *multi-step* approach consisting in the successive coordination of the precursors $Ni^{II}(BF_4)_2 \cdot 6H_2O$, pyrazine and $[N(C_4H_9]_4]_2[Ni^{II}(CN)_4]$ to the functionalized silica matrix (mesoporous silica or porous beads) (Fig. 1), by adapting protocols from literature.[17,23,25] A schematic representation of the approach is shown in Figure 4. In the following sections the materials Sil@NP (nanoparticles supported by mesoporous silica) and Glass@NP (nanoparticles supported by porous glass beads) will be treated separately.

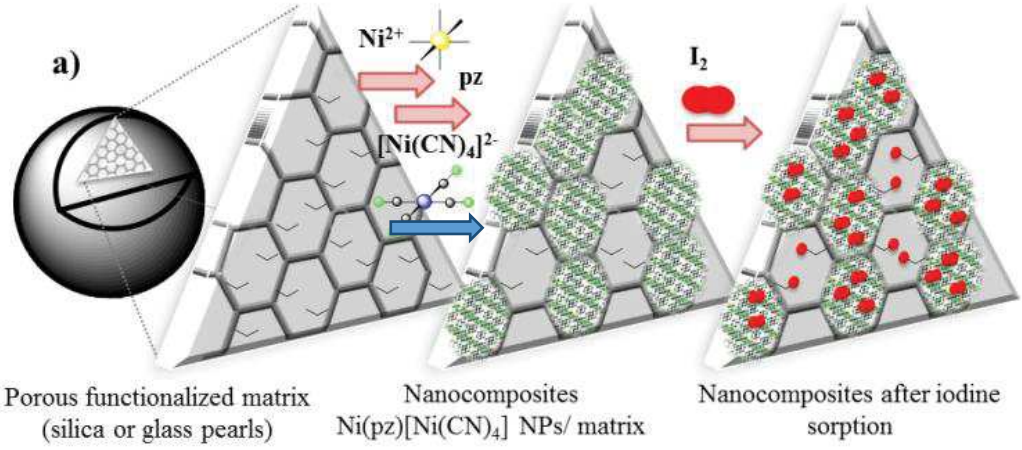

Figure 4 – Schematic representation of the used approach to the synthesis of silica based nanocomposites.

2.1.2 - Mesoporous silica based nanocomposite (Sil@NP) containing $Ni^{II}(pz)[Ni^{II}(CN)_4]$ nanoparticles and the iodine entrapment.

A grafted mesoporous silica was prepared by complexation of tetraethoxysilane (TEOS) around micelles of P123 polymer in an acidic solution (full description of the method is given in the *Experimental Section*). A larger pore size with respect to the classic SBA-15 was achieved by introduction in solution of mesytilene, which was responsible to increase the diameter of the micelles.[26] Final mesoporous silica was obtained with a calcination process at 550 °C. As the TEM image in Figure 5 shows, a disordered open porosity was obtained as well.

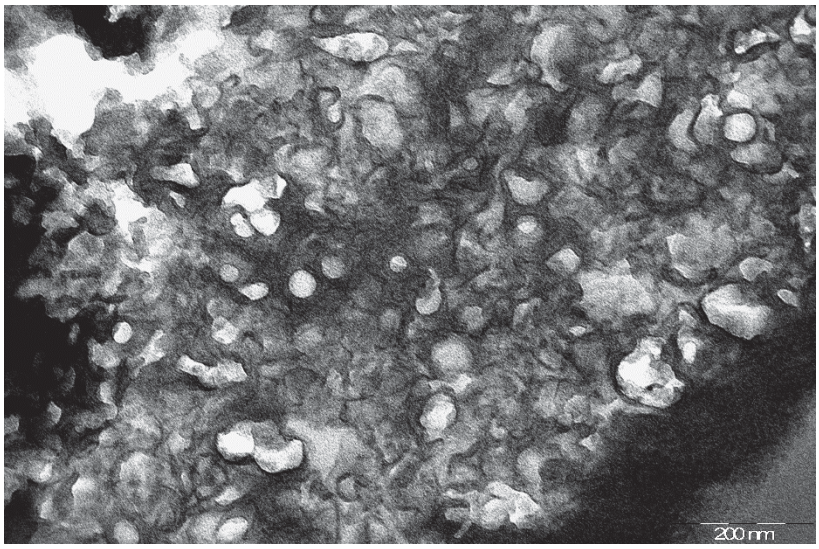

Figure 5 – TEM image for the mesoporous silica.

Before impregnation, silica was grafted to ensure covalent anchoring of nanoparticles to the support. The chosen grafting agent was the bidentate diamine 2-aminoethyl 3-aminopropyl timethoxysilane (Figure 6).

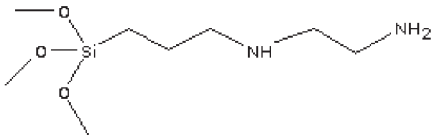

Figure 6 - Representation of the grafting agent.

A bidentate grafting was preferentially chosen to a monodentate molecule as pyridine, because coordination of the latter to the metallic cation failed due to excess of pyrazine used for the formation of the Hofmann-type nanoparticles. The grafting process was performed in distilled toluene under inert conditions since the diamine is water sensitive.

For this discussion, the diamine-grafted silica was labelled *Sil*. Elemental analyses indicated: C, 10.50%; N, 4.11%; H, 2.37, meaning that around 16 wt% of diamine was grafted on the silica. The material *Sil* was then functionalized with the $Ni^{II}(pz)[Ni^{II}(CN)_4]$ nanoparticles to obtained the hybride material Sil@NP. For this purpose, the material *Sil* was impregnated with a methanolic solution of $Ni(BF_4)_2$/pyrazine (2 hours) and then with a methanolic solution of $[N(C_4H_9)_4]_2[Ni(CN)_4]$ (tetrabutyl ammonium tetracyanonickelate)[27] for 2 hours, completing one impregnation cycle. The impregnation was performed by agitation in a round-bottom flask with a magnetic stirrer at 150 rpm. In order to grow $Ni^{II}(pz)[Ni^{II}(CN)_4]$ nanoparticles, 5 impregnation cycles were performed (overall time of 20 hours). During the first cycle the silica turned to green-blue since the precursors were immediately deposited, but only during the third cycle the silica started exhibiting a light violet colour. The material was analyzed by solid UV-VIS in reflectance mode to check the correspondence of the absorption bands with the bulk $Ni^{II}(pz)[Ni^{II}(CN)_4]$. Effectively, the appearance of an absorption band around 550 nm matched with the spectrum of the bulk material (Figure 7).

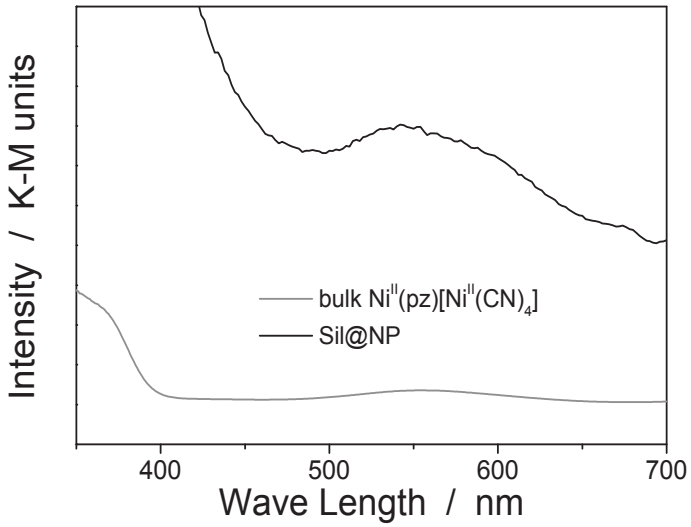

Figure 7 – Reflectance mode UV-VIS spectra for Sil@NP and $Ni^{II}(pz)[Ni^{II}(CN)_4]$.

The N_2 adsorption isotherms performed at 77 K for the non-grafted silica, grafted silica *Sil* and Sil@NP nanocomposite were analyzed with BET (Brunauer-Emmett-Teller) method to find the specific surface area (SSA) and with the BJH (Barrett-Joyner-Halenda) method to trace the pores distribution. For a description of the methods, see the section *Annexes*. For all materials *type IV* isotherms were observed (Figure 8) due to the presence of a hysteresis. The hysteresis upon desorption was due to the presence of mesopores. Porous silica initially showed a SSA = 646 $m^2.g^{-1}$ with average pores dimension 9 nm. After grafting the diamine, the SSA decreased to 270 $m^2.g^{-1}$ with average pores to 7 nm for material *Sil*. For Sil@NP the SSA turned out to be only 37 $m^2.g^{-1}$. The initial porosity of the silica was strongly reduced by the growth of the intra-pore nanoparticles. The shape of the hysteresis for Sil@NP suggested that the geometry of the pores changed as well with

respect diamine-grafted silica, after the growth of the nanoparticles. According to literature,[28] so-called *ink-bottle* pores with a neck typically give hysteresis as the one measured for Sil@NP (details about hysteresis are reported in the section *Annexes*).

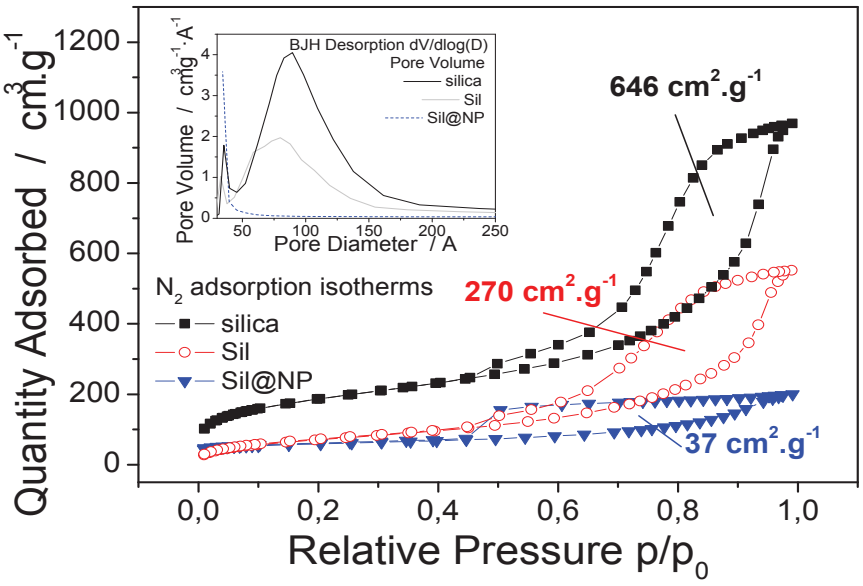

Figure 8 - Nitrogen adsorption isotherms at 77 K for mesoporous silicas

An attempt to quantify the deposited nanoparticles was performed by TGA (Figure 9) but the overlapping decompositions hindered a right calculation. TGA curve showed indeed overlapped decompositions of diamine grafting ligand (after 250 °C) and $Ni^{II}(pz)[Ni^{II}(CN)_4]$ structure (dramatic loss from 350 °C). The lower decomposition temperature for the nanoparticles with respect to the bulk material (400 °C) could be associated to the smaller grain size and the higher surface energy of the nanoparticles. Dependence of the decomposition temperature with respect to the particle size was observed in literature as well, for instance, for TiO_2 particles.[29] Since the grafted silica has a loss by 16% of diamine and EDX analysis on the final nanocomposite indicated a weight ratio Ni/Si = 0.55 (molar ratio Ni/Si = 0.28), it was estimated a deposition of 39 wt% of nanoparticles.

The presence of the attended compound inside the silica pores was confirmed by FT-IR analyses. Infrared spectrum for Sil@NP showed the ν(C≡N) mode at 2174 cm^{-1} which is the characteristic value for the coordinated cyanides in this Hofmann-type structure. Pyrazine bands were not detected since silica matrix gave a very large band in the same region, overlapping the bands for the diamine and the pyrazine. Also, the presence of the $Ni^{II}(pz)[Ni^{II}(CN)_4]$ was detected by recording the XPRD pattern, where the same diffraction pattern of $Ni^{II}(pz)[Ni^{II}(CN)_4]$ was recognized. The characteristic peaks with Miller indices (001)/(100), (110)/(101) and (111) diffracted at the same angles as the bulk material. Larger peaks were due to particle size (Figure 10). The Scherrer equation applied on the peak (111), the only peak which is not superposed to the other ones, indicated a mean

particles size of 28 nm, which was too large for the expected nanoparticles. It is worth to note that the Scherrer equation is indeed reliable only for particles with the mean size in the interval 10-200 nm. For smaller nanoparticles, other methods for the determination of the mean size should be preferred.

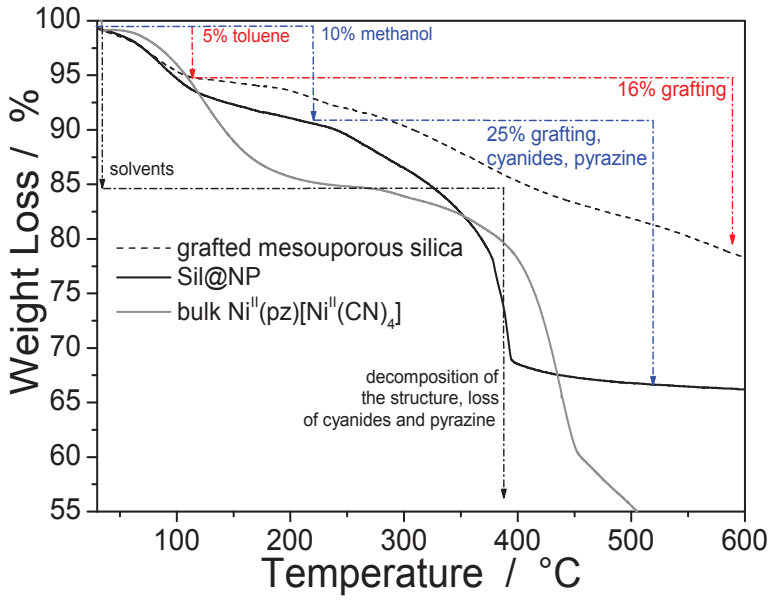

Figure 9 - TGA curves mesoporous silicas.

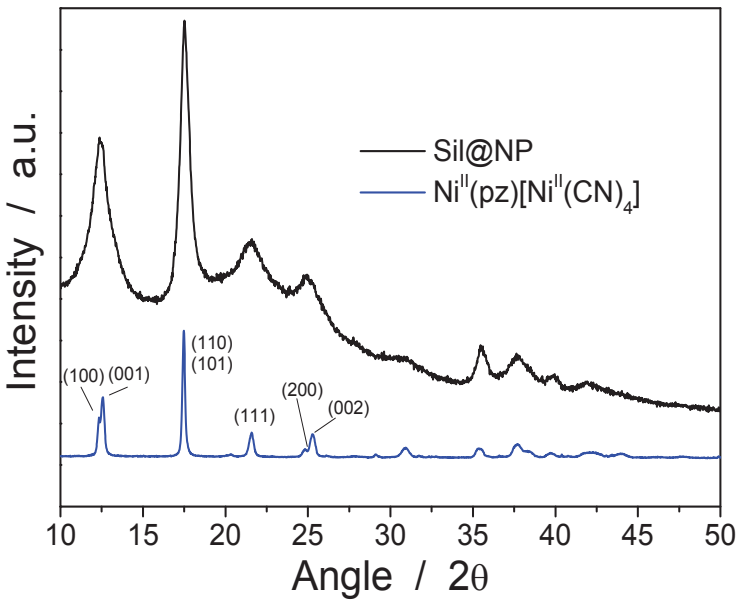

Figure 10 – XRPD for Sil@NP and Ni^{II}(pz)[Ni^{II}(CN)$_4$].

In order to estimate the average size of the nanoparticles, direct observation of the nanoparticles by TEM was possible by extractive replica with HF. Figure 11 reports some

images of the extracted nanoparticles. Size distribution revealed an average size of 2.809 ± 0.915 nm (Figure 11 inset), with however the presence of few bigger agglomerates.

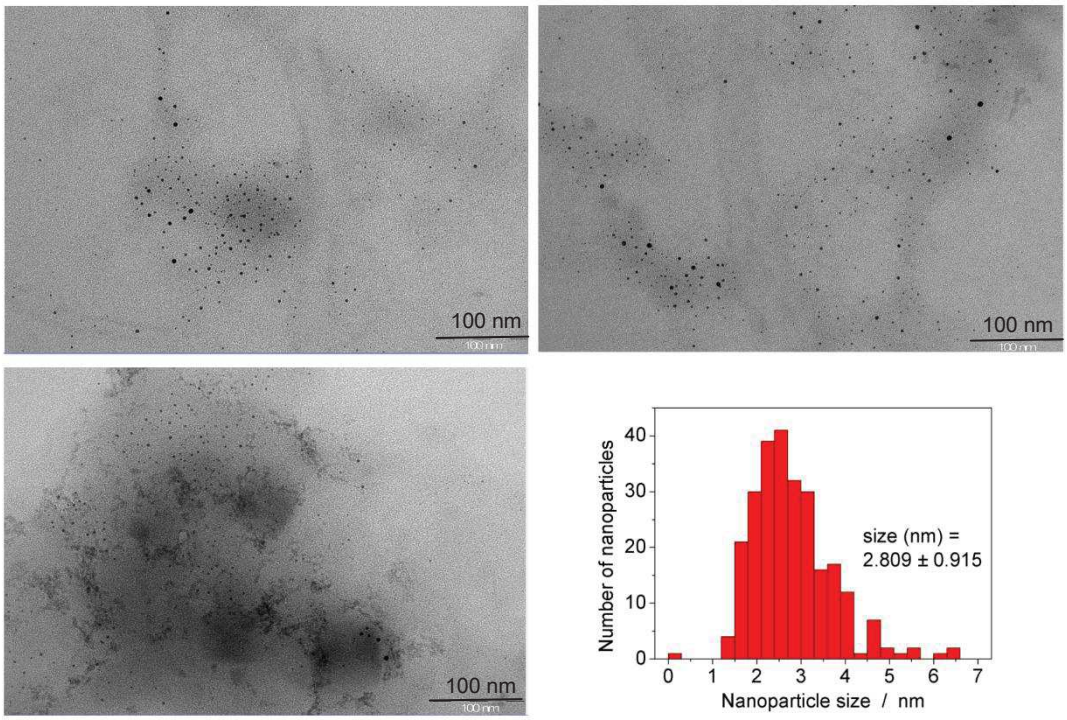

Figure 11 – TEM images after extractive replica of Sil@NP and size distribution of the nanoparticles.

The nanocomposite Sil@NP was then employed for the entrapment of iodine in solutions of cyclohexane. The relative grafted support without nanoparticles was also used to capture iodine in order to evaluate the role of the grafting agent. A thermal activation of the nanocomposite was performed at 80 °C under primary vacuum for 8 hours. Kinetics studies were performed at a concentration C = $3 \cdot 10^{-3}$ M to determine the equilibrium time and the reaction order. All kinetic curves were fitted with the pseudo-second order model already used for the bulk Hofmann-type networks.

For the material *Sil* an equilibrium time around 40 hours was observed, whereas for Sil@NP it was around 15 hours (Figure 12). A comparison with the bulk $Ni^{II}(pz)[Ni^{II}(CN)_4]$ (equilibrium time = 2 hours) showed that the iodine uptake with the so-prepared nanocomposites performed lower kinetics. With respect to the NP-free silica, the presence of the nanoparticles seemed to speed up the uptake of iodine from the solution. We can reasonably motivate the longer equilibrium times for silica-based materials because of the chemisorption of iodine on the diamine. As described in literature[15], when iodine interacts with electron donors a strong charge transfer occurs. The σ-electrons of the diamine are given to the σ^* anti-bonding orbital of iodine, bringing to ionic dissociation. We can assume the following reaction where N: is an amino group of the grafting ligands:

Reaction 1 – Dissociative charge transfer

$$N: + 2\ I_2 \rightarrow N: I^+ + I_3^-$$

so that a theorical maximal capacity is 4 moles of iodine per mole of diamine. The chemisorption on the grafted nanocomposites showed a longer equilibrium time with respect to the physisorption process in bulk $Ni^{II}(pz)[Ni^{II}(CN)_4]$. When nanoparticles were introduced, both mechanisms were present giving an intermediate equilibrium time. For a complete characterization of the iodine uptake, isotherms were performed by iodine capture in solution of cyclohexane at increasing concentrations. The isotherms were fitted with the Langmuir model.

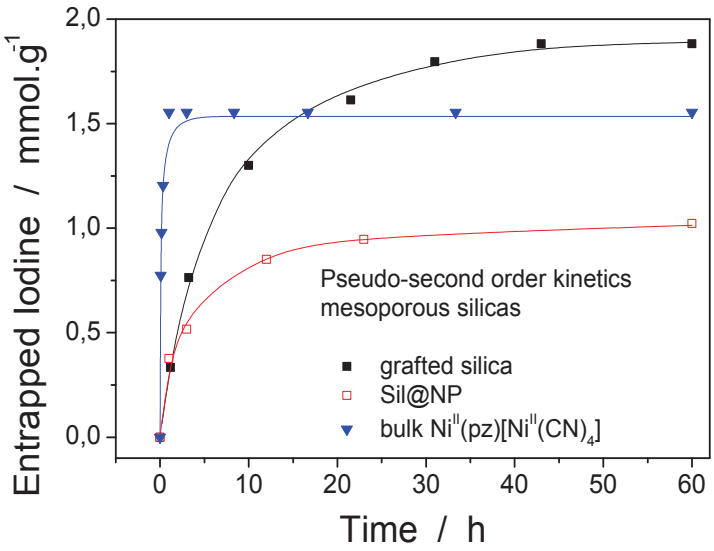

Figure 12 - Kinetic curves for the grafted silica, Sil@NP and bulk $Ni^{II}(pz)[Ni^{II}(CN)_4]$.

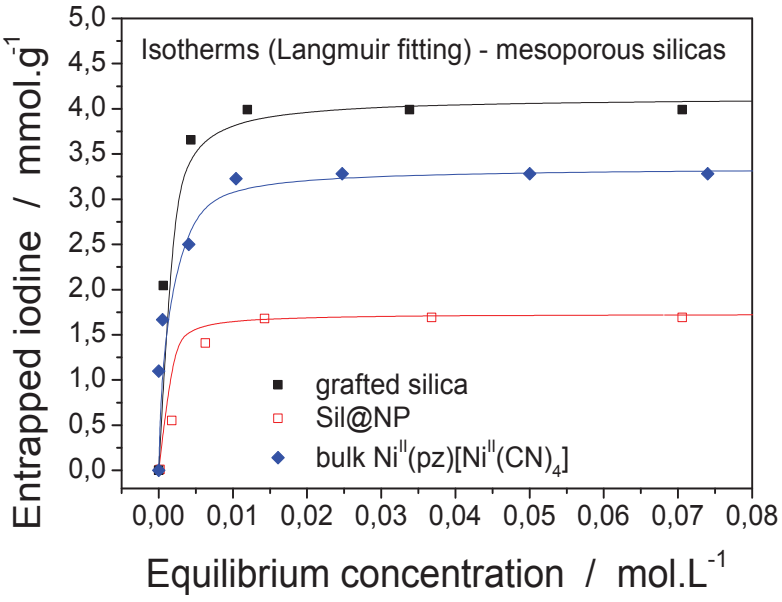

Figure 13 - Isotherms for the grafted silica, Sil@NP and the bulk $Ni^{II}(pz)[Ni^{II}(CN)_4]$.

All isotherms showed a *type I* progression, with a steep increase at low concentration indicating a good affinity with iodine. A maximal capacity of 1.7 ± 0.1 mmol.g^{-1} for Sil@NP and 3.9 ± 0.1 mmol.g^{-1} for diamine-grafted silica were found. The amount of iodine entrapped on the diamine-grafted silica was lower than expected considering a theorical capacity of 4 I_2 per mole of grafting (which is 6.4 mmol.g^{-1}). When the nanoparticles were introduced, iodine was shared between the grafting ligand and the nanoparticles. Reflectance mode UV-VIS spectra for the iodine-loaded silica materials indicated that, when iodine was chemisorbed on the diamine-grafted mesoporous silica, only the UV-VIS band for triiodide (360 nm) was detected. When nanoparticles were added, the concomitant presence of the band at 470 nm for the confined iodine I_2 inside the nanoparticles and the band at 360 nm for the triiodides on the grafting is observed. Raman spectra were also performed as supporting analysis (Figure 15). For diamine-grafted mesoporous silica (*Sil*) the Raman band at 110 cm^{-1} was associated to the I_3^- symmetric stretching mode and the band at 150 cm^{-1} is the I_3^- asymmetric stretching mode. An additional band at 165 cm^{-1} was detected for iodine on Sil@NP due to the presence of confined I_2. It is important to notice that some polyiodides were observed as well when iodine was absorbed by the bulk $Ni(pz)[Ni^{II}(CN)_4]$, which was not the main mechanism of entrapment and it was very likely due to presence of defects like mono-coordinated cyanides. XRPD for Sil@NP after uptake showed a small shift to lower 2θ values of the peak at 25° related to the plane (200), as observed for $Ni^{II}(pz)[Ni^{II}(CN)_4]\bullet I_2$ in Figure 16. Comparison of the XRPD patterns for the bulk and the nanoparticles after I_2 uptake indicated other similarities, as the change in relative intensity among the diffraction peaks (100) and (110). Also, IR spectra of Sil@NP at maximal capacity indicated a shift of the stretching mode for the bridging cyanides from 2174 to 2167 cm^{-1}. As reported in the previous chapter, this is an indication of the insertion of iodine inside the structure $Ni(pz)[Ni^{II}(CN)_4]$. A comparison of the IR spectra for bulk and nanoparticles of $Ni(pz)[Ni^{II}(CN)_4]$ after iodine entrapment in reported in Figure 17.

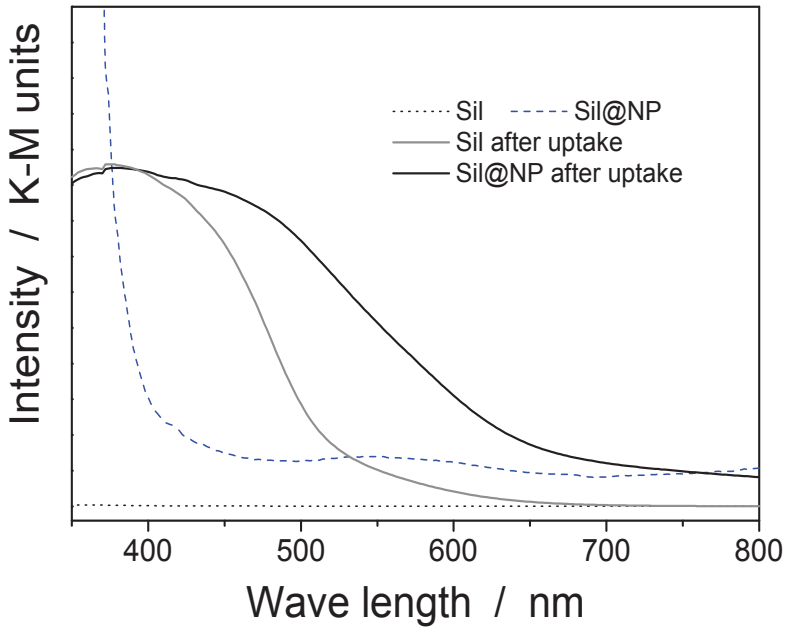

Figure 14 – UV-VIS spectra for UV-VIS spectra in solid state performed for a) grafted silica; b) Sil@NP; c) grafted silica after iodine capture; d) Sil@NP after iodine capture.

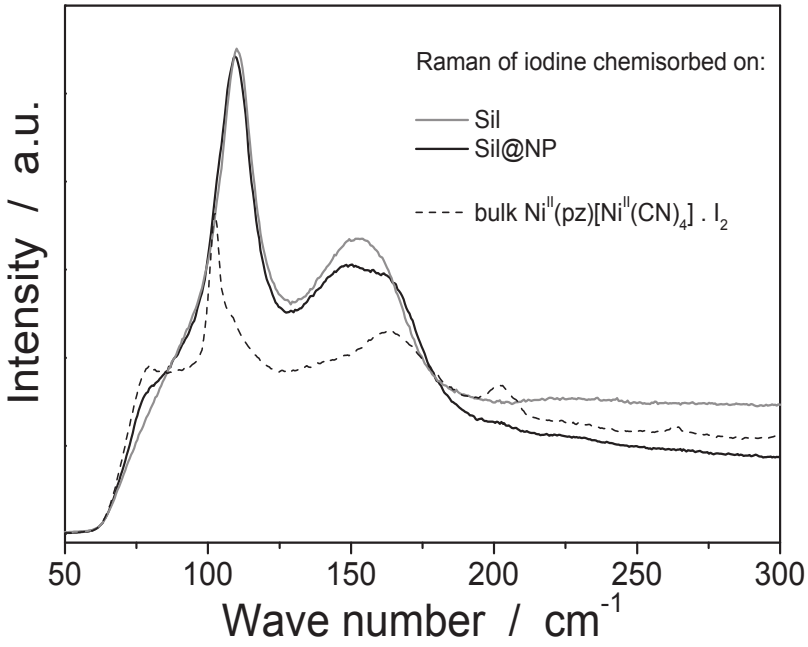

Figure 15 – Raman spectra for iodine-loaded silicas and bulk $Ni^{II}(pz)[Ni^{II}(CN)_4]$.

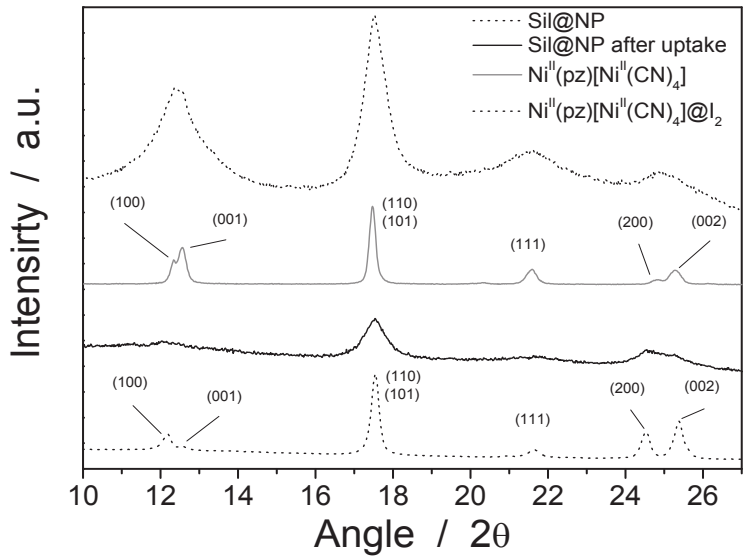

Figure 16 – Comparative XRPD for Sil@NP and bulk $Ni^{II}(pz)[Ni^{II}(CN)_4]$ before and after iodine capture.

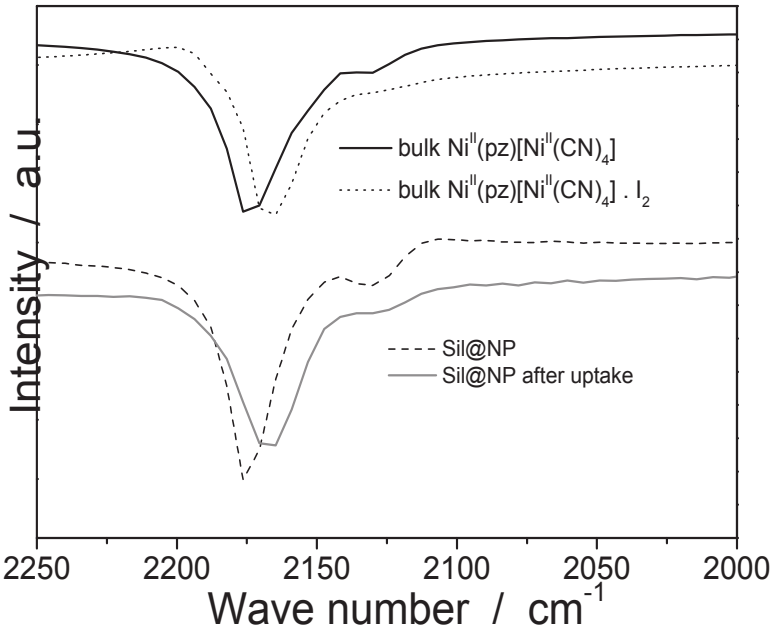

Figure 17 – FT-IR spectra for silica and bulk $Ni^{II}(pz)[Ni^{II}(CN)_4]$, before and after iodine capture.

2.1.2 - Porous glass beads based nanocomposite (Glass@NP) containing $Ni^{II}(pz)[Ni^{II}(CN)_4]$ nanoparticles and the iodine entrapment.

Mesoporous glasses (Figure 18) coming from Vitrabio® with pore size of approximately 30 nm and grain sizes from 200 to 500 µm were also used to prepare the nanocomposite Glass@NP containing nanoparticles of $Ni^{II}(pz)[Ni^{II}(CN)_4]$. They are composed mainly by SiO_2, with a very low content of other elements as Na. Since the declared surface area for the glass beads was around 130 $m^3.g^{-1}$, the beads had to be activated overnight at 150 °C under vacuum, in order to incentivise the following deposition of the grafting agent. During this activation process, indeed, the number of reactive silanols (≡Si-OH) on the surface was increased by elimination of water molecules providing more anchoring sites for the grafting agent. The grafting process was performed by using the same procedure as in the case of the silica matrix but without stirring to avoid breaking the beads. The diamine-grafted beads were labelled as *Glass*. Elemental analyses gave: C, 5.45%; N, 2.16%; H, 1.42%. Hence, an amount of 9 wt% of grafting agent was estimated. That meant that the deposition of the grafting ligand, expressed as grams per unit surface, was $6.9 \cdot 10^{-4}$ g/m^2 for *Glass* and $2.4 \cdot 10^{-4}$ g/m^2 for *Sil*: the activation of the glass beads actually brought to a higher surface density of grafting agent. The *Glass* sample exhibited a decrease of the specific surface to 83 $m^2.g^{-1}$ and pores around 30 nm.

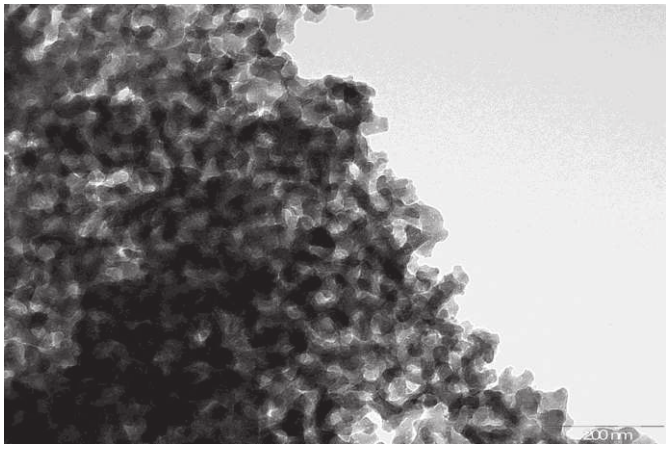

Figure 18 – TEM image of VItrabio glass beads.

The nanoparticles growth was performed as previously illustrated for the mesoporous silicas-based materials. Agitation was performed on a vibrating plate at 150 rpm, to avoid to break the beads with the magnetic stirrer. Difficulty in performing the extractive replica on glass beads hindered a direct observation of the nanoparticles, so that to confirm the presence of grown $Ni^{II}(pz)[Ni^{II}(CN)_4]$ both solid

UV-VIS and infrared spectroscopy were used. The UV-VIS spectrum of Glass@NP showed the typical band for the $Ni^{II}(pz)[Ni^{II}(CN)_4]$ at 550 nm (Figure 19). Infrared spectroscopy indicated the cyanide band at 2172 cm^{-1}, close to the value for the bulk compound.

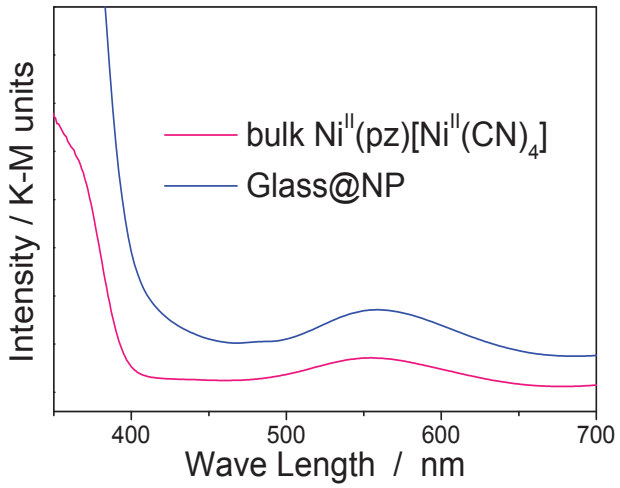

Figure 19 – reflectance mode UV-VIS specta for Glass@NP and $Ni^{II}(pz)[Ni^{II}(CN)_4]$.

TGA curves (Figure 20) show the decomposition of the grafting agent after 250 °C and decomposition of $Ni^{II}(pz)[Ni^{II}(CN)_4]$ at 350 °C, as it was observed for Sil@NP. With EDX analysis weight ratio Ni/Si = 0.24 (molar ratio Ni/Si = 0.11) was detected, which corresponded to a deposition of 18 wt% of nanoparticles inside the pores of the glass beads.

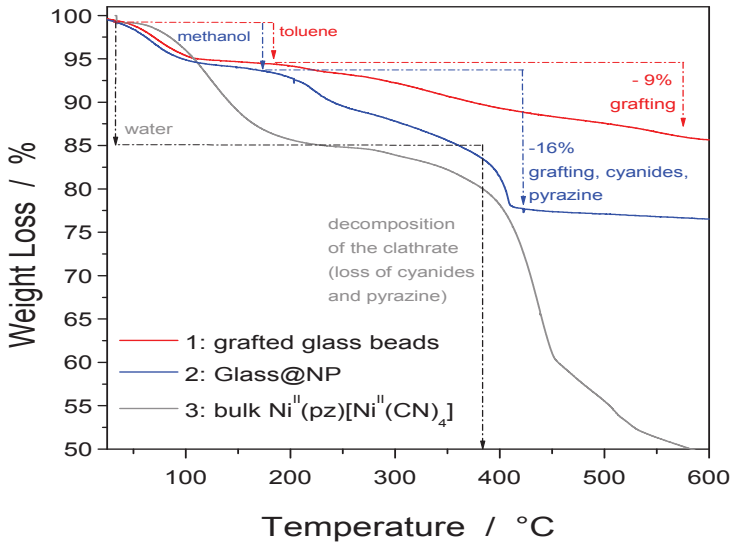

Figure 20 – TGA curves for the glass beads and Glass@NP.

BET and BJH methods were then used on the N_2 adsorption isotherms to determine the evolution of the specific surface area and accessible porosity. Isotherms for all glass beads-based materials (type IV), reported in (Figure 21) showed a very narrow hysteresis due to the large size of the mesopores. The initial glass beads have a SSA = 130 m^2g^{-1} with average pore size ≈ 40 nm. After grafting SSA decreased to 83 $m^2.g^{-1}$ with pore size between 25 and 40 nm. Finally, Glass@NP nanocomposite exposed a low surface around 66 $m^2.g^{-1}$ due to partial occupation of the porosity. Anyway, average pore size between 20 and 30 nm was still detected for Glass@NP.

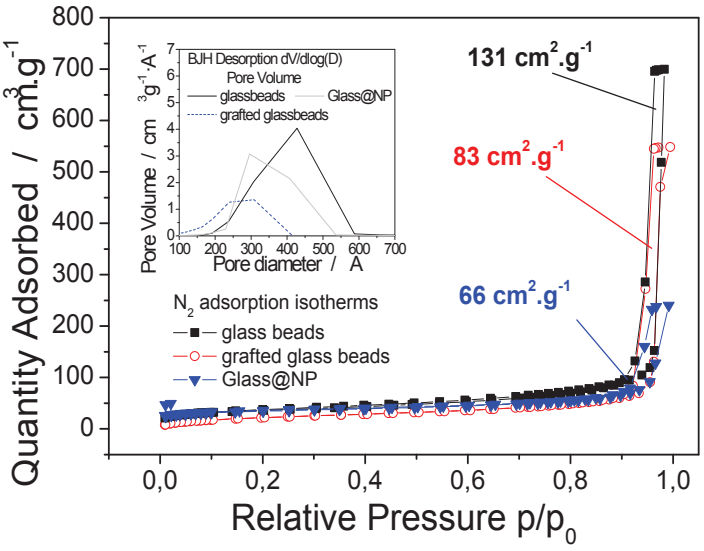

Figure 21 – Nitrogen adsorption isotherms for glass beads, Glass and Glass@NP.

The nanocomposite Glass@NP was then tested for the iodine entrapment in cyclohexane solution. The kinetic study reported that diamine-grafted beads entrapped iodine at lower rates than the bulk $Ni^{II}(pz)[Ni^{II}(CN)_4]$, but the presence of nanoparticles speeded up the capture with respect the grafted glass beads (Figure 22). The tendency was the same as for the silica-based materials, *i.e.* an equilibrium time of 14 hours for Glass@NP and Sil@NP and 48 hours for *Sil* and *Glass*.

Room temperature isotherms in solution showed that the maximal capacity observed was 1.1 ± 0.1 $mmol.g^{-1}$ (28 wt%) for the Glass@NP and 2.1 ± 0.1 $mmol.g^{-1}$ (53 wt%) for the *Glass* (Figure 23). The lower capacity with respect to the silica-based materials is consistent with the lower amount of deposited grafting agent and consequent lower quantity of nanoparticles. The decrease in amount of NPs anyway does not seem linear with the decrease in capacity. Indeed, Glass@NP with respect to the amount of NPs had a better efficiency probably due to larger pores and better accessibility to the iodine solution, than Sil@NP.

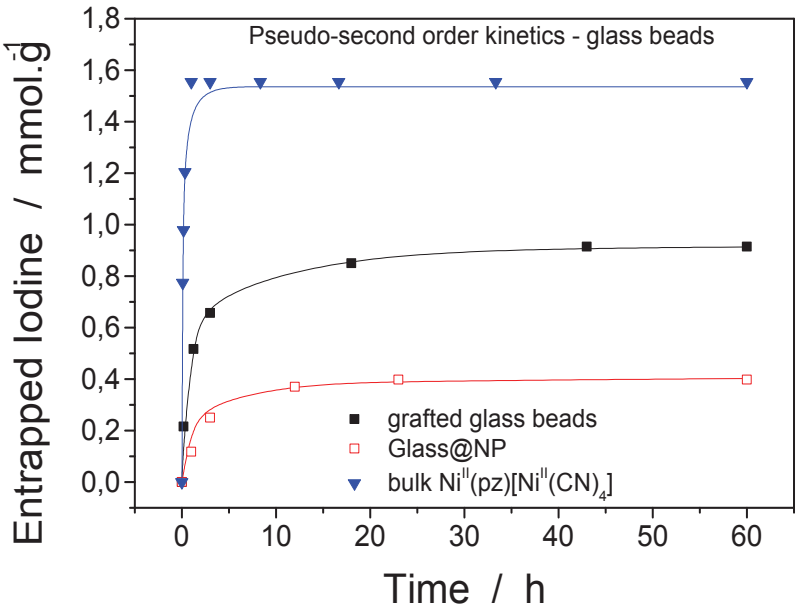

Figure 22 - Kinetics for glass bead.

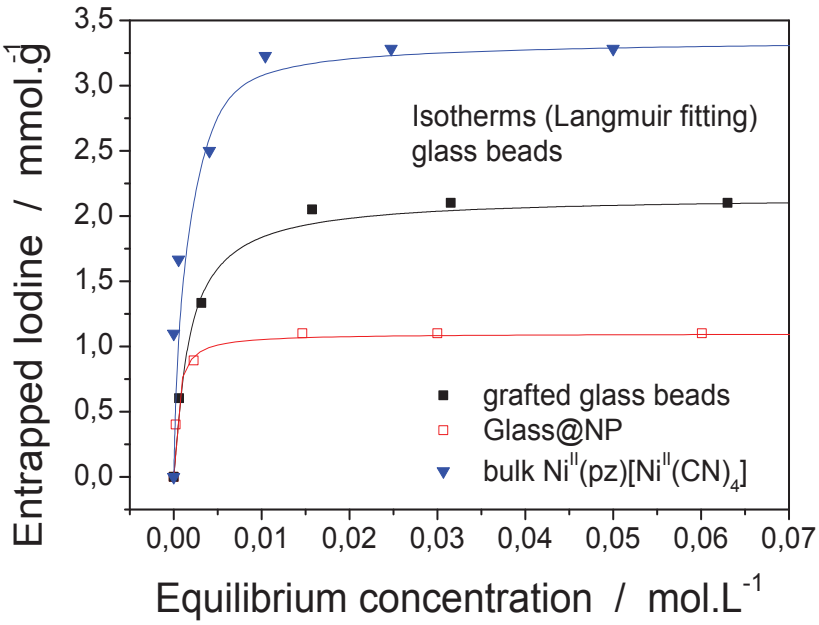

Figure 23 - Isotherms for glass beads.

About the UV-VIS spectra registered in reflectance mode, when iodine was confined on *Glass*, a different spectrum was observed with respect to *Sil* (Figure 24): two bands were present, suggesting the presence of I_5^- due to interaction between I_3^- (360 nm) and confined I_2 (450 nm). The colour of this sample was indeed red, whereas the grafted silica with iodine was yellow (preferential formation of I_3^-). We stated that the polyiodide I_5^- may be present because the thermal decomposition occurred in two steps: 1) $I_5^- \rightarrow I_3^- + I_2$ (low temperature) and 2) decomposition of I_3^-

(high temperature). The reason of the different interaction on *Glass* with respect to *Sil* was not totally clear. A possible explanation could be the eventual contribution given by residual Si-OH groups on the glass bead surface. The OH group may create an interaction similar to the iodine in the ethanol, that brings to the formation of a I_3^-/I_5^- solution due to partial charge transfer. When nanoparticles were deposited within the porosity of the glass beads (Glass@NP), the material turned black and a larger UV-VIS band around 500-550 nm appears after uptake, indicating a predominant presence of I_2 located inside the nanoparticles.

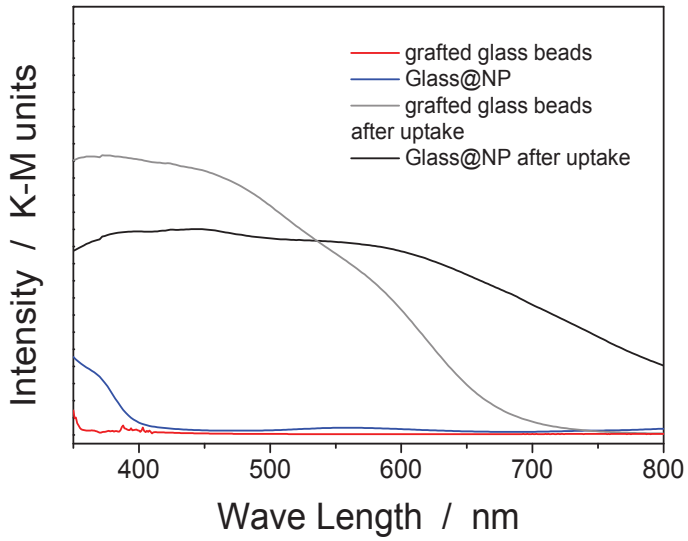

Figure 24 - UV-VIS spectra for Glass, Glass@NP and related iodine-loaded materials.

Raman spectra show as well a difference with respect to the silica-based materials. For the iodine on *Glass* three bands were detected: two bands for I_3^-, *i.e.* the symmetric ν(I-I) mode at 110 cm^{-1} and the asymmetric ν(I-I) mode at 150 cm^{-1}, and an additional band at 160 cm^{-1} for the interacting I_2 in the complex I_5^-. This third band broadened a little up to 170 cm^{-1} after uptake with Glass@NP as result of increase in I_2 content. Again, this extra I_2 amount had to be located in the nanoparticles.

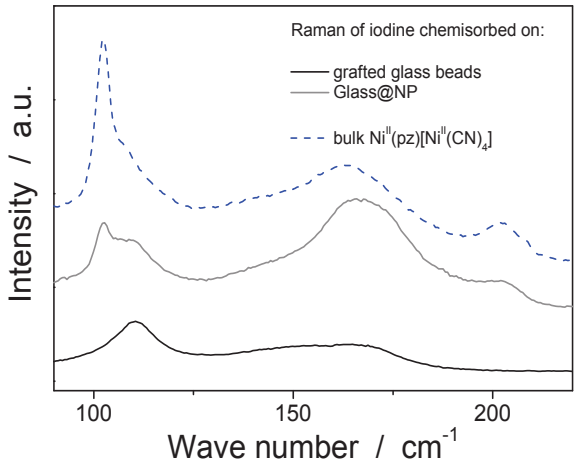

Figure 25 - Raman spectra for iodine-loaded glass beads and bulk $Ni^{II}(pz)[Ni^{II}(CN)_4]$.

In the next section the thermal analyses on the iodine-loaded materials are discussed, together with the possibility of reversible desorption of iodine.

2.1.3 - Cycling ability of Sil@NP and Glass@NP.

As demonstrated in the previous chapters with bulk $Ni^{II}(pz)[Ni^{II}(CN)_4]$, a full regeneration after iodine capture was possible by heating the iodine clathrate in the temperature range 150-300 °C. However, full reversibility for Sil@NP and Glass@NP could not be achieved, because of the presence of the chemisorbed polyiodides on the diamine grafting stable up to 270 °C, which is also the decomposition temperature of the grafting agent. Nevertheless, the large portion of molecular iodine entrapped in the nanoparticles could eventually be desorbed and a cycling ability can be studied as well. The desorption process also permitted a better quantification of iodine and iodides. The temperature range where iodine desorption was allowed without decomposing the material Sil@NP was 150-270 °C which was shorter than the range for the bulk clathrate, as seen in Figure 26. Upon decomposition of the diamine, the nanoparticles are not anchored anymore to the silica matrix, so that 270 °C was considered the decomposition temperature of the nanocomposite. Because of this upper limit, iodine was removed at 250 °C for 4 hours. Desorbed material was analyzed at solid UV-VIS spectroscopy and no band for the confined I_2 was anymore detected, but only the I_3^- band at 360 nm (Figure 27, curve 3). TGA of the desorbed material also shows only loss at 270 °C (Figure 26, green curve).

MEB/EDX analysis reported I/Ni molar ratio = 0.20, meaning that 0.25 mmol.g^{-1} of I_2 were still chemisorbed on the grafting as I_3^-/I^+ and about 1.49 mmol.g^{-1} of I_2 was thermically removed from the nanoparticles. Thus we can estimate that nanoparticles, when filled with iodine, have formula $Ni^{II}(pz)[Ni^{II}(CN)_4]\bullet 1.15I_2$ which was close to the observed formula for the bulk clathrate $Ni^{II}(pz)[Ni^{II}(CN)_4]\bullet I_2$.

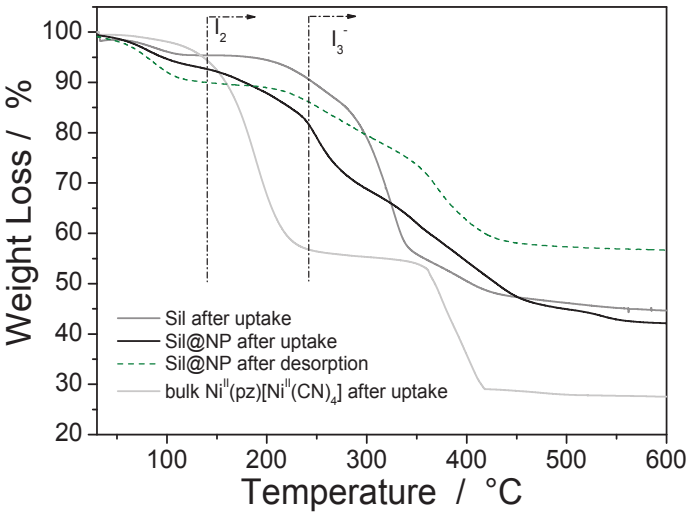

Figure 26 - TGA curves: mesoporous silicas; after uptake and comparison with clathrate $Ni^{II}(pz)[Ni^{II}(CN)_4]$. I_2.

A second cycle of capture in an iodine solution $6.6\bullet 10^{-2}$ M gave a close maximal capacity, as detected by TGA. The sample showed newly UV-VIS band at 470 nm (Figure 27, curve 4). Finally, desorption after second cycle removed again the molecular iodine off the nanocomposite (Figure 27, curve 5) showing, indeed, cycling ability.

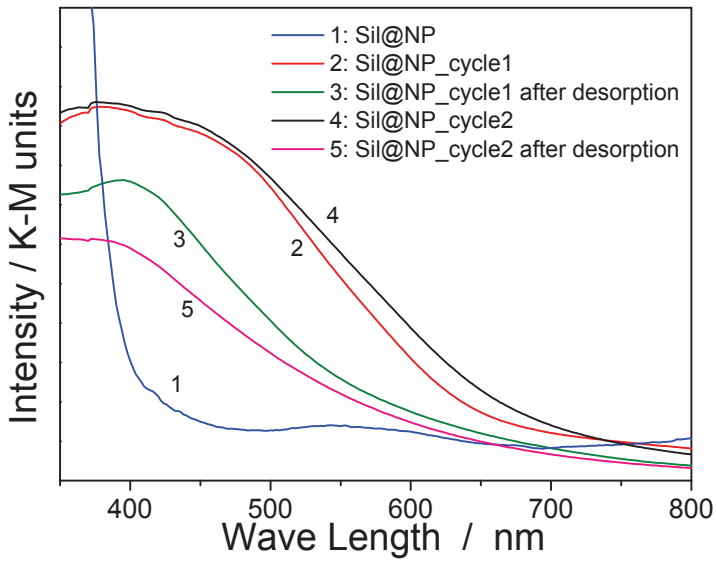

Figure 27 - Cycling ability for the Sil@NP nanocomposite.

In the case of Glass@NP, thermal analyses showed a partial release of iodine below 250 °C even for the grafted glass beads. This must be due to the partial decomposition of the pentaiodides I_5^- that triggered the release of I_2 and left chemisorbed I_3^-, which was later decomposed with the grafting agent.

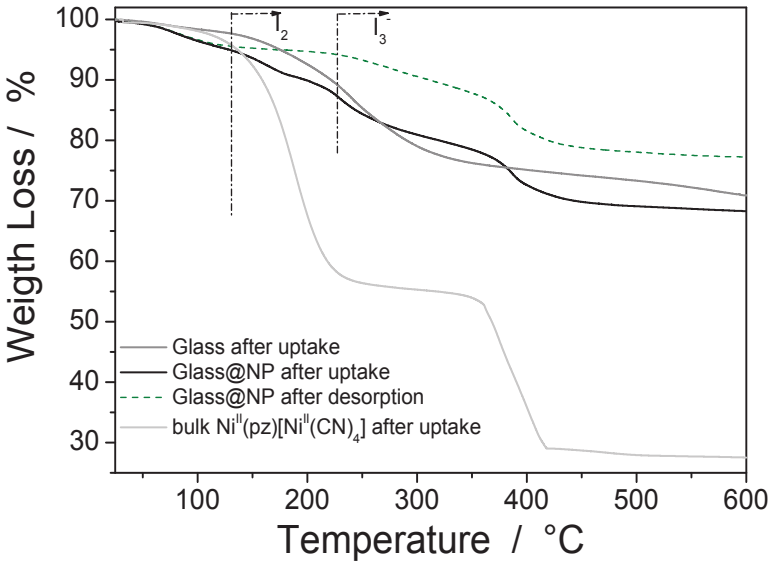

Figure 28 - TGA curves: glass beads after uptake and comparison with clathrate $Ni^{II}(pz)[Ni^{II}(CN)_4]$. I_2

The presence of I_5^- on the diamine ligand did not allow a simple observation of the reversibility, anyway it was clear that the UV-VIS spectrum changed after desorption and the intensity of the confined I_2 band increased with the uptake and decreased with the desorption (Figure 29, curve 3). After the first desorption a molar ratio I/Ni = 0.12 is found at EDX, indicating that 0.07 mmol.g^{-1} of iodine were still chemisorbed and that 1.03 mmol.g^{-1} were thermically decomposed. The molar ratio between the nanoparticles amount and removed iodine was $Ni^{II}(pz)[Ni^{II}(CN)_4]$@1.82 I_2, which was higher than the actual capacity of the clathrate. Explanation for this difference was that, since I_5^- was formed on the diamine, an imprecise amount of I_2 was partially desorbed from the diamine as well. The TGA of the desorbed Glass@NP however did not show any loss anymore before 250 °C for the iodine indicating that mainly I_3^- remained after desorption. That meant, that for the glass beads-based nanocomposite a partial reversibility from the grafting was observed as well, even though an exact quantification of I_2 and I_3^- was possible since not all I_5^- decomposed after thermal treatment. Cycling ability for Glass@NP was performed for a second cycle of capture and subsequent desorption (Figure 29, curves 4 and 5). Intensities of bands suggested that a partial reversibility existed even though the complexity for this system did not allow a precise description.

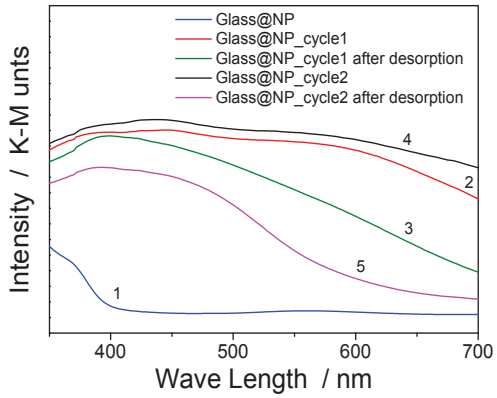

Figure 29 - Cycling ability for the Glass@NP nanocomposite.

Finally, the reversible desorption of the iodine inside the nanoparticles was observed by FT-IR spectroscopy. The spectra of Sil@NP and Glass@NP after desorption at 250 °C indicated the ν(C≡N) mode at 2175 cm^{-1} (initial value before iodine uptake at 2174 cm^{-1}). Also, FT-IR spectra registered after a thermal treatment at 300 °C did not show any band for ν(C≡N) due to decomposition of the material. The evolution in temperature for the ν(CN) mode on both iodine-laded nanocomposites is reported in Figure 30.

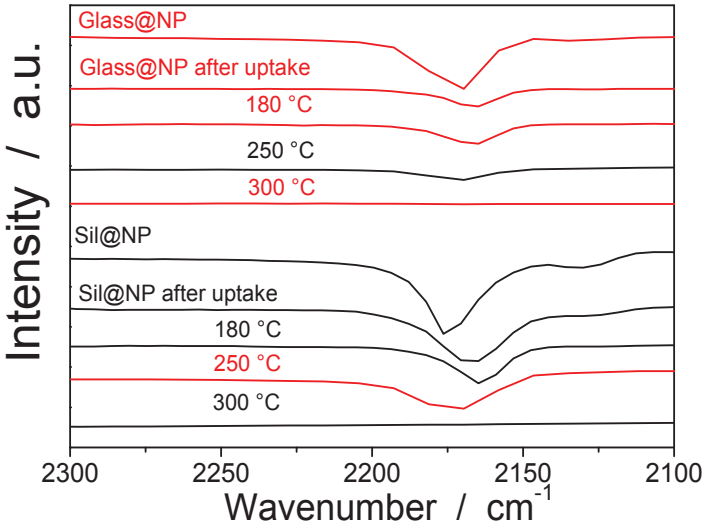

Figure 30 - Evolution in temperature of the stretching mode.

The next and the last section will introduce a different topic, with respect to the previous discussion: supported nanoparticles of Prussian Blue analogues will be evaluated for the selective entrapment of Co^{2+} in aqueous mean. Then the conclusions for families of nanocomposites will be reported at the end of the chapter.

2.2 - Nanocomposites of Prussian Blue for the selective entrapment of cobalt.

Beyond the out-gases decontamination of the reprocessing processes, another relevant issue is the decontamination of the water used to cool down the core of the nuclear power plant from the fission products. The most abundant are the γ-emitter $^{134}Cs^{+}$ and $^{137}Cs^{+}$ (life-time about 30 years) but also other radioactive isotopes as $^{90}Sr^{2+}$, $^{63}Ni^{2+}$, $^{60}Co^{2+}$ and actinides that are produced demanding specific selective decontaminations.[22] Production of these radionuclides also occurs in laboratories and medical clinics for radiotherapy so that the issue is not forcedly limited to nuclear power plants. Specifically for the $^{60}Co^{2+}$, this radionuclide has a life-time of 5.27 years and decays to stable Ni, with massive activity $4.2 \cdot 10^{13}$ $Bq.g^{-1}$.[30] If ingested with water or inhaled with dust, it can reach vital organs through the blood (liver, kidney, bones) and then it is expelled with urines after a period that can last 800 days. Long exposure to γ-rays is the cause of genetic mutations and cancer occurrence.[31] Typical medical treatments for $^{60}Co^{2+}$ consist in administration of 0.5 g of DTPA (diethylene triamine pentaacetic acid) that complexes the cation Co^{2+} and the complex is expelled with urines. The European directive 96/29/EURATOM reported that for an average adult the efficient dose of ^{60}Co over a period of 50 years is around 1.1 10^{-8} $Sv.Bq^{-1}$ by inhalation of aerosols (1 μm) and $3.4 \cdot 10^{-9}$ $Sv.Bq^{-1}$ by ingestion. The same directive imposed a maximal annual exposure of 1 mSv in the case of publics and 50 mSv in the case of workers. State of art for the decontamination of Co^{2+} from water, not limited to the nuclear fields, includes polyurethane foams,[32] ion exchange resins as IRN77 and SKN1[33] and Lewatit MonoPlus SP 112,[34] ion exchange Na-zeolites[35] and H-zeolites.[36] With the development of mesoporous materials in the 90s it was suggested to use functionalized silicas for the entrapment of cations in water in several fields of application. The silicas were functionalized with organic molecules disposing of –SH or NH_2 groups that could complex with a large set of bivalent metals: for instance, Schiff base ligands,[37] cyanide and carboxylate groups,[38] 1,4-bis(3-aminopropyl)piperidine,[39] 5-amino-1,3,4-thizdiazole-2-thiol,[40] 5-formyl-8-hydroxyquinoline,[41] 2-(2-pyridyl)ethyl groups,[42] 3-mercaptopropyl groups,[43] dithiocarbamate,[44-45] poly(ethyleneimine),[46] acetylacetone,[47] thioglycolic acid.[48] These already existing systems anyway do not show selectivity against competitive cations as K^{+}, Na^{+}, Ca^{2+} that can be present in water. Alternative solutions were found in the last decades in the domain of the coordination chemistry. The coordination polymer $Fe^{III}_4[Fe^{II}(CN)_6]_3$, historically known as Prussian Blue, was initially used exclusively as colorant for painting and dying since the 18th century. Later in the 20th century, researchers found later potential applications of this compound, due to the microporosity (≈5 Å) of this compound and its analogues. As reported in the introduction to this chapter, Prussian Blue was then used for the sorption of $^{137}Cs^{+}$ in waste nuclear solutions.[49] Due to the biocompatibility of $Fe^{III}_4[Fe^{II}(CN)_6]_3$ it was also studied as ingestible

medical treatment for the body decontamination, after the Chernobyl accident in 1986.[50] The US Food and Drug Administration (FDA) authorized in 2003 the use of this compound, under the name Radiogardase®, to treat people exposed to $^{137}Cs^{+}$ contamination.[51] As reported in the introduction to the present chapter, the different analogues of Prussian Blue were studied as supported nanoparticles for the selective capture of $^{137}Cs^{+}$ and other radionuclides. In the present thesis, for the entrapment of the bivalent cobalt in aqueous solution we considered silica-based materials functionalized with Prussian Blue, $Fe^{III}_4(Fe^{II}(CN)_6]_3$, and analogue structures with precursors $Ni^{II}/[Fe^{III}(CN)_6]^{3-}$ and $Cu^{II}/[Fe^{III}(CN)_6]^{3-}$. The preparation of the mesoporous silica was prepared according to the same protocol in the previous section, consisting of of *step-by-step* impregnation of mesoporous silicas. The silicas exposed a specific surface area of around 700 $m^2.g^{-1}$ with average pore size 10-15 nm. Moreover, the silicas has no ordered mesostructure due to the use of mesytilene that triggered the maturation of larger and disordered pores with enhanced accessibility. Also, the grafting agent was again a bidentate organic molecule as a diamine. For the infiltration with the precursors of Prussian Blue analogues, two different protocols were considered: P1) deposition of molecular fragments; P2) growth of nanoparticles.

In protocol P1, the silica was infiltrated with a methanolic solution 10^{-2} M of $M'(BF_4)\cdot 6H_2O$ (where M' could be Fe^{2+}, Ni^{2+} or Cu^{2+}) for 24 hours. The material was then filtered under vacuum and washed with pure methanol. In the second step the material, on which the cations were desposited, was infiltrated with a methanolic solution 10^{-2} M of tetrabutyl ammonium hexacyanoferrate for 24 hours. This method was intended to depose only one layer of precursors without triggering the growth of nanoparticles as illustrated in Figure 31. Since just one cycle of infiltration was carried out to obtain the final materials, the samples were labelled 1-M where M is the different cation (1-Fe, 1-Ni and 1-Cu).

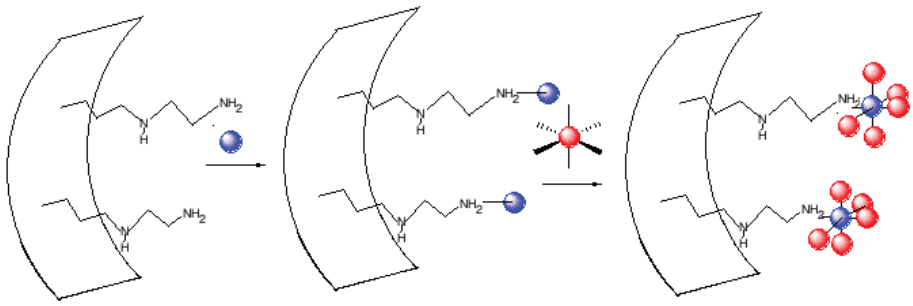

Figure 31 - Protocol P1: deposition of molecular fragments.

The prepared materials exhibited the following colours: light blue for 1-Fe, light yellow for 1-Ni and light purple for 1-Cu. BET method applied on the N_2 adsorption isotherm indicated 111 $m^2.g^{-1}$ for 1-Fe and 110 $m^2.g^{-1}$ for 1-Ni $m^2.g^{-1}$, with pore size ranging from 4 to 8 nm according to BJH method on the desorption branch. Only 21 $m^2.g^{-1}$ were found for 1-Cu, even though BJH method indicated pore size between 5 and 10 nm. Then the materials

were characterized by FT-IR spectroscopy in KBr matrix. The main vibration modes of cyanides that were observed were the stretching $\nu(C\equiv N)$ in the range 2000-2100 cm^{-1} and the bending δ(M-CN) at lower frequencies (500-400 cm^{-1}). In the case of 1-Fe only one intense band for $\nu(C\equiv N)$ was detected, whereas 1-Ni and 1-Cu showed two distinct bands for $\nu(C\equiv N)$ indicating probably different arrangements of cyanides as terminal and bridging cyanides (Table 2). Since only one layer of precursors was deposited, we did not expect a good organization of the building blocks in 3-D structures. The values for the stretching mode of the cyanide in the three materials (lower bands for 1-Ni and 1-Cu) was actually lower than expected.[52] It was assumed that the building blocks $[Fe^{III}(CN)_6]^{3-}$ actually reduced to $[Fe^{II}(CN)_6]^{4-}$.

Table 2 - IR-active modes for cyanides in 1-M series

	$\nu(C\equiv N)$	δ(M-CN)
1-Fe	2041 cm^{-1}	466 cm^{-1}
1-Ni	2096 cm^{-1}; 2059 cm^{-1}	464 cm^{-1}
1-Cu	2100 cm^{-1}; 2036 cm^{-1}	464 cm^{-1}

The weight percentages of deposited moieties was estimated by SEM/EDX, knowing that on the mesoporous silica an average amount of 15 wt% of organic grafting agent was deposited. For all materials, detected amount of Si was converted in weight of SiO_2 (molecular weight = 60 $g.mol^{-1}$) and the multiplied by coefficient 1.15 to consider the proportional weight increase after reaction with the organic grafting. The so calculated amount was the relative weight of the amount labelled *Sil*. The amount of Fe detected for 1-Ni and 1-Cu was proportionally converted in weight of $[Fe(CN)_6]^{4-}$ (molecular weight = 211.8 $g.mol^{-1}$) and summed to the weight of Ni or Cu amount. The sum of precursors constituted the amount labelled *NP*. Both *Sil* and *NP* were divided over the sum *Sil* + *NP* to obtain an estimated weight percentage of deposited precursors per gram of diamine-grafted silica. Final percentages were 8.6 wt% for 1-Ni and 6.6 wt% for 1-Cu. In the case of 1-Fe, since no distinction among the precursors Fe^{2+} and $[Fe(CN)_6]^{3-}$ was possible by EDX and it could be erroneous to consider the molar weight of 3-D structure $Fe^{III}_4(Fe^{II}(CN)_6]_3$, it was assumed that the molar ratio $Fe^{2+}/[Fe(CN)_6]^{4-}$ was close to 1.33; this was indeed the molar ratio for $Ni^{2+}/[Fe(CN)_6]^{2-}$ in the material 1-Ni. These considerations brought to estimate ≈ 11 wt% of precursors in 1-Fe.

In protocol P2, the diamine-grafted silica was infiltrated with a methanolic solution 10^{-3} M of $M'(BF_4)\cdot 6H_2O$ (M' could be Fe^{2+}, Ni^{2+} or Cu^{2+}) for 2 hours. After washing with pure methanol, the material was infiltrated with methanolic solution 10^{-3} M of $[N(C_4H_9)_4][Fe^{III}(CN)_6]$ for 2 hours. The cycle was repeated in total 5 times, to saturate the porosity with the growth of nanoparticles (Figure 32). The materials were labelled 5-M, where M is the different used cation (5-Fe, 5-Ni, 5-Cu).

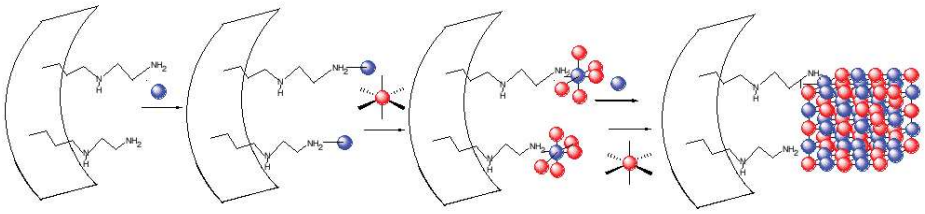

Figure 32 – Protocol P2: deposition of nanoparticles

The final materials exhibited the typical colours for the respective bulk PB's analogues: dark blue for 5-Fe, intense yellow for 5-Ni and dark purple for 5-Cu. BET method applied on the N_2 adsorption isotherm indicated very low specific surface areas for all the samples. FT-IR spectra registered in KBr matrix reported more intense bands for $\nu(C\equiv N)$ and δ(M-CN) with respect the large signal of Si-O bonds around 1100 cm^{-1}. Note that the values for $\nu(C\equiv N)$ registered for the series 5-M (Table 2) were generally higher with respect to the values recorded for the series 1-M (Table 2), due to the formation of bridging cyanides Fe-C≡N-M to create the 3-D structures (nanoparticles). The values match with reported data in literature for nanoparticles of Prussian Blue ananlogues.[53,54] Also, bands confirmed that in the materials 1-Ni and 1-Cu the cyanides were partially bridging. Indeed, the band at 2098 cm^{-1} in 5-Ni matched with band at 2096 cm^{-1} in 1-Ni (regardless the small difference) and band at 2100 cm^{-1} was present in both 1-Cu and 5-Cu. In the region of δ(M-CN) all materials 5-M showed several values indicating an heterogeneous arrangement of the coordinated cyanides. Also, the weak mode ν(M-CN) was visible for the series 5-M around 590 cm^{-1}.

Table 3 - IR-active modes for cyanides in 5-M series.

	$\nu(C\equiv N)$	ν(M-CN)	δ(M-CN)
1-Fe	2080 cm^{-1}	596 cm^{-1}	482 cm^{-1}; 464 cm^{-1}
1-Ni	2098 cm^{-1}	591 cm^{-1}	482 cm^{-1} (shoulder); 462 cm^{-1}
1-Cu	2100 cm^{-1}	589 cm^{-1}	481 cm^{-1}; 468 cm^{-1} (shoulder)

Estimation of the amount of precursors deposited on the support after 5 cycles was carried out the same way as for the series 1-M. Final weight ratios were: 31 wt% for 5-Ni, 25 wt% for 5-Fe and 18 wt% for 5-Cu. To estimate the size of the nanoparticles, we registered

XRPD on the samples as well as TEM images. The diffraction patterns indicated the typical pattern of nanoparticles, with large peaks (Figure 33). The curved baseline was due to the amorphism of the silica. For 5-Ni and 5-Cu the Miller planes (200) and (220) were easily recognized by comparison with published XRPD patterns for Prussian Blue in literature.[55] In the case of 5-Fe, the peaks were less intense and diffraction of plane (200) was the most visible.

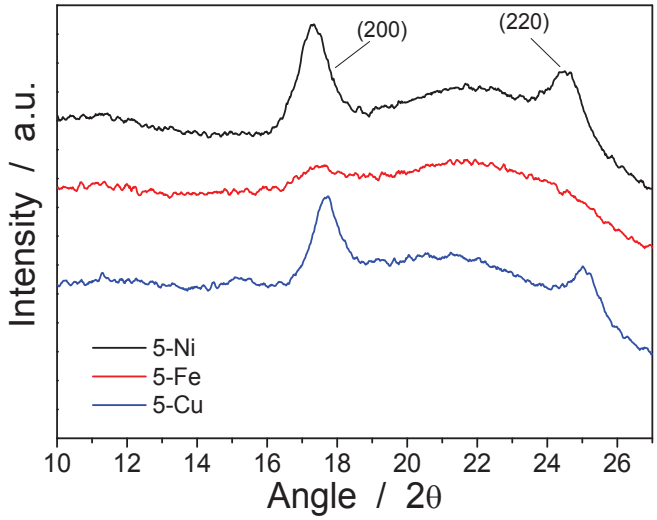

Figure 33- XRPD for series 5-M.

The mean size (τ) of the nanoparticles were estimated with the Sherrer's law on the main peak around $2\theta = 17°$:

Equation 1 - Scherrer equation

$$\tau = \frac{K\lambda}{\beta cos\theta}$$

where K is the shape factor usually ≈ 0.89; λ is X-ray wavelength 0.154 nm (Cu target); β is the broadening at mid-height of the main peak and θ is the diffraction angle. Calculations were supported by software X'Pert. Obtained mean sizes were 8.9 nm for 5-Fe, 9.1 nm for 5-Ni and 14.4 nm for 5-Cu. These values match with the mean pore diameter in a diamine-grafted silica prepared with mesytilene (≈ 7-15 nm). Also, the lattice parameters of the cubic unit cell were estimated on the peak (200) around $2\theta = 17$. The atomic distance obtained with Bragg's law were multiplied by 2 to obtain the parameter *a*. The materials showed very close lattice parameters (Figure 33).

Table 4 - Lattice parameters and mean size of nanoparticles obtained from (200) peaks.

	Lattice Parameter *a*	Scherrer's mean size
5-Ni	10.2 Å	8.9 nm
5-Fe	10.2 Å	9.1 nm
5-Cu	10.0 Å	14.4 nm

Extractive replica with HF were carried out as well, to directly observe using Transmission Electronic Microscopy (TEM) the nanoparticles. Images indicated the presence of nanoparticles (Figure 34).

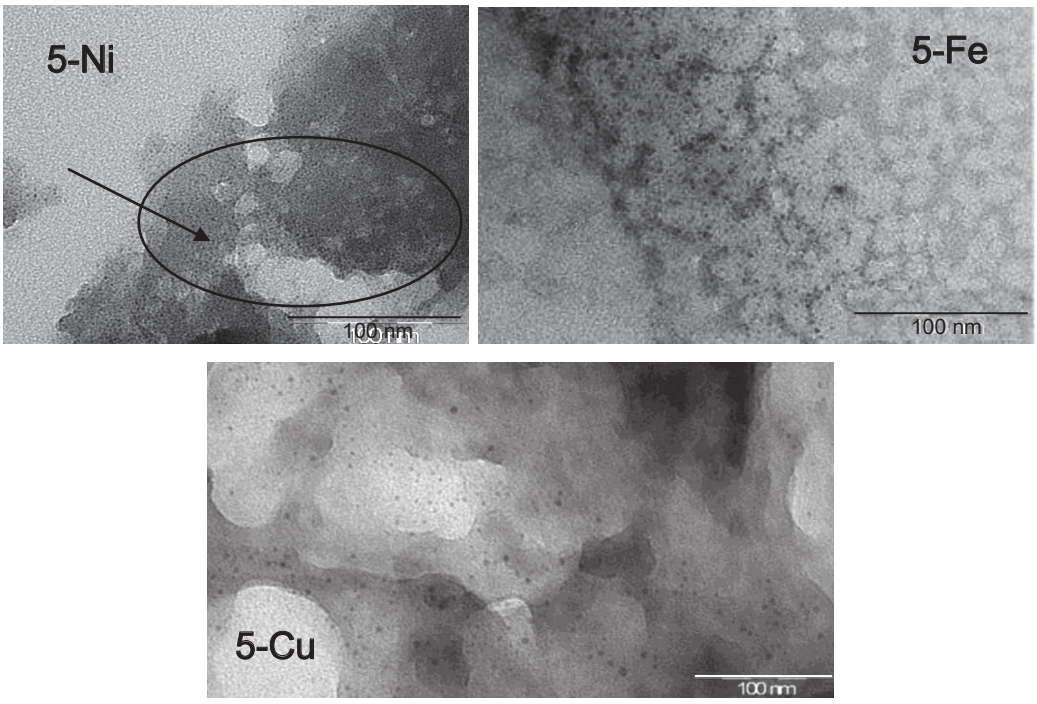

Figure 34 - TEM images of nanoparticles extracted from materials of 5-M series. The scale reported for 5-Ni is the same as for 5-Fe and 5-Cu.

Once the materials 1-M and 5-M were characterized, we proceeded with the adsorption analyses to entrap the Co^{2+} in aqueous solutions. All captures were carried out in solutions of stable $Co^{II}(NO_3)_2 \cdot 6H_2O$ in distilled water. All residual concentrations after capture were analyzed by ICP technique at the ICSM (Marcoule), in collaboration with Dr. Agnès Grandjean. For the kinetic study, we chose initial concentration 10^{-3} M and times of analysis 0, 2, 6 and 24 hours. For the series 1-M, the kinetic curves are reported in Figure 35. The curves were fitted with a pseudo-second order model that is generally adapted to phenomena of adsorption on solids. The equilibrium time was around 10 hours.

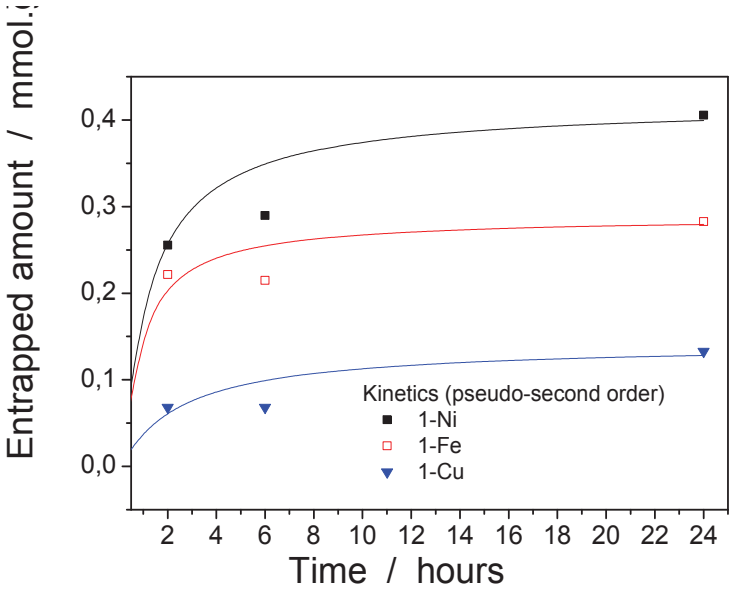

Figure 35 - Kinetic curves for the series 1-M.

Comparison between the entrapped amounts after 24 hours at the concentration of 10^{-3} M indicated that 1-Ni showed the best performance (0.40 mmol.g^{-1}) and 5-Cu was the weakest adsorbent (0.11 mmol.g^{-1}). Material 1-Fe indicated an adsorption of 0.25 mmol.g^{-1}. In this type of materials, the cobalt was expected to coordinate to terminal cyanides or be exchanged with cations M^{2+}. ICP analyses showed that in the case of 1-Ni and 1-Cu, cations Ni^{2+} or Cu^{2+} were released off the material indicating that ion exchange occurred. Since Co^{2+} has the same charge as Ni^{2+} (or Cu^{2+}), the release of one cation corresponded to the adsorption of one Co^{2+}. To quantify how much Co^{2+} was entrapped by this mechanism, the following equation was used:

Equation 2 - Estimation of the exchanged Co^{2+}

$$\%\ of\ exchanged\ Co^{2+} = \frac{C_{fin,M^{2+}}}{(C_{in,Co^{2+}} - C_{fin,Co^{2+}})} \cdot 100$$

Where C_i are the initial concentration of Co^{2+} and C_{fin} are the final concentrations of Co^{2+} and exchanged M^{2+} cations. The relationship indicated 19% for 1-Ni and 11% for 1-Cu. The remaining amount of adsorbed Co^{2+} was supposed to coordinate with terminal cyanides. In the case of 5-Fe, no release of cations was detected. In this case the only mechanism was supposed to be the chemisorption on the terminal cyanides. FT-IR spectra were measured for 1-Ni and 1-Fe after the Co^{2+} entrapment. For 1-Ni, the initial band for $\nu(C\equiv N)$ at 2096 cm^{-1} (higher band, bridging cyanides) slightly decreased to 2091 cm^{-1} due to exchange with Co^{2+}. For 1-Fe, the only detected band at 2044 cm^{-1} shifted to 2070 cm^{-1} indicating that in this case terminal cyanides bridged the Co^{2+} cations forming the bond Fe^{III}-CN-Co^{II}.

In the case of the nanoparticles (series 5-M), cations can enter as well the microporosity (≈1 nm) of the lattice. To maintain the electroneutrality, however, two NO_3^- anions are expected as well to be physisorbed to balance the change of one Co^{2+}. The kinetics were performed on the series 5-M as well with starting concentration 10^{-3} M and by measuring the residual concentration after 2, 6 and 24 hours (Figure 36).

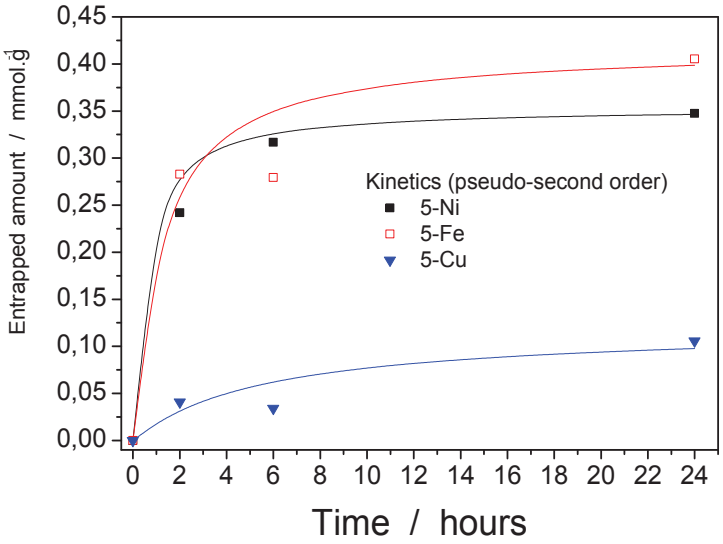

Figure 36 - Figure 37 - Kinetic curves for the series 1-M.

The equilibrium times did not change sensitively with respect to the 1-M series and were again around 10 hours. In the case of the series 5-M, the best performance was observed for 5-Fe (0.40 mmol.g^{-1}). The material 5-Ni showed a lower capacity (0.32 mmol.g^{-1}), whereas the analogue containing Cu^{2+} was again the weakest adsorbent (0.10 mmol.g^{-1}). With respect the series 1-Ni, the change in performance was different according to the composition so that it was not possible to establish which one between protocol P1 and protocol P2 was better. It was estimated that 35% of Co^{2+} entrapped by 5-Ni was captured by ion exchange, which is higher with respect to 1-Ni (19%). In the case of 5-Cu the amount of exchange Co^{2+} was always around 11%. Again, no exchange of Fe^{2+} was detected for 5-Fe. In the case of material 5-Fe, we can explain the lack of ion exchange since during formation of $Fe^{III}_4(Fe^{II}(CN)_6]_3$ a redox reaction occurred in the following way:

Equation 3 - Redox reaction during the preparation of Prussian Blue

$$Fe^{2+} \rightarrow Fe^{3+} + e^-$$
$$[Fe^{III}(CN)_6]^{3-} + e^- \rightarrow [Fe^{II}(CN)_6]^{4-}$$

so that the bivalent cation Fe^{2+} is coordinated with 6 cyanides and it is not available to exchange with Co^{2+}. FT-IR spectrum for 5-Fe after Co^{2+} capture, showed an increase of the $\nu(C\equiv N)$ mode from 2080 cm^{-1} to 2089 cm^{-1} due to formation of Fe^{II}-C≡N-Co^{II} bonds. FT-IR spectrum for 5-Ni after capture, by contrast, did not show any shift. In Table 5, capacities (Q) for all materials after capture with initial concentration 10^{-3} M are reported. The

advantage to have nanoparticles was clearly observed exclusively in the case of 5-Fe, with respect 1-Fe.

Table 5 - Amount of Co^{2+} captured at concentration 10^{-3} M and change in performance passing from 1-M to 5-M series.

	M = Fe	M = Ni	M = Cu
1-M [mmol.g^{-1}]	0.25	0.40	0.11
5-M [mmol.g^{-1}]	0.40	0.32	0.10

According to the captures performed at 10^{-3} M, material 1-Ni showed the best performance in the series 1-M and material 5-Fe was the best adsorbent of the series 5-M. Therefore, we decided to focus on these two materials to trace the isotherms for the adsorption of Co^{2+}. Several entrapments were performed at room temperature in the range 10^{-4} M - 10^{-2} M and then the entrapped amount were plotted as function of equilibrium concentrations. The isotherms reported in Figure 38 were obtained.

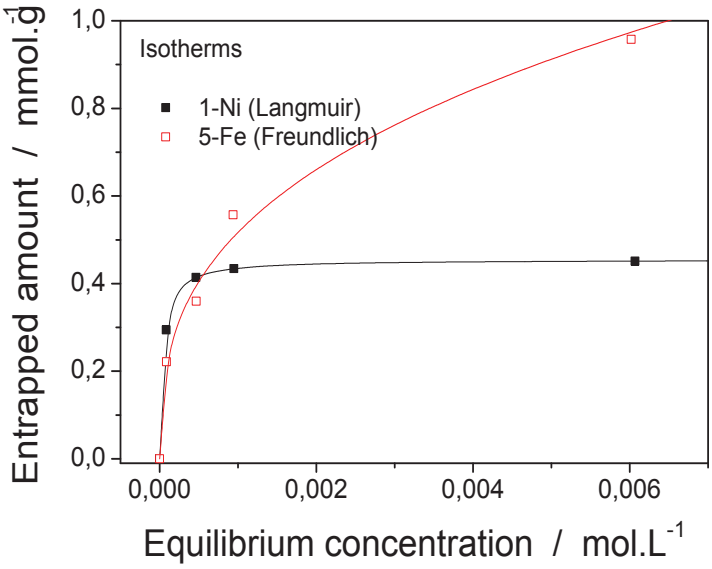

Figure 38 - Isotherms at room temperature for 1-Ni and 5-Fe.

The experimental isotherms were linearized with 3 different models: Langmuir, Freundlich and Temkin models (for a description of the models, see *Annexes*). In the case of M-Ni, best linearization was obtained with Langmuir model (R = 0,99). This model approximates very well chemisorption phenomena that stop at one monolayer of adsorbate onto the surface. The model indicated a maximal capacity of 0.45 mmol.g^{-1} and Langmuir constant k = 21990 L.mol^{-1}. In the case of 5-Fe, Langmuir linearization did not work at all. Freundlich linear form worked better with R = 0, 98 and it was employed for the fitting. Freundlich model is generally used to describe adsorption phenomena on heterogeneous surface.[56] This model is not helpful to estimate the maximal capacity. Approximately, we could say

that the maximal capacity must be around 1 mmol.g^{-1} which is higher with respect to material 1-Ni.

As extension of the work, the materials 1-Ni and 5-Fe were tested for the selective entrapment in 2 different type of complex solutions. In order to prepare the complex solutions, a simulant solution was furnished by ICSM with typical concentrations of the most important competitive cations as Ca^{2+}, Mg^{2+}, K^{+} and Na^{+} (Table 6) that are found in aqueous effluents.

Table 6 - Composition of the complex solution for the selectivity tests.

Nitrates	Sulfates	Ca^{2+}	Mg^{2+}	K^{+}	Na^{+}
33'593 ml.L^{-1}	758 ml.L^{-1}	45.5 ml.L^{-1}	49.1 ml.L^{-1}	57.2 ml.L^{-1}	15'000 ml.L^{-1}

The cation Co^{2+} is especially in competition with Mg^{2+} and Ca^{2+} since they are bivalent cations as well. However, a preferable adsorption of monovalent cations inside the nanoparticles could occur too, since high affinity of Prussian Blue was previously detected for Cs^{+}. The first type of solution (labelled *S-Co*) consisted of the complex solution with 10^{-4} M of $Co^{II}(NO_3)_2 \cdot 6H_2O$. A second type of complex solution (labelled *S-CoCs*) consisted in the simulant with 10^{-4} M of $Co^{II}(NO_3)_2 \cdot 6H_2O$ and $2 \cdot 10^{-4}$ M of $Cs^{I}(NO_3)$ as well, by considering the same equivalents of charges between Co^{2+} and Cs^{+}. The adsorbed amounts of Co^{2+} are compared in Table 7 with the result obtained in a solution of Co^{2+} 10^{-4} M without competitive cations (labelled *Co*).

Table 7 - Selectivity tests - adsorption of Co^{2+} in pure water and in present of other cations.

	Co	*S-Co*	*S-CoCs*
1-Ni	0.047 mmol.g^{-1}	0.051 mmol.g^{-1}	0.008 mmol.g^{-1}
5-Fe	0.044 mmol.g^{-1}	0.064 mmol.g^{-1}	0.011 mmol.g^{-1}

In the solution *S-Co*, adsorption of Co^{2+} was not affected (or even slightly improved according to experimental data) meaning that the adsorption of Co^{2+} is highly selective with respect to the adsorption of Mg^{2+}, Ca^{2+}, K^{+} and Na^{+}. However, when Cs^{+} was present, adsorption of Co^{2+} decreased. The entrapment of Cs^{+} was 0.005 mmol.g^{-1} by material 1-Ni and 0.022 mmol.g^{-1} by 5-Fe.

Conclusion.

In summary, in the present chapter we have described for the preparation of supported nanoparticles of coordination polymers using mesoporous silicas as templates and a diamine grafting to covalently link the nanoparticles into the pores.

The use of nanocomposites containing Hofmann-type nanoparticles appeared to be a promising approach for an efficient iodine capture. We synthesised for the first time two type of nanocomposites Sil@NP and Glass@NP, based on the growth of $Ni^{II}(pz)[Ni^{II}(CN)_4]$ nanoparticles respectively into the pores of a modified SBA-15 (*Sil*) and of the porous glass pearls (*Glass*), by a *step-by-step* method for the successive coordination of nickel salts, pyrazine and tetracyanonickelate precursors. The small spherical nanoparticles of 2 – 3 nm were characterized by IR and Raman spectroscopy, UV-VIS spectroscopy, X-Ray diffraction and TEM analysis. The obtained nanocomposites contain 39 wt% of nanoparticles for the modified SBA-15 and 18 wt% for glass pearls matrixes. The as-obtained nanocomposites were employed for the entrapment of iodine in cyclohexane solutions and their performance was compared with the related diamine-grafted supports *Sil* and *Glass*. The first point to note is that the iodine sorption kinetics of nanocomposites was four times faster in comparison with the one of the parent matrixes, thanks to the presence of the nanoparticles. A direct comparison of the nanoparticles with the bulk $Ni^{II}(pz)[Ni^{II}(CN)_4]$ was not possible due to the participation of the diamine in the confinement of the iodine. Indeed, a strong charge transfer process arose between iodine and σ-electron donor diamine functionality and the formation of the I_3^- or I_5^- species for *Sil* and *Glass*. Secondly, both nanocomposites Sil@NP and Glass@NP present interesting sorption capacity (1.7 $mmol.g^{-1}$ for silica-based and 1.1 $mmol.g^{-1}$ for glass pearls based nanocomposites), with iodine captured both inside the nanoparticles and on the residual grafting groups. By normalizing the entrapped amounts of iodine over the amount of deposited nanoparticles, it was detected respectively 1.15 I_2 and 1.8 I_2 per mole of $Ni^{II}(pz)[Ni^{II}(CN)_4]$, which is comparable or higher than the maximal capacity for the bulk material. Thermal treatments at 250 °C show that in the case of *Sil@NP* reversible desorption only from the nanoparticles was possible and a cycling ability was clearly observed. For *Glass@NP* a partial amount of iodine desorbed from the grafting as well due to the different species of polyiodides formed on this support.

To show an advantage in using such nanocomposites with respect to previously reported materials, we can report here a comparison with the Ag^+-based mordenite published by Chapman *et al*. [57] The mordenite was charged up to a maximum of 15 wt% of Ag particles, *i.e.* 1.39 mmol of Ag per unit mass. By considering a full reaction with I_2 to form AgI, the final material would entrap 1.39 mmol of atomic

iodine (I) or 0.69 mmol of molecular iodine (I_2) per unit mass. Thus, with respect to this example, the nanocomposites Sil@NP and Glass@NP show a storage improvement, respectively, by 250% and 160%.

In parallel, Prussian Blue-functionalized mesoporous materials for the selective entrapment of Co^{2+} in aqueous solutions were prepared following two distinct protocols: one impregnation cycle (1-M) and 5 impregnation cycles (5-M). The entrapment tests indicated that the capacity of a single material depended from different factors: the synthesis protocol and the chosen composition. The materials that showed the best performance were 1-Ni and 5-Fe. The isotherms performed at room temperature indicated a maximal capacity of 0.45 $mmol.g^{-1}$ for 1-Ni and around 1 $mmol.g^{-1}$ for 5-Fe. The selectivity tests indicated that in presence of cations Mg^{2+}, Ca^{2+}, Na^{+} and K^{+} the selective entrapment of Co^{2+} is efficient. However, in presence of Cs^{+} the selectivity decreased.

Bibliography

[1] Basic research needs for advanced nuclear energy systems, U.S. Department of Energy, 2006.

[2] Makowski P., Deschanel X., Grandjean A., Meyer D., Toquer G., Goettmann F. *New. J. Chem.* (2012) 36, 531.

[3] Patent US3556725 – 19 Jan 1971

[4] Beck J. S., Vartuli K. D., Roth W. J., Leonowitz M. E., Kresge C. T., Schmitt K. D., Chu C.T.W., Olson D.H., Sheppard E.W., Schlenker J.L., *J. Am. Chem Soc.*, (1992) 114, 10834.

[5] Yang P., Zhao D., Chmelka B.F., Stucky G.D. *Chem. Mater.* (1998) *10,* 2033.

[6] Dongyuan Z., Huo Q., Feng J., Chmelka B.F., Stucky G.D. *J. Am. Chem. Soc.* (1998) *120,* 6024.

[7] Wang L., Qi T., Zhang Y., Chu J., *Microporous and Mesoporous Materials* (2006) 91, 156.

[8] Balmaseda J., Reguera E., Gomez A., Diaz B., Autie M. *Microp. Mesop. Mat.* (2002) 54, 285.

[9] Reguera E., Fernandez J., Duque J., *Polyhedron* (1994) 13, 479.

[10] Wenker D., Spiess B., Laugel P. C., *Food Addit. Contamin.* (1989) 6, 351.

[11] Neff V.D., *Electrochem. Soc.* (1985) 132, 1382.

[12] DeBerry D.W., Viehbeck A., *J. Electrochem. Soc.* (1983) 130, 249.

[13] Ayrault S., Loos-Neskovic C. Fredoroff M., Garnier E., *Talanta* (1994) 41, 41, 1435.

[14] Larionova J., Guari Y., Sayegh H., Guérin C. *Inorg. Chim. Acta* (2007) 36, 3829.

[15] Catala L., Gacoin T., Boilot J-p., Riviere E., Lhotel E., Mallah T., *Adv. Mater.* (2003) 15, 826.

[16] Chelebaeva E., Guari Y., Larionova J., Trifonov A., Guérin C. Chem. Mater. (2008) 20, 1367.

[17] Clavel G., Guari Y., Larionova J., Guérin C. *New. J. Chem.* (2005) 29, 275.

[18] Kolb H.C., Finn M.G., Sharpless K.B., *Angew. Chem. Int. Ed.* (2011) 40, 2004.

[19] Sangvanich T., Sukwarotwat V., Wiacke R.J., Grudzien R.M., Frywell G.E., Addleman R.S., Timchalk C., Yantasee W. *J. Hazardous Mat.* (2010) 182, 225.

[20] Turgis R., Arrachert G., Delchet C., Rey C., Barre Y., Pellet-Rostaing S., Guari Y., Larionova J., Grandjean A. *J. Che. Mater.* (2013) 25, 4447.

[21] Causse J., Tokarev A., Ravaux J., Moloney M., Barré Y., Grandjean A. *J. Mater. Chem.* (2014) 2, 9461.

[22] Delchet C., Tokarev A., Dumail X., Toquer G., Barré Y., Guari Y., Guerin C., Larionova J. Grandjean A., *RSC Adv.* (2012) 2, 5707.

[23] Tokarev A, Long J., Guari Y., Larionova J., Quignard F., Agulhon FP., Robitzer M., Molnar G., Salmon L., Boussaksou A., *NewJ.Chem.,* 2013, 37, 3420.

[24] Raza Y., Volatron F., Moldovan S., Ersen O., Huc V., Martini C., Brisset F., Bousseksou A., Catala L., Mallah T., *Chem. Commun.,* (2011) 47, 11501.

[25] Tokarev A., Grandjean A., Guari Y., Larionova J., Pflieger R., Guérin C., *J. Nucl. Mat.* (2010) 400, 25.

[26] Cao L., Man T., Kruk M., *Chem. Mater.* (2009) 21, 1144.

[27] Das B., Carlin R., Osteryoung R.A., *Inorg. Chem.* (1989) 28, 421.

[28] Grosman A., Ortega C., *Langmuir*, 2008, *24* (8), pp 3977.

[29] Hutchinson R.W.; Kleinberg S.; Stein F.P.; The Journal of Physical Chemistry, 1973, 77, 7, 870.

[30] irsn.fr (website of the Institut of the Radioprotection and the Nuclear Safety)

[31] cpa.gov.com

[32] Lemos V.A., Santos M.A., Santos E.S., Santos M.J.S., dos Santos W.N.L., Souza A.S, Oleszczuk N., Vale M.G.R., Ferreira S.L.C. *Spectroch. Acta B* (2007), 62, 4.

[33] Rengaraj S., Moon Seung-Hyeon *Water Research* (2002) 36, 1783.

[34] Asci Y., Kaya S. *Desal. Water Treat.* (2014) 52, 1.

[35] Cecal A., Bilba N., Iancu G. J. *Radioanal. Nucl. Chem.* (1984), 85, 4, 195.

[36] Zola A.S., Barros M.A.S.D., Souse-Aguiar E.F., Arroyo P.A., *Braz. J. Chem. Eng*. (2012) 29, 2, 385.

[37] Kursunlu A.N., Guler E., Dumrul H., Kocyigit O., Gubbuk I.H. *Appl. Surf. Sc.* (2009) 255, 8798.

[38] Pan Y., Wu H., Lee L., Jheng G., Fey G.T.K., Kao H. *Microp. and Mesop. Mat*. (2009) 123, 78.

[39] Dey R.T., Airoldi C. J. *Hazar. Mat*. (2008) 156, 95.

[40] Sales J. A.A., Petrucelli G.C., Olivieira F.J.V.E., Airoldi C. *J. Coll. and Interf. Sc.* (2007) 297, 95.

[41] Goswami A. Singh A.K., Venkataramani B. *Talanta* (2003) 60, 1141.

[42] Djekic T., van der Ham A.G.J., de Haan A.B. *J. Chromat. A*, (2007) 1142, 32.

[43] Arakaki L. N. H., Nunes L. M., Simoni J. A., Airoldi C. *J. Coll.. Interf. Sc.* (2000) 228, 46.

[44] Espinola J. G.P., de Freitas J. M.P., de Olivieira S.F., Airoldi C. *Coll. and Surf. Sc.* 1 (1994) 87, 33.

[45] Venkatesan K. A., Srinivasan T.G., Rao V. *Coll. and Surf. Sc.A* (2001) 180, 277.

[46] Sirola K., Laatikainen M., lahtinen M., Patero E. *Separ. Purif. Techn.* (2008) 64, 88.

[47] Airoldi C., Alcantara E. F. C., *Thermoch. Acta* (1995) 259, 95.

[48] Arakaki L.N.H., Pinto V.H.A., Augusto Filha V.L.S., Fonseca M.G., Espinola J.G.P., Arakaki T., Airoldi C., *J. Therm. Anal. Calorim.* (2011) 104, 749.

[49] Ayrault S., Loos-Neskovic C. Fredoroff M., Garnier E., *Talanta* (1994) 41, 41, 1435.

[50] Robert S., *Science* (1987) 238, 1028.

[51] fda.gov (website for of the agency for the Food and Drugs Administration)

[52] Idemura S., Suzuki E., Ono Y., *Clays and Clays Mat.* (1989) 37, 6, 553.

[53] Yamada M., Ohnishi N., Watanabe M., Hino Y., *Chem. Commun.* (2009) 7203.

[54] Xia L., McCreery R.L. *Journal of The Electrochemical Society* (1999) 146, 10, 3696.

[55] Ming H., Torad N.L., Chiang Y., Wu K.C., Yamauchi Y. *CrystEngComm*, (2012),14, 3387.

[56] Dada A.O., Olalekan A.P., Olatunya A.M., *J. Applied Chem.* (2012) 3, 1, 2278.

[57] Chapman, K. W.; Chupas, P. J.; Nenoff, T. M. *J. Am. Chem. Soc*. (2010) 132, 8897.

General conclusion.

Nuclear power industry still demands further research to improve the methods for the storage and the confinement of hazardous radioactive wastes coming from the fission of the radionuclide ^{235}U. Especially the entrapment of mobile radionuclides in out-gases of the reprocessing processes and in aqueous effluents requires a higher efficiency and an improved selectivity. The volatile radioactive ^{129}I (half-life time $15x10^7$ years) is one of the most critical products coming from the reprocessing plants in fuel-closed cycles. Nowadays iodine is entrapped by reaction with NaOH solution (scrubbing solutions) to precipitate the insoluble NaI or with solid Ag-loaded materials (zeolites) to precipitate thermally stable AgI. In the present thesis the family of coordination solid networks, known as Hofmann-type structures, was studied in the form as both bulk and supported nanoparticles for the selective entrapment of the molecular iodine. This set of investigated materials exhibited the general formula $M'(L)[M''(CN)_4]$ where M' = Ni^{II} or Co^{II}; L = pyrazine, 4,4'-bipyridine, 4,4'-azopyridine; M'' = Ni^{II}, Pd^{II} or Pt^{II}. These materials were previously well known for their ability to form clathrates *i.e.* for the ability to include small guest molecules in their microporosity (≈ 0.5 nm) and to retain the molecules generally by weak (Van der Waals) forces. Initially, the material $Ni^{II}(pz)[Ni^{II}(CN)_4]$ and its analogue structures were precipitated as microcrystalline bulky compounds and fully characterized. The insertion of the iodine in the bulky host structures was performed through different methods: 1) adsorption of iodine in solutions of cyclohexane at room temperature; 2) adsorption of iodine vapours at 80 °C; 3) adsorption of iodine vapours at 80 °C in presence of water steam (for few selected materials). The I_2-loaded materials were fully characterized with the techniques FT-IR and Raman spectroscopies, XRPD patterns and related LeBail refinements, solid UV-VIS spectroscopy, TGA-mass spectroscopy, conductivity measurements. The different methods of iodine insertion showed sometimes a difference in adsorption capacity, but the nature of the confined iodine only relied on the type of host structure. For the entrapment in solution, results indicated that the Hofmann-type structures $Ni^{II}(pz)[Ni^{II}(CN)_4]$, $Ni^{II}(pz)[Pd^{II}(CN)_4]$ and $Co^{II}(pz)[Ni^{II}(CN)_4]$ could host one I_2 molecule per unit cell. The iodine resulted physisorbed as molecular iodine in interaction with the host structure. GCMC simulations confirmed the maximal capacities and indicated that iodine could interact with both the pyrazine and the coordinated cyanides. Experimentally, however, the modulation of the metallic centres showed a slightly different strength of interaction I_2-lattice bringing to a different lattice adaptation. The lattice adaptation was correlated with the Raman signal of the stretching mode of the interacting iodine, as well as with the temperature range of iodine desorption. The structure $Ni^{II}(pz)[Ni^{II}(CN)_4]$ showed a slight swelling of the unit cell (about 2%) after the adsorption of iodine and we recorded Raman signal for the confined iodine at 165 cm^{-1} and desorption of iodine from 150 °C. For $Ni^{II}(pz)[Pd^{II}(CN)_4]$, a higher Raman signal (167 cm^{-1}) and a lower desorption temperature (140 °C) were observed, with respect to recorded values for $Ni^{II}(pz)[Ni^{II}(CN)_4]$, indicating a slightly weaker iodine-host structure interaction. Further, the

$Co^{II}(pz)[Ni^{II}(CN)_4]$ showed a contraction of the lattice by about 5%, due to a stronger interaction. This stronger interaction was confirmed by the lower Raman signal (160 cm^{-1}) and the higher desorption temperature (180 °C) with respect to recorded values for $Ni^{II}(pz)[Ni^{II}(CN)_4]$. The materials also could be fully regenerated since the complete desorption of iodine occurred before the decomposition of the host structure. Reiterated adsorption-desorption steps (3 cycles) on the networks $Ni^{II}(pz)[Ni^{II}(CN)_4]$ and $Ni^{II}(pz)[Pd^{II}(CN)_4]$ indicated an excellent structural resistance to cycling and a maintained high capacity. Further investigations on these three Hofmann-type structures concerned the selective entrapment of iodine in water steam. Results indicated that a detrimental effect of water especially occurred for the structures containing Ni^{2+} cations (in octahedral position). The results were correlated with *in-situ* FT-IR measurement of the adsorption on water on the investigated structures and it was detected that the network $Ni^{II}(pz)[Ni^{II}(CN)_4]$ formed more stable complexes with water with respect to $Co^{II}(pz)[Ni^{II}(CN)_4]$. It was supposed that the detrimental effect was due to the formation of stable complexes between water molecules and the unsaturated Ni^{2+} cations on the grain surface, partially influencing the diffusion of the iodine from the surface to the bulk.

A different mechanism of confinement was detected for the structure $Ni^{II}(pz)[Pt^{II}(CN)_4]$ which reacted with iodine giving complex $Ni^{II}(pz)[Pt^{II/IV}(CN)_4].I^-$. The formation of this complex was already reported in literature by Ohtani *et al.* who prepared the complex with an *in-situ* preparation. The Pt^{IV}-I iodide was decomposed after 250 °C and gave a characteristic Raman signal at 129 cm^{-1}. Measurement of conductivity also showed that the iodide in the complex $Ni^{II}(pz)[Pt^{II/IV}(CN)_4].I^-$ did not have any mobility and conductivity was not increased by the insertion of the iodine. By contrast, an increase in conductivity was observed when the iodine was physisorbed in the networks due to the charge propagation among the iodine molecules. Finally, the modulation of the organic ligand L indicated that the replacement of the ligand pyrazine with longer ligands as 4,4'-bipyridine (bpy) or 4,4'-azopyridine (azpy), to obtain larger pores, had a detrimental effect on the maximal iodine loading. These data suggested that for a high capacity the cages had to exhibit a size close to the dimension of the iodine molecule (0.5 nm). However, the use of the 4,4'-azopyridine as ligand brought to a doubled iodine loading with respect to the use of the 4,4'-bipyridine ligand, *i.e.* $Ni^{II}(azpy)[Ni^{II}(CN)_4]\bullet 0.5I_2$ against $Ni^{II}(bipy)[Ni^{II}(CN)_4]\bullet 0.25I_2$, probably due to a different interaction with the organic ligand.

After the study of the bulk materials, we considered the preparation of supported nanoparticles of $Ni^{II}(pz)[Ni^{II}(CN)_4]$ for the entrapment of iodine. The nanoparticles were obtained by a *step-by-step* method, impregnating a set of diamine-grafted mesoporous silicas with the precursors of $Ni^{II}(pz)[Ni^{II}(CN)_4]$. Modified SBA-15 and porous glass beads were used as supported to obtain respectively final materials Sil@Np and Glass@NP. It was estimated a deposition of 39 wt% of NPs on Sil@NP and 17 wt% on Glass@NP. The difference of deposited amount was related to the different specific surface area of the starting support and to the amount of grafted diamine ligands. We detected nanoparticles with a mean size of 2.8 nm by transmission electronic microscopy for material Sil@NP. The adsorption of iodine with the nanocomposites was carried out in solutions of cyclohexane, indicating that iodine tended to adsorb both on the diamine ligand

and inside the nanoparticles giving different iodine species. The insertion of iodine in the nanoparticles was confirmed by FT-IR by checking the shift of the stretching mode of the cyanide moieties, which was the same as observed for the bulky $Ni^{II}(pz)[Ni^{II}(CN)_4]$ (from 2174 cm^{-1} before insertion to 2165 cm^{-1} after insertion). Thermal treatments indicated that the portion of iodine inside the nanoparticles could be reversibly desorbed in the range 150-250 °C and reintroduced in a cyclic process, whereas the amount of polyiodides chemisorbed on the diamine were retained up to decomposition of the support. It was estimated that the amount of physisorbed iodine in the NPs, with respect to the amount of deposited NPs matched with the maximal capacity $Ni^{II}(pz)[Ni^{II}(CN)_4]\bullet I_2$. In conclusion, Hofmann-type structures as bulk materials and nanoparticles indicated a high affinity to the molecular iodine and high capacity of capture in different conditions.

As side-project, hybrids materials consisting of mesoporous silicas impregated with Prussian Blue analogues were considered for the selective entrapment of Co^{2+} in aqueous solutions. The project aimed to test the adsorption properties of Prussian blue-based materials for the entrapment of the radionuclide $^{60}Co^{2+}$ in the aqueous effluents of the nuclear power plant. The best performance was observed for the supported nanoparticles of $Fe_4[Fe(CN)_4]_3$ even in solutions containing other bivalent cations as Ca^{2+} and Mg^{2+}.

As perspective of the present work, further investigations will be necessary in order to optimize the decontaminant materials and to tailor them for the final application. First of all, since the entrapment tests were performed with stable elements ($^{127}I_2$ and $^{59}Co^{2+}$) for safety reasons, it will be important to evaluate, with adapted systems, the structural resistance to the emitted radioactivity of the radionuclides. Moreover, in the case of the iodine entrapment, only the selective entrapment of iodine against water was evaluated, indicating the $Co^{II}(pz)[Ni^{II}(CN)_4]$ as the best candidate. Further tests may extend the study to other competitive species as NO_x, other halogens and other radionuclides as ^{133}Xe and ^{85}Kr. Also, the necessity to covalently anchor the nanoparticles of coordination polymers to the support with a diamine ligand, actually hindered a real comparison between the performance of the bulk Hofmann-type nanoparticles and the related bulk materials. Novel syntheses without the grafting agent may be eventually investigated, for instance, by insertion of metallic cations inside the silica matrix, to trigger a direct growth of coordination polymers nanoparticles on the surface, as reported in the work by Fornasieri *et al.*[*] for the case of Prussian Blue-analogues' nanoparticles. For the fundamental studies about the replacement of the building blocks in the Hofmann-type structures, further DFT simulation will be needed to confirm the hypotheses presented in this work.

[*] Fornasieri G., Aouadi M., Delahaye E., Beaunier P., Durand D., Rivière E., Albouy P., Brisset F., Bleuzen A., *Materials* (2012) 5, 385.

Experimental Section.

In this section, all details related to the experimental work are reported. All materials were purchased from commercially available sources (Sigma Aldrich and Alfa Aesar), and used without further purification.

General instrumentation.

The **UV-VIS spectra** in transmission mode for the detection of the residual concentration of iodine in cyclohexane were recorded on a SPECOORD 210 UV-VIS spectrometer. For the spectra in reflectance mode on the solid samples, a Perkin Elmer Lambda 35 spectometer with integration sphere was used. A reference background was registered with $BaSO_4$ (white powder, 100% reflectance). The **infrared spectra** in transmission mode for all materials were recorded in a dried (oven, 60 °C) KBr matrix on a Nicolet Model 510P spectrophotometer. The *in-situ* IR spectroscopic analyses for the adsorption of water on the Hofmann-type networks were performed in the laboratories of the Technical University of Turin on an Equinox55 (Bruker) spectrometer. For both techniques a background without the sample was recorded. **Raman spectroscopic analyses** were performed in reflectance mode for all materials on the solid samples with a LabRAM ARAMIS IR^2 (Horiba Jobin Yvon). Two lasers were employed to record the spectra: laser Helium Neon (HeNe), with λ = 633 nm and power 440 μW, and laser D473, with λ = 473 nm ans power 1.3 mW.

X-Ray Powder Diffraction patterns (XRPD) for all materials were recorded in the interval 2θ = 5-90° at room temperature with the XPERTPro Panalytical diffractometer mounted in a Debye-Sherrer configuration and equipped with a Cu Kα radiation. For the bulk Hofmann-type networks without iodine the XRPD patterns were recorded in 0.5 mm a capillary, after sieving the powder with a 45 μm steel sieve. For the iodine-loaded materials, for which the introduction in the capillary was difficult, a planar configuration with fixed sample and rotating diffraction angle was preferred. The XRPD in planar configuration were recorded with a long exposure of 12 hours (1000 s on each step with interval 0.16°). The same procedure was employed for the nanocomposites as well. The eventual impurities were indexed with the *X'Pert High Score* software and database PDF-2. The Miller planes of the Hofmann-type structures were indexed by simulating with the X-ray powder patterns with *Mercury* software, by using Crystallographic Information Files (CIFs) of analogue structures, available in the literature. **TGA curves** shown in the present work, by contrast, were registered in the laboratory CMOS (UM2) with a thermal analyser STA 409 Luxx (Netzsch) on the range 25 – 1000 °C at the speed 5 °C/min. The TGA

coupled mass spectroscopy for the iodine-loaded materials was carried out at the Institut of Separative Chemistry of Marcoule. TGA curves were recorded on a Setsys Evolution 16-18 (Setaram) provided of the *Calisto* software and the molecular masses of the exiting volatile gases were detected by a mass spectrometer Hiden Analytical QGA with software MASsoft 7 Professional.

The samples of the silicas and the glass beads-based materials for the **TEM images** (Transmission Electron Microscopy) were prepared by introducing a small amount of samples in a thermo-hardening resin. The resin was hardened in oven at 60 °C for 48 hours, then it was cut in thin slices and deposited on a copper grid. Images were recorded with a microscope JEOL 1200 EXII operated at 100 kV. The extractive replica to isolate the nanoparticles for the samples Sil@NP, 5-Fe, 5-Ni and 5-Cu were carried out in the following steps: 1) a diluted suspension of the hybrid materials in ethanol was prepared by ultrasonic disaggregation; 2) the suspension was deposited on a thin cleaved mica slice and dried in air; 3) a carbon film was deposited on the mica; 4) the mica was gently dipped in a diluted HF solution (2.5 % HF, 10.5 % acetone, 87 % bidistilled water) up to the carbon film started detaching and floating on the solution; 4) the floating film was recovered with filtration paper and detached in the water-acetone solution to wash away the HF; 5) finally, after two washing processed the film was recovered with a TEM grid and dried in air.

SEM/EDX microscopy was performed on a FEI Quanta FEG 200 instrument. The powders were deposited on an adhesive carbon film and analyzed under high vacuum. The quantification of the heavy elements was carried out with the *INCA* software, with a dwell time of 3 µs.

The residual Co^{2+} amount in water was analyzed at the Institut of Separative Chemistry of Marcoule by **ICP-OES** on a SPECTRO ARCOS spectrometer, with plasma ionization. The liquid sample was introduced through a peristaltic pompe and nebulized. The aerosol was transported in the plasma where it underwent desolvation, vaporization, atomization or ionization. A monochromator allowed the separation of the wavelengths which were screened by a spectrometer. To detecte the final concentration, a standard curve was previously traced by standard solutions of elements Fe, NI, Cu, Co in the range 0-20 $mg.L^{-1}$. **Elemental analyses** for were performed by the Service Central d'Analyse (CNRS, Villeurbanne, France). The **N_2 isotherms** were recorded at 77 K in liquid nitrogen, with instrument Tristar Suface Area and Porosity Analyzer (Micromeritics). **Electrical properties** of the materials were recorded with a Novocontrol alpha analyzer, using an alternative electrical field in the 10^{-2}-10^{6} Hz frequency (f) domain. The temperature (T), ranging from -140 to 200°C, was controlled by the Novocontrol cryosystem operating with a dry nitrogen gas stream.

Preparation of the bulk Hofmann-type structures.

$Ni^{II}(pz)[Ni^{II}(CN)_4]\cdot 2H_2O$. In 40 ml of a mixture of water and methanol (vol/vol = 1/1), 3 mmol of $Ni(NO_3)_2\cdot 6H_2O$ (or alternatively $Ni(BF_4)_2\cdot 6H_2O$) and 3 mmol of pyrazine were dissolved. Separately, 3 mmol of $K_2[Ni(CN)_4]$ were dissolved in 10 ml of bidistilled water and the solution was added to the $Ni(NO_3)_2\cdot 6H_2O$-pyrazine solution. Colour of the precipitate: violet. Aspect: microcrystalline powder. Anal. Calcd for $C_8H_8N_6O_2Ni_2$: C, 28.45; H, 2.37; N, 24.89; O, 9.50; Ni, 34.79. Found: C, 28.69; H, 1.95; N, 25.26; O, 8.98; Ni, 35.12. Selected IR (KBr, cm^{-1}): (pyrazine) 810, 1088, 1129, 1160, 2170; (cyanides) 2174, 474; (Ni-pz) 485. Selected Raman (cm^{-1}): 699, 1035, 1233, 2182, 2194. XPS (Ni2p, eV): 855, 873. Weight losses at TGA: 12 wt% at 100 °C (solvents), 38 wt% at 400 °C (ligands).

$Ni^{II}(pz)[Pd^{II}(CN)_4]\cdot 2H_2O$. In 40 ml of a mixture of water and methanol (vol/vol = 1/1), 3 mmol of $Ni^{II}(NO_3)_2\cdot 6H_2O$ (or alternatively $Ni^{II}(BF_4)_2\cdot 6H_2O$) and 3 mmol of pyrazine were dissolved. Separately, 3 mmol of $K_2[Pd^{II}(CN)_4]$ was dissolved in 10 ml of bidistilled water and the solution was added to the $Ni^{II}(NO_3)_2\cdot 6H_2O$-pyrazine solution. Colour: violet microcrystalline powder. CHN Anal. Calcd for $C_8H_8N_6O_2NiPd$: C, 24.93; H, 2.09; N, 21.81; Ni, 15.25; Pd, 27.55 Found: C, 24.23; H, 1.12; N, 22.07; Ni, 14.45; Pd, 26.53. EDX/SEM atomic ratio: Ni/Pd ≈ 1. Selected IR (KBr, cm^{-1}): (pyrazine) 1420, 1215, 1161, 1129, 1088, 1060, 809; (cyanide) 2188, 428; (Ni-pz) 485. TGA (%): 10% at 100 °C (solvents), 41% (ligands) at 425 °C.

$Ni^{II}(pz)[Pt^{II}(CN)_4]\cdot 2H_2O$. In 40 ml of a mixture of water and methanol (vol/vol = 1/1), 3 mmol of $Ni^{II}(NO_3)_2\cdot 6H_2O$ (or alternatively $Ni^{II}(BF_4)_2\cdot 6H_2O$) and 3 mmol of pyrazine were dissolved. Separately, 3 mmol of $K_2[Pt^{II}(CN)_4]$ was dissolved in 10 ml of bidistilled water and the solution were added to the $Ni^{II}(NO_3)_2\cdot 6H_2O$-pyrazine solution. Colour: violet microcrystalline powder. CHN Anal. Calcd for $C_8H_8N_6O_2NiPt$: C, 20.06; H, 1.68; N, 17.73; Ni, 12.39; Pt, 41.16. Found: C, 20.04; H, 0.94; N, 18.05; Ni, 12.77; Pt, 40.77. EDX/SEM atomic ratio Ni/Pt ≈ 1. Selected IR (KBr, cm^{-1}): (pyrazine) 1420, 1215, 1161, 1129, 1088, 1060, 809; (cyanides) 2184, 471; (Ni-pz) 485. TGA: 13% at 100 °C (solvents), 29%at 450 °C (ligands).

$Co^{II}(pz)[Ni^{II}(CN)_4]\cdot 2H_2O$. In 40 ml of a mixture of water and methanol (vol/vol = 1/1), 3 mmol of $Co^{II}(NO_3)_2\cdot 6H_2O$ (or alternatively $Co^{II}(BF_4)_2\cdot 6H_2O$) and 3 mmol of pyrazine were dissolved. Separately, 3 mmol of $K_2[Ni^{II}(CN)_4]$ is dissolved in 10 ml of bidistilled water and the solution was added to the $Co^{II}(NO_3)_2\cdot 6H_2O$-pyrazine solution. Colour of the precipitate: pink. Aspect: microcrystalline powder. Anal. Calcd for $C_8H_8N_6O_2NiCo$: C, 30.05; H, 1.87; N, 26.29; O, 5.00; Ni, 18.37; Co, 18.37. Found: C, 30.31; H, 1.74; N, 26.21; Ni, 18.59. Co, 18.48. Selected IT (KBr, cm^{-1}): (pyrazine) 3115, 1417, 1160, 1130, 1086, 1055, 1030, 806; (cyanide) 2167, 442: (Co-pz) 472. TGA: 13% at 100 °C (solvents), 37% at 350 °C (ligands).

$Ni^{II}(bpy)[Ni^{II}(CN)_4]\cdot H_2O$. In 40 ml of a mixture of water and methanol (vol/vol = 1/1), 3 mmol of $Ni^{II}(NO_3)_2\cdot 6H_2O$ and 3 mmol of 4,4'-bipyridine were dissolved. Separately, 3 mmol of $K_2[Ni^{II}(CN)_4]$ was dissolved in 10 ml of bidistilled water and the solution was added to the $Ni^{II}(NO_3)_2\cdot 6H_2O$-pyrazine solution. CHN anal. Calcd for $C_8H_6N_6ONi_2$: C, 42.48; H, 2.02; N, 21.24. Found: C, 42.76; H, 2.98; N, 21.90. Selected IR (KBr, cm^{-1}): (bipyridine) 1534, 1488, 1411, 1218, 1064, 805; (cyanides) 2167, 440; (Ni-pz) 486. TGA: 11% at 100 °C (solvents), 59% at 400 °C (ligands).

$Ni^{II}(azpy)[Ni^{II}(CN)_4]\cdot H_2O$ (IP batch). In 40 ml of a mixture of water and methanol (vol/vol = 1/1), 3 mmol of $Ni^{II}(NO_3)_2\cdot 6H_2O$ (or alternatively $Ni^{II}(BF_4)_2\cdot 6H_2O$) and 3 mmol of 4,4'-azopyridine were dissolved. Separately, 3 mmol of $K_2[Ni^{II}(CN)_4]$ was dissolved in 10 ml of bidistilled water and the solution was added to the $Ni^{II}(NO_3)_2\cdot 6H_2O$-pyrazine solution. Colour: orange microcrystalline powder. CHN anal. Calcd for $C_8H_6N_6ONi_2$: C, 39.67; H, 1.88; N, 26.45. Found: C, 39.76; H, 2.25; N, 26.52. Selected IR (KBr, cm^{-1}): (azopyridine) 1530, 1487, 1406, 1220, 1077, 1036, 990, 810, 615, 496; (cyanides) 2163, 440. TGA: 7% at 100 °C (solvents), 4% at 120% (water), 55% at 400 °C (ligands).

$Ni^{II}(azpy)[Ni^{II}(CN)_4]$ (SC batch). The preparation was made by slow diffusion of the precursors inside an H-tube. 1 mmol of $Ni^{II}(BF_4)_2\cdot 6H_2O$ was placed in the left side, whereas 1 mmol of 4,4'-azopyridine and 1 mmol of $K_2[Ni^{II}(CN)_4]$ were placed in the right side. In the left side a solution 50% bidistilled water – 50% methanol was slowly added dropwise with a syringe, without reaching the middle connection. In the right side, bidistilled water was slowly added dropwise until the middle connection was filled. The precursors were left diffusing through the solvents for 1 month. A precipitation of an orange crystalline powder occurred. The compound was recovered by filtration. Selected IR (KBr, cm^{-1}): (azopyridine) 1489, 1411, 1227, 1046, 1018, 839, 569; (cyanides) 2164, 442.

Notes:

It is relevant to note that, when the precursors $M'(BF_4)_2\bullet 6H_2O$ (M' = Ni^{II}, Co^{II}), the impurity KBF_4 can precipitate. In order to avoid this inconvenient without changing the precursors, it is suggested to prepare small amounts (typically 3 mmol or less) in the indicated amount of water (or more). Dilution allows a better solubility of the impurity. By contrast, if it is necessary to produce larger quantities at once, it is strongly recommended to use the precursors $M'(NO_3)_2\bullet 6H_2O$ (M' = Ni^{II}, Co^{II}) due to the higher solubility of KNO_3 in water. Also, the powders that crystallized in presence of BF_4^- counteranions showed a slightly higher thermal stability than the powders that formed in presence of NO_3^- counteranions, due to enhanced crystallinity.

The precipitated powders were recovered by centrifugation at 10'000 rpm and then they were thoroughly washed 3 times by bidistilled water and 2 times in methanol (99.8%).

When the powders still contained traces of water, the grinding step could be difficult due to the “suction effect” of the water layer among the particles. It was useful to wash at least 2 times with acetone to remove the inter-particle water and permitting an easy grinding process. The acetone easily evaporated in air. However, residual traces of acetone could be detected by FT-IR spectra by checking if a band around 1700 cm^{-1} appears (corresponding to the ν(C=O) mode).

The preparation of the dehydrated host structures was performed by heating under vacuum. The treatment was performed at 80 °C for 8 hours but it could be carried out as well at higher temperature (200 °C) for 2 hours, for a faster preparation of the samples. The samples were kept in hermetically closed flasks to minimize the contact with water vapours. The host structures presented the following colours before and after treatment (Table 1):

Table 1 - Aspect of the powders before and after dehydration.

	Before dehydration	After dehydration
$Ni^{II}(pz)[Ni^{II}(CN)_4]$	violet	Grey
$Ni^{II}(pz)[Pd^{II}(CN)_4]$	violet (bright)	violet (pale)
$Ni^{II}(pz)[Pt^{II}(CN)_4]$	violet (bright)	violet (pale)
$Co^{II}(pz)[Ni^{II}(CN)_4]$	pink	blue-violet
$Ni^{II}(bpy)[Ni^{II}(CN)_4]$	green	grey-blue
$Ni^{II}(azpy)[Ni^{II}(CN)_4]$	orange	orange

Preparation of the nanocomposites for the entrapment of I_2.

Mesoporous silica (modified SBA-15). For the preparation of the mesoporous silica 4 g of PEO-PPO-PEO triblock copolymer (P123) were dissolved in an acidic solution prepared with 8.75 g of HCl (37%) in 120 ml of bidistilled water. Subsequently, the temperature was raised to 35 °C and 6.8 g of mesitylene (1,3,5-trimethyl benzene) were added and the mixture was stirred for 3 hours. 8.5 g of TEOS were then added to the solution and stirred for 1 hour. A hydrothermal treatment was performed in a 600 ml Teflon autoclave at 100 °C for 24 hours. The obtained gel was filtered and treated at 550 °C for 6 hours under air flux in order to remove the organic phase.

***Sil* (diamine-grafted mesoporous silica).** The grafting process of the mesoporous silica was carried out in inert conditions (Ar flux) in order to avoid oxidation of the grafting agent. 2 g of the silica and 2 g of grafting agent (2-aminoethyl 3-aminopropyl trymethyloxylsilane) were mixed in a large amount (about 250 ml) of bidistilled toluene under Ar atmosphere. Reflux conditions were set at 110 °C, for 48 hours. After filtration the materials were

washed with toluene and dried at 90 °C. Elemental analysis: C, 10.50%; N, 4.11%; H, 2.37.

Activated porous glass beads. The glass beads were purchased from Vitrabio®. The preparation of the commercial glass beads consisted in a pre-treatment at 150 °C under vacuum and overnight, in order to activate the OH groups on the surface.

***Glass* (diamine-grafted porous glass beads).** The grafting process of the mesoporous silica was carried out in inert conditions (Ar flux) in order to avoid oxidation of the grafting agent. 2 g of the activated glass beads and 2 g of grafting agent (2-aminoethyl 3-aminopropyl trymethyloxylsilane) were mixed in a large amount (about 250 ml) of bidistilled toluene under Ar atmosphere. No agitation was used to avoid breaking the beads. Reflux conditions were set at 110 °C, for 48 hours. After filtration the materials were washed with toluene and dried at 90 °C. Elemental analysis: C, 5.45%; N, 2.16%; H, 1.42%.

Nanocomposite Sil@NP (diamine-grafted mesoporous silica with nanoparticles of $Ni^{II}(pz)[Ni^{II}(CN)_4]$). The nanocomposite was obtained by impregnation of *Sil* with precurors for $Ni^{II}(pz)[Ni^{II}(CN)_4]$. Five cycles were performed overall. A cycle consisted of agitating 1 g of *Sil* with a methanolic solution containing $4•10^{-2}$ M of $Ni^{II}(BF_4)_2•6H_2O$ and $4•10^{-2}$ M of pyrazine, for 2 hours. Subsequently the material was filtered under vacuum, thoroughly washed with pure methanol and kept in contact for 2 hours with a methanolic solution of $[(C_4H_9)_4N]_2[Ni^{II}(CN)_4]$ with concentration $4•10^{-2}$ M. It was very important to wash with pure methanol after each cycle in order to avoid precipitation of the bulk Hofmann-type structure outside the silica. The filtered material was treated at 80 °C under primary vacuum. During the 5 cycles the silica turned to pink due to the growth of the Hofmann-type structure nanoparticles. EDX: Ni/Si = 0.55 Elemental analysis: Calcd: C, 17,98; N, 13.19; H, 1.13; O, 27.26; Ni; 14.45, Si, 24.16. Found (for CNH): C, 14.79%; N, 10.76%; H, 2.18%. Selected IR (KBr, cm^{-1}): (cyanides) 2174; (silica) broad band around 1000.

Nanocomposite Glass@NP (diamine-grafted porous glass beads with nanoparticles of $Ni^{II}(pz)[Ni^{II}(CN)_4]$). The nanocomposite was obtained by impregnation of *Glass* with precurors for $Ni^{II}(pz)[Ni^{II}(CN)_4]$. Five cycles were performed overall. Agitation was performed with a vibrant plate to avoid breaking the beads. A cycle consisted of agitating 1 g of *Sil* with a methanolic solution containing $4•10^{-2}$ M of $Ni^{II}(BF_4)_2•6H_2O$ and $4•10^{-2}$ M of pyrazine, for 2 hours. Subsequently the material was filtered under vacuum, thoroughly washed with pure methanol and kept in contact for 2 hours with a methanolic solution of $[(C_4H_9)_4N]_2[Ni^{II}(CN)_4]$ with concentration $4•10^{-2}$ M. During the 5 cycles the beads turned to pink due to the growth of the Hofmann-type structure nanoparticles. The filtered material was treated at 80 °C under primary vacuum. EDX molar ratio Ni/Si = 0.25. Elemental analysis Glass@NP: Calcd C, 10.41; N, 7.22; H, 0.84; Si, 33.76; Ni, 7.44; O, 38.99. Found C, 9.44%; N, 5.18 %; H, 1.23 %, Si, 29.47 %; Ni, 7.00 %. Selected IR (KBr, cm^{-1}): (cyanides) 2172; (silica) broad band around 1000.

Preparation of other I_2-loaded materials.

We report here the protocols for the preparation of the I_2-loaded materials that were fully characterized in the present thesis.

I_2-loaded materials prepared in solution.

A solution of I_2 in cyclohexane ≈ $7 \cdot 10^{-2}$ M (1.77 g in 100 ml) was initially prepared and stirred for 12 hours to completely solubilize I_2. For the bulk Hofmman-type structures, a quantity of 0.332 mmol was kept in dynamic contact for 24 hours with 100 ml of the prepared solution in a hermetically closed round bottom flask. In the case of the hybride materials (Sil, Glass, Sil@NP and Glass@NP) 50 mg were agitated in 50 ml, respecting all the other parameters. Then the powders were placed in a cartridge in a Soxhlet apparatus and thoroughly washed with cyclohexane for 24 hours.

I_2-loaded materials prepared in I_2 vapours.

For the preparation in gaseous phase, 0.332 mmol of the dehydrated Hofmann-type structure were weighed in a glass flask. The flask was kept open inside a hermetically closed glass container where iodine crystals were placed (around 800 mg). The container was kept in an oil bath at 80 °C for 72 hours (iodine vapour pressure about 1 kPa) in order to enhance the sublimation and the diffusion of iodine. A representation of the employed system is reported in Figure 1 (expect for the presence of water that was not used in this type of entrapment). In order to recover the powders after the entrapment, the container was cooled down at room temperature and then opened. The powders were placed in a cartridge in a Soxhlet apparatus and thoroughly washed with pentane (or cyclohexane) for 24 hours.

I_2-loaded materials prepared in I_2 / H_2O vapours.

For the preparation in presence of water steam, 0.332 mmol of the dehydrated Hofmann-type structure were weighed in a glass flask. The flask was kept open inside a hermetically closed glass container where iodine crystals (around 800 mg) and 10 ml of bidistilled water were placed. The container was kept in an oil bath at 80 °C for one week in order to enhance the sublimation of the iodine and the diffusion though the condensed water in the flask. A representation of the employed system is reported in Figure 1. In order to recover the powders after the entrapment, the container was cooled down at room temperature and then opened. The powder was dried in air.

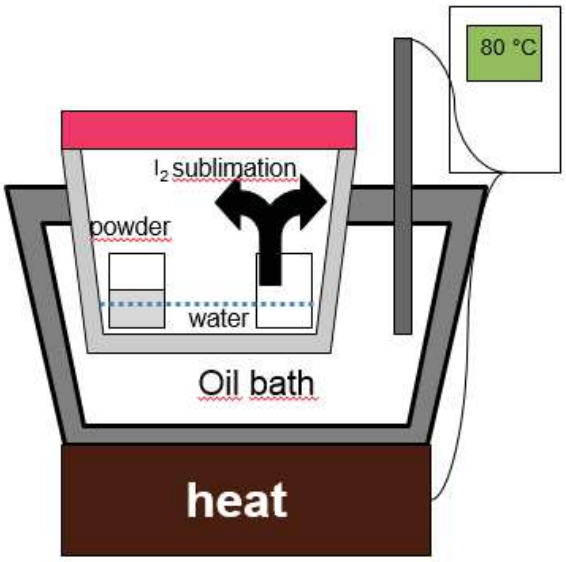

Figure 1 – Representation of the system for the entrapment of iodine in gaseous phase at 80 °C.

Preparation of the hybride materials for the entrapment of Co^{2+}.

Hybride material 1-Ni (diamine-grafted mesoporous silica with molecular fragments of $Ni^{2+}/[Fe^{II}(CN)_6]^{4-}$). The hybride material by impregnation of *Sil* with precursors for $Ni^{II}_2[Fe^{II}(CN)_6]$. One cycle of impregnation was performed by agitating 1 g of *Sil* with a methanolic solution containing 10^{-2} M of $Ni^{II}(BF_4)_2 \bullet 6H_2O$ for 24 hours. Then the material was filtered under vacuum, thoroughly washed with pure methanol and kept in contact for 24 hours with a methanolic solution of $[(C_4H_9)_4N]_4[Fe^{II}(CN)_6]$ with concentration 10^{-2} M. Colour: light yellow. Selected IR (KBr, cm^{-1}): (cyanides) 2096, 2059, 464; (silica) broad band around 1000.

Hybride material 1-Fe (diamine-grafted mesoporous silica with molecular fragments of $Fe^{3+}/[Fe^{II}(CN)_6]^{4-}$). The hybride material by impregnation of *Sil* with precursors for $Fe^{III}_4[Fe^{II}(CN)_6]_3$. One cycle of impregnation was performed by agitating 1 g of *Sil* with a methanolic solution containing 10^{-2} M of $Fe^{II}(BF_4)_2 \bullet 6H_2O$ for 24 hours. Then the material was filtered under vacuum, thoroughly washed with pure methanol and kept in contact for 24 hours with a methanolic solution of $[(C_4H_9)_4N]_4[Fe^{II}(CN)_6]$ with concentration 10^{-2} M. Colour: light blue. Selected IR (KBr, cm^{-1}): (cyanides) 2041, 466; (silica) broad band around 1000.

Hybride material 1-Cu (diamine-grafted mesoporous silica with molecular fragments of $Cu^{2+}/[Fe^{II}(CN)_6]^{4-}$). The hybride material by impregnation of *Sil* with precursors for $Cu^{II}_2[Fe^{II}(CN)_6]$. One cycle of impregnation was performed by agitating 1 g of *Sil* with a methanolic solution containing 10^{-2} M of $Cu^{II}(BF_4)_2 \bullet 6H_2O$ for 24 hours. Then the material was filtered under vacuum, thoroughly washed with pure methanol and kept in contact for 24 hours

with a methanolic solution of $[(C_4H_9)_4N]_4[Fe^{II}(CN)_6]$ with concentration 10^{-2} M. Colour: light purple. Selected IR (KBr, cm^{-1}): (cyanides) 2100, 2036, 464; (silica) broad band around 1000.

Nanocomposite 5-Ni (diamine-grafted mesoporous silica with nanoparticles of $Ni^{II}_2[Fe^{II}(CN)_6]$). The hybride material by impregnation of *Sil* with precursors for $Ni^{II}_2[Fe^{II}(CN)_6]$. Five cycles of impregnation were carried out overall. A cycle of impregnation was performed by agitating 1 g of *Sil* with a methanolic solution containing 10^{-2} M of $Ni^{II}(BF_4)_2 \bullet 6H_2O$ for 2 hours. Then the material was filtered under vacuum, thoroughly washed with pure methanol and kept in contact for 2 hours with a methanolic solution of $[(C_4H_9)_4N]_4[Fe^{II}(CN)_6]$ with concentration 10^{-2} M. Colour: yellow. Selected IR (KBr, cm^{-1}): (cyanides) 2098, 591, 482, 462; (silica) broad band around 1000.

Nanocomposite 5-Fe (diamine-grafted mesoporous silica with nanoparticles of $Fe^{III}_4[Fe^{II}(CN)_6]_3$). The hybride material by impregnation of *Sil* with precursors for $Fe^{III}_2[Fe^{II}(CN)_6]_3$. Five cycles of impregnation were carried out overall. A cycle of impregnation was performed by agitating 1 g of *Sil* with a methanolic solution containing 10^{-2} M of $Fe^{II}(BF_4)_2 \bullet 6H_2O$ for 2 hours. Then the material was filtered under vacuum, thoroughly washed with pure methanol and kept in contact for 2 hours with a methanolic solution of $[(C_4H_9)_4N]_4[Fe^{II}(CN)_6]$ with concentration 10^{-2} M. Colour: blue. Selected IR (KBr, cm^{-1}): (cyanides) 2080, 596, 482, 464; (silica) broad band around 1000.

Nanocomposite 5-Cu (diamine-grafted mesoporous silica with nanoparticles of $Cu^{II}_2[Fe^{II}(CN)_6]$). The hybride material by impregnation of *Sil* with precursors for $Cu^{II}_2[Fe^{II}(CN)_6]$. Five cycles of impregnation were carried out overall. A cycle of impregnation was performed by agitating 1 g of *Sil* with a methanolic solution containing 10^{-2} M of $Cu^{II}(BF_4)_2 \bullet 6H_2O$ for 2 hours. Then the material was filtered under vacuum, thoroughly washed with pure methanol and kept in contact for 2 hours with a methanolic solution of $[(C_4H_9)_4N]_4[Fe^{II}(CN)_6]$ with concentration 10^{-2} M. Colour: purple. Selected IR (KBr, cm^{-1}): (cyanides) 2100, 589, 481, 468; (silica) broad band around 1000.

Precursors and other coordination complexes.

$[(C_4H_9)_4N]_2[Ni(CN)_4]$ (precursor for the impregnations). The preparation consisted in a metathesis reaction. 10 mmol of $K_2[Ni^{II}(CN)_4] \bullet H_2O$ and 20 mmol of $(C_4H_9)_4NBr$ were dissolved into a biphasic system, consisting of 50 vol% of bidistilled water and 50 vol% of organic solvent – CH_2Cl_2 or $CHCl_3$. The system was agitated for 1 hour with a rotor driver at room temperature. The organic phase was separated through a separatory funnel and dried with $MgSO_4$. The organic solvent was evaporated with a rotovapor at p = 300 mbar

and T = 50 °C. In order to eliminate the exceeded TBABr the powder was purified in hot diethyl ether at 50 °C for 3 H and filtered. The final product was dried in oven at 80 °C. Final aspect: pale orange powder. IR (KBr, cm^{-1}): ν(C≡N) 2109.

$[(C_4H_9)_4N]_3[Fe^{III}(CN)_6]$ (precursor for the impregnations). The preparation consisted in a metathesis reaction. 10 mmol of $K_3[Fe^{III}(CN)_6]•H_2O$ and 30 mmol of $(C_4H_9)_4NBr$ were dissolved into a biphasic system, consisting of 50 vol% of bidistilled water and 50 vol% of organic solvent – CH_2Cl_2 or $CHCl_3$. The system was agitated for 1 hour with a rotor driver at room temperature. The organic phase was separated through a separatory funnel and dried with $MgSO_4$. The organic solvent was evaporated with a rotovapor at p = 300 mbar and T = 50 °C. In order to eliminate the exceeded TBABr the powder was purified in hot diethyl ether at 50 °C for 3 H and filtered. The final product was dried in oven at 80 °C. Final aspect: bright yellow powder. IR (KBr, cm^{-1}): ν(C≡N) 2096.

$Ni^{II}[Ni^{II}(CN)_4]$: In a 1:1 water-methanol solution, 1 mmol of $Ni^{II}(NO_3)_2•6H_2O$ was dissolved under stirring; then 1 mmol of $K_2[Ni^{II}(CN)_4]$ was added with instantaneous precipitation of a green powder of estimated formula $Ni^{II}(H_2O)_2[Ni^{II}(CN)_4]•xH_2O$. The compound was treated at 200 °C for 2 hours to remove adsorbed water and coordinated water. Final aspect: brown fine powder.

$Co^{II}[Ni^{II}(CN)_4]$: In a 1:1 water-methanol solution, 1 mmol of $Co^{II}(NO_3)_2•6H_2O$ was dissolved under stirring; then 1 mmol of $K_2[Ni^{II}(CN)_4]$ was added with instantaneous precipitation of a green powder of estimated formula $Co^{II}(H_2O)_2[Ni^{II}(CN)_4]•xH_2O$. The compound was treated at 200 °C for 2 hours to remove adsorbed water and coordinated water. Final aspect: blue fine powder.

$Ni^{II}(NO_3)_2$ / pyrazine complex: the Ni^{II}-pyrazine complex was obtained in the solid state by grinding 1 mmol of $Ni^{II}(NO_3)_2•6H_2O$ (green powder) with 1 mmol of pyrazine (white powder). Final aspect: blue powder.

$Co^{II}(NO_3)_2$ / pyrazine complex: the Ni^{II}-pyrazine complex was obtained in the solid state by grinding 1 mmol of $Co^{II}(NO_3)_2•6H_2O$ (red powder) with 1 mmol of pyrazine (white powder). Final aspect: orange powder.

$Ni^{II}(NO_3)_2$ / bipyridine complex: the Ni^{II}-pyrazine complex was obtained in the solid state by grinding 1 mmol of $Ni(NO_3)_2$ (green powder) with 1 mmol of bipyridine (white powder). Final aspect: green powder.

$Ni^{II}(pz)[Ni^{II}(CN)_4]·0.05\ I_2$ (*in-situ* synthesis). A concentrated solution of iodine (0.07 M) was prepared by dissolution of 0.88 g of I_2 in 50 ml of C_6H_{12} (cyclohexane). Then 20 ml of this solution was vigorously agitated with an aqueous solution prepared with 1 mmol $K_2[Ni^{II}(CN)_4]•H_2O$ in 50 ml (biphasic extraction). After complete decoloration of the organic phase,

the aqueous phase was separated with a separatory fannel and it was poured in a solution of 1 mmol $Ni^{II}(NO_3)_2 \bullet 6H_2O$ + 1 mmol pyrazine in 40 ml of bidistilled water, under stirring. The precipitated compound was centrifuged and dried in air. Final aspect: yellow microcrystalline powder.

$Co^{II}(pz)[Pd^{II}(CN)_4]$. In 40 ml of a mixture of water and methanol (vol/vol = 1/1), 3 mmol of $Co^{II}(NO_3)_2 \cdot 6H_2O$ (or alternatively $Co^{II}(BF_4)_2 \cdot 6H_2O$) and 3 mmol of pyrazine were dissolved. Separately, 3 mmol of $K_2[Pd^{II}(CN)_4]$ was dissolved in 10 ml of bidistilled water and the solution was added to the $Co^{II}(NO_3)_2 \cdot 6H_2O$-pyrazine solution. The compound was treated at 200 °C to desorb the water off the cages. Final aspect: blue microcrystalline powder. EDX analysis: Co/Pd ≈ 1.

Annexes.

Annex 1 - Quantification of the entrapped amount of iodine by UV-VIS spectroscopy.

The entrapment of iodine in solution with the Hofmann-type structures was performed with solutions of I_2 in cyclohexane (C_6H_{12}). Iodine (MW † = 253.8 g.mol^{-1}) is highly soluble in cyclohexane and it solubility limit at room temperature is around 7•10^{-2} M (21 g.L^{-1}). The amount of captured I_2 by the Hofmann-type structure was quantified by observing the extinction of the absorption band of I_2 (525 nm) with the UV-VIS spectrometer. In UV-VIS spectroscopy in transmission mode, the absorption spectrum in the range λ = 200-800 nm is measured. The radiation at different wavelength is produced by a set of UV-VIS lamps and passed through a cell where the solution to analyse is placed. The *transmittance* (T) is defined as the transmitted radiation (I) over the incident radiation I_0. The transmittance relies on physical parameters as the path through the solution (l) measured in [cm] and the molar concentration (C) measured in [mol.L^{-1}] following the relationship:

Equation 1 – Definition of transmittance.

$$T\ (transmittance) = \frac{I}{I_0} = e^{-(\varepsilon \cdot l \cdot C)}$$

where ε is defined the *molar extinction coefficient* and it is an experimental parameter that depends on the solvent, the solute and the temperature. The UV-VIS spectrometer in transmission mode generally shows an absorption spectrum and the intensity on the y-axis is expressed as *absorbance* (A). The absorbance is related to the transmittance through the following equation:

Equation 2 – Definition of absorbance.

$$\boldsymbol{A\ (absorbance) = -\ln\ (T) = \varepsilon \cdot l \cdot C}$$

As the equation shows, there is a linear relationship between the absorbance and the molar concentration of the solution. This relationship is valuable exclusively for low concentrations. In order to convert the measured absorbance in the concentration, we had to determine the molar extinction coefficient. With a solution of I_2 in C_6H_{12} with known concentration, a series of diluted concentrations were prepared and their concentrations were plotted versus the measured

† MW = molar weight [g.mol^{-1}]

absorbances (Figure 2). Since the width of the cell for the measurement was unitary (1 cm), the parameter ε was directly the slope of the linear regression for the set of points. The value for the slope was ε = 929.61 L.mol^{-1}.cm^{-1}. Thus, this value was used to convert the absorbance in molar concentrations. The concentration was measured before and after the entrapment and it was assumed that the difference in concentration was due to I_2 capture inside the Hofmann-type structure.

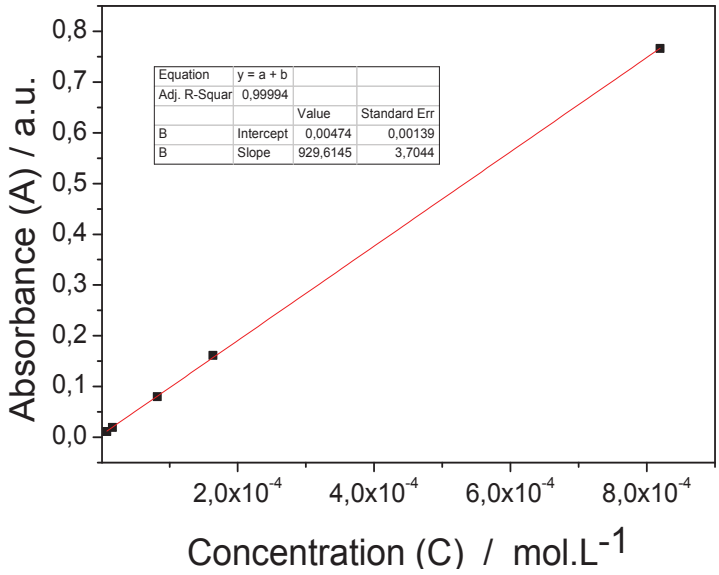

Figure 2 - Absorbance-to-concentration linear plot (Beer-Lambert equation).

To perform all entrapment tests in solution with the dehydrated Hofmann-type structures, a fixed powder-to-volume ratio was chosen in order to compare all data: the ratio was 3.32•10^{-6} mol per ml of solution. Examples of employed quantities for the different powders: for the $Ni^{II}(pz)[Ni^{II}(CN)_4]$ and the $Co^{II}(pz)[Ni^{II}(CN)_4]$ (MW = 301.4 mol.g^{-1}), 20.0 mg in 20 ml; for the $Ni^{II}(pz)[Pd^{II}(CN)_4]$ (MW = 349.1 mol.g^{-1}), 23.1 mg in 20 ml; for the $Ni^{II}(pz)[Pt^{II}(CN)_4]$ (MW = 437.1 mol.g^{-1}), 29.0 mg in 20 ml; for the $Ni^{II}(bpy)[Ni^{II}(CN)_4]$ (MW = 377.4 mol.g^{-1}), 25.0 mg in 20 ml; for the $Ni^{II}(azpy)[Ni^{II}(CN)_4]$ (MW = 406.4 mol.g^{-1}), 26.9 mg in 20 ml. The entrapments were performed rigorously in round bottom flasks, since iodine showed a certain reactivity toward all plastics and metallic surfaces as well. The flasks were hermetically closed to avoid evaporation of the solution. The final entrapped amount was expressed in units [mmol.g^{-1}], *i.e.* mmol of entrapped I_2 per unit mass of used powder. An example of calculation is now reported. All experimental errors were determined with the following error propagation equation:

Equation 3 – Gauss law of error propagation.

$$(Example)\ n = f(C;V)$$

$$\Delta n = \sqrt{\left(\frac{dn}{dC}\Delta C\right)^2 + \left(\frac{dn}{dV}\Delta V\right)^2}$$

Example.

For the adsorption of iodine, 20 mg $Ni^{II}(pz)[Ni^{II}(CN)_4]$ were mixed to 20 ml of a I_2 solution close to saturation ≈ $7•10^{-2}$ M. The initial concentration should have a theorical absorbance of A = 0.7 [$mol.L^{-1}$] • 1[cm^{-1}] • 929.61[$L.mol^{-1}.cm^{-1}$] = 65. Since the UV-VIS spectrometer could correctly measure only absorbances A < 3, a dilution 1:50 was performed. The diluted initial concentration showed A = 1.2577±0.0001 at λ = 525 nm (maximal absorbance) on the spectrometer that corresponded to effective concentration C_1 = 1.2577•50/929.61 = $6.764•10^{-2}$ M (estimated instrumental error ≈ 10^{-6} M). After 24 hours of agitation with the powder, solution was separated by filtration and then diluted 50 times to check the absorbance at UV-VIS spectrometer. It was found A = 1.1965±0.0001 at λ = 525 nm (maximal absorbance). This value corresponded to C_2 = 1.1965•50/929.61 = $6.435•10^{-2}$ M. The initial concentration C_1 and the final concentration C_2 were normalized on the employed volume V = 20 ml in order to have the absolute amounts of iodine before and after entrapment. The amounts Q_1 (moles of I_2 initially present in the solution) and the amount Q_2 (residual moles of I_2 in the solution after the capture) were subtracted to determine the moles of entrapped iodine:

Equation 4 – Entrapped moles of iodine.

$$Q_1 - Q_2 = C_1 \cdot V - C_2 \cdot V = 1.353\ mmol - 1.287\ mmol = 0.065 \pm 0.002\ mmol$$

By normalisation on the employed mass (20 mg), we obtained the final entrapment 0.0658/0.02 = 3.28 ± 0.1 $mmol.g^{-1}$. Since in the value employed 20 mg there were 0.02/301.4 = $6.63•10^{-5}$ mol of $Ni^{II}(pz)[Ni^{II}(CN)_4]$, the ratio of the moles of entrapped I_2 over the moles of $Ni^{II}(pz)[Ni^{II}(CN)_4]$ was about 0.99 per unit cell. For the maximal capacities, the quantification by UV-VIS was confirmed by TGA (see related annex). Using UV-VIS spectroscopy, the entrapments in solution of iodine were used to determine the kinetics of adsorption and the isotherms at room temperature.

Annex 2 - Kinetic curves and pseudo-second order model.

For the kinetic study an initial concentration around $3•10^{-3}$ M of iodine in cyclohexane was chosen, in order to directly observe the real absorbance without dilution. Different amounts of powder (for instance, 20 mg of $Ni^{II}(pz)[Ni^{II}(CN)_4]$ for each) were kept in equal volumes (for instance, 20 ml) and each test was stopped at a different time, *i.e.* 5 min, 10 min, 20 min, 1 h, 2 h, 3 h, 20 h, 50 h. Then, at each time 3 ml were rapidly extracted with a millipore filter and placed in the UV-VIS cell for detecting the residual concentration. The entrapped amounts of I_2 at each time were expressed in $mmol.g^{-1}$ and plotted as function of time. The kinetic studies for the adsorption of Co^{2+} with the hybrid materials were obtained in a similar way with initial concentration of Co^{2+} in water 10^{-3} M and time tests at 2h, 6h, 24h. The residual amount of Co^{2+} were analyzed by ICP-OES. All data were fitted with the pseudo-second order model. The model

is largely used for the adsorption phenomena on solids, where the amount of solid is a constant and does not influence the rate and the concentration is related to the rate through a quadratic relationship. The differential equation for this model is the following:

Equation 5 – Pseudo-second order model (differential equation).

$$\frac{dQ}{dt} = k(Q_e - Q)^2$$

where t is the time, Q is the entrapped amount at time t, k is the kinetic constant with unit [g•mmol^{-1}min^{-1}] and dQ/dt is the reaction rate. Integrations on range 0-t for t → ∞ and on the range 0-Q for Q → Q_e (amount at equilibrium) brings to the solution:

Equation 6 – Solution for the differential equation.

$$Q = \frac{kQ_e^2 t}{1 + kQ_e t}$$

The linearized form for this equation is:

Equation 7 – Linear shape for the pseudo-second order model.

$$\frac{\mathbf{t}}{\mathbf{Q}} = \frac{\mathbf{1}}{\mathbf{kQ_e^2}} + \frac{\mathbf{t}}{\mathbf{Q_e}}$$

As example, the linearization for the kinetic curve for the adsorption of iodine with $Ni^{II}(pz)[Ni^{II}(CN)_4]$ is reported. By plotting the time t as a function of t/Q, the following linear graph was obtained:

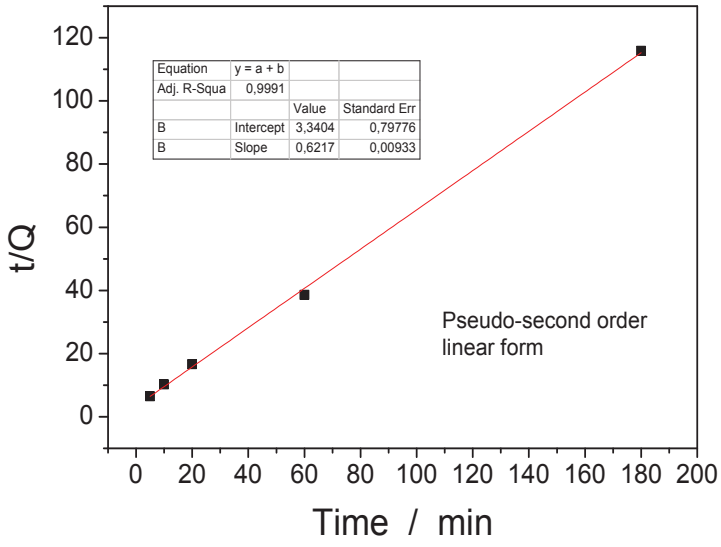

Figure 3 - Linear form for the pseudo-second order model.

From the slope *a* = 3.34 and the intercept *b* = 0.62 of the linear regression it was possible to obtain the entrapped amount at the equilibrium Q_e and the kinetic constant k, with the following relationships:

Equation 8 – Entrapped amount at the equilibrium.

$$Q_e = \frac{1}{a} = \frac{1}{3.34} = 1.6\ mmol.\ g^{-1}$$

Equation 9 – Kinetic constant.

$$k = \frac{1}{b \cdot Q_e^2} = \frac{1}{0.62 \cdot 11.15} = 0.14\text{g} \cdot mmol^{-1} min^{-1}$$

These values were used in Equation 6 to trace the fitting curve for the pseudo-second order model. A summary of the parameters to fit all curves presented in the present work is reported in Table 2.

Table 2 - Parameters for the pseudo-second order fitting (C = 3•10^{-3} M; standard conditions).

I_2 capture	Capture amount at t_{eq} [mmol.g^{-1}]	Kinetic constant [mmol.g^{-1}.min^{-1}]
$Ni^{II}(pz)[Ni^{II}(CN)_4]$	1.6	0.14
$Ni^{II}(pz)[Pd^{II}(CN)_4]$	1.3	0.15
$Ni^{II}(pz)[Pt^{II}(CN)_4]$	0.7	0.04
$Co^{II}(pz)[Ni^{II}(CN)_4]$	1.5	0.28
$Ni^{II}(bpy)[Ni^{II}(CN)_4]$	0.4	0.05
$Ni^{II}(azpy)[Ni^{II}(CN)_4]$	0.9	0.02
Sil	1.5	0.08
Sil@NP	0.9	0.44
Glass	0.8	1.33
Glass@NP	0.4	2.53
Co^{2+} capture	Capture amount at t_{eq} [mmol.g^{-1}]	Kinetic constant [mmol.g^{-1}.min^{-1}]
1-Ni	0.41	1.99
1-Fe	0.28	4.39
1-Cu	0.14	2.74
5-Ni	0.35	5,48
5-Fe	0.42	2.05
5-Cu	0.12	1.48

Annex 3 – Experimental isotherms and models.

An isotherm is a curve that shows the evolution of a physical parameter at constant temperature. Adsorption isotherms for the study of the adsorption phenomena of a molecule (in gas or in solution) onto a solid are obtained by plotting the adsorbed amount, at constant temperature, with respect to the equilibrium pressure (or concentration) between the free molecules and the adsorbed molecules. A classification for isotherms was carried out by the IUPAC international system (Figure 4). The most common isotherms are: *type I*, which is related to a chemisorption or a physisorption of a monolayer; *type II*, which is typical for non-porous or macroporous materials, where the adsorption is beyond the multilayer and t*ype IV*, which typically shows a hysteresis due to the presence of mesopores. Type III and V refer to weak interactions adsorbate-adsorbent where the shape of the isotherm is convex to the pressures axis.

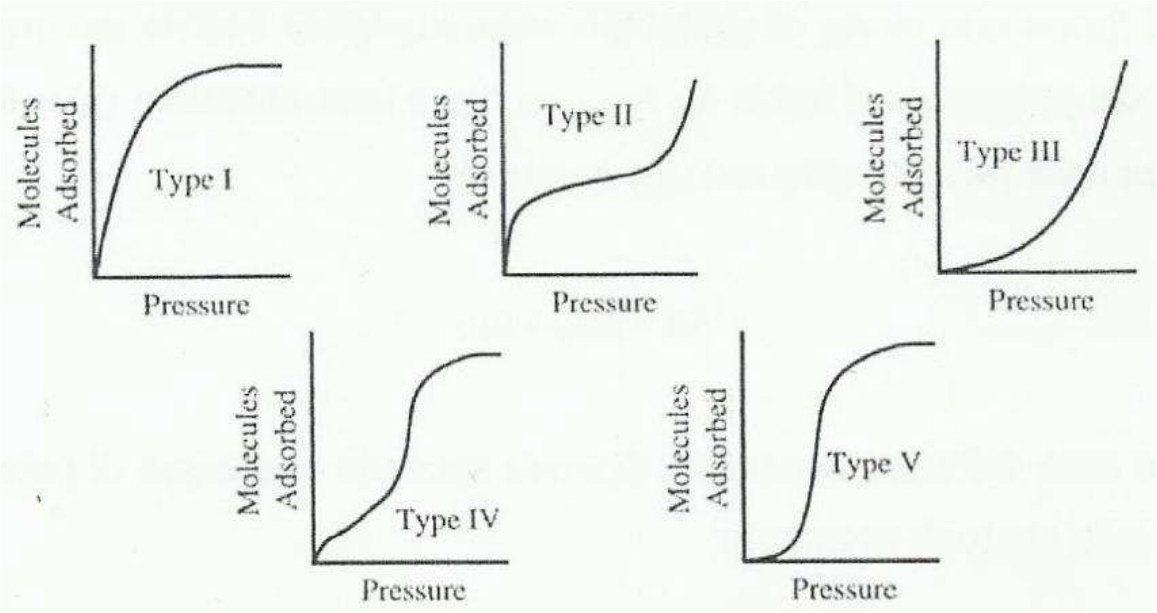

Figure 4 - IUPAC classification of isotherms.
(http://pac.iupac.org/publications/pac/pdf/1982/pdf/5411x2201.pdf)

In the present work we presented different type of experimental isotherms: I_2 adsorption isotherms in organic solution; Co^{2+} adsorption isotherms in aqueous solution; N_2 adsorption isotherms in gaseous phase. We report the preparation for each isotherm and then the applied models to obtain specific information from the adsorption curves.

I_2 adsorption isotherms in organic solution.

In order to trace the iodine adsorption isotherm at room temperature, different batches of the material (Hofmann-type structures or nanocomposites) were kept in dynamic contact with different concentrations of iodine in cyclohexane, *i.e.* $1.3 \cdot 10^{-3}$ M, $2.6 \cdot 10^{-3}$ M, $5.2 \cdot 10^{-3}$ M, $1.5 \cdot 10^{-2}$ M, $3 \cdot 10^{-2}$

M, $7 \bullet 10^{-2}$ M (saturation). The time of contact had to be higher than the equilibrium time determined by the kinetic studies. The I_2-loaded materials were placed in a cartridge in a Soxhlet apparatus and thoroughly washed with cyclohexane for 24 hours.

Co^{2+} adsorption isotherms in aqueous solution.

The set of material 1-M and 5-M (M = Fe, Ni, Cu) was used for the selective entrapment of Co^{2+} in water. The Co^{2+} solutions were prepared with $Co^{II}(NO_3)_2 \bullet 6H_2O$ in bidistilled water. A conventional mass-volume ratio was chosen for all adsorption tests, *i.e.* 10 mg of material in 20 ml of solution, in order to compare the results from different adsorption tests. For the kinetics, a set of solutions with concentration $2 \bullet 10^{-4}$ M was prepared and the capture tests were arrested at different times *i.e.* 2 hours, 6 hours and 24 hours. The solutions were quickly separated with Millipore filters. For the isotherms of 5-Fe and 1-Ni we performed adsorption tests by choosing at least 4 points in the concentration range $5 \bullet 10^{-4}$ – 10^{-2} M. The tests were arrested after 24 hours. The analyses of the residual concentration after the kinetic and the isotherm adsorption were performed by the analytical laboratory of the Institute of Separative Chemistry in Marcoule. The employed technique to detect the residual metals in solution was the Inductively Couple Plasma (ICP). The experimental isotherms were fitted with different models to choose the more suitable for each adsorption process.

N_2 adsorption isotherms in gaseous phase.

For these isotherms, a specific instrument (Tristar) was used. The powdered were treated under vacuum and in temperature (temperature value chosen below the decomposition temperature for each sample) for 8 hours. The volumetric cells were weighed on an analytic balance, without the powder and with the degased powder (under Ar) to determine the mass of the sample. The samples were connected to the vacuum line of the Tristar instrument and the dewar below the samples were filled with liquid nitrogen, since the measurement had to be performed at 77 K. The instrument descended the samples in the liquid nitrogen after the vacuum was reached, and recorded both adsorption and desorption branches as a plot of adsorbed volume versus relative pressure p/p_0.

3.1 - Langmuir model.

For the adsorption of iodine, the Langmuir model was chosen. The Langmuir model is a model for the adsorption on gaseous phase and it assumes some ideal and simple conditions due to the following reasons: 1) the gas adsorbs in a localized state; 2) the adsorption sites are equivalent; 3) on one site only one molecule can adsorb; 4) the interactions adsorbate-substrate are more important that the interactions adsorbate-adsorbate. The Langmuir model is obtained by

describing the adsorption as a reaction at equilibrium:

Equation 10 – Adsorption process.

$$[S] + C \leftrightarrow [M_{ads}]$$

where [S] is the concentration of available sites per unit surface, C is the activity of the free molecule (in this case, the concentration of the molecule in solution) and [M_{ads}] is the concentration of sites, occupied by adsorbed molecules per unit surface. The equilibrium constant for the reaction is:

Equation 11 – Equilibrium constant for the adsorption process.

$$\boldsymbol{K = \frac{[M_{ads}]}{C \cdot [S]}}$$

where [S] is the concentration of available sites per unit surface, C is the activity of the free molecule (in this case the concentration of the molecule in solution) and [M_{ads}] is the concentration of sites, occupied by adsorbed molecules per unit surface. We can express the occupied sites [M_{ads}] as the adsorbed amount of molecules (Q) per unit mass of adsorbent at a certain concentration C. Also, the available sites can be expressed by the difference between the maximal amount of molecules that could be adsorbed (Q_{max}) and the adsorbed amount (Q_{max} – Q). By substituting [M_{ads}] with Q and [S] with (Q_{max} – Q) in Equation 11 and expressing the coverage (Q/Q_{max}) as a function of C, the final equation for the model is obtained:

Equation 12 – Langmuir isotherm.

$$\frac{Q}{Q_{max}} = \frac{KC}{(1 + KC)}$$

where C is the equilibrium concentration ($mol.L^{-1}$), Q is the amount entrapped at the corresponding equilibrium concentration ($mmol.g^{-1}$), Q_{max} is the maximal amount of entrapped iodine ($mmol.g^{-1}$) and K is the equilibrium constant or adsorption energy ($l.mol^{-1}$). The ratio Q/Q_{max} tends to unity for $C \rightarrow \infty$. The linear form for the model is:

Equation 13 – Linear equation for the Langmuir isotherm.

$$\frac{1}{Q} = \frac{1}{Q_{max}} + \frac{1}{KQ_{max}}\frac{1}{C}$$

The application of the model for the adsorption of I_2 on $Ni^{II}(pz)[Ni^{II}(CN)_4]$ is now reported. The inverse of the entrapped amount 1/Q were plotted versus the inverse of the concentration 1/C (Figure 5) giving a straight line (R = 0.99).

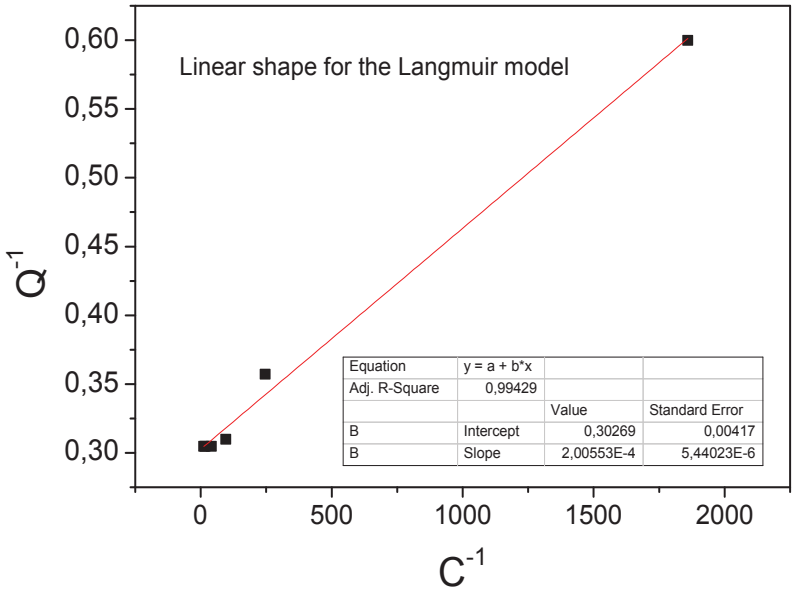

Figure 5 – Linear form for the Langmuir model

From the slope a = 2•10^{-4} and the intercept b = 0.302 of the linear regression, the parameters Q_{max} and K were found with the following relationships:

Equation 14 - Determination of the maximal storage capacity.

$$Q_{max} = \frac{1}{b} = \frac{1}{0.302} = 3.32\ mmol.g^{-1}$$

Equation 15 – Determination of the Langmuir constant (equilibrium constant).

$$K = \frac{1}{a \cdot Q_{max}} = \frac{1}{0.0002 \cdot 3.32} = 1506\ L.mol^{-1}$$

These values were employed in Equation 12 for the fitting of the experimental isotherm. We summarize in the values for Q_{max} and K that were found for the fitting of all I_2 adsorption isotherm. The higher is the Langmuir constant, the higher is the affinity between the adsorbate and the adsorbent.

Table 3 - Langmuir Parameters for all curved fitted with this model.

Adsorbent for I_2	*Maximal capacity [mmol.g^{-1}]*	*Adsorption energy [mol.L^{-1}]*
$Ni^{II}(pz)[Ni^{II}(CN)_4]$	3.32	1506
$Ni^{II}(pz)[Pd^{II}(CN)_4]$	3.0	1100
$Ni^{II}(pz)[Pt^{II}(CN)_4]$	1.10	550
$Co^{II}(pz)[Ni^{II}(CN)_4]$	3.35	2946
$Ni^{II}(bpy)[Ni^{II}(CN)_4]$	0.70	3448
$Ni^{II}(azpy)[Ni^{II}(CN)_4]$	1.30	2385
Sil	4.12	1211
Sil@NP	1.73	1924
Glass	2.15	580
Glass@NP	1.09	2274
Adsorbent for Co^{2+}	*Maximal capacity [mmol.g^{-1}]*	*Adsorption energy [mol.L^{-1}]*
1-Ni	0.45	21990

3.2 - Empirical models: Freundich's and Temkin's isotherms.

Two empirical models were used. The Freundlich's model and the Temkin's model. These models were formulated to describe real phenomena that do not respect the ideal conditions imposed by the theorical Langmuir's model. This model describes adsorption on heterogeneous surfaces. Also, the second derivative of this isotherm is typically used to see if the absorption is thermodynamically favorable. It is indeed favorable for $d^2q/dC^2 < 0$. The Freundlich's experimental model is based on following equation:

Equation 16 – Freundlich's isotherm.

$$Q = F \cdot C^{1/n}$$

where F and n are the Frendlich's constants, Q is the entrapped amount and C is the equilibrium concentration. The linear shape for this model for the determination of the constants is the following:

Equation 17 –Linear shape for the Freundlich's isotherm.

$$\ln(Q) = \ln(F) + \frac{1}{n}\ln(C)$$

Using this method, ln(Q) was plotted as function of ln(C) and a linear regression was traced with software OriginPro. The constant F was obtained by *exp*(intercept), whereas the constant 1/n was obtained by the slope. The parameters for the only presented Freundlich fitting (5-Fe) are reported in Table 4.

Table 4 - Freundich's parameters for the cobalt adsorption on 5-Fe.

Adsorbent	*F*	*1 / n*
5-Fe	1.77	0.35

Another experimental model is the Temkin's isotherm. This model is based on following equation:

Equation 18 – Temkin's isotherm.

$$Q = B \cdot \ln(A \cdot C)$$

where *A* and *B* are the constants and *Q* is the entrapped amount at equilibrium concentration *C*. The linear shape for the determination of the constant is the following:

Equation 19 – Linear shape for the Temkin's isotherm.

$$Q = B \cdot \ln(A) + B \cdot \ln(C)$$

Using this method, *Q* was plotted as function of ln(*C*) and a linear regression was traced with OriginPro. The constant *B* was obtained from the slope, whereas the constant *A* was obtained from the intercept after the calculation of *B*.

3.3 - BET and BJH models.

The N_2 adsorption isotherms recorded for the silica-based materials were useful for the determination of some structural features, as the exposed specific surface areas and the pore size distribution. On the adsorption isotherm, the methods Brunauer-Emmett-Teller (BET) and Barrett-Joyner-Halenda (BJH) were applied for the determination of the specific surface area (BET) and the pore distribution (BJH).

The BET model is an extension of the ideal Langmuir model, since it considers the formation of multilayers of adsorbate on the substrate. In this model a new equilibrium constant is defined (K_m) for the adsorption of molecules on already formed adsorbate layers. The constant K_m is different from the constant K that describes the adsorption of a monolayer in the Langmuir model. Also, when the coverage tends to infinity, the constant K_m tends to $\frac{1}{P_0}$ where P_0 is the saturation pressure. Since in the instrument measures the volumes of adsorbed N_2 at equilibrium, the coverage is expressed as $\frac{V}{V_1}$, where V is the adsorbed volume and V_1 is the volume to form a monolayer. The coverage can be written as a function of the relative pressure $x = \frac{P}{P_0}$ and the ration between the equilibrium constants $c = \frac{K}{K_m}$ as follows:

Equation 20 – BET model.

$$\frac{V}{V_1} = \frac{c \cdot x}{(1-x)[1+(c_1)x]}$$

In a specific range of relative pressures i.e. between x = 0.05 and x = 0.35, this relationship allows an estimation of the surface area exposed per unit mass. For this purpose, the linear shape of Equation 20 is necessary:

Equation 21 - Linear shape for the BET isotherm.

$$\frac{x}{V(1-x)} = \frac{1}{V_1} + \frac{x(c-1)}{V_1 c}$$

The parameters c and V_1 are determined by plotting $\frac{x}{V(1-x)}$ as a function of x, in the interval of validity of the BET model. The slope a and the intercept b of the linear regression allow the determination of the c and V_1 as follows:

Equation 22 – BET parameters.

$$V_1 = \frac{1}{a+1} \qquad\qquad c = \frac{a}{b} + 1$$

The model has physical meaning exclusively, when c > 0. The parameter V_1 (the volume for the formation of a monolayer) is generally in the unit [cm^3] or [$cm^3.g^{-1}$]. In the present work, the value for V_1 was converted in moles of N_2 by the molar volume v = 22.414 $L.mol^{-1}$ (or 22'414 $cm^3.mol^{-1}$). Number of moles was converted then in number of molecules by the Avogadro's number (N_A = $6.023 \bullet 10^{23}$ mol^{-1}) and finally the cross-sectional area of N_2 (A = 0.162 nm^2) was used to find the surface area. Normalization on the mass of adsorbent (m) gave the specific surface area (SSA), generally expressed in units [$m^2.g^{-1}$]. In summary, the SSA was found with the following relationship:

Equation 23 – Specific Surface Area.

$$SSA = \frac{V_1 \cdot N_A \cdot A}{v \cdot m}$$

The method of Barrett-Joyner-Halenda (BJH) is a technique to find the distribution of the pore size (< 60 nm). The method is based on the assumption that pores have a cylindrical shape and that pore radius is equal to the sum of the Kelvin radius and the thickness of the film adsorbed on the pore wall. The Kelvin radius (r) is the the equilibrium radius that satisfies the following relationship:

Equation 24 – Kelvin equation.

$$\ln\left(\frac{P}{P_0}\right) = \frac{2\gamma V_A}{rRT}$$

where P/P_0 is the relative pressure, γ is the surface tension, V_A is the molar volume, R is the gas constant, T is the temperature and r is the Kelvin radius. The desorption branch of isotherm in the relative pressure range P/P_0 = 0.4-0.967 is generally used as initial data for BJH calculations (although the use of the adsorption branch is also possible).

In conclusion, when the adsorption isotherm exhibits a hysteresis due to the presence of mesopores, the shape of the hysteresis can give information about the pore shape. An interpretation of the relationship between hysteresis shape and pore shape was proposed by DeBoer in 1968 (Figure 5).‡

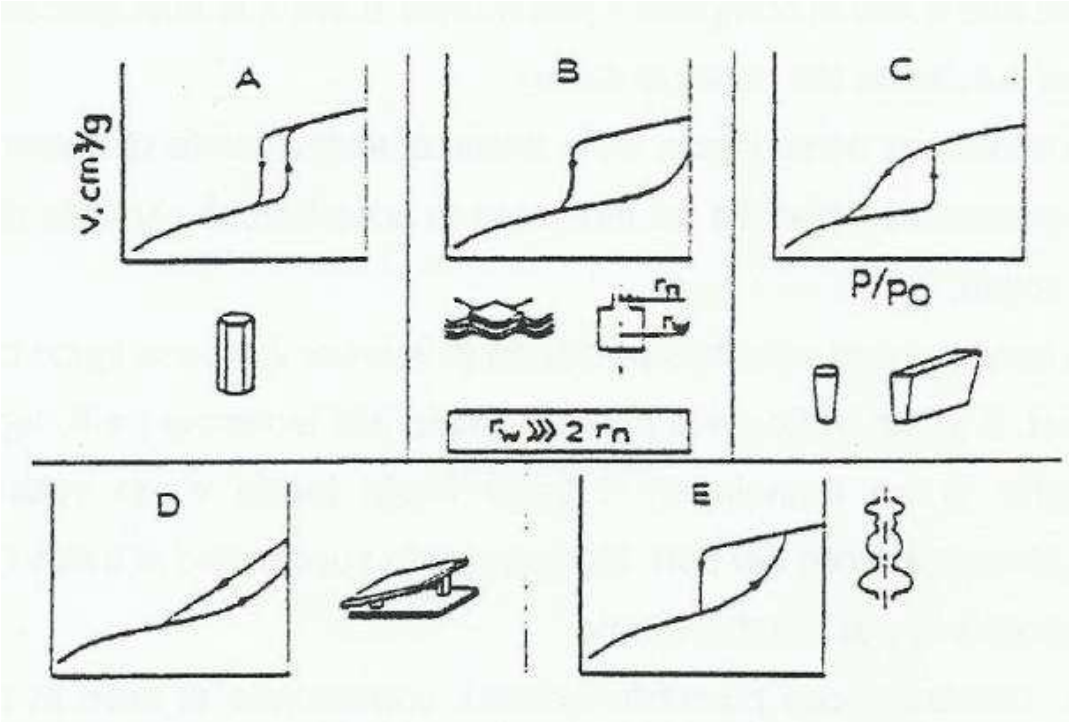

Figure 6 - DeBoer classification of the hystereses according to the pore shape.

‡‡ Broekenhoff J..P. De Boer H.H. J. *Catal.* (1968) 10, 153-165.

Annex 4 - Mass spectroscopy and thermogravimetric analysis.

The desorption temperature of the iodine was detected my mass spectroscopy. The exiting volatile molecules were detected by their molecular weight, by analysing the air stream out of the instrument. For a specific detected molecule, data consisted in two plots: 1) the raise in temperature as a function of time; 2) the amount of the released molecule as function of time. An example for the release of I_2 off a Hofmann-type structure as $Co^{II}(pz)[Ni^{II}(CN)_4]$ is now reported. The curve of the release of I_2 as function of time showed a steep increase starting at t = 2439 s with a maximum at 3082 s. With the temperature-to-time plot it was possible to associate the temperature values to the time values (in Figure 7).

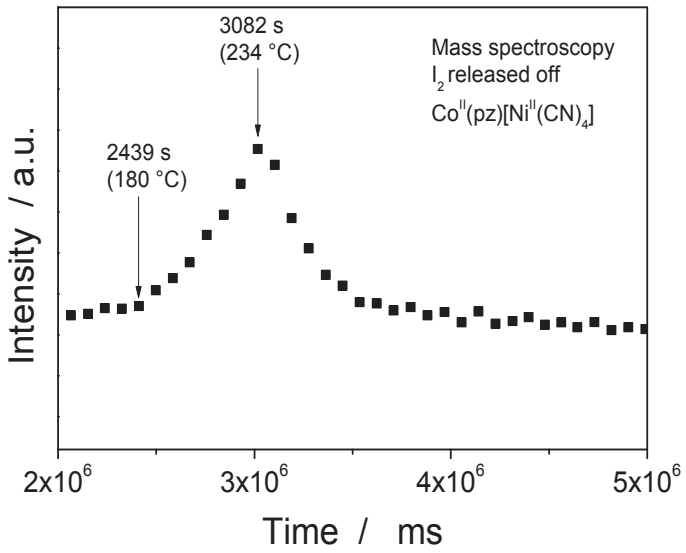

Figure 7 - Mass spectroscopy plot for $Co^{II}(pz)[Ni^{II}(CN)_4].I_2$

TGA analysis was very important to support the quantification of the maximal capacities after capture of I_2 for the family of the Hofmann-type clathrates and the nanocomposites Sil@NP and Glass@NP. We report here an example of calculation of the amount of entrapped iodine for the host clathrate $Co^{II}(pz)[Ni^{II}(CN)_4]$ at maximal loading. The TGA curve for this clathrate is reported in Figure 8. We detected an initial loss of solvent that was quantified as a loss of -9% of mass. The loss of iodine was comprised between 150°C and 200 °C, this corresponded to a loss of -34% of mass and finally the decomposition of ligands (4 equivalents of CN^- and one equivalent of pyrazine) occurred after 350 °C and corresponded to a loss of -25% of mass. Coupled mass spectroscopy was fundamental to confirm the chemical species that decomposed at each transformation.

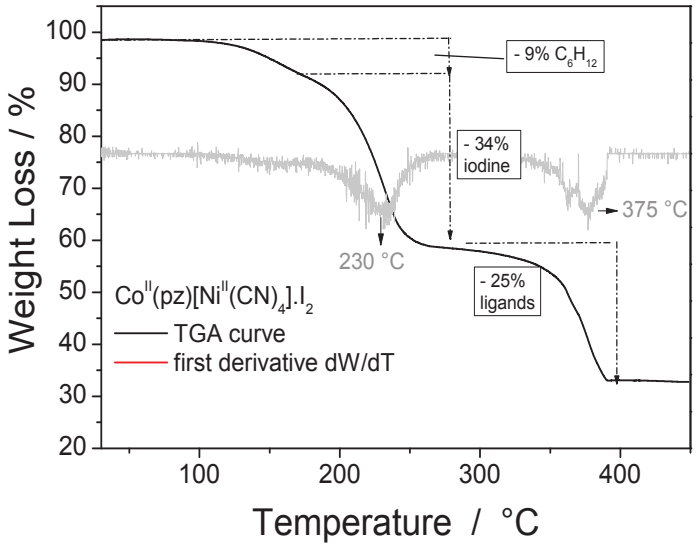

Figure 8 - TGA for $Co^{II}(pz)[Ni^{II}(CN)_4].I_2$

It was estimated an error of ±0.5% on the quantification for each percentage value. In the hypothesis to have 100 g of starting material, each loss of mass (in unit mass [g]) was divided by the molar weight of the released species:

Table 5 – Estimation by TGA of the molar ratios among the released species.

Decomposed species	Molar weight (MW) [g/mol^{-1}]	Mass loss on 100 g (ML) [g]	MW / ML [mol]
C_6H_{12}	84	9	0.1071
I_2	253.8	34	0.1339
4 CN^- + $C_4H_4N_2$	184	25	0.1358

The respective ratios among the species gave the maximal capacity of $Ni^{II}(pz)[Ni^{II}(CN)_4]$ calculated by TGA:

$$[mol]\ I_2 / [mol]\ (4\ CN^- + C_4H_4N_2) = 0.1339 / 0.1358 = 0.98 \pm 0.02 \approx 1\ I_2 \text{ per unit cell}$$

Finally, TGA curves were used to determine the temperature with the higher rate of decomposition, measured in weight loss per unit temperature. For this purpose the first derivative was calculated using software OriginPro (Figure 8, grey curve). The negative peaks corresponded to the inflection point in the TGA curves, *i.e.* the points where the decomposition rate in a specific transformation was the faster. For instance, for the decomposition of the iodine off $Co^{II}(pz)[Ni^{II}(CN)_4]$, the faster rate was at 230 °C.

Annex 5 - X-ray diffraction and LeBail refinement.

Experimental X-Ray diffraction patterns were registered in good quality for the determination of the lattice parameters. The determination was carried out approximately using the Bragg's law and the results were refined by LeBail method.

5.1 – Experimental determination of the lattice parameters.

The relationship that describes the X-ray diffraction is the Bragg's law (Equation 25). The law determines the geometrical condition that the reflecting X-ray radiation, with wavelength λ and reflecting angle θ, must satisfy in order to give a diffraction phenomenon through a set of ordered atomic planes distancing from each other by length *d*.

Equation 25 – Bragg's law.

$$n\lambda = 2d \cdot sin\theta$$

The resulting patterns shows intense peaks at the angles that satisfied the Bragg's law, so that from the x-axis values (expressed in units 2θ) it is possible to determine the distance of the associated set of atomic planes (expressed in [Å] or [nm]). By knowing the values for d, an estimation of the lattice parameters *a*, *b*, and *c* of the unit cell can be carried out. At first, it is necessary to index the diffraction peaks with the corresponding Miller indices (hkl). Miller indices are parameters to label a set of planes in a crystal lattice. Ech index denotes a plane which is orthogonal to a direction in the basis of the reciprocal lattice vectors. Some examples of indexations are reported in Figure 9 for a cubic lattice.

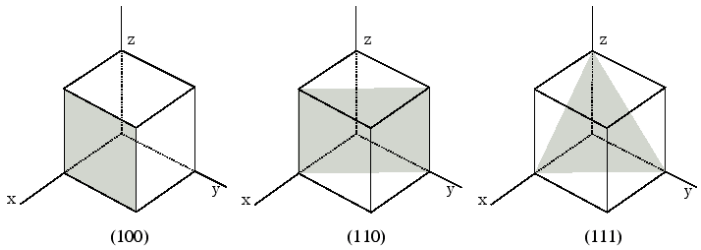

Figure 9 – Miller indices (examples).

In the present work, it was helpful to find in literature the Crystallographic Information Files (CIFs) for analogue structures, in order to index correctly recognize the diffraction peaks in the studied materials. The Miller indices *(hkl)* and the lattice parameters *a, b*, and *c* are related to a specific interatomic distance by the following relationship:

Equation 26 – Relationship between the lattice parameters and the Miller indices.

$$\frac{1}{d^2} = \frac{h^2}{a^2} + \frac{k^2}{b^2} + \frac{l^2}{c^2}$$

The equation can be simplified for a specific Miller plane. For instance, we report in some simplified equations.

Table 6 – Examples of simplified relationship for some used Miller planes.

Miller indices (hkl)	Simplified equation	Lattice parameters
(100)	$\frac{1}{d^2} = \frac{1}{a^2}$	$a = d$
(001)	$\frac{1}{d^2} = \frac{1}{c^2}$	$c = d$
(110) *with a = b*	$\frac{1}{d^2} = \frac{2}{a^2}$	$a = b = \sqrt{2}d$
(200)	$\frac{1}{d^2} = \frac{4}{a^2}$	$a = 2d$
(020)	$\frac{1}{d^2} = \frac{4}{b^2}$	$b = 2d$
(002)	$\frac{1}{d^2} = \frac{4}{c^2}$	$c = 2d$

In the present work, unfilled Hofmann-type networks exhibited a tetragonal lattice with $a = b \neq c$ and $\alpha = \beta = \gamma = 90°$. The planes used to estimate the lattice parameters were the (100), (001), (110), (200), (002). For the structures that after I_2-loading indicated a change of symmetry from tetragonal to orthorhombic ($a \neq b \neq c$, $\alpha = \beta = \gamma = 90°$) the Miller plane (020) was used as well.

5.1 – Lebail Refinement.

In this section we report all data related to the LeBail refinement. The nature of the crystalline phase was confirmed by indexing the whole diffraction pattern, then a whole-pattern decomposition (LeBail fitting) with constant scale factor and a Pseudo-Voigt function profile, to approximate the mine-broadening, was applied.[§] LeBail refinement techniques using Fullproff software[**] were conducted in order to perform a profile refinement of diffraction peaks. The scale factor, zero point of detector, background parameters and lattice constants were refined in the first round, then peak shape and asymmetry parameters were added at latest when the models already converged. Finally, instrumental or physical aberration corrections were added to the least squares refinement by using parameters sycos and sysin. In the following pages the refined XRPD pattern for the following Hofmann-type structures will be reported: $Ni^{II}(pz)[Ni^{II}(CN)_4]$, $Ni^{II}(pz)[Pd^{II}(CN)_4]$, $Ni^{II}(pz)[Pt^{II}(CN)_4]$, $Co^{II}(pz)[Ni^{II}(CN)_4]$ and $Ni^{II}(bpy)[Ni^{II}(CN)_4]$ and related I_2-loaded structures. The found lattice parameters will be reported under each refinement.

[§] Favre-Nicolin V., Cermy R. *J. Appl. Cryst.* (2002) 35, 734.

[**] Fullprof 2000 version July 2001, Juan Rodrigues-Carvajal, Laboratoire Leon Brillouin (CEA-CNRS), 91191 Gif sur Yvette Cedex, France.

Refinement for $Ni^{II}(pz)[Ni^{II}(CN)_4]$

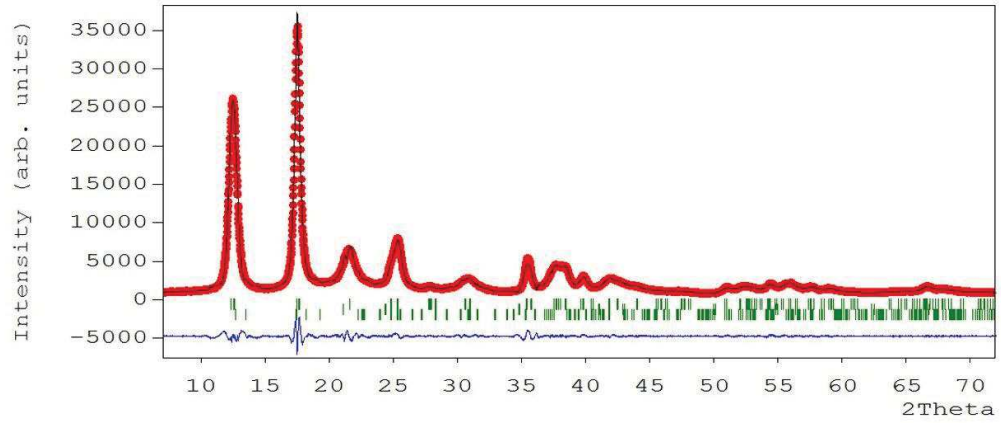

Figure 10 - Tetragonal system; Space group P 4/m. Cell Parameters: a = b = 7.1762(3) Å, c = 7.0316(5) Å, $\alpha = \beta = \gamma = 90.0°$, Vol: 362.10(3) $Å^3$.

Refinement for $Ni^{II}(pz)[Ni^{II}(CN)_4]\bullet I_2$

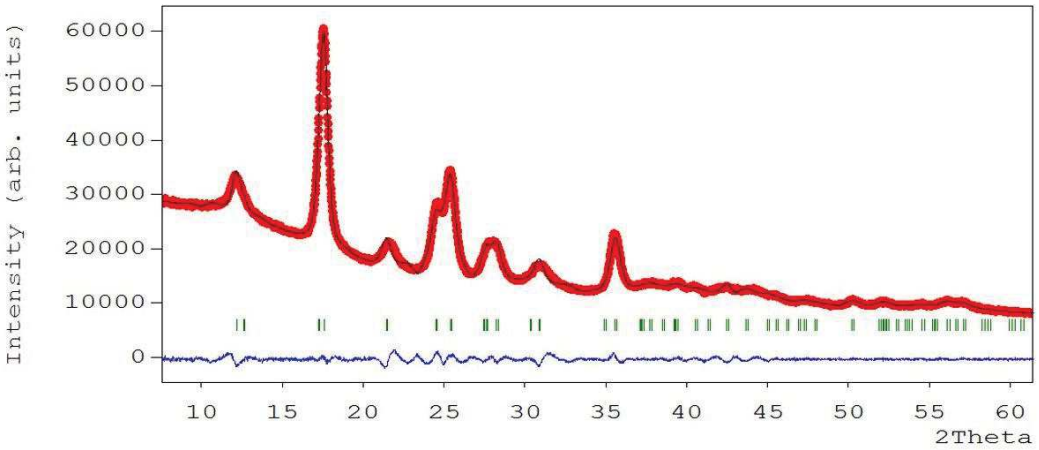

Figure 11 - Tetragonal system; Space group P 4/m. Cell parameters: a = b = 7.2605(6) Å, c = 7.0072(5) Å, $\alpha = \beta = \gamma = 90.0°$, Vol: 369.385(2) $Å^3$.

Refinement for $Ni^{II}(pz)[Pd^{II}(CN)_4]$

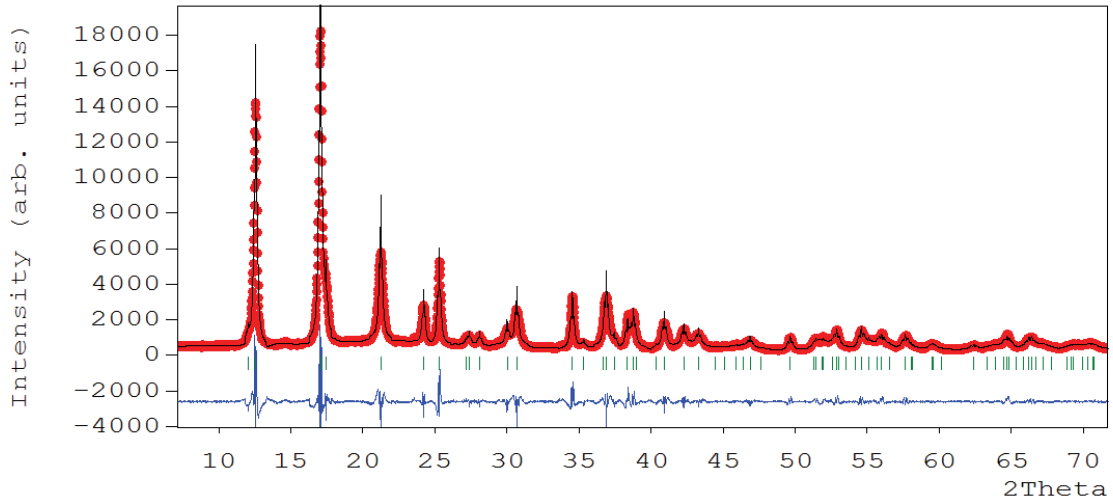

Figure 12 - Tetragonal system; Space group P 4/m. *Cell parameters: a = b = 7.3384(2) Å, c = 7.0325(3) Å α = β = γ = 90.0° Vol: 378.71(4)* $Å^3$.

Refinement for $Ni^{II}(pz)[Pd^{II}(CN)_4]•I_2$

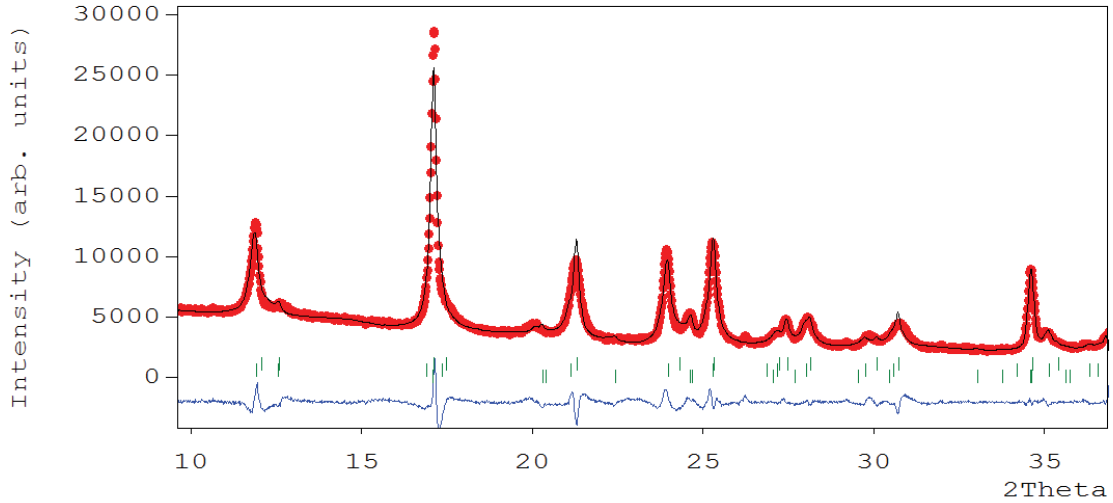

Figure 13 - *Orthorombic system; Space group Pcmm. Cell parameters: a = 7.4310(5) Å, b = 7 .2319(7) Å, c = 7 .0382(7) Å α = β = γ = 90.0°. Vol: 378.23(4)* $Å^3$.

Refinement for $Ni^{II}(pz)[Pt^{II}(CN)_4]$

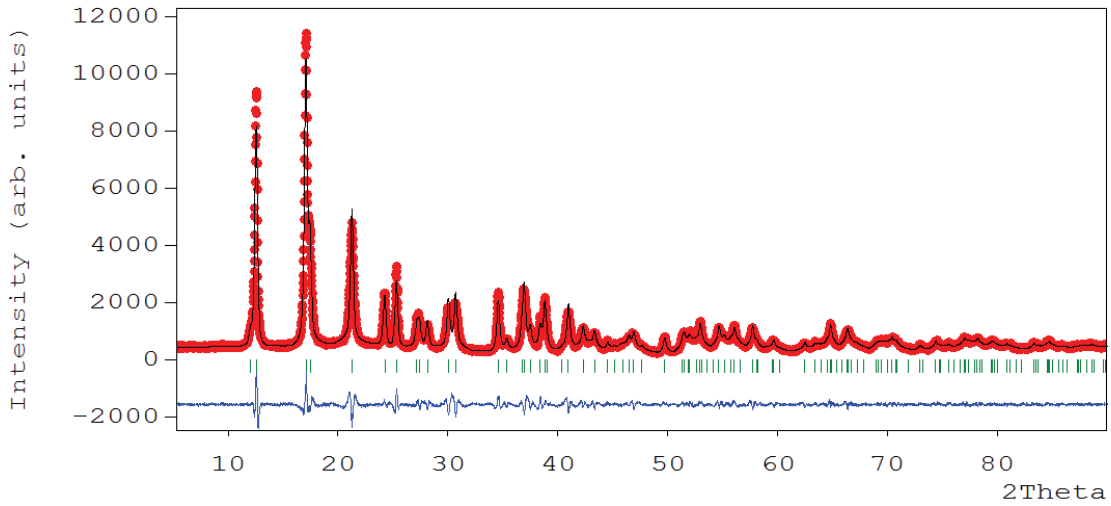

Figure 14 - Tetragonal system; Space group P 4/m, cell parameters: Cell parameters: *a = b = 7.3310(3) Å, c = 7.0299(8) Å α = β = γ = 90.0°*, Vol: 377.81(1) $Å^3$.

Refinement for $Ni^{II}(pz)[Pt^{II/IV}(CN)_4]•I^-$

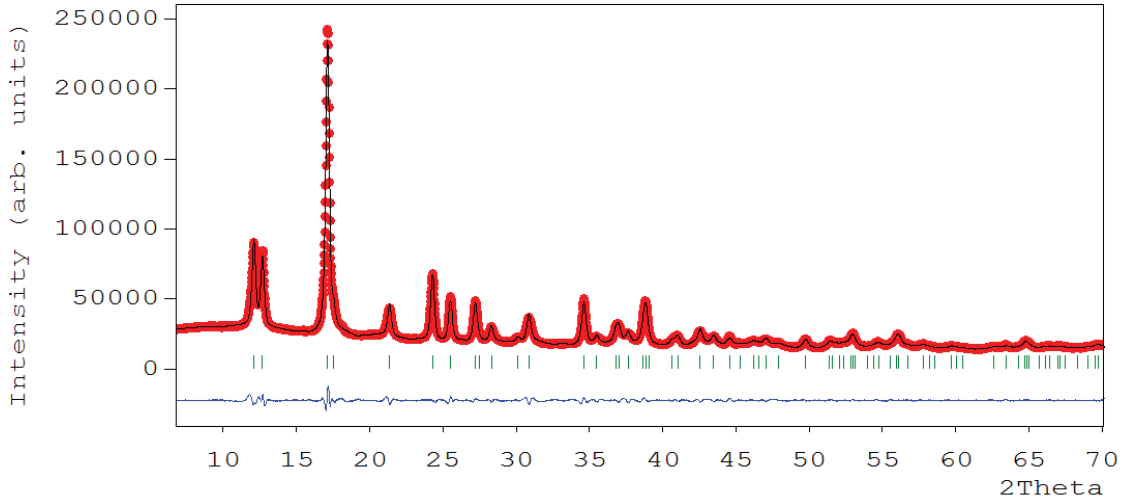

Figure 15 - Tetragonal system; Space group P 4/m. Cell parameters: *a = b = 7.1775(3) Å, c = 6.9789(4) Å α = β = γ = 90.0°*, Vol: 359.53(3) $Å^3$.

Refinement for $Co^{II}(pz)[Ni^{II}(CN)_4]$

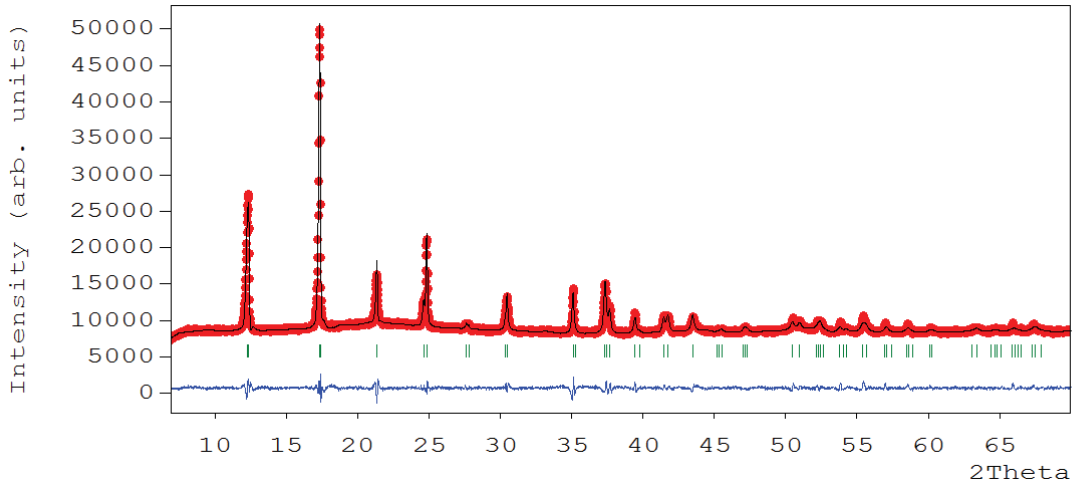

Figure 16 - Tetragonal system; Space group P 4/m. Cell parameters: $a = b = 7.2262(7)$ Å, $c = 7.1594(9)$ Å, $\alpha = \beta = \gamma = 90.0°$, Vol: 373.84(9) $Å^3$.

Refinement for $Co^{II}(pz)[Ni^{II}(CN)_4]\bullet I_2$

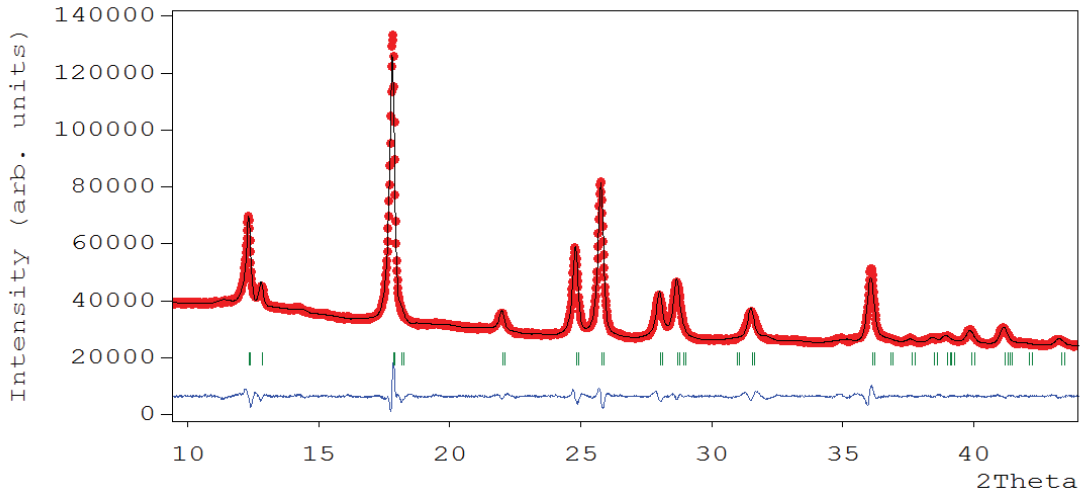

Figure 17 - Tetragonal system; Space group P 4/m, Cell parameters: $a = b = 7.1593(5)$ Å, $c = 6.8942(5)$ Å, $\alpha = \beta = \gamma = 90.0°$, Vol: 353.3(6) $Å^3$.

Refinement for $Ni^{II}(bpy)[Ni^{II}(CN)_4]$

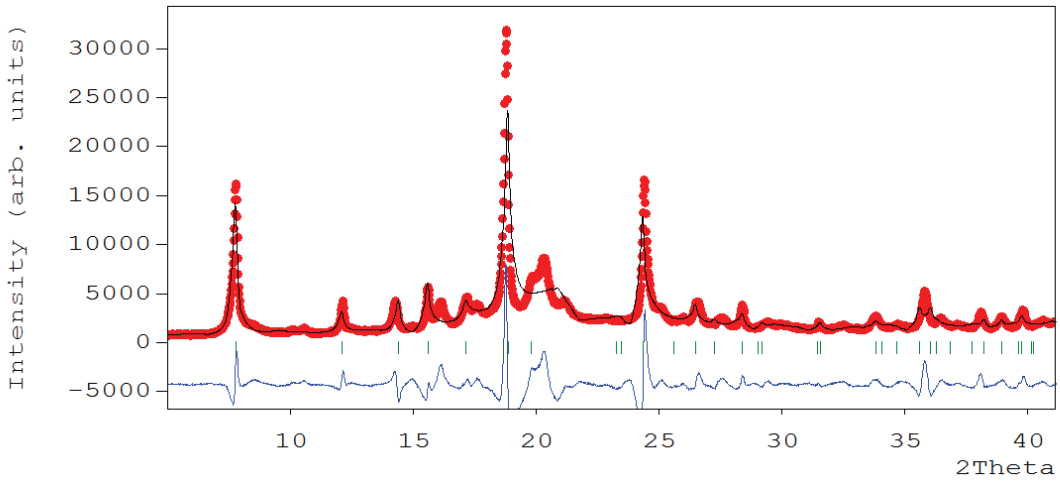

Figure 18 - Tetragonal system; Space group P 4/mmm, Cell parameters: $a = b = 7.30(9)$ Å, $c = 11.36(3)$ Å, $\alpha = \beta = \gamma = 90.0°$, Vol: 605.3(7) $Å^3$.

Refinement for $Ni^{II}(bpy)[Ni^{II}(CN)_4]\bullet 0.25\ I_2$

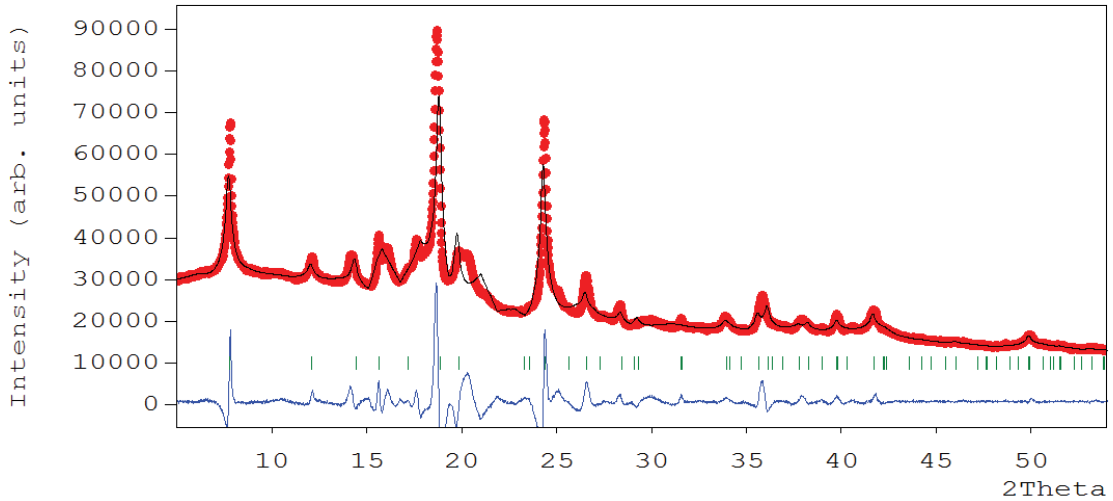

Figure 19 - Figure 20 - Tetragonal system; Space group P 4/mmm. Cell parameters: $a = b = 7.29(9)$ Å, $c = 11.32(3)$ Å, $\alpha = \beta = \gamma = 90.0°$, Vol: 601.5(9) $Å^3$.

Annex 6 - UV-VIS spectroscopy in reflectance mode.

To study the electronic state of iodine in the solid samples, the materials were analysed by UV-VIS spectroscopy in reflectance mode, using an integrating sphere. The integrating sphere is a hollow element where the scattered radiation from the surface is collected and analysed. A representation of the geometry of the system is reported in Figure 21.

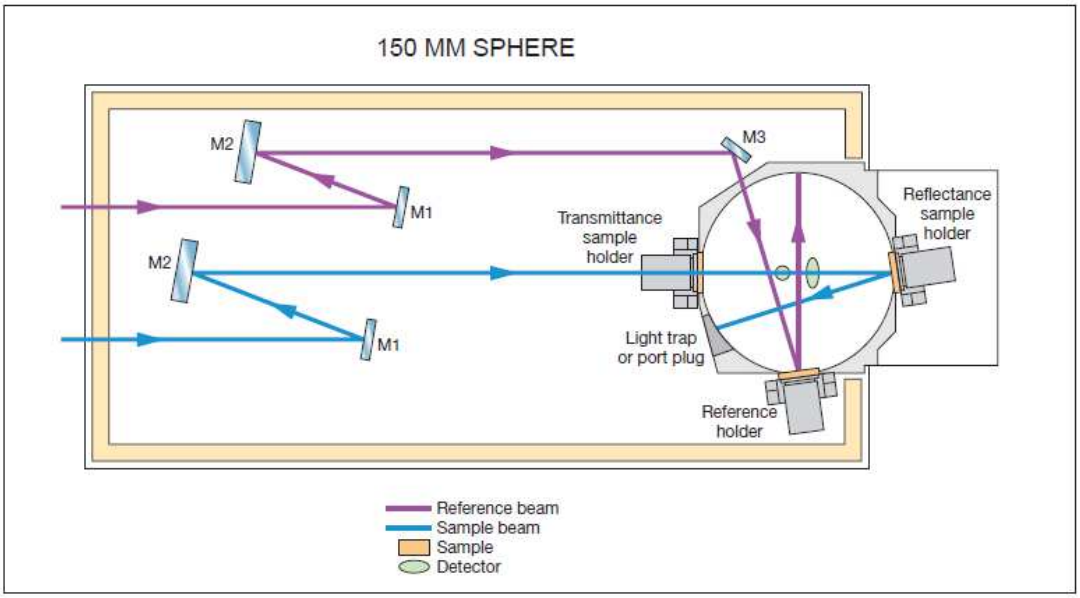

Figure 21 - Representation of the integrating sphere in a UV-VIS spectrometer in reflectance mode. (www.perkinelmer.com)

The spectra were registered in the range λ = 300-800 nm and then converted in Kubelka-Munk function. This function is generally used to compensate the differences between reflectance and the transmission spectra. The function is applied on the reflectance values (R) as follows:

Equation 27 – Kubelka Munk function (K-M)

$$F(R) = \frac{(1-R)^2}{2R}$$

The resulting spectrum shows positive “absorption” bands in the intervals where the reflectance of the materials was low.

Annex 7 – Estimation of the composition of the nanocomposites by elemental analysis and SEM/EDX.

We report here an example of calculation to estimate the amount of $Ni^{II}(pz)[Ni^{II}(CN)_4]$ deposited on a diamine-grafted silica support. Since in the diamine ligand used to graft the silica (MW = 100 $g.mol^{-1}$), there are 2 equivalents of N (MW = 14 $g.mol^{-1}$), the wt% of grafting agent was determined by:

Equation 28 – Estimated amount of grafting agent.

$$wt\%\ diammine = \frac{wt\%\ N}{2} \cdot \frac{100}{14}$$

For instance, for a diamine-grafted silica with 2.16 wt% N, elemental analyses indicated 8 wt% of diamine ligand. To quantify the weight increase after the grafting process, the following formula can be used:

Equation 29 – Weight increase after grafting.

$$y = \frac{wt\%\ diammine}{100 - wt\%\ diammine}$$

then the masse of silica has to be multiplied times (1+y). For instance, with 9 wt% of diamine, 1 g of non-grafted SiO_2 will weighs 1.098 g after the grafting process.

For the amount of deposited $Ni^{II}(pz)[Ni^{II}(CN)_4]$ (301.4 $g.mol^{-1}$), the wt% of Ni was used for a direct quantification, knowing that the formula for the Hofmann-type structure contains 2 equivalents of Ni (58.6 $g.mol^{-1}$):

Equation 30 – Relationship between the amount of Ni and the amount of nanoparticles.

$$wt\%\ NP = \frac{wt\%\ Ni}{2} \cdot \frac{301.4}{58.6}$$

For a Glass@NP, the amount wt% Ni = 7.0 % gave 17.9 wt% of NP. Another way to estimate the amount of $Ni^{II}(pz)[Ni^{II}(CN)_4]$ demanded to know the wt% amount of diamine and the weight ratio wt% Ni over wt% Si registered by SEM/EDX. An unknown amount of wt% Si was called *x*. In the hypothesis to have wt% grafting = 9% and Ni/Si = 0.22 (wt%/wt%), the amount of diamine-grafted silica (Glass) and of $Ni^{II}(pz)[Ni^{II}(CN)_4]$ (NP) were estimated as follows:

Equation 31 – Estimation of the amount of nanoparticles.

$$Glass = \left(\frac{x}{28} \cdot 60\right) \cdot 1.098 = 2.352x$$

$$NP = \frac{0.22x}{2} \cdot \frac{301.4}{58.6} = 0.565x$$

knowing that MW for Si is 28 g.mol^{-1} and MW for SiO_2 is 60 g.mol^{-1}. The coefficient 1.09 is the weight increase after grafting and 0.25x is the proportional amount of Ni. By dividing the two amounts by the sum Glass + NP = 2.917x :

Equation 32 – Final results.

$$wt\%\ Glass = \frac{2.352}{2.917} = 81\ wt\%$$

$$wt\%\ NP = \frac{0.643}{2.917} = 19\ wt\%$$

By comparing the two calculations, a small difference was noticed due to the presence of impurities. To estimate the attended wt% value of a specific element, for instance, the wt% values were multiplied by the respective weight ratios of the element. For instance, the $Ni^{II}(pz)[Ni^{II}(CN)_4]$ has 8 equivalent of C (12 g.mol^{-1}) and the diamine-grafted glass contains 5.45 wt% of C. Thus the total estimated amount of wt% C is given by sum:

Equation 33 – Estimation for the other elements.

$$wt\%\ C = \frac{8 \cdot 12}{301.4} \cdot wt\%NP + z \cdot wt\%Glass$$

where *z* is the weight ratio of C found in *Glass* material by elemental analysis. Similarly, the estimations for the elements N, H, Ni and O were carried out.

Summary.

Nuclear power industry still demands further research to improve the methods for the storage and the confinement of the hazardous radioactive wastes coming from the fission of radionuclide ^{235}U. The volatile radioactive ^{129}I (half-life time $15x10^7$ years) is one of the most critical products coming from the reprocessing plants in the fuel-closed cycles. In the present thesis the family of coordination solid networks, known as Hofmann-type structures, was studied in the form as both bulk and supported nanoparticles for the selective entrapment of the molecular iodine. This set of investigated materials exhibited a general formula M'(L)[M''(CN)4] where M' = Ni^{II} or Co^{II}; L = pyrazine, 4,4'-bipyridine, 4,4'-azopyridine; M'' = Ni^{II}, Pd^{II} or Pt^{II}. Initially, the material $Ni^{II}(pz)[Ni^{II}(CN)_4]$ and its analogue structures were precipitated as microcrystalline bulky compounds and fully characterized. The insertion of the iodine in the bulky host structures was performed with different methods: 1) adsorption of iodine in solutions of cyclohexane at room temperature; 2) adsorption of iodine vapours at 80 °C; 3) adsorption of iodine vapours at 80 °C in presence of water steam (for few selected materials). The different methods did not affect the nature of the confined iodine. For the entrapment in solution, results indicated that the Hofmann-type structures $Ni^{II}(pz)[Ni^{II}(CN)_4]$, $Ni^{II}(pz)[Pd^{II}(CN)_4]$ and $Co^{II}(pz)[Ni^{II}(CN)4]$ could host one I_2 molecule per unit cell. The iodine resulted physisorbed as molecular iodine in interaction with the host structure. GCMC simulations confirmed the maximal capacities and indicated that iodine could interact with both the pyrazine and the coordinated cyanides. Experimentally, however, the modulation of the metals showed a slightly different strength of interaction I_2-lattice bringing to a different lattice adaptation. The materials also could be fully regenerated since the complete desorption of iodine occurred before the decomposition of the host structure. Reiterated adsorption-desorption steps (3 cycles) on the networks $Ni^{II}(pz)[Ni^{II}(CN)_4]$ and $Ni^{II}(pz)[Pd^{II}(CN)_4]$ indicated an excellent structural resistance to cycling and a maintained high capacity. A different mechanism of confinement was detected for the structure $Ni^{II}(pz)[Pt^{II}(CN)_4]$ which reacted with iodine giving complex $Ni^{II}(pz)[Pt^{II/IV}(CN)_4].I^-$. Finally, the modulation of the organic ligand L indicated that the replacement of the ligand pyrazine with longer ligands, to obtain larger pores, had a detrimental effect on the maximal iodine loading due to a weaker confinement. After the study of the bulk materials, we considered the preparation of supported nanoparticles of $Ni^{II}(pz)[Ni^{II}(CN)_4]$ for the entrapment of iodine. The nanoparticles were obtained by a step-by-step method, impregnating a set of diammine-grafted mesoporous silicas with the precursors of $Ni^{II}(pz)[Ni^{II}(CN)_4]$. We detected nanoparticles with mean size 2.8 nm by transmission electronic microscopy. The insertion of iodine in the nanoparticles was confirmed by FT-IR. Thermal treatments indicated that the portion of iodine inside the nanoparticles could be reversibly desorbed in the range 150-250 °C and reintroduced in a cyclic process. It was estimated that the amount of physisorbed iodine in the NPs, with respect to the amount of deposited NPs matched with the maximal capacity $Ni^{II}(pz)[Ni^{II}(CN)4]\bullet I_2$.

Key-words : coordination chemistry, radioactive elements, nanoporous materials, selective decontamination.

Resumé.

La production d'énergie nucléaire nécessite des systèmes avancés pour améliorer les procédures de stockage et de confinement des déchets radioactifs. Par ailleurs, la capture d'éléments radioactifs mobiles dans les effluents des centrales nucléaires demande une amélioration de la capacité e de la sélectivité. L'iode 129-I est un des produits les plus critiques à confiner et il est produit pendant les procédés de recyclage des déchets nucléaires. Dans ce travail de thèse, la classe de matériaux moléculaires, dénommée structures de type Hofmann, a été étudiée en tant que matériaux massifs et nanoparticules supportées pour la capture sélective de l'iode moléculaire. En premier lieu, les matériaux M'(L)[M''$(CN)_4$] ont été précipités sous la forme de poudres microcristallines. L'insertion d'iode dans le réseau des matériaux massifs a été effectuée par différents protocoles: 1) adsorption d'iode dans des solutions de cyclohexane à température ambiante; 2) adsorption d'iode en phase gazeuse à 80 °C; 3) adsorption de vapeurs d'iode en phase gazeuse à 80 °C et en présence de vapeurs d'eau. Les différents protocoles pour l'insertion d'iode n'ont pas influencé la nature de l'iode confiné. Pour la capture en solution, les structures $Ni^{II}(pz)[Ni^{II}(CN)_4]$, $Ni^{II}(pz)[Pd^{II}(CN)_4]$ et $Co^{II}(pz)[Ni^{II}(CN)_4]$ ont montré une capacité d'une molécule d'iode par unité de maille. L'iode confiné est physisorbé en tant qu'iode moléculaire en interaction avec le réseau. Les modélisations GCMC ont confirmé la capacité maximale et ils ont indiqué que l'iode interagit avec la pyrazine et avec les cyanures. Sur la base des données expérimentales, la modulation des métaux dans le réseau a montré une légère différence dans la force d'interaction entre l'iode et le réseau et une adaptation de la maille spécifique pour chaque composition. Une complète régénération du réseau a été possible, puisque l'iode était complètement désorbé avant la décomposition du réseau. Pour le réseau $Ni^{II}(pz)[Pt^{II}(CN)_4]$, on a observé un mécanisme différent de capture puisque ce réseau contenant Pt a réagi avec l'iode en donnant le complexe de coordination $Ni^{II}(pz)[Pt^{II/IV}(CN)_4].I^-$. La formation de ce type de complexe était déjà observée dans la littérature par Ohtani *et al.* lesquels avaient préparé le complexe *via* une synthèse *in-situ.* Ensuite, le changement du ligand organique pyrazine avec d'autres ligands plus longs, c'est-à-dire la 4,4'-bipyridine (bpy) ou 4,4'-azopyridine (azpy), pour avoir des cages plus grandes a montré une diminution de la capacité maximale de capture d'iode. Les données expérimentales ont suggéré que pour un confinement d'iode optimisé, le réseau doit disposer de cages avec une dimension très proche de la molécule d'iode (0.5 nm). Après l'étude des matériaux massifs, nous avons considéré la préparation de nanoparticules supportées de $Ni^{II}(pz)[Ni^{II}(CN)_4]$ pour la capture d'iode. Nous avons obtenu les nanoparticules *via* un procédé étape par étape*,* par imprégnation d'une série de silices mésoporeuses greffées avec un ligand diamine, puis avec les précurseurs de $Ni^{II}(pz)[Ni^{II}(CN)_4]$. Nous avons utilisé en tant que supports, une silice SBA-15 modifiée et des billes de verre poreux pour obtenir respectivement les nanocomposites Sil@NP and Glass@NP. Par microscopie électronique à transmission, nous avons détecté pour Sil@NP des nanoparticules de diamètre moyen 2.8 nm. L'adsorption d'iode dans les nanoparticules a été confirmée par spectroscopie FT-IR. Les traitements thermiques ont indiqué que la portion d'iode dans les nanoparticules pouvait être désorbé dans l'intervalle 150-250 °C. Nous avons pu estimer que la capacité de capture des nanoparticles était très proche de la capacité du massif $Ni^{II}(pz)[Ni^{II}(CN)_4]\bullet I_2$.

Mots-clé : chimie de coordination, éléments radioactifs, matériaux nanoporeux, décontamination sélective.